INVESTIGATING THE COSMIC-RAY IONIZATION RATE IN THE GALACTIC
INTERSTELLAR MEDIUM THROUGH OBSERVATIONS OF H_3^+

BY

NICHOLAS INDRIOLO

DISSERTATION

Submitted in partial fulfillment of the requirements
for the degree of Doctor of Philosophy in Astronomy
with a concentration in Astrochemistry
in the Graduate College of the
University of Illinois at Urbana-Champaign, 2011

Urbana, Illinois

Doctoral Committee:

      Assistant Professor Benjamin J. McCall, Chair
      Associate Professor Brian D. Fields
      Associate Professor Leslie Looney
      Professor Richard M. Crutcher
      Professor You-Hua Chu

Abstract

Observations of H_3^+ in the Galactic diffuse interstellar medium (ISM) have led to various surprising results, including the conclusion that the cosmic-ray ionization rate (ζ_2) is about 1 order of magnitude larger than previously thought. The present survey expands the sample of diffuse cloud sight lines with H_3^+ observations to 50, with detections in 21 of those. Ionization rates inferred from these detections are in the range $(1.7 \pm 1.0) \times 10^{-16}$ s^{-1} $< \zeta_2 < (10.6 \pm 6.8) \times 10^{-16}$ s^{-1} with a mean value of $\zeta_2 = (3.3 \pm 0.4) \times 10^{-16}$ s^{-1}. Upper limits (3σ) derived from non-detections of H_3^+ are as low as $\zeta_2 < 0.4 \times 10^{-16}$ s^{-1}. These low upper-limits, in combination with the wide range of inferred cosmic-ray ionization rates, indicate variations in ζ_2 between different diffuse cloud sight lines.

Calculations of the cosmic-ray ionization rate from theoretical cosmic-ray spectra require a large flux of low-energy (MeV) particles to reproduce values inferred from observations. Given the relatively short range of low-energy cosmic rays — those most efficient at ionization — the proximity of a cloud to a site of particle acceleration may set its ionization rate. Variations in ζ_2 are thus likely due to variations in the cosmic-ray spectrum at low energies resulting from the effects of particle propagation. To test this theory, H_3^+ was observed in sight lines passing through diffuse molecular clouds known to be interacting with the supernova remnant IC 443, a probable site of particle acceleration. Where H_3^+ is detected, ionization rates of $\zeta_2 = (20 \pm 10) \times 10^{-16}$ s^{-1} are inferred, higher than for any other diffuse cloud. These results support both the concept that supernova remnants act as particle accelerators, and the hypothesis that propagation effects are responsible for causing spatial variations in the cosmic-ray spectrum and ionization rate. Future observations of H_3^+ near other supernova remnants and in sight lines where complementary ionization tracers (OH^+, H_2O^+, H_3O^+) have been observed will further our understanding of the subject.

In loving memory of Mary Indriolo

Acknowledgments

Who I am today is without a doubt the product of my interactions with those around me. I would be remiss, then, to not thank everyone who significantly influenced my professional and personal development during my graduate career.

First thanks go to my advisor, Ben McCall, who taught me so much over the past 5 years. As an advisor, Ben was patient and understanding, while also motivational when my "lazy astronomer" side kicked in. He allowed me to pursue projects of my own choosing, and fully supported my research, even when it strayed from astrochemistry to theoretical particle astrophysics. He also encouraged me to write a great many observing proposals, a task which both improved my scientific writing skills, and gave me the opportunity to travel to Hawaii. Most importantly, Ben introduced me to several senior members in our field of research, which allowed me to build scientific collaborations, and gave me the opportunity to present my work at multiple international conferences. I have enjoyed my graduate career here at Illinois, and thank Ben 1000 times over for his influence on my scientific career, and for letting a random 1st year astronomy student join his chemistry lab.

I must also thank Brian Fields for agreeing to work with me on a collaborative project, and for patiently explaining theory to an observer on many occasions. Brian's pure enthusiasm for science is contagious and never failed to get me highly excited about whatever we were working on at the time.

Both Tom Geballe and Takeshi Oka made me feel welcome upon joining the group of H_3^+ observers. I thank them for their mentoring, and for invitations to join an observing run in Chile and to speak at a conference in Greece. Perhaps one day I will also have the opportunity to relate stories of famous scientists and Nobel Laureates to the next generation. My thanks go as well to Geoff Blake, Miwa Goto, Tomonori Usuda, Ken Hinkle, and Lew Hobbs, all of whom have been essential collaborators in both getting observing time and preparing observations. My gratitude also goes to the those members of my prelim and defense committees not already mentioned, including You-Hua Chu, Leslie Looney, Dick Crutcher, and Bill Watson.

Mom, Dad, there are no words sufficient to describe the overwhelming amount of gratitude I have toward you. Alas, I am an astronomer, and they should have sent a poet. You support me in everything that I undertake, respond with love and kindness in times of crisis, and generally put up with a sparse amount of communication on my side. You taught me to regard the world around us with wonder and curiosity and nurtured my interest in science for as long as I have walked this earth. Only as my life has progressed have I realized that not all parents so enthusiastically teach their children about trees, birds, flowers, plants, and stars. I would not be where I am today, nor would this dissertation be possible without your love and support. Thank you, thank you, thank you. And thank you too, Emily. As my sister, everything above goes for you as well. By virtue of being the elder, you have had to experience everything first: high school, college, graduate school, and now post-doctoral research. Every time you leap into the unknown, and every time you come out successful on the other side. I cannot express how much confidence I draw from you knowing that the next step can be done, that it *has* been done (Indriolo, 2009). Continue driving forward, and I will do my best to keep up.

Table of Contents

List of Figures

List of Tables

Chapter 1

Introduction

Over 70 years ago, CH^+ was the first molecule to be detected in interstellar space (Dunham, 1937; Douglas & Herzberg, 1941). Since then, the catalogue of species known to exist in the interstellar medium (ISM) has grown to over 160 (Lovas & Snyder, 2010). For such a plethora of molecules to exist, there must be a rich, complex chemistry taking place in the void between the stars. Both Watson (1973) and Herbst & Klemperer (1973) proposed that gas phase chemistry could be responsible for producing the majority of the smaller molecules observed in the ISM. Specifically, they considered ion-molecule reactions, which, with no activation energy barriers, typically have larger rate coefficients ($k \sim 10^{-9}$ cm^3 s^{-1}) than neutral-neutral reactions ($k \sim 10^{-11}$ cm^3 s^{-1}), although the importance of some neutral-neutral reactions has recently been re-visited (Smith et al., 2004, and references therein).

If ion-molecule reactions are responsible for driving the chemistry in the ISM though, there must be some source of ionization operating throughout both diffuse ($n \sim 100$ cm^{-3}, $T \sim 70$ K) and dense ($n \sim 10^4$ cm^{-3}, $T \sim 30$ K) molecular clouds. The large amount of atomic hydrogen in the ISM prevents most photons with $E > 13.6$ eV from penetrating very far into clouds, so photoionization is only efficient for species with ionization potentials below that of hydrogen. One such example is atomic carbon, which, with a first ionization potential of 11.3 eV, is expected to be singly ionized in diffuse clouds. For species with higher ionization potentials though (e.g., IP(He)=24.6 eV; IP(N)=14.5 eV; IP(O)=13.62 eV; IP(H$_2$)=15.4 eV), there is a lack of ionizing photons in cloud interiors, and so another ionization mechanism must be at work. Cosmic rays provide just such a mechanism.

Almost 100 years ago Victor Hess discovered via balloon flights that the rate of ionization as measured by an electrometer increased with altitude to several times that measured on the ground (Hess, 1912). Hess concluded that a large source of radiation must be impinging on the atmosphere from above, and is generally credited with the discovery of what would later be dubbed "cosmic rays" (Millikan, 1926). The present understanding of cosmic rays is that they are highly energetic charged particles primarily consisting of protons, with lesser contributions from electrons, positrons, and helium and other bare nuclei (see, e.g., Meyer

et al., 1998, for relative abundances). The all-particle energy spectrum of cosmic rays is fit rather well by a power law distribution ($\phi \propto E^{-2.7}$) from 10^9 eV all the way to 10^{21} eV (Swordy, 2001, and references therein). Below about 10^9 eV the spectrum cannot be measured as lower-energy particles are deflected from the solar system by the magnetic field coupled to the solar wind (an effect known as modulation), although as the *Pioneer* and *Voyager* spacecraft continue outward new data are being taken (Webber, 1998; Webber & Higbie, 2009). Furthermore, the deflection of cosmic rays of all energies by the Galactic magnetic field means that particles do not point back to their places of origin. This makes it impossible to directly pinpoint the sources responsible for particle acceleration. However, energetics arguments and mounting evidence suggest that most Galactic cosmic rays are likely accelerated by the shock waves expanding in supernova remnants through a process known as diffusive shock acceleration.

As cosmic rays propagate away from their acceleration sites, they interact with the interstellar medium in various ways. Some of these interactions include the production of neutral pions (π^0) through inelastic collisions, excitation of atomic nuclear states, spallation of ambient nuclei, and the excitation and ionization of atoms and molecules. Several of these processes are discussed in more detail in Chapters 7 and 8. However, it is the process of ionization by cosmic rays in which I am most interested, as it will operate throughout the entirety of both diffuse and dense molecular clouds. This is demonstrated by the fact that 100 MeV protons can travel through a column of about 10^{24} cm^{-2} before losing all energy to ionization interactions (Cravens & Dalgarno, 1978; Padovani et al., 2009).

Given a highly penetrating ionization mechanism, some fraction of the most abundant species in molecular clouds (H_2, H, and He) will be ionized to form H_3^+, H^+, and He^+ (H_2^+ rapidly reacts to form H_3^+; this is discussed in more detail below). These, in turn, initiate the network of ion-molecule reactions that drive interstellar chemistry. This is especially true of H_3^+ as the relatively low proton affinity of H_2 means that it will readily donate the extra proton to most other neutral atomic and molecular species.

1.1 H_3^+ Chemistry

The chemistry associated with H_3^+ in the interstellar medium is rather simple. H_3^+ is formed in a two-step process, beginning with the ionization of H_2 by cosmic rays,

$$H_2 + CR \rightarrow H_2^+ + e^- + CR' \tag{1.1}$$

and quickly followed by a collision of H_2^+ with H_2,

$$H_2^+ + H_2 \rightarrow H_3^+ + H. \tag{1.2}$$

Some amount of H_2^+ will be destroyed by dissociative recombination with electrons,

$$H_2^+ + e^- \rightarrow H + H, \tag{1.3}$$

or charge transfer to atomic hydrogen,

$$H_2^+ + H \rightarrow H_2 + H^+, \tag{1.4}$$

before it can form H_3^+, but these processes are slow compared to reaction (1.2). Overall, reaction (1.1) is the rate-limiting step (it is many orders of magnitude slower than reaction (1.2)) and can be taken as the formation rate of H_3^+. Photoionization of H_2 also occurs, but is negligible compared to ionization by cosmic rays. This is because the ultraviolet and soft X-ray photons capable of ionizing H_2 ($E > 15.4$ eV) are severely attenuated in the outer layers of diffuse clouds by atomic hydrogen, which has a lower ionization potential (13.6 eV). While higher energy photons (e.g., hard X-rays and γ-rays) can penetrate diffuse molecular clouds, the lower ionization cross sections at these energies and smaller flux of such photons make their contribution to the ionization rate minimal. As a result, H_3^+ should be formed primarily through the ionization of H_2 by cosmic rays.

The primary destruction mechanisms for H_3^+ are dependent on the environment under consideration. In diffuse molecular clouds, H_3^+ is predominantly destroyed via dissociative recombination with electrons,

$$\begin{aligned} H_3^+ + e^- &\rightarrow H_2 + H \\ &\rightarrow H + H + H. \end{aligned} \tag{1.5}$$

In dense clouds however, where the electron fraction is much lower, H_3^+ is destroyed by proton transfer to neutrals such as CO, O, and N_2:

$$H_3^+ + CO \rightarrow H_2 + HCO^+, \tag{1.6a}$$
$$H_3^+ + CO \rightarrow H_2 + HOC^+, \tag{1.6b}$$
$$H_3^+ + O \rightarrow H_2 + OH^+, \tag{1.7}$$
$$H_3^+ + N_2 \rightarrow H_2 + HN_2^+. \tag{1.8}$$

These ion-molecule reactions demonstrate how H_3^+ essentially drives the chemistry in the ISM by generating molecular ions which can then go on to form even more complex species.

Because the chemistry surrounding H_3^+ is so simple, and because its formation arises directly as a result of ionization by cosmic rays, observations of H_3^+ can be a powerful probe of the cosmic-ray ionization rate (i.e., the rate at which cosmic rays ionize a given atom or molecule). The cosmic-ray ionization rate, ζ, is an important parameter in modeling interstellar chemistry, and the use of H_3^+ in inferring ζ is discussed in detail in Chapter 5. However, this has only occurred within the last decade, and to understand why requires a quick aside into the history of H_3^+.

1.2   A Brief History of H_3^+

Nearly coincident with the discovery of cosmic rays was the discovery of the molecular ion H_3^+ in a laboratory plasma by J. J. Thomson, who correctly ascribed the signal from the newfound gas with a mass-to-charge ratio of 3, dubbed X_3, to triatomic hydrogen (Thomson, 1911). Fifty years later, Martin et al. (1961) first proposed that H_3^+ might be present in the interstellar medium. Prior to the acquisition of a laboratory spectrum of H_3^+ (Oka, 1980) though, an observational search was impossible. This long delay was primarily caused by H_3^+ having neither a stable electronic excited state, nor a permanent dipole moment, such that it cannot be probed by electronic (ultraviolet-visible) or rotational (microwave) spectroscopy. As a result, only the weaker vibrational (infrared) transitions can be accessed spectroscopically, and it was not until Oka's work that the technology necessary for such a study was available. This initial spectroscopic study of H_3^+ focused on transitions between the ground vibrational state, a diagram of which is shown in Figure 1.1, and the ν_2 vibrationally excited state.

Even with transition wavelengths known, various attempts to observe H_3^+ in the ISM (Oka, 1981; Geballe & Oka, 1989; Black et al., 1990) were unsuccessful. It was not until advances in instrumentation allowed for high resolution spectroscopic observations in the 3–4 μm region that Geballe & Oka (1996) made the first detection of H_3^+ in the ISM toward AFGL 2136 and W33 A. Since then, H_3^+ has been detected in various dense clouds (McCall et al., 1999; Kulesa, 2002; Brittain et al., 2004; Gibb et al., 2010), diffuse clouds (McCall et al., 1998, 2002, 2003; Indriolo et al., 2007, 2010a; Crabtree et al., 2011), toward the Galactic Center (Geballe et al., 1999; Goto et al., 2002, 2008, 2011; Oka et al., 2005; Geballe & Oka, 2010), and in one external galaxy (Geballe et al., 2006).
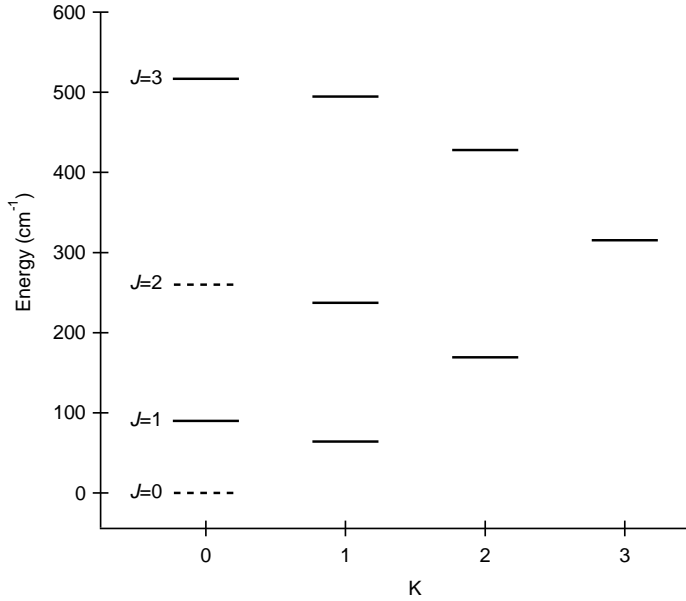
Figure 1.1: Energy level diagram for the ground vibrational state of H_3^+ through $J = K = 3$. The (J, K)=(0,0) and (2,0) levels are forbidden by the Pauli principle. Transitions observed in the interstellar medium arise from the lowest-lying (1,1) and (1,0) levels.

1.3 Observational and Theoretical Inferences of the Cosmic-Ray Ionization Rate

Prior to the first detections of H_3^+ in the ISM, the cosmic-ray ionization rate was estimated from observations of various other molecules, most commonly OH and HD. One of the first studies to do so used column densities of HD derived from *Copernicus* observations to place upper limits on the total ionization rate in a few diffuse cloud sight lines (O'Donnell & Watson, 1974). Shortly thereafter, Black & Dalgarno (1977) and Black et al. (1978) used OH abundances in concert with a chemical model and various other observations to infer ionization rates along the sight lines toward ζ Oph and ζ Per. The resulting values were $\zeta_H = 1.6 \times 10^{-17}$ s^{-1} and 2.2×10^{-17} s^{-1}, respectively[1]. Other estimates using OH and/or HD include those by Hartquist et al. (1978a), Hartquist et al. (1978b), and Federman et al. (1996), all of which gave ionization rates typically on the order of a few times 10^{-17} s^{-1}. Results from these studies and others are plotted in Figure 1.2, which shows the cosmic-ray ionization rate in diffuse molecular clouds inferred over the past 50 years. Also included are

---

[1]ζ_H refers to the cosmic-ray ionization rate of atomic hydrogen, and is different from ζ_2, the cosmic-ray ionization rate of molecular hydrogen (derived from H_3^+ observations). A simple relation that can be used to directly compare atomic and molecular ionization rates is given by $1.5\zeta_2 = 2.3\zeta_H$ (Glassgold & Langer, 1974).
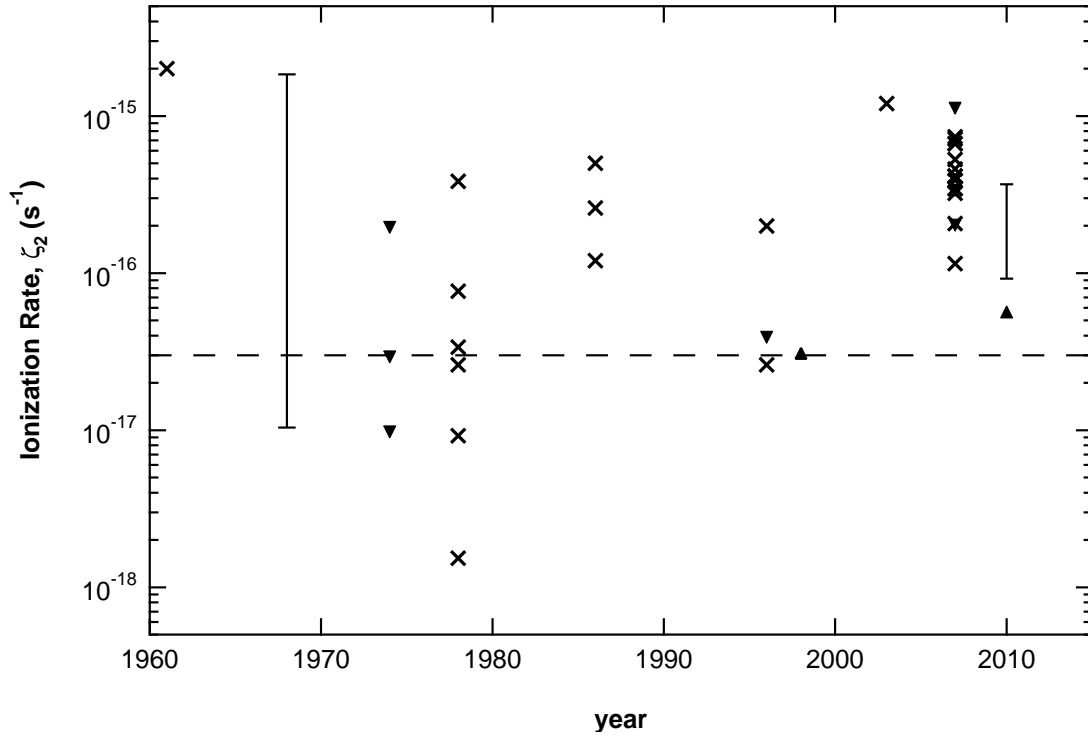
Figure 1.2: Estimates of the cosmic-ray ionization rate in diffuse molecular clouds over the past 50 years. In chronological order, data points and ranges are from: Hayakawa et al. (1961), theory; Spitzer & Tomasko (1968), theory; O'Donnell & Watson (1974), HD; Hartquist et al. (1978b), HD and OH; van Dishoeck & Black (1986), various species; Federman et al. (1996), OH; Webber (1998), theory; McCall et al. (2003), H_3^+; Indriolo et al. (2007), H_3^+; Gerin et al. (2010), OH^+, H_2O^+, and H_3O^+; Neufeld et al. (2010), OH^+ and H_2O^+. Triangles pointing downward are upper limits, while those pointing upward are lower limits. The dashed horizontal line shows the frequently adopted "canonical" ionization rate of $\zeta_2 = 3 \times 10^{-17}$ s^{-1}. In cases where published values were ζ_H, the aforementioned conversion factor from Glassgold & Langer (1974) was utilized.

some theoretical estimates of the ionization rate based on the cosmic-ray spectrum measured within our solar system (Hayakawa et al., 1961; Spitzer & Tomasko, 1968; Webber, 1998).

Clearly, there have been wide variations in inferred cosmic-ray ionization rates over the past 50 years. Differences in theoretical estimates (e.g., the factor of 200 difference between the ionization rate found by Hayakawa et al. (1961) and the lower limit reported by Spitzer & Tomasko (1968)) are easily explained by the assumed shape of the cosmic-ray spectrum below about 1 GeV, and are discussed in Chapter 7 in greater detail. Understanding differences in observational inferences, however, is more subtle.

In the case of OH, the adopted temperature has a large effect on the rate at which the

species is produced. This is because the charge transfer reaction

$$H^+ + O \rightarrow H + O^+, \qquad\qquad (1.9)$$

that begins the reaction pathway to forming OH is endothermic by about 230 K ($k_{1.9} = 7.31 \times 10^{-10}(T/300)^{0.23}\exp(-225.9/T)$; Stancil et al., 1999). At 120 K (temperature adopted by Black et al., 1978) reaction (1.9) proceeds about 8 times faster than at 60 K (temperature derived from H_2 observations; Savage et al., 1977). Because oxygen competes with deuterium and electrons in destroying H^+, the rate of reaction (1.9) determines what percentage of H^+ eventually leads to OH. An overestimate of T, and thus $k_{1.9}$, assumes that a larger fraction of H^+ eventually forms OH, and so underestimates the production rate of H^+ (i.e., ζ_H) necessary to produce observed OH abundances. The OH analysis is further complicated by the fact that OH is destroyed by photodissociation. This requires an estimate of the interstellar radiation field (Federman et al., 1996), a parameter much more difficult to constrain than interstellar abundances.

In contrast, the simple chemistry of H_3^+ means that it does not suffer from many of these uncertainties. As such, it is widely regarded as likely the most accurate probe of the cosmic-ray ionization rate (Dalgarno, 2006), and many diffuse cloud models now use the higher ionization rate (a few times 10^{-16} s^{-1}) inferred from H_3^+ observations. To further our understanding of the cosmic-ray ionization rate throughout Galactic diffuse molecular clouds, I have undertaken a survey of H_3^+ in over 50 sight lines. This is the central focus of my dissertation, the remainder of which is organized as follows. Chapter 2 describes the overall observing campaign. Chapter 3 describes the data reduction procedures used. Chapter 4 presents spectra toward the observed sight lines. Chapter 5 explains how column densities are extracted from spectra and then used to compute the ionization rate. Chapter 6 investigates correlations of $N(H_3^+)$ and ζ_2 with various other parameters and discusses the interpretation of these results. Chapter 7 presents theoretical work that discusses the implications of a high cosmic-ray ionization rate on light element abundances and gamma-ray fluxes, and is published as Indriolo et al. (2009a). Chapter 8 is adapted from Indriolo et al. (2010a), and presents observations of H_3^+ near the supernova remnant IC 433, a suspected site of cosmic-ray acceleration. Chapter 9 presents an attempt to use metastable helium as a complementary tracer of the ionization rate, and is published as Indriolo et al. (2009b). Finally, Chapter 10 summarizes the work that I have done, reiterating the most important conclusions, and briefly describes some of the next steps to be taken in constraining the cosmic-ray ionization rate.

Chapter 2

Observations

In diffuse molecular clouds, conditions are such that only the 2 lowest energy levels of H_3^+—the $(J, K)=(1, 1)$ *para* and $(1, 0)$ *ortho* states—are expected to be significantly populated. As a result, observations that probe transitions arising from these 2 states will trace the entire content of H_3^+ along a line of sight. Five such ro-vibrational transitions are accessible in the infrared: the $R(1, 1)^u$, $R(1, 0)$, $R(1, 1)^l$, $Q(1, 1)$, and $Q(1, 0)$. Transition properties, including wavelength and dipole moment, are given in Table 2.1, and Figure 2.1 shows the atmospheric transmission spectrum near these transitions. As the weak H_3^+ lines are located near various atmospheric CH_4, HDO, and N_2O lines, precise removal of the telluric lines is vital for the purpose of accurately determining H_3^+ column densities. Because the $R(1, 1)^u$ and $R(1, 0)$ transitions are easily observed simultaneously (they are separated by about 4 Å), and because together they probe the entire population of H_3^+, they are the most frequently observed transitions. A complete log of observations of H_3^+ in diffuse molecular cloud sight lines is presented in Table 2.4.

Although observations of H_3^+ have become more commonplace, as evidenced by the publication list in section 1.2, they are still rather difficult. Given the transition dipole moments (see Table 2.1) and a typical relative abundance of about 10^{-7}–10^{-8} with respect to H_2, H_3^+ absorption lines in diffuse molecular clouds are usually about 1–2% deep, and thus require a signal-to-noise ratio (S/N) greater than about 300 on the continuum to achieve 3σ detections. As a result, background sources must have L-band (3.5 μm) magnitudes brighter than about $L = 7.5$ mag ($L = 5.5$ mag) to be feasible targets for 8 m (4 m) class telescopes. Ideally, these background sources should also be early-type stars (OB) such that the continuum is free of stellar absorption features. In addition, to adequately sample the intrinsically narrow interstellar absorption lines requires high spectroscopic resolving power ($R \gtrsim 20,000$). Instrument/telescope combinations that operate in the 3–4 μm region with the necessary high resolving power include: CRIRES/VLT, NIRSPEC/Keck, IRCS/Subaru, GNIRS/Gemini North, CSHELL/IRTF, *Phoenix*/Gemini South (no longer available), and GCS4/UKIRT (no longer available). Details regarding observations made at these various facilities are given below.
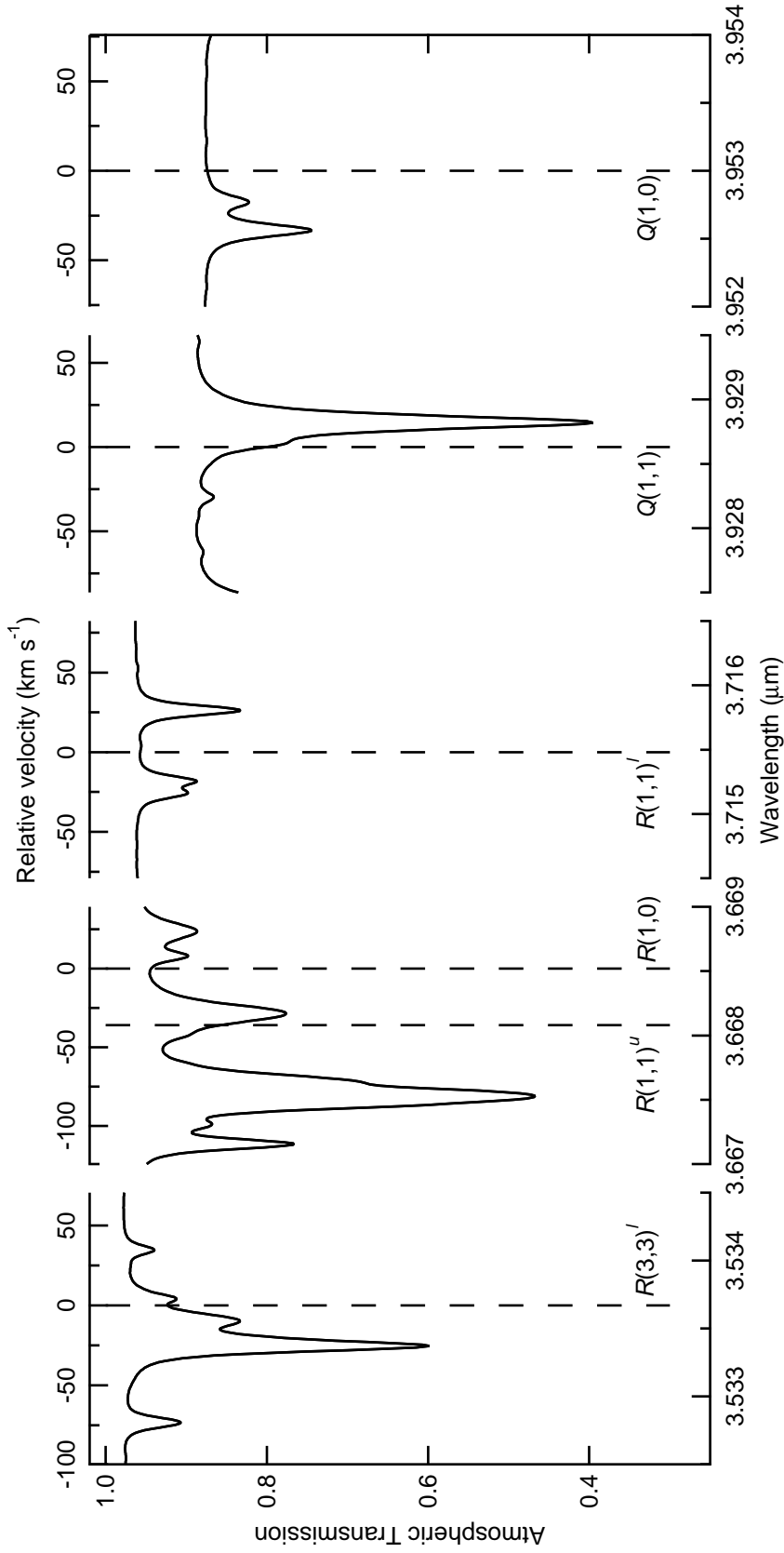
Figure 2.1: Model atmospheric transmission spectra at wavelengths near targeted H_3^+ transitions, generated by ATRAN (Lord, 1992) assuming observations were performed from Mauna Kea, 1.6 mm precipitable water vapor, and an airmass of 1.15, with a resolving power of about 70,000. Dashed vertical lines mark the rest positions of H_3^+ transitions, and are labeled accordingly. The bottom axes give the rest wavelengths in μm, while the top axes show the effect of relative motion between the observer and interstellar gas. Adapted from Figure 2 in Indriolo et al. (2010a).

Table 2.1: Select H_3^+ Transition Properties

Transition	Wavelength (μm)	Wavenumber (cm^{-1})	$\|\mu\|^2$ (D^2)
$R(1,1)^u$	3.668083	2726.219	0.0158
$R(1,0)$	3.668516	2725.898	0.0259
$R(1,1)^l$	3.715479	2691.444	0.0141
$Q(1,1)$	3.928625	2545.420	0.0128
$Q(1,0)$	3.953000	2529.724	0.0254
$R(3,3)^l$	3.533666	2829.922	0.0191

Notes: Transition wavelengths, wavenumbers, and dipole moments for targeted transitions in the $\nu_2 \leftarrow 0$ band of H_3^+ (values from Goto et al., 2002, and references therein).

2.1 General Techniques

Although many instrument/telescope combinations were used in acquiring data for this project, there are several common techniques used for spectroscopic observations in the near to mid infrared wavelength regime. Some of these include the acquisition of bias, dark, and flat frames, nodding the star along the slit so that the spectral image falls on different portions of the detector, and the observation of "standard" stars. Bias, dark, and flat frames are common calibration images and will be mentioned in the chapter on data reduction. For all observations the target star was nodded along the slit in an ABBA pattern (i.e. exposure at position A; nod telescope to position B; exposure at position B; exposure at position B; nod telescope to position A; exposure at position A). Nodding the target star along the slit axis is a technique that facilitates the removal of atmospheric emission lines and dark current via the subtraction of subsequent images from one another. In addition to science targets, bright, early-type stars were observed for use as telluric standard stars[1]. These standard stars were observed either immediately before or after each science target to minimize the difference in atmospheric conditions, and chosen so as to optimize the mean airmass match between the two observations. Division of the science target spectra by these telluric spectra

---

[1]A list of the stars used as telluric standards is presented in Table 2.2.

allows for the removal of atmospheric absorption lines.

2.2 Telescope and Instrument Configurations

In addition to the general techniques discussed above, each instrument/telescope combination has methods and parameters specific to that setup. These are addressed for each telescope individually in the following sections.

2.2.1 UKIRT

Observations made at the United Kingdom Infrared Telescope (UKIRT) utilized the Cooled Grating Spectrometer 4 (CGS4; Mountain et al., 1990). CGS4 was used with its echelle grating, $0\rlap{.}''6$ wide slit, and long camera to provide a resolving power (resolution) of about 40,000 (8 km s^{-1}). A circular variable order-blocking filter was used to select the order containing the $R(1,1)^u$ and $R(1,0)$ transitions. The telescope was nodded $7\rlap{.}''13$ along the slit between the A and B positions, corresponding to about 8 pixels on the detector. Using this method, the spectral image was concentrated on either 1 or 2 rows of the detector per exposure. The 3×2 sampling mode was used such that at each nod position 6 exposures were taken, where the array was stepped by one-third of a pixel along the dispersion direction between exposures. Details regarding the combination of these exposures are given in Section 3.1.1. Spectra resulting from observations made at UKIRT are presented in McCall et al. (1998), Geballe et al. (1999), McCall (2001), McCall et al. (2002), McCall et al. (2003), Indriolo et al. (2007), and Crabtree et al. (2011).

2.2.2 Gemini South

Observations performed at the Gemini South Telescope were done so using the *Phoenix* spectrometer (Hinkle et al., 2003). They were made in queue mode, and the spectrometer was used with its echelle grating and $0\rlap{.}''17$ slit to produce a resolving power (resolution) of about 70,000 (5 km s^{-1}), and with the L2734 filter to select the order containing the $R(1,1)^u$ and $R(1,0)$ transitions. For science targets the nod positions were $\pm 2\rlap{.}''5$ from the rest setting, while for telluric standards they were $\pm 4\rlap{.}''0$. The difference in nod positions was employed so that the science images would not be affected by ghosting artifacts left over from observations of the bright standard stars. The spectrum of HD 154368 obtained at Gemini South is presented in Crabtree et al. (2011).

2.2.3 Keck

Spectra were obtained at the W. M. Keck Observatory using the Near-Infrared Echelle Spectrograph (NIRSPEC; McLean et al., 1998) on Keck II. The spectrograph was used with the 3 pixel (0.''432) slit to provide a resolving power (resolution) of about 25,000 (13 km s^{-1}). The KL filter was used in combination with two different echelle grating/cross-disperser settings: 64.82/33.5 and 64.00/33.45, both of which cover the $R(1,1)^u$ and $R(1,0)$ transitions, while the prior also covers the $R(3,3)^l$ transition in an adjacent order. Some of the data obtained at Keck are reported in Indriolo et al. (2010a).

2.2.4 Subaru

Spectroscopic observations at the Subaru Telescope were made using the Infrared Camera and Spectrograph (IRCS; Kobayashi et al., 2000) in combination with the adaptive optics system (AO188) to maximize starlight passing through the narrow slit. Observations were made in the echelle mode using the 2 pixel (0.''14) slit to provide a resolving power (resolution) of about 17,500 (16 km s^{-1}). The L filter was used in combination with the echelle grating/cross-disperser settings of 8350/6100 in order to simultaneously cover the $R(1,1)^u$, $R(1,0)$, $R(1,1)^l$, $Q(1,1)$, and $Q(1,0)$ transitions. Some of the data obtained at Subaru are reported in Indriolo et al. (2010a).

2.2.5 VLT

Observations performed at the Very Large Telescope (VLT) were made using the Cryogenic High-resolution Infrared Echelle Spectrograph (CRIRES; Käufl et al., 2004) on UT1. All such observations were made in service mode, and CRIRES was used with its 0.''2 slit to provide a resolving power (resolution) of about 100,000 (3 km s^{-1}), and a reference wavelength of 3715 nm to cover the $R(1,1)^u$ and $R(1,0)$ transitions on detector 1 and the $R(1,1)^l$ transition on detector 3. The adaptive optics system was utilized to maximize starlight passing through the narrow slit. The difference between the A and B nod positions was set to be 10'' with a jitter width of $\pm 3''$. Spectra from 2 of the 3 stars observed at the VLT are presented in Crabtree et al. (2011).

2.2.6 KPNO

All observations performed at Kitt Peak National Observatory (KPNO) were made using the *Phoenix* spectrometer on the Mayall 4 m telescope between 1997 and 2001. Details regarding

these observations are presented in McCall et al. (1998), Geballe et al. (1999), McCall (2001) and McCall et al. (2002). As I am including the results from these observations in my study, they are mentioned here and presented in Table 2.4 for the sake of completeness.

2.3   Tables

The tables in this section contain information regarding the sight lines targeted in the observing campaign. Table 2.2 lists the bright stars used as telluric standards throughout this project. Table 2.3 presents general information for all of the diffuse cloud sight lines where H_3^+ observations have been performed. Table 2.4 is a comprehensive log of H_3^+ observations in diffuse clouds.

Table 2.2: Telluric Standard Stars

Standard Star	Name	α (J2000.0) (hh:mm:ss.s)	δ (J2000.0) (dd:mm:ss.s)	Spectral Type
HR 838	HD 17573	02:49:59.0	+27:15:37.8	B8 Vn
HR 936	β Per	03:08:10.1	+40:57:20.3	B8 V
HR 1122	δ Per	03:42:55.5	+47:47:15.2	B5 III
HR 1165	η Tau	03:47:29.1	+24:06:18.5	B7 III
HR 1641	η Aur	05:06:30.9	+41:14:04.1	B3 V
HR 1791	β Tau	05:26:17.5	+28:36:26.8	B7 III
HR 2004	κ Ori	05:47:45.4	-09:40:10.6	B0 Iab
HR 2421	γ Gem	06:37:42.7	+16:23:57.3	A0 IV
HR 2491	α CMa	06:45:08.9	-16:42:58.0	A1 V
HR 3165	ζ Pup	08:03:35.0	-40:00:11.3	O5 Ia
HR 5440	η Cen	14:35:30.4	-42:09:28.2	B1.5 Vne
HR 5685	HD 135591	15:18:49.1	-60:29:46.8	O8 III
HR 5953	δ Sco	16:00:20.0	-22:37:18.2	B0.2 IVe
HR 6165	τ Sco	16:35:53.0	-28:12:57.7	B0.2 V
HR 6378	η Oph	17:10:22.7	-15:43:29.7	A2 IV-V
HR 6527	λ Sco	17:33:36.5	-37:06:13.8	B2 IV
HR 7001	α Lyr	18:36:56.3	+38:47:01.3	A0 V
HR 7740	HD 192696	20:13:23.9	+56:34:03.8	A3 IV-Vn
HR 7924	α Cyg	20:41:25.9	+45:16:49.2	A2 Iae

Note: Spectral types are from the SIMBAD database

13

Table 2.3: Science Targets

Object	HD num.	α (J2000) (hh:mm:ss.s)	δ (J2000) (dd:mm:ss.s)	l (deg.)	b (deg.)	Spectral Type	$E(B-V)$ (mag.)	Ref.	Distance (pc)	Ref.
κ Cas	2905	00:33:00.0	+62:55:54.4	120.8361	0.1351	B1 Iae	0.33	4	1370	13
HD 20041	20041	03:15:48.0	+57:08:26.2	141.5719	-0.4119	A0 Ia	0.72	5	1400	5
HD 21483	21483	03:28:46.7	+30:22:31.2	158.8727	-21.3030	B3 III	0.56	5	440	5
HD 21389	21389	03:29:54.7	+58:52:43.5	142.1883	2.0644	A0 Iab	0.57	5	940	5
HD 21856	21856	03:32:40.0	+35:27:42.2	156.3159	-16.7535	B1 V	0.19	6	502	13
40 Per	22951	03:42:22.6	+33:57:54.1	158.9199	-16.7030	B0.5 V	0.27	4	283	13
o Per	23180	03:44:19.1	+32:17:17.7	160.3637	-17.7399	B1 III	0.31	5	280	5
BD +31 643	281159	03:44:34.2	+32:09:46.1	160.4908	-17.8022	B5	0.85	5	240	5
ζ Per	24398	03:54:07.9	+31:53:01.1	162.2891	-16.6904	B1 Ib	0.31	5	301	5
X Per	24534	03:55:23.1	+31:02:45.0	163.0814	-17.1362	O9.5 IIIe	0.59	5	590	13
ϵ Per	24760	03:57:51.2	+40:00:36.8	157.3538	-10.0885	B0.5 V	0.09	6	196	5
ξ Per	24912	03:58:57.9	+35:47:27.7	160.3723	-13.1065	O7.5 IIIe	0.33	5	470	5
62 Tau	27778	04:23:59.8	+24:18:03.6	172.7629	-17.3928	B3 V	0.37	5	223	5
HD 29647	29647	04:41:08.0	+25:59:34.0	174.0529	-13.3487	B8 III	1.00	5	177	5
α Cam	30614	04:54:03.0	+66:20:33.6	144.0656	14.0424	O9.5 Ia	0.30	5	820	5
NGC 2024 IRS 1	...	05:41:37.9	-01:54:36.5	206.5281	-16.3773	B0.5 V	1.69	7	450	7
χ^2 Ori	41117	06:03:55.2	+20:08:18.4	189.6918	-0.8604	B2 Iae	0.45	5	1000	5
ALS 8828	...	06:16:13.3	+22:45:48.6	188.7745	2.9135	B2 V[1]	0.82	1	1500	1
HD 254577	254577	06:17:54.4	+22:24:32.9	189.2713	3.0885	B0.5 II	0.92	1	1500	1
HD 43582	43582	06:18:00.3	+22:39:30.0	189.0620	3.2262	B0 IIIn	0.62	1	1500	1
HD 254755	254755	06:18:31.8	+22:40:45.1	189.1006	3.3426	O9 Vp	0.73	1	1500	1
HD 43703	43703	06:18:39.4	+23:00:25.5	188.8238	3.5232	B1 IV	0.59	1	1500	1
HD 43907	43907	06:19:45.2	+22:06:38.9	189.7364	3.3253	B1 V	0.56	1	1500	1
HD 47129	47129	06:37:24.0	+06:08:07.4	205.8740	-0.3111	O8 I	0.36	4	1514	14

14

Table 2.3: (continued)

Object	HD num.	α (J2000) (hh:mm:ss.s)	δ (J2000) (dd:mm:ss.s)	l (deg.)	b (deg.)	Spectral Type	$E(B-V)$ (mag.)	Ref.	Distance (pc)	Ref.
HD 53367	53367	07:04:25.5	-10:27:15.7	223.7092	-1.9008	B0 IV	0.74	5	780	5
HD 73882	73882	08:39:09.5	-40:25:09.3	260.1816	0.6431	O9 III	0.70	8	1000	15
HD 110432	110432	12:42:50.3	-63:03:31.0	301.9580	-0.2031	B2pe	0.51	8	300	16
o Sco	147084	16:12:38.2	-24:10:09.6	352.3279	18.0503	A4 II/III	0.74	7	270	13
ρ Oph D	147888	16:25:24.3	-23:27:36.8	353.6500	17.7100	B3/B4 V	0.47	5	136	5
HD 147889	147889	16:25:24.3	-24:27:56.6	352.8573	17.0436	B2 III/IV	1.07	5	136	5
χ Oph	148184	16:27:01.4	-18:27:22.5	357.9328	20.6766	B2 Vne	0.52	4	161	8
μ Nor	149038	16:34:05.0	-44:02:43.1	339.3797	2.5129	B0 Ia	0.38	6	1122	14
HD 149404	149404	16:36:22.6	-42:51:31.9	340.5375	3.0058	O9 Ia	0.68	4	417	13
ζ Oph	149757	16:37:09.5	-10:34:01.5	6.2812	23.5877	O9 V	0.32	5	140	5
HD 152236	152236	16:53:59.7	-42:21:43.3	343.0275	0.8700	B0.5 Ia	0.68	8	600	17
HD 154368	154368	17:06:28.4	-35:27:03.8	349.9702	3.2151	O9.5 Iab	0.78	8	909	18
WR 104	...	18:02:04.1	-23:37:42.0	6.4433	-0.4851	WC9[2]	2.30	9	2600	19
HD 168607	168607	18:21:14.9	-16:22:31.8	14.9679	-0.9397	B9 Ia	1.61	2	1100	2
HD 168625	168625	18:21:19.5	-16:22:26.1	14.9781	-0.9554	B6 Ia	1.86	10	2800	20
BD -14 5037	...	18:25:06.2	-14:38:57.7	16.9282	-0.9509	B1.5 Ia[3]	1.57	7	1700	7
HD 169454	169454	18:25:15.2	-13:58:42.3	17.5385	-0.6697	B1 Ia[3]	1.12	5	930	5
W 40 IRS 1A	...	18:31:27.8	-02:05:23.0	28.7886	3.4852	...	2.90	11	400	11
WR 118	...	18:31:42.3	-09:59:15.0	21.8056	-0.2125	WC9[2]	4.57	9	3900	9
WR 121	...	18:44:13.2	-03:47:57.8	28.7283	-0.1289	WC9[2]	1.75	9	2600	9
HD 183143	183143	19:27:26.6	+18:17:45.2	53.2447	0.6268	B7 Ia	1.28	2	1000	2
P Cygni	193237	20:17:47.2	+38:01:58.5	75.8268	1.3194	B2pe	0.63	2	1800	2
HD 193322A	193322A	20:18:07.0	+40:43:55.5	78.0986	2.7807	O9 V	0.40	6	830	21
HD 229059	229059	20:21:15.4	+37:24:31.1	75.6992	0.4007	B1.5 Iap	1.71	5	1000	5

15

Table 2.3: (continued)

Object	HD num.	α (J2000) (hh:mm:ss.s)	δ (J2000) (dd:mm:ss.s)	l (deg.)	b (deg.)	Spectral Type	$E(B-V)$ (mag.)	Ref.	Distance (pc)	Ref.
HD 194279	194279	20:23:18.2	+40:45:32.6	78.6779	1.9865	B1.5 Ia	1.22	2	1100	2
Cyg OB2 5	…	20:32:22.4	+41:18:19.0	80.1190	0.9147	O7e	1.99	2	1700	2
Cyg OB2 12	…	20:32:41.0	+41:14:29.3	80.1021	0.8301	B5 Iab[2]	3.35	2	1700	2
Cyg OB2 8A	…	20:33:15.1	+41:18:50.5	80.2240	0.7873	O6 If	1.60	12	1700	2
HD 204827	204827	21:28:57.8	+58:44:23.2	99.1667	5.5525	O9.5 V	1.11	5	600	5
HD 206267	206267	21:38:57.6	+57:29:20.5	99.2904	3.7383	O6e	0.53	5	1000	5
19 Cep	209975	22:05:08.8	+62:16:47.3	104.8706	5.3906	O9 Ib	0.36	4	1300	22
λ Cep	210839	22:11:30.6	+59:24:52.2	103.8279	2.6108	O6 If	0.57	5	505	5
1 Cas	218376	23:06:36.8	+59:25:11.1	109.9477	-0.7834	B0.5 IV	0.25	5	339	5

Notes: MK spectral types are from the SIMDAD database unless otherwise marked.

References: (1) Hirschauer et al. (2009); (2) McCall et al. (2002, and references therein); (3) Słyk et al. (2008); (4) McCall et al. (2010); (5) Thorburn et al. (2003); (6) Savage et al. (1977); (7) van Dishoeck & Black (1989); (8) Rachford et al. (2009); (9) Conti & Vacca (1990); (10) Nota et al. (1996); (11) Shuping et al. (1999); (12) Snow et al. (2010); (13) van Leeuwen (2007); (14) Fruscione et al. (1994); (15) Nichols & Slavin (2004); (16) Chevalier & Ilovaisky (1998); (17) Ritchey et al. (2011); (18) Maíz-Apellániz et al. (2004); (19) Tuthill et al. (2008); (20) Pasquali et al. (2002); (21) Roberts et al. (2010); (22) Sheffer et al. (2008)

16

Table 2.4: Log of H$_3^+$ Observations

Object	Date(s) of Observation	Telescope	Transition(s) Observed	Integration Time (sec)	Standard	Published
κ Cas	2009 Nov 5	Keck	$R(1,1)^u$, $R(1,0)$	960	HR 7924	1
HD 20041	2001 Mar 13	KPNO	$R(1,1)^l$	6000	HR 2491	1
HD 20041	2001 Sep 5	UKIRT	$R(1,1)^u$, $R(1,0)$	1728	HR 936	2
HD 21483	2005 Jan 25	UKIRT	$R(1,1)^u$, $R(1,0)$	1536	HR 838	2
HD 21483	2009 Nov 6	Keck	$R(1,1)^u$, $R(1,0)$	1200	HR 936	2
HD 21389	2001 Sep 5	UKIRT	$R(1,1)^u$, $R(1,0)$	1536	HR 936	2
HD 21389	2002 Dec 30	UKIRT	$R(1,1)^u$, $R(1,0)$	1152	HR 936	2
HD 21389	2002 Dec 31	UKIRT	$R(1,1)^u$, $R(1,0)$	1536	HR 936	2
HD 21389	2003 Jan 1	UKIRT	$R(1,1)^u$, $R(1,0)$	1152	HR 936	2
HD 21856	2009 Nov 6	Keck	$R(1,1)^u$, $R(1,0)$	1200	HR 936	2
40 Per	2004 Jan 23	UKIRT	$R(1,1)^u$, $R(1,0)$	3600	HR 838	2
40 Per	2005 Jan 6	UKIRT	$R(1,1)^u$, $R(1,0)$	2880	HR 1641	2
40 Per	2009 Nov 5	Keck	$R(1,1)^u$, $R(1,0)$	720	HR 936	
o Per	2002 Dec 30	UKIRT	$R(1,1)^u$, $R(1,0)$	2304	HR 936	2
o Per	2002 Dec 31	UKIRT	$R(1,1)^u$, $R(1,0)$	1152	HR 936	2
o Per	2008 Jan 23	UKIRT	$R(1,1)^u$, $R(1,0)$	3840	HR 936	
o Per	2008 Jan 24	UKIRT	$R(1,1)^u$, $R(1,0)$	3840	HR 936	
BD +31 643	2009 Nov 6	Keck	$R(1,1)^u$, $R(1,0)$	1440	HR 838	
ζ Per	2001 Sep 5	UKIRT	$R(1,1)^u$, $R(1,0)$	2304	HR 936	3
ζ Per	2002 Dec 30	UKIRT	$R(1,1)^u$, $R(1,0)$	1152	HR 936	2
ζ Per	2002 Dec 31	UKIRT	$R(1,1)^u$, $R(1,0)$	1152	HR 936	2
ζ Per	2003 Jan 1	UKIRT	$R(1,1)^u$, $R(1,0)$	1440	HR 1122	2
ζ Per	2008 Jan 26	UKIRT	$R(3,3)^l$	1440	HR 936	

Table 2.4: (continued)

Object	Date(s) of Observation	Telescope	Transition(s) Observed	Integration Time (sec)	Standard	Published
X Per	2002 Dec 31	UKIRT	$R(1,1)^u$, $R(1,0)$	1920	HR 936	2
X Per	2004 Jan 22	UKIRT	$R(1,1)^u$, $R(1,0)$	3600	HR 838	2
X Per	2005 Jan 5	UKIRT	$R(1,1)^u$, $R(1,0)$	4320	HR 838	2
X Per	2005 Jan 6	UKIRT	$R(1,1)^u$, $R(1,0)$	2880	HR 1641	2
X Per	2005 Mar 3	UKIRT	$R(1,1)^u$, $R(1,0)$	5040	HR 838	2
X Per	2005 Mar 4	UKIRT	$R(1,1)^u$, $R(1,0)$	5040	HR 838	2
ϵ Per	2004 Jan 23	UKIRT	$R(1,1)^u$, $R(1,0)$	1800	HR 1641	2
ϵ Per	2005 Jan 5	UKIRT	$R(1,1)^u$, $R(1,0)$	1440	HR 1641	2
ϵ Per	2005 Jan 6	UKIRT	$R(1,1)^u$, $R(1,0)$	1440	HR 1641	2
ϵ Per	2008 Jan 24	UKIRT	$R(1,1)^u$, $R(1,0)$	3840	HR 936	
ϵ Per	2008 Jan 25	UKIRT	$R(1,1)^u$, $R(1,0)$	3840	HR 936	
ξ Per	2002 Dec 30	UKIRT	$R(1,1)^u$, $R(1,0)$	1920	HR 936	2
ξ Per	2002 Dec 31	UKIRT	$R(1,1)^u$, $R(1,0)$	1920	HR 936	2
ξ Per	2003 Jan 1	UKIRT	$R(1,1)^u$, $R(1,0)$	1536	HR 936	2
ξ Per	2008 Jan 23	UKIRT	$R(1,1)^u$, $R(1,0)$	3840	HR 936	
ξ Per	2008 Jan 25	UKIRT	$R(1,1)^u$, $R(1,0)$	3840	HR 936	
62 Tau	2003 Jan 1	UKIRT	$R(1,1)^u$, $R(1,0)$	2688	HR 936	2
62 Tau	2009 Nov 5	Keck	$R(1,1)^u$, $R(1,0)$	1200	HR 936	
HD 29647	2008 Jan 23	UKIRT	$R(1,1)^u$, $R(1,0)$	2520	HR 1165	
HD 29647	2009 Jan 8	UKIRT	$R(1,1)^u$, $R(1,0)$	3600	HR 1165	
HD 29647	2009 Jan 9	UKIRT	$R(1,1)^u$, $R(1,0)$	3600	HR 1165	
HD 29647	2009 Jan 12	UKIRT	$R(1,1)^u$, $R(1,0)$	3600	HR 2004	
HD 29647	2009 Jan 22	UKIRT	$R(1,1)^u$, $R(1,0)$	3600	HR 1165	
α Cam	2009 Nov 5	Keck	$R(1,1)^u$, $R(1,0)$	1200	HR 936	

Table 2.4: (continued)

Object	Date(s) of Observation	Telescope	Transition(s) Observed	Integration Time (sec)	Standard	Published
NGC 2024 IRS 1	2008 Jan 24	UKIRT	$R(1,1)^u$, $R(1,0)$	4320	HR 2421	
NGC 2024 IRS 1	2009 Jan 12	UKIRT	$R(1,1)^u$, $R(1,0)$	3600	HR 2004	
NGC 2024 IRS 1	2009 Jan 22	UKIRT	$R(1,1)^u$, $R(1,0)$	3600	HR 2004	
NGC 2024 IRS 1	2009 Jan 24	UKIRT	$R(1,1)^u$, $R(1,0)$	3600	HR 2004	
NGC 2024 IRS 1	2009 Jan 25	UKIRT	$R(1,1)^u$, $R(1,0)$	3600	HR 2004	
χ^2 Ori	2001 Mar 13	KPNO	$R(1,1)^l$	3600	HR 2491	1
ALS 8828	2009 Nov 5	Keck	$R(1,1)^u$, $R(1,0)$	2400	HR 1791	4
ALS 8828	2009 Nov 6	Keck	$R(1,1)^u$, $R(1,0)$	1440	HR 1791	4
HD 254577	2009 Nov 5	Keck	$R(1,1)^u$, $R(1,0)$	2400	HR 1791	4
HD 254577	2009 Nov 6	Keck	$R(1,1)^u$, $R(1,0)$	1200	HR 1791	4
HD 254577	2009 Dec 12	Subaru	$R(1,1)^u$, $R(1,0)$, $R(1,1)^l$, $Q(1,1)$, $Q(1,0)$	5760	HR 1791	4
HD 254577	2009 Dec 13	Subaru	$R(1,1)^u$, $R(1,0)$, $R(1,1)^l$, $Q(1,1)$, $Q(1,0)$	2160	HR 1791	4
HD 43582	2009 Nov 5	Keck	$R(1,1)^u$, $R(1,0)$	1680	HR 1791	4
HD 43582	2009 Nov 6	Keck	$R(1,1)^u$, $R(1,0)$	2400	HR 1791	4
HD 43582	2009 Dec 12	Subaru	$R(1,1)^u$, $R(1,0)$, $R(1,1)^l$, $Q(1,1)$, $Q(1,0)$	7200	HR 1791	4
HD 254755	2009 Nov 5	Keck	$R(1,1)^u$, $R(1,0)$	2400	HR 1791	4
HD 254755	2009 Nov 6	Keck	$R(1,1)^u$, $R(1,0)$	1200	HR 1791	4
HD 254755	2009 Dec 13	Subaru	$R(1,1)^u$, $R(1,0)$, $R(1,1)^l$, $Q(1,1)$, $Q(1,0)$	7200	HR 1791	4
HD 43703	2009 Nov 6	Keck	$R(1,1)^u$, $R(1,0)$	4080	HR 1791	4
HD 43703	2009 Dec 13	Subaru	$R(1,1)^u$, $R(1,0)$, $R(1,1)^l$, $Q(1,1)$, $Q(1,0)$	7200	HR 1791	4
HD 43907	2009 Dec 12	Subaru	$R(1,1)^u$, $R(1,0)$, $R(1,1)^l$, $Q(1,1)$, $Q(1,0)$	2520	HR 1791	4
HD 47129	2008 Jan 24	UKIRT	$R(1,1)^u$, $R(1,0)$	2880	HR 2004	
HD 53367	2008 Jan 23	UKIRT	$R(1,1)^u$, $R(1,0)$	2400	HR 1165	
HD 53367	2008 Jan 25	UKIRT	$R(1,1)^u$, $R(1,0)$	2400	HR 2421	
HD 53367	2009 Dec 3	VLT	$R(1,1)^u$, $R(1,0)$, $R(1,1)^l$	1800	HR 2004	
HD 73882	2009 Dec 3	VLT	$R(1,1)^u$, $R(1,0)$, $R(1,1)^l$	1800	HR 3165	5
HD 73882	2010 Jan 17	VLT	$R(1,1)^u$, $R(1,0)$, $R(1,1)^l$	1800	HR 3165	5

19

Table 2.4: (continued)

Object	Date(s) of Observation	Telescope	Transition(s) Observed	Integration Time (sec)	Standard	Published
HD 110432	2010 Jan 17	VLT	$R(1,1)^u$, $R(1,0)$, $R(1,1)^l$	600	HR 5440	5
HD 110432	2010 Feb 28	VLT	$R(1,1)^u$, $R(1,0)$, $R(1,1)^l$	1200	HR 5440	5
HD 110432	2010 Mar 2	VLT	$R(1,1)^u$, $R(1,0)$, $R(1,1)^l$	2400	HR 5440	5
o Sco	2001 May 26	UKIRT	$R(1,1)^u$, $R(1,0)$	960	HR 5953	2
o Sco	2007 Jul 1	UKIRT	$R(1,1)^u$, $R(1,0)$	1200	HR 5953	
o Sco	2007 Jul 2	UKIRT	$R(1,1)^u$, $R(1,0)$	1200	HR 5953	
ρ Oph D	2007 Jul 3	UKIRT	$R(1,1)^u$, $R(1,0)$	5760	HR 5953	
HD 147889	2001 May 24	UKIRT	$R(1,1)^u$, $R(1,0)$	5760	HR 5953	2
HD 147889	2007 Jul 25	UKIRT	$R(1,1)^u$, $R(1,0)$	5760	HR 5953	
χ Oph	2009 Aug 30	Gemini S	$R(1,1)^u$, $R(1,0)$	720	HR 6527	
μ Nor	2010 Apr 5	Gemini S	$R(1,1)^u$, $R(1,0)$	4320	HR 6527	
HD 149404	2009 Aug 5	Gemini S	$R(1,1)^u$, $R(1,0)$	1920	HR 6527	
ζ Oph	2000 Jun 26	KPNO	$R(1,1)^l$	2880	HR 7001	1
ζ Oph	2001 May 24	UKIRT	$R(1,1)^u$, $R(1,0)$	576	HR 5953	2
ζ Oph	2001 May 25	UKIRT	$R(1,1)^u$, $R(1,0)$	1344	HR 5953	2
ζ Oph	2007 Jul 2	UKIRT	$R(1,1)^u$, $R(1,0)$	2160	HR 5685	
ζ Oph	2007 Jul 3	UKIRT	$R(1,1)^u$, $R(1,0)$	2160	HR 5953	
HD 152236	2009 Aug 30	Gemini S	$R(1,1)^u$, $R(1,0)$	960	HR 6527	
HD 154368	2009 Aug 30	Gemini S	$R(1,1)^u$, $R(1,0)$	1920	HR 6527	5
WR 104	1998 Jul 4	KPNO	$R(1,1)^l$	2100	HR 7001	1
WR 104	2001 May 24	UKIRT	$R(1,1)^u$, $R(1,0)$	480	HR 6378	1
HD 168607	2000 Jul 7	UKIRT	$R(1,1)^u$, $R(1,0)$	1500	HR 6378	1
HD 168607	2007 Jul 1	UKIRT	$R(1,1)^u$, $R(1,0)$	3840	HR 6378	
HD 168607	2007 Jul 2	UKIRT	$R(1,1)^u$, $R(1,0)$	3456	HR 6378	
HD 168625	2001 May 26	UKIRT	$R(1,1)^u$, $R(1,0)$	1440	HR 6378	2
HD 168625	2007 Jul 1	UKIRT	$R(1,1)^u$, $R(1,0)$	3840	HR 7001	

Table 2.4: (continued)

Object	Date(s) of Observation	Telescope	Transition(s) Observed	Integration Time (sec)	Standard	Published
BD -14 5037	2001 May 28	UKIRT	$R(1,1)^u$, $R(1,0)$	2016	HR 6378	2
HD 169454	2001 May 25	UKIRT	$R(1,1)^u$, $R(1,0)$	4224	HR 5685	2
HD 169454	2001 May 27	UKIRT	$R(1,1)^l$	5184	HR 6378	2
HD 169454	2007 Jul 2	UKIRT	$R(1,1)^u$, $R(1,0)$	4800	HR 6378	
W 40 IRS 1A	2001 May 25	UKIRT	$R(1,1)^u$, $R(1,0)$	1800	HR 6378	2
W 40 IRS 1A	2001 May 26	UKIRT	$R(1,1)^u$, $R(1,0)$	1800	HR 7001	2
W 40 IRS 1A	2001 May 27	UKIRT	$R(1,1)^l$	2400	HR 6165	
WR 118	1998 Jul 4	KPNO	$R(1,1)^l$	2760	HR 7924	1
WR 118	2001 May 24	UKIRT	$R(1,1)^u$, $R(1,0)$	360	HR 7924	1
WR 121	1998 Jul 4	KPNO	$R(1,1)^l$	6720	HR 7001	1
HD 183143	2000 Jun 25	KPNO	$R(1,1)^l$	5040	HR 7001	1
HD 183143	2000 Jul 6	UKIRT	$R(1,1)^u$, $R(1,0)$	1740	HR 7001	1
P Cygni	2000 Jun 25	KPNO	$R(1,1)^l$	4680	HR 7001	1
HD 193322A	2009 Nov 6	Keck	$R(1,1)^u$, $R(1,0)$	1200	HR 7924	
HD 229059	2001 May 27	UKIRT	$R(1,1)^u$, $R(1,0)$	1800	HR 7924	2
HD 229059	2001 Sep 5	UKIRT	$R(1,1)^u$, $R(1,0)$	1800	HR 7924	2
HD 194279	1998 Jul 4	KPNO	$R(1,1)^l$	5520	HR 7924	1
Cyg OB2 5	1998 Jul 3	KPNO	$R(1,1)^l$	9840	HR 7924	1
Cyg OB2 5	2000 Jul 6	UKIRT	$R(1,1)^u$, $R(1,0)$	2580	HR 7924	1
Cyg OB2 12	1997 Jul 11	UKIRT	$R(1,1)^u$, $R(1,0)$	600	HR 7924	6,7
Cyg OB2 12	1997 Sep 5	KPNO	$R(1,1)^l$	3600	HR 7924	6,7
Cyg OB2 12	1998 Jul 3	KPNO	$R(1,1)^l$	1800	HR 7924	1
Cyg OB2 12	2000 Jun 25	KPNO	$R(1,1)^l$	3600	HR 7924	1
Cyg OB2 8A	2009 Nov 6	Keck	$R(1,1)^u$, $R(1,0)$	1200	HR 7924	1

Table 2.4: (continued)

Object	Date(s) of Observation	Telescope	Transition(s) Observed	Integration Time (sec)	Standard	Published
HD 204827	2007 Jun 30	UKIRT	$R(1,1)^u$, $R(1,0)$	5040	HR 7924	
HD 204827	2007 Jul 3	UKIRT	$R(1,1)^u$, $R(1,0)$	5040	HR 7924	
HD 204827	2007 Jul 13	UKIRT	$R(1,1)^u$, $R(1,0)$	5760	HR 7740	
HD 204827	2009 Nov 6	Keck	$R(1,1)^u$, $R(1,0)$	960	HR 7924	
HD 206267	2007 Jul 1	UKIRT	$R(1,1)^u$, $R(1,0)$	6120	HR 7740	
HD 206267	2007 Jul 2	UKIRT	$R(1,1)^u$, $R(1,0)$	5760	HR 7924	
HD 206267	2009 Nov 6	Keck	$R(1,1)^u$, $R(1,0)$	1440	HR 7924	
19 Cep	2009 Nov 5	Keck	$R(1,1)^u$, $R(1,0)$	1200	HR 7924	
λ Cep	2001 May 24	UKIRT	$R(1,1)^u$, $R(1,0)$	4320	HR 7001	2
λ Cep	2009 Nov 5	Keck	$R(1,1)^u$, $R(1,0)$	720	HR 7924	
1 Cas	2009 Nov 5	Keck	$R(1,1)^u$, $R(1,0)$	1200	HR 7924	

References: (1) McCall et al. (2002); (2) Indriolo et al. (2007); (3) McCall et al. (2003); (4) Indriolo et al. (2010a); (5) Crabtree et al. (2011); (6) McCall et al. (1998); (7) Geballe et al. (1999)

Chapter 3

Data Reduction

Data processing was primarily performed using 2 programs: IRAF and Igor Pro. IRAF — the Image Reduction and Analysis Facility — is freely available for download[1], and is written and supported by the IRAF programming group at the National Optical Astronomy Observatories (NOAO). Igor Pro is a commercially available[2] data analysis software tool.

3.1 Image Processing in IRAF

At different telescopes, data are given to the observer after having undergone various amounts of processing. Below are the procedures used in IRAF to process raw images and extract one-dimensional TXT spectra (i.e., a .txt file containing 2 columns: pixel number and intensity) from each observatory.

3.1.1 UKIRT

A reduction procedure for CGS4 data that relies on Starlink's ORAC-DR[3] pipeline and FIGARO[4] package is described in Indriolo et al. (2007). However, this procedure was found to be inadequate due to its inability to properly remove bad pixels. Because of the 3×2 sampling mode that was used, each single bad pixel on the array translates to 6 consecutive bad pixels in the spectrum output by the ORAC-DR pipeline. To work around this problem, I developed the following reduction procedure for CGS4 data. All of the UKIRT spectra presented herein (including those previously presented in Indriolo et al., 2007) were (re)reduced using this procedure.

Data downloaded from Joint Astronomy Centre's Observations Management Project are in the SDF file format, with 1 SDF file for each observation in the nightly log. Starlink's

---

[1]http://iraf.noao.edu/
[2]http://www.wavemetrics.com/
[3]http://www.oracdr.org/
[4]http://www.starlink.rl.ac.uk/star/docs/sun86.htx/sun86.html.

CONVERT[5] package was used to convert files from SDF to FITS format via the command:

ndf2fits "c*yyyymmdd_*" "*|.fit|.fits|".

The standard naming convention for CGS4 data is c*yyyymmdd_nnnnn*.sdf, where *yyyymmdd* is the UT date of observations and *nnnnn* is the observation number. As such, the unix wildcard character in the second argument serves to select all observations from a given night. In the third argument the wildcard preserves the input filename(s), and the remainder switches the file extension to ".fits" from the default ".fit". For observations of science and standard stars using 3×2 sampling, this command will generate 7 FITS files: 1 header file (c*yyyymmdd_nnnnn*.HEADER.fits) and 6 image files (c*yyyymmdd_nnnnn*.IZ.fits, where $1 \leq Z \leq 6$).

Pixel labels are in the form i-n, where
i = image number
n = pixel number

6-1	6-2	6-3	6-4	6-5
5-1	5-2	5-3	5-4	5-5
4-1	4-2	4-3	4-4	4-5

Individual Images

3-1	3-2	3-3	3-4	3-5
2-1	2-2	2-3	2-4	2-5
1-1	1-2	1-3	1-4	1-5

4-1	5-1	6-1	4-2	5-2	6-2	4-3	5-3	6-3	4-4	5-4	6-4	4-5	5-5	6-5
1-1	2-1	3-1	1-2	2-2	3-2	1-3	2-3	3-3	1-4	2-4	3-4	1-5	2-5	3-5

Interwoven Images
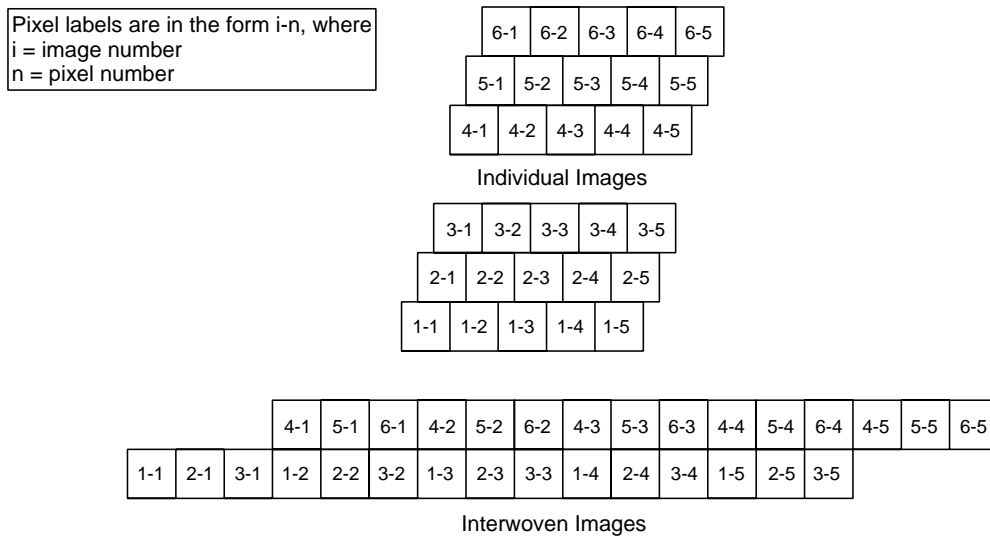
Figure 3.1: A cartoon showing how pixels along a single row from individual GCS4 images are woven together to provide images with higher spectral resolution. Pixels are labeled as *i-n*, where *i* is the image number and *n* is the pixel number.

As mentioned before, the array was shifted by one-third of a pixel along the dispersion direction between each of the 6 image files, such that the average wavelength sampled by pixel *n* along the dispersion direction increased between consecutive images; i.e.

$$\lambda[\text{I}1(n)] < \lambda[\text{I}2(n)] < \lambda[\text{I}3(n)] < \lambda[\text{I}4(n)] = \lambda[\text{I}1(n+1)].$$

This is shown in the upper portion of Figure 3.1. Because pixel *n* in images 2 and 3 sample the spectrum "between" pixels *n* and $n+1$ in image 1, images 1, 2, and 3 can be "woven"

[5]http://star-www.rl.ac.uk/star/docs/sun55.htx/sun55.html

together to provide a single image with increased spectral resolution. Likewise, images 4, 5, and 6 can be interwoven, and the wavelength sampled by pixel k in the combined image 456 will be the same as that sampled by pixel $k + 3$ in the combined image 123. This is shown in the lower portion of Figure 3.1. Unfortunately, this processing scheme means that a single bad pixel in the array is spread across 3 consecutive pixels in the interwoven image, and 6 consecutive pixels in the sum of the interwoven images. While a single bad pixel could be interpolated across in the original individual images, this would mean that in the interwoven spectrum a bad pixel k would have been fixed using the values in pixels $k - 3$ and $k + 3$. To interpolate across bad pixels using more relevant data, I developed the method discussed here and in Section 3.2.1.

The 6 raw image files (256×178 pixels) belonging to a single observation are woven into 2 larger images (768×178 pixels), one formed from images 1, 2, and 3, and the other from images 4, 5, and 6, and are labeled with a 123 and 456 accordingly. The 123 image taken when the telescope was nodded to the A position is then subtracted from the 123 image taken when the telescope was nodded to the subsequent B position, and likewise for the 456 images. This subtraction of neighboring images serves to remove dark current and atmospheric emission features. These processes are automated in IRAF using a .cl file, and a sample of the code used to perform these two steps is given in Section A.1. One-dimensional spectra in TXT format are then extracted from the neighbor-subtracted images from each of the 3 rows on the array containing the most flux from the spectral image. File names for these spectra include the identifiers $\_i\_r$, where $i = 1$ or 4 designates the 123 or 456 image, and $r = a$, b, or c designates the row of the array from which the spectrum was extracted (e.g., if the spectral image was centered on row 96, the labels are as follows: row $95 \rightarrow a$, row $96 \rightarrow b$, row $97 \rightarrow c$). A sample of the IRAF script used to perform this task is given in Section A.2.

3.1.2   Gemini South

The reduction process for *Phoenix* data, starting from raw FITS files, is described in Section 2 of Crabtree et al. (2011) and reproduced here. For each night of *Phoenix* observations a bad pixel map was created from the average of several dark frames, and these pixels were interpolated over in the object and flat frames. Flats were combined to create a normalized flat field which was divided out of the object frames. Neighboring AB image pairs were subtracted from each other to remove atmospheric emission and dark current. One-dimensional spectra were then extracted in ec.FITS format from the two-dimensional spectral images using the *apall* routine in IRAF. The ec.FITS spectra were then converted to TXT format using

IRAF's *wspectext* routine.

3.1.3 Keck

The reduction process for NIRSPEC data, starting from raw FITS files, is described in Section 3.1 of Indriolo et al. (2010a) and reproduced here. A bad pixel map was created from the average of several dark frames, and these pixels were interpolated over in the flat-field and object images. Images were then cut into two sections, with each section containing one of the orders of interest from the cross-dispersed spectrograph. These sections were then treated as individual images for the remainder of the reduction process. The flats were then combined, and each object frame was divided by the normalized, averaged flat-field. Neighboring AB image pairs were subtracted from each other to remove atmospheric emission and dark current. One-dimensional spectra were then extracted in ec.FITS format for each order using the *apall* routine in IRAF. The ec.FITS spectra were then converted to TXT format using IRAF's *wspectext* routine.

3.1.4 Subaru

The reduction process for IRCS data, starting from raw FITS files, is described in Section 3.2 of Indriolo et al. (2010a) and reproduced here. While no dark frames were taken at Subaru, calibration frames with the lamp off were used to create a bad pixel map. These pixels were interpolated over in the object and flat-field frames, and each image was cut into two sections containing an order of interest. Inspection of the averaged, normalized flat-field frame for each order showed a low S/N, so object frames were not divided by these flats. Neighboring AB image pairs were subtracted from each other to remove atmospheric emission and dark current. One-dimensional spectra were then extracted in ec.FITS format for each order using the *apall* routine in IRAF. The ec.FITS spectra were then converted to TXT format using IRAF's *wspectext* routine.

3.1.5 VLT

The reduction process for CRIRES data is described in Section 2 of Crabtree et al. (2011), and partially reproduced here. Data taken with CRIRES at the VLT were processed through the CRIRES specific pipeline. This pipeline performs several calibration and reduction steps, including dark subtraction, correction for detector non-linearity, flat-fielding, and the combination of all nodded images for a given target. The result is a single output FITS file with 4 extensions (one for each detector in the mosaic) that contains the fully reduced

two-dimensional spectral image for a given target. These files are identified by the product codes SCOM (for science targets) or PCOM (for telluric calibration targets) in the ESO file nomenclature.

To continue the reduction process beyond these files generated by the CRIRES pipeline, each multi-extension FITS file was split into 4 new FITS files — again, one for each detector. As the H_3^+ lines appear on detectors 1 and 3, the files containing data from detectors 2 and 4 are disregarded from this point on. One-dimensional spectra were then extracted in ec.FITS format from the two-dimensional spectral images using the *apall* routine in IRAF. The ec.FITS spectra were then converted to TXT format using IRAF's *wspectext* routine.

3.2 Spectral Processing in Igor Pro

One-dimensional TXT format spectra were then imported into Igor Pro where further spectral processing was performed. Again, slightly different processing was required for data from different telescopes, and is discussed below. The majority of this processing was done using custom macros written by Ben McCall that are described in detail in his PhD thesis (McCall, 2001).

3.2.1 UKIRT

As described above, CGS4 spectra are produced by weaving together 3 individual images. Because the intensity of light varies slightly between images 1, 2, and 3 for a given observation, the interwoven 123 spectra suffer from a 3-pixel "ripple" pattern (see the bottom panel of Figure 3.2). To remove this pattern, an interwoven spectrum is split back into its 3 original components. The continuum level for each component is then fit with a quadratic function. Intensity values in component 2 are multiplied by a scaling factor equal to the continuum fit level of component 1 divided by the continuum fit level of component 2. Similarly, component 3 is also scaled to match component 1. The spectra are then re-woven together to create a "de-rippled" spectrum, as shown in the top panel of Figure 3.2. This correction occurs as spectra are loaded into Igor Pro.

At this point in the reduction, each observation consists of 6 separate spectra: rows a, b, and c from images 123 and 456. If the intensity on row b is significantly higher than on rows a and c, then only row b is considered from here on. If the intensity on row a or c is comparable to that on b though, then both row b and the row with comparable signal are used. In the case where only row b is used, the procedure to combine these spectra and interpolate over bad pixels is now described.
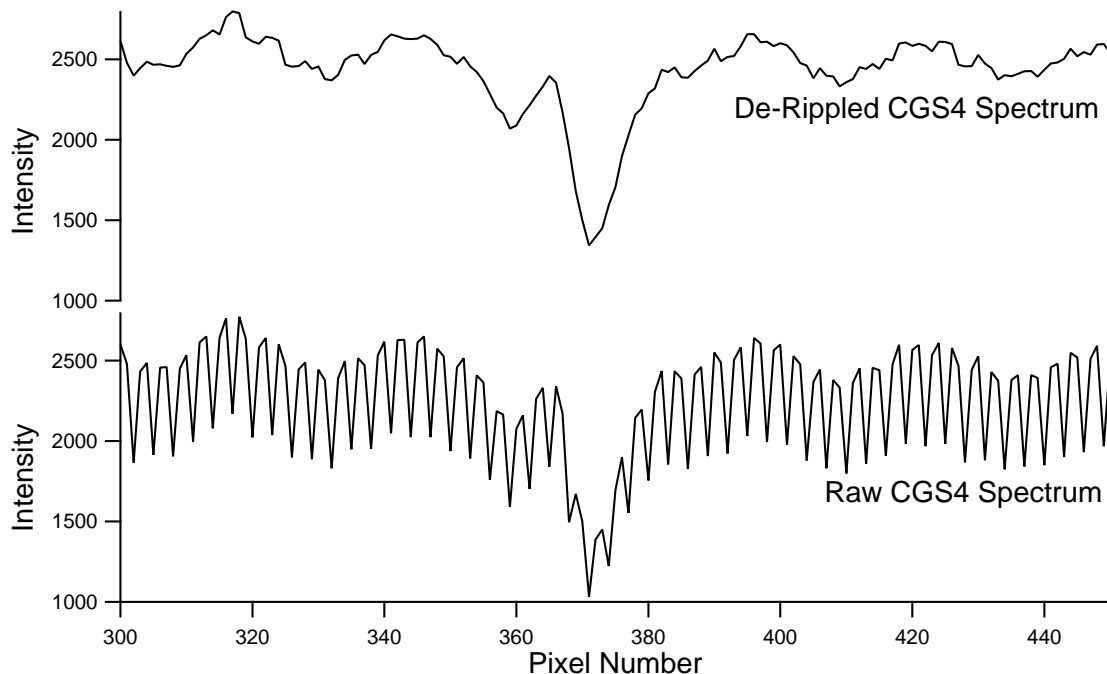
Figure 3.2: A raw CGS4 spectrum (bottom panel) that demonstrates the 3-pixel ripple pattern, and the same spectrum having been corrected (top panel). The strong feature near the middle is an atmospheric CH_4 line at 3.66753 μm.

Both spectra (_1_b and _4_b) are added together, with the _1 spectrum shifted by $(x + 3)$ to account for the difference in wavelength. An array that contains a list of bad pixels on row b is then loaded. Starting from $x = 0$, a routine checks pixel x in the combined spectrum against the bad pixel list. When a group of bad pixels in the _1 spectrum is reached, the values in the _4 spectrum are scaled up to the level of the sum of both spectra, and vice versa. This serves to use actual data in interpolating across the bad pixels. Figure 3.3 shows the difference between a corrected and uncorrected spectrum. The procedure for performing this correction in the case where 2 rows have comparable signal is similar to that presented here.

Upon correcting for bad pixels, each observation from the UKIRT night log is represented by a single spectrum. The ensuing reduction process is very similar to that used previously (McCall, 2001; Indriolo et al., 2007), and is described here for completeness. All spectra for a given target in an observing sequence are added together using the *AutoCombine* routine. In some cases, the wavelength coverage is shifted by about 1 pixel between spectra taken in the A and B nod positions. During more lengthy observing sequences the wavelength coverage for both nod positions may also drift by about 1 pixel. As such, it is imperative that the user check the position of atmospheric features in spectra from the A nod position

versus the B nod position, and in spectra from the beginning of an observing sequence versus the end of an observing sequence. If these shifts are apparent, the user should then check the "shift" box in the *AutoCombine* routine. This will perform a cross-correlation between spectra that are being added together, and shift spectra in the x-direction accordingly. If a shift in wavelength is not present though, the "shift" box should remain unchecked as sometimes the cross-correlation will incorrectly cue on the fringing pattern instead of the atmospheric features.
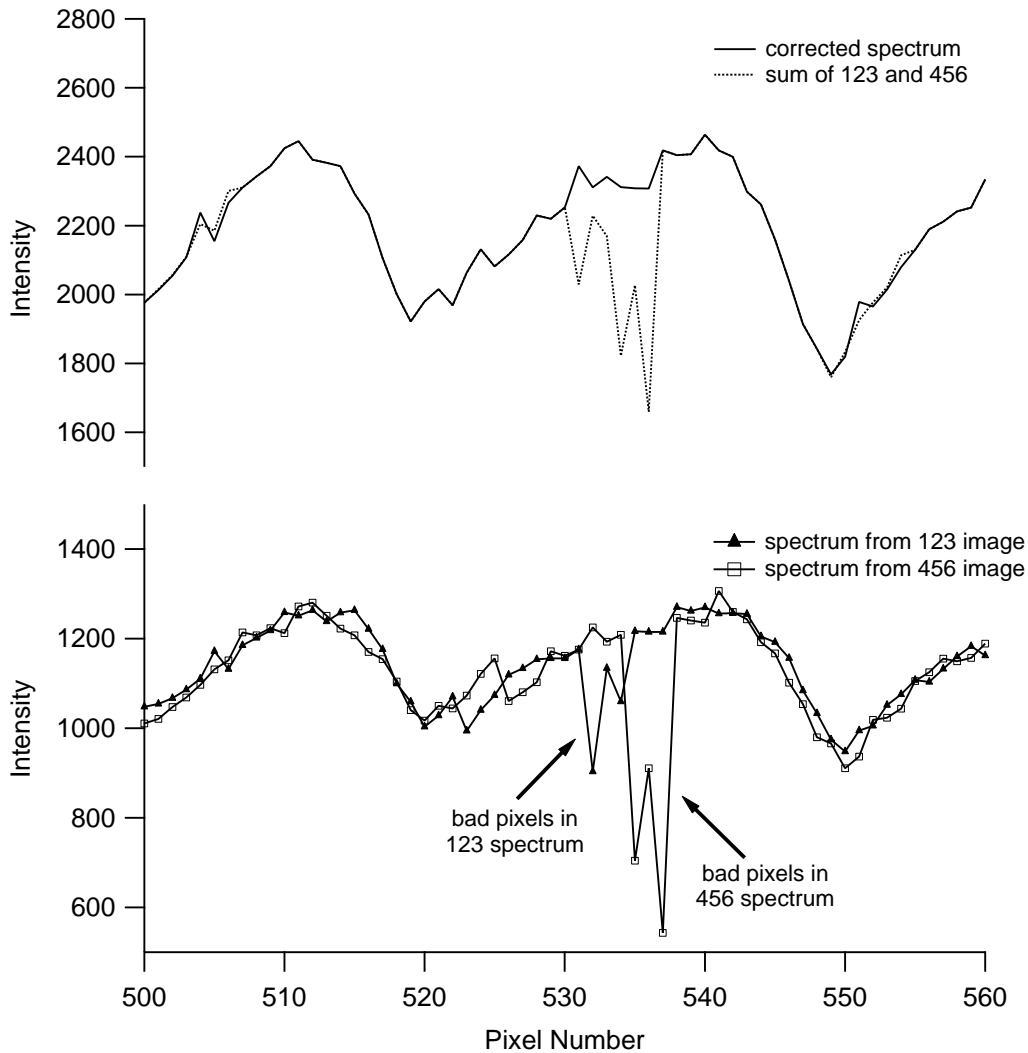
Figure 3.3: The bottom panel shows sample spectra from a single row of the 123 and 456 images. The 456 spectrum has been shifted 3 pixels to the right so that atmospheric features line up. The top panel shows the sum of the 123 and 456 images (dotted line) and the corrected spectrum (solid line) after the bad pixels have been interpolated across.

With all spectra for a given target combined, the next step in the reduction process is the

removal of atmospheric absorption lines via division by a standard star spectrum. This is done using the *Process* routine. The user selects a target and suitable standard and follows the procedure outlined in McCall (2001). I suggest using the "Tweak/FT" option, which will simultaneously divide the object by the standard, and remove the fringing in the continuum caused by the circular variable filter by cutting out a particular component in Fourier space. The range in Fourier space that is cut can be changed by opening the Igor Pro Procedure window, going to the function *ReDrawFT*, finding the comment in the code that says "Third, FT Cut", and editing the variables *start* and *stop*. In the division process, the user can shift the standard star spectrum in wavelength and scale the strength of atmospheric lines to best match those in the object spectrum. When a suitable result is obtained, click the "StoreFT" button to save the normalized spectrum.

Wavelength calibration is performed using the atmospheric absorption lines present in a spectrum before division by a standard star. The procedure is outlined in McCall (2001), and is expected to produce a calibrated spectrum that is accurate to within about 2 km s^{-1}. If, however, the "FitPeaks" function does not automatically identify atmospheric features — as is frequently the case with very low S/N spectra — the user can still start the "Setup Identify" function and simply input the x-position and known wavelengths manually to perform the calibration. While the above procedure will calibrate a spectrum with an observed wavelength, the Earth's motion around the sun causes interstellar absorption lines to shift position with respect to atmospheric lines throughout the year. The *rvcorrect* routine in IRAF is used to determine the Earth's velocity in the Local Standard of Rest (LSR) frame along each line of sight at the time an observation was made. Spectra are then shifted into the LSR frame such that interstellar features will appear at the same wavelength no matter when observations occurred.

The last step in our reduction process is to remove any large fluctuations or slope from the continuum. This is done using a baseline removal tool developed for Igor Pro by Mike Lindsay, a former member of the Oka group at the University of Chicago. Files containing the baseline removal procedure are freely available for download[6]. In cases where the baseline was rather smooth but not constant, spectra were divided by 3rd–5th order polynomial fits to the continuum. In cases where smaller scale variations could not be removed by polynomial fitting, spectra were divided by a 20–40 point moving average (the H$_3^+$ lines and other sharp features were excluded from the average). The result of all of the above processing is a single spectrum for a given target from a given night that is normalized and wavelength calibrated in the LSR frame. My naming convention for output files in this

---

[6]http://fermi.uchicago.edu/freeware/IgorPlugins/

state is *objectname_yyyymmdd*y and *objectname_yyyymmdd*LSRx for the files containing intensity and wavelength, respectively.

3.2.2   Gemini South

Phoenix spectra are loaded into Igro Pro and are again added together using the *Autocombine* routine. During this process the user should check for offsets in wavelength between the A and B spectra and utilize the cross-correlation feature accordingly. Science targets are divided by telluric standards as before, but a cut in Fourier space is not necessary. Wavelength calibration, shift to the LSR frame, and baseline removal are performed as before.

3.2.3   Keck

NIRSPEC spectra are loaded into Igor Pro and added together using the *Autocombine* routine. The cross-correlation feature is used if necessary. Science targets are then divided by telluric standards. Depending on the echelle grating/cross-disperser setting used and the brightness of the background source, fringing may or may not be present on the continuum. If it is, the *FFT* (Fast Fourier Transform) routine is used to cut out the fringing as described in McCall (2001). Once fringes are removed, wavelength calibration, shift to the LSR frame, and baseline removal are performed as before.

3.2.4   Subaru

Data taken with IRCS suffer from a saw-tooth pattern (2-pixel ripple) that results from different readout channels on the array. In order to remove this pattern, a moving average was taken for both the odd and even numbered pixels, and the even pixels were then scaled by the ratio of these averages. This correction occurs as spectra are loaded into Igor Pro. Spectra are added together with *AutoCombine* and the cross-correlation is used as necessary. Science targets are divided by telluric standards, and, as for NIRSPEC data, an FFT cut is performed if required. The "FitPeaks" function does a poor job of fitting atmospheric absorption lines in IRCS data — primarily due to the lower resolution — so line position must be determined and entered manually in the wavelength calibration process. After calibration is complete, shift to the LSR frame and baseline removal are performed as before.

3.2.5　VLT

The majority of the reduction process for CRIRES data is performed by the aforementioned pipeline. As such, spectra that are loaded into Igor Pro are in fact the final, summed spectra for each target on a given night. Division of science targets by standard stars, wavelength calibration, shift to the LSR frame, and baseline removal are handled as above.

3.2.6　Combination of Spectra from Different Nights

For sight lines that were observed only once, the data reduction process is complete at this point. However, for sight lines that were observed on multiple nights, the spectra from each night can be combined. To account for variations in the S/N between spectra from different nights, spectra are combined using a variance-weighted mean,

$$\bar{x} = \sum_{i=1}^{n}(x_i/\sigma_i^2)/\sum_{i=1}^{n}(1/\sigma_i^2),\tag{3.1}$$

where x_i is a normalized spectrum, σ_i is the standard deviation on the continuum near the expected position of H_3^+ lines, and i loops over all spectra of a given target from a particular telescope. This averaging scheme is equivalent to weighting spectra by the continuum level $(S/N)^2$, adding them together, and re-normalizing. For sight lines observed on multiple nights with only 1 telescope, this step completes the reduction procedure. If a sight line was observed with multiple telescopes these spectra can also be combined, but the different spectral resolutions make this slightly more complicated. In this case, all spectra from a single telescope are first combined as above. The combined spectrum with higher spectral resolution is then recast onto the wavelength scale of the lower-resolution combined spectrum. Continuum-level standard deviations are calculated for each combined, normalized spectrum, and these are in turn combined using the same variance-weighted mean as before. This completes the description of the spectral reduction procedure utilized for all cases encountered.

Chapter 4

H$_3^+$ Spectra

Spectra resulting from the data reduction procedures described in Chapter 3 are presented here. Figures 4.1 through 4.12 are uniform in size, wavelength coverage (0.004 μm), and relative intensity (0.17) so that they can be easily compared by eye. Spectra are shifted in the y-direction for clarity. Gaps in various spectra are regions where the removal of atmospheric features was particularly poor. The expected positions of H$_3^+$ absorption features — as determined from previous measurements of the gas velocity along a line of sight — are marked with vertical lines. Table 4.1 gives details concerning what is contained in the figures within this chapter.

Table 4.1: List of H$_3^+$ Spectra in Chapter 4

Figure	Sight Line	Transitions	LSR Gas Velocity (km s^{-1})	Reference Species	Reference
4.1	HD 20041	$R(1,1)^u$, $R(1,0)$	-1.6	K I	1
4.1	HD 21389	$R(1,1)^u$, $R(1,0)$	-0.5	CH	1
4.1	ζ Per	$R(1,1)^u$, $R(1,0)$	6.9	CH	1
4.1	X Per	$R(1,1)^u$, $R(1,0)$	6.6	CH	1
4.1	HD 29647	$R(1,1)^u$, $R(1,0)$	6.3	C$_2$	2
4.2	HD 168607	$R(1,1)^u$, $R(1,0)$	22.0	CO	3
4.2	HD 168625	$R(1,1)^u$, $R(1,0)$	22.0	CO	3
4.2	HD 204827	$R(1,1)^u$, $R(1,0)$	-4.3 & 0.5	CH	4
4.2	HD 229059	$R(1,1)^u$, $R(1,0)$	4.0	K I	5
4.3	HD 169454	$R(1,1)^u$, $R(1,0)$	5.3	CH	1
4.3	W 40 IRS 1A	$R(1,1)^u$, $R(1,0)$	8	^{13}CO emission	6
4.4	HD 169454	$R(1,1)^l$	5.3	CH	1
4.4	W 40 IRS 1A	$R(1,1)^l$	8	^{13}CO emission	6
4.5	o Per	$R(1,1)^u$, $R(1,0)$	7.3	CH	1
4.5	ϵ Per	$R(1,1)^u$, $R(1,0)$	2.2	K I	7
4.5	ξ Per	$R(1,1)^u$, $R(1,0)$	0.6 & 3.8	CH	8
4.5	NGC 2024 IRS 1	$R(1,1)^u$, $R(1,0)$	12.0	^{12}CO emission	9
4.5	HD 47129	$R(1,1)^u$, $R(1,0)$	10.1	CH	10
4.6	o Sco	$R(1,1)^u$, $R(1,0)$	2.3	K I	1

Figure	Sight Line	Transitions	LSR Gas Velocity (km s^{-1})	Reference Species	Reference
4.6	HD 147888	$R(1,1)^u$, $R(1,0)$	2.0	CH	4
4.6	HD 147889	$R(1,1)^u$, $R(1,0)$	2.7	K I	1
4.6	ζ Oph	$R(1,1)^u$, $R(1,0)$	-1.0	CH	1
4.6	BD -14 5037	$R(1,1)^u$, $R(1,0)$	7 & 18	CH	11
4.6	HD 206267	$R(1,1)^u$, $R(1,0)$	-3 & 1	CH	4
4.7	HD 53367	$R(1,1)^u$, $R(1,0)$	15.5	CH	11
4.7	HD 73882	$R(1,1)^u$, $R(1,0)$	4.5	CH & CN	11
4.7	HD 110432	$R(1,1)^u$, $R(1,0)$	-4.7 & -0.7	CH	12
4.8	HD 53367	$R(1,1)^l$	15.5	CH	11
4.8	HD 73882	$R(1,1)^l$	4.5	CH & CN	11
4.8	HD 110432	$R(1,1)^l$	-4.7 & -0.7	CH	12
4.9	χ Oph	$R(1,1)^u$, $R(1,0)$	1.1	CH	8
4.9	μ Nor	$R(1,1)^u$, $R(1,0)$	2.2	CH	10
4.9	HD 149404	$R(1,1)^u$, $R(1,0)$	5	CH & CH$^+$	11
4.9	HD 152236	$R(1,1)^u$, $R(1,0)$	-4.5 & 6.5	CH & CN	12
4.9	HD 154368	$R(1,1)^u$, $R(1,0)$	4.6	CH	11
4.10	HD 21483	$R(1,1)^u$, $R(1,0)$	10.3	CH	1
4.10	40 Per	$R(1,1)^u$, $R(1,0)$	6.8	K I	13
4.10	λ Cep	$R(1,1)^u$, $R(1,0)$	-1.7	CH	1
4.11	HD 21856	$R(1,1)^u$, $R(1,0)$	1	Ca II	14
4.11	BD +31 643	$R(1,1)^u$, $R(1,0)$	5	CH	15
4.11	62 Tau	$R(1,1)^u$, $R(1,0)$	4.8	CH	1
4.11	α Cam	$R(1,1)^u$, $R(1,0)$	0.3	CH	8
4.12	HD 193322A	$R(1,1)^u$, $R(1,0)$	3.5	K I	13
4.12	Cyg OB2 8A	$R(1,1)^u$, $R(1,0)$	5	CH$^+$	16
4.12	19 Cep	$R(1,1)^u$, $R(1,0)$	-5.8	CH$^+$	4
4.12	1 Cas	$R(1,1)^u$, $R(1,0)$	1.6	CH	17
4.12	κ Cas	$R(1,1)^u$, $R(1,0)$	-10.7	CH	17
4.13	ζ Per	$R(3,3)^l$	6.9	CH	1

Notes: Column 4 gives the LSR gas velocity along the line of sight previously determined from observations of the species listed in column 5.

References: (1) D. E. Welty 2002, private communication; (2) Hobbs et al. (1983); (3) our work, unpublished; (4) Pan et al. (2004); (5) Federman & Lambert (1992); (6) Crutcher & Chu (1982); (7) Welty & Hobbs (2001); (8) Crane et al. (1995); (9) Emprechtinger et al. (2009); (10) Danks et al. (1984); (11) Gredel et al. (1993); (12) Crawford (1995); (13) Chaffee & White (1982); (14) Cohen (1973); (15) Allen (1994); (16) Snow et al. (2010); (17) Federman (1982)
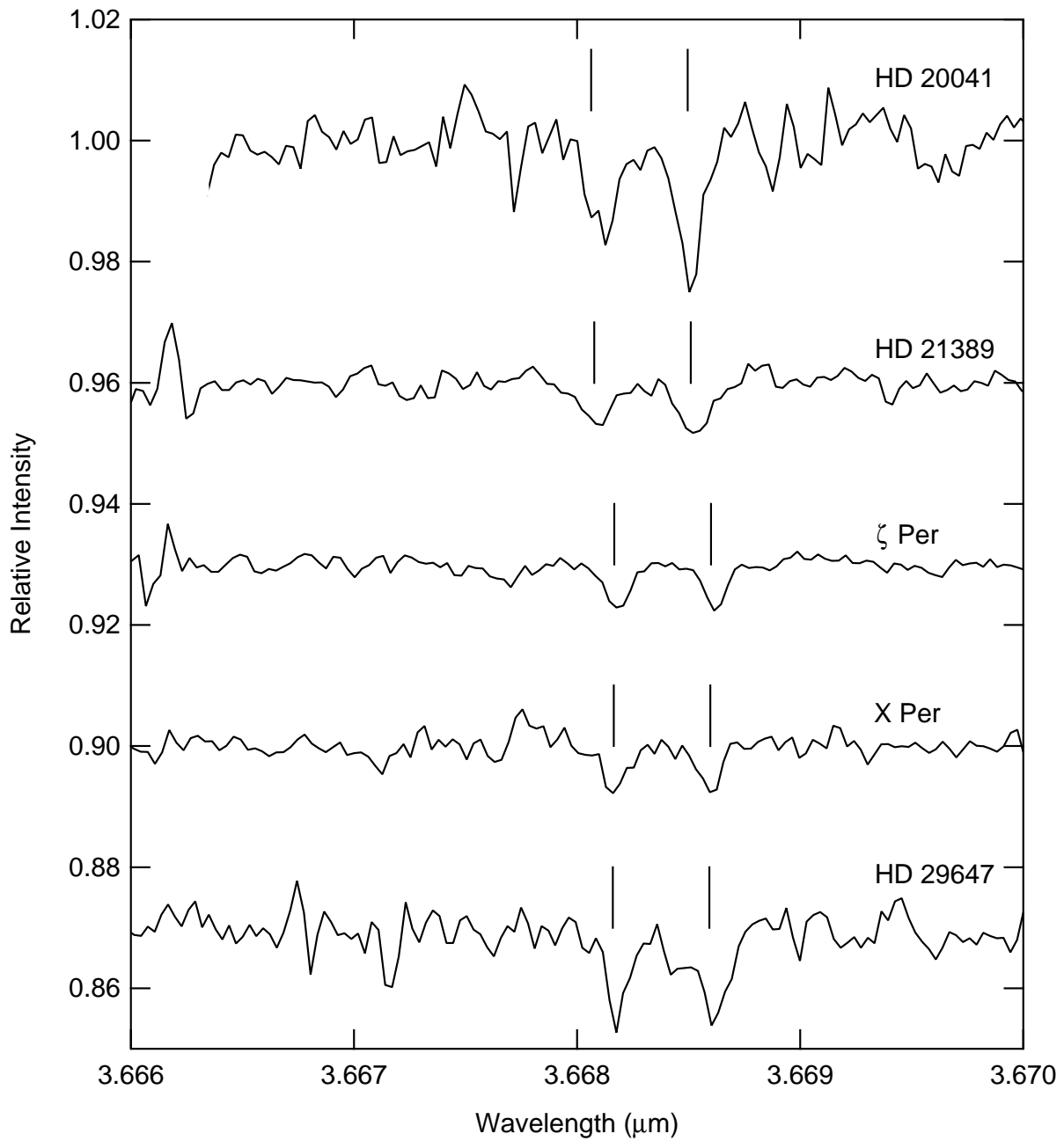
Figure 4.1: Detections of the $R(1,1)^u$ and $R(1,0)$ lines of H_3^+ taken with CGS4 at UKIRT. Sight lines include HD 20041, HD 21389, ζ Per, X Per, and HD 29647. Vertical lines mark the expected positions of absorption lines given gas velocities along each line of sight. Gaps in spectra are where the removal of atmospheric features was particularly poor.
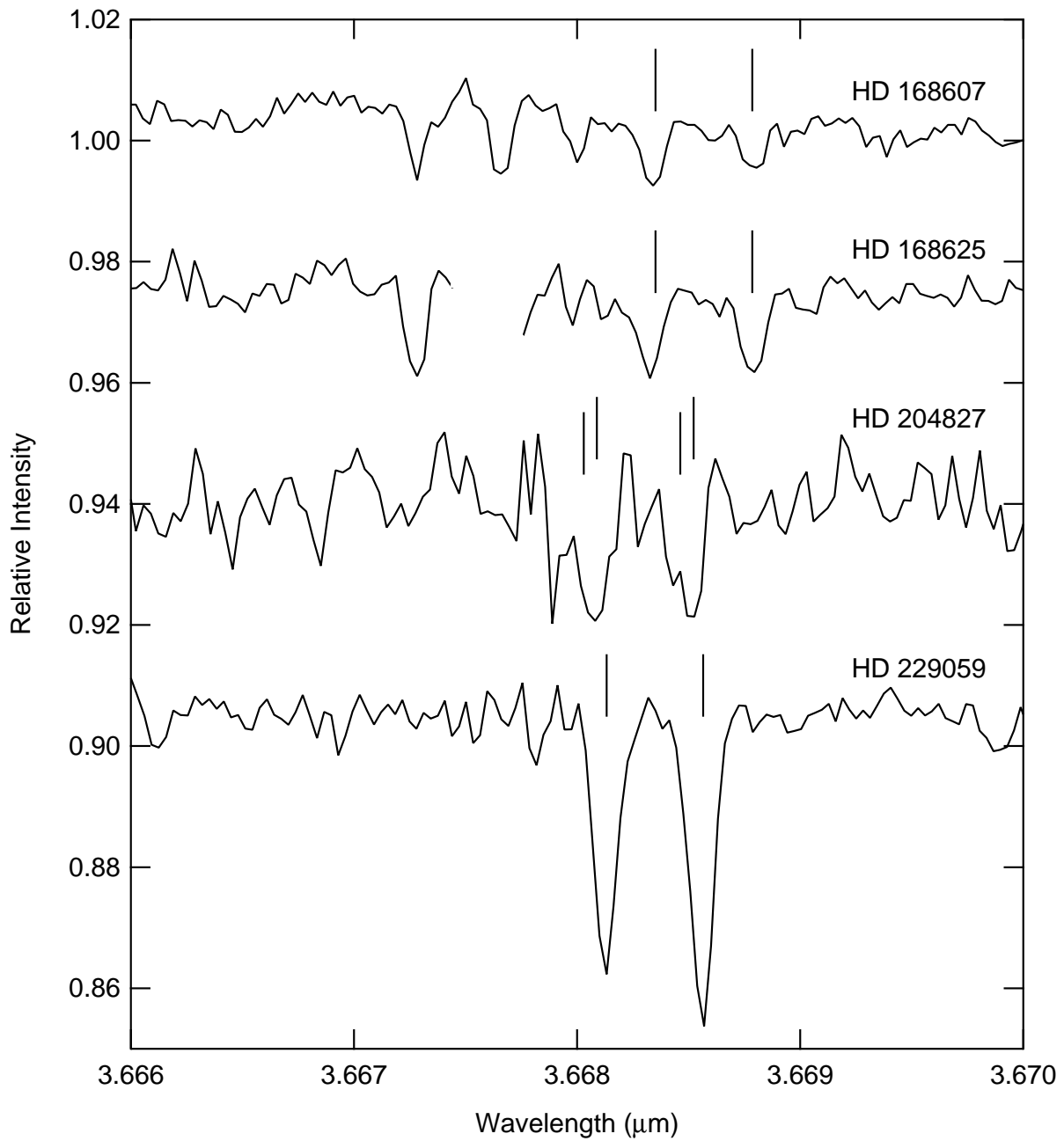
Figure 4.2: Detections of the $R(1,1)^u$ and $R(1,0)$ lines of H_3^+ taken with CGS4 at UKIRT. Sight lines include HD 168607, HD 168625, HD 204827, and HD 229059. Vertical lines mark the expected positions of absorption lines given gas velocities along each line of sight. Gaps in spectra are where the removal of atmospheric features was particularly poor.
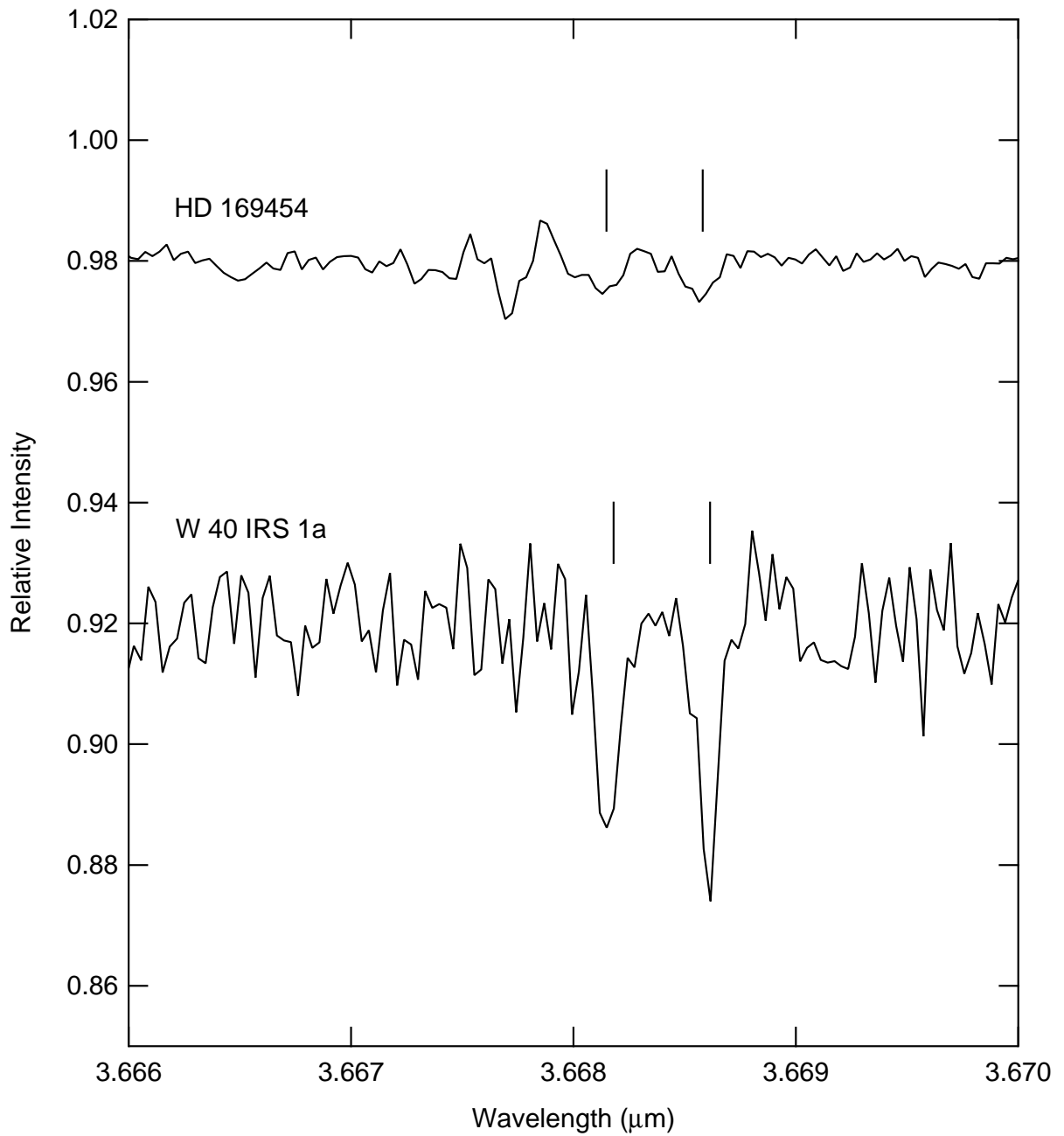
Figure 4.3: Detections of the $R(1,1)^u$ and $R(1,0)$ lines of H_3^+ taken with CGS4 at UKIRT. Sight lines include HD 169454 and W 40 IRS 1A. Vertical lines mark the expected positions of absorption lines given gas velocities along each line of sight.
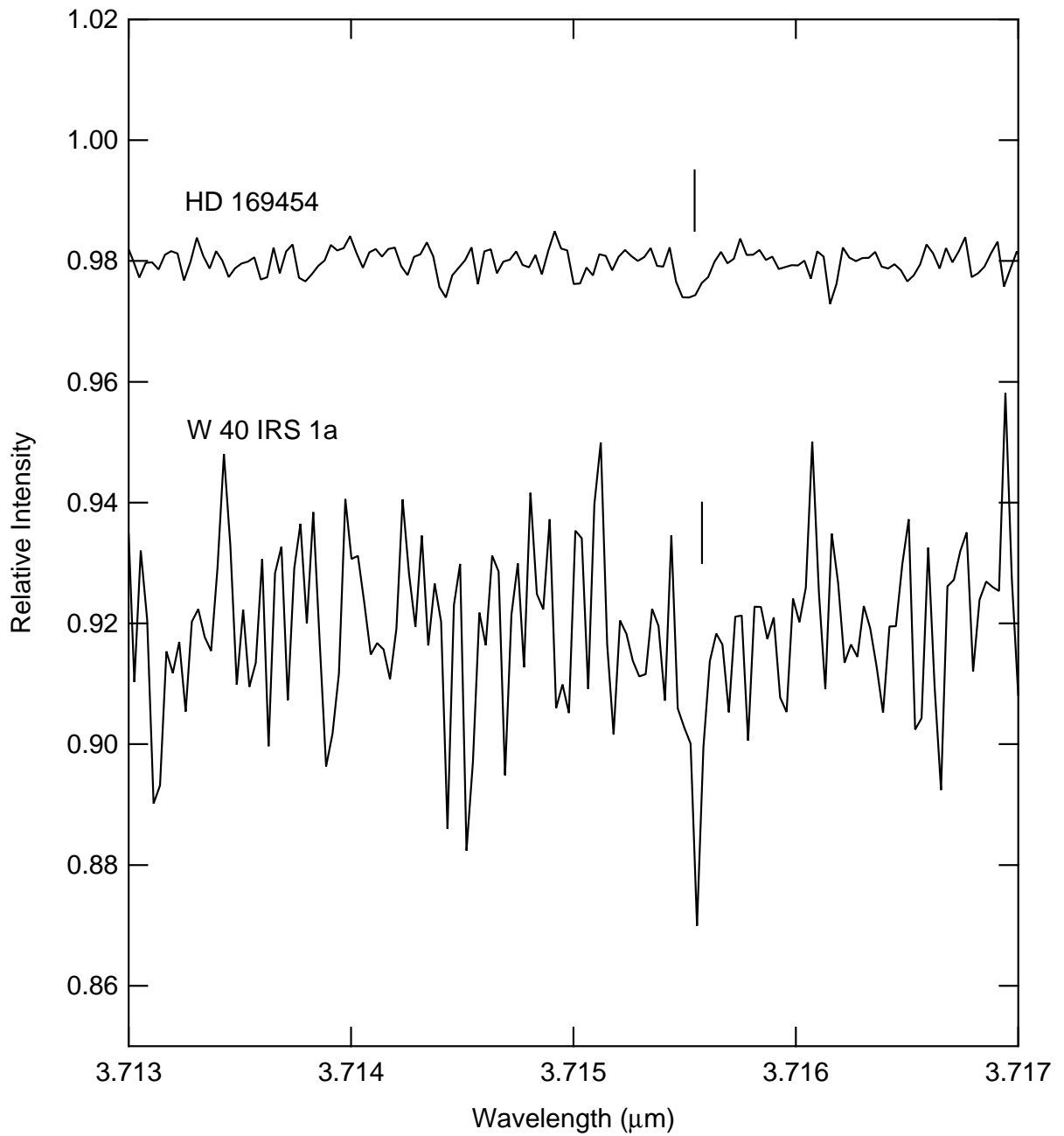
Figure 4.4: Detections of the $R(1,1)^l$ line of H_3^+ taken with CGS4 at UKIRT. Sight lines include HD 169454 and W 40 IRS 1A. Vertical lines mark the expected positions of absorption lines given gas velocities along each line of sight.
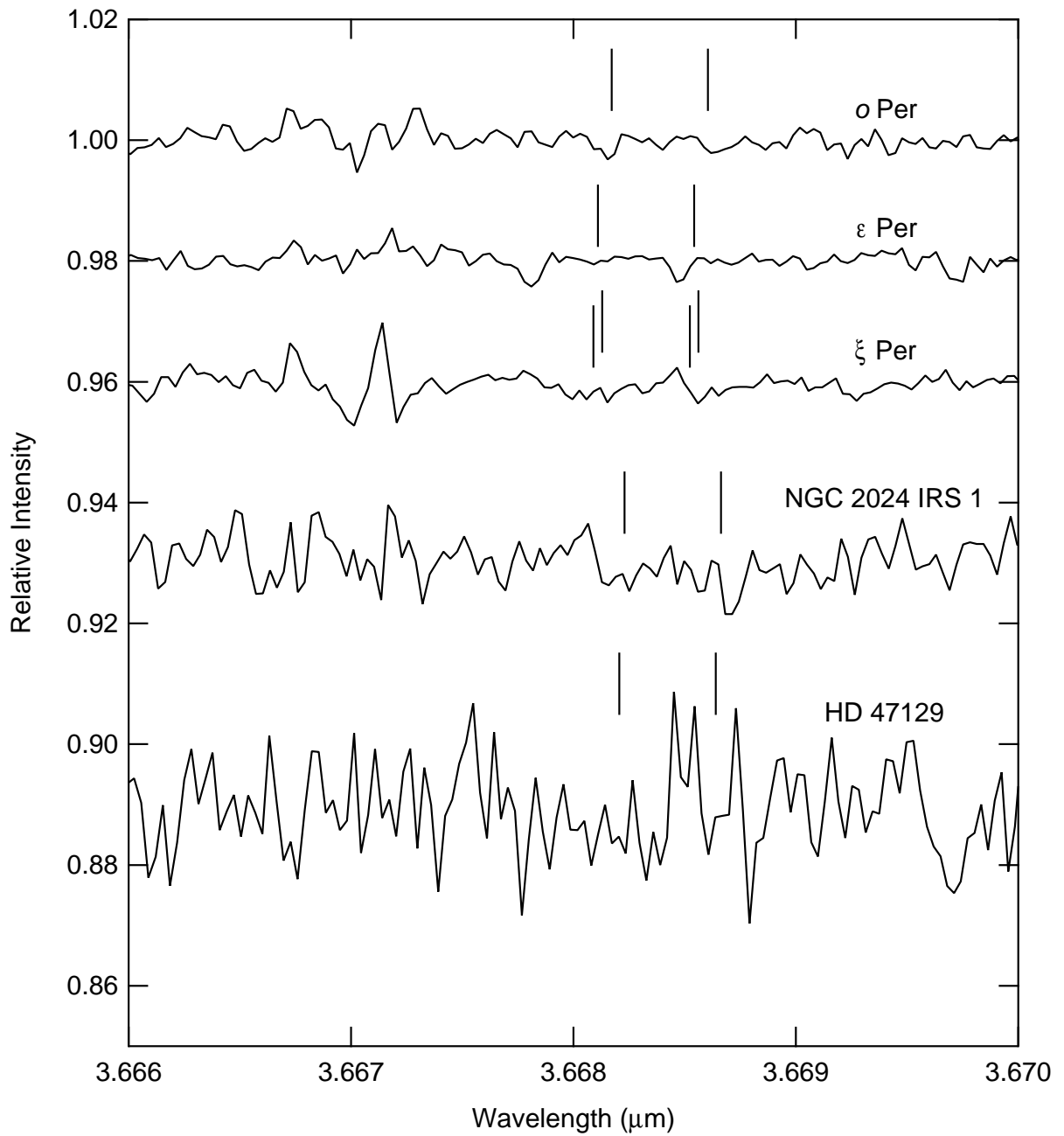
Figure 4.5: Non-detections of the $R(1,1)^u$ and $R(1,0)$ lines of H_3^+ taken with CGS4 at UKIRT. Sight lines include o Per, ϵ Per, ξ Per, NGC 2024 IRS 1, and HD 47129. Vertical lines mark the expected positions of absorption lines given gas velocities along each line of sight.
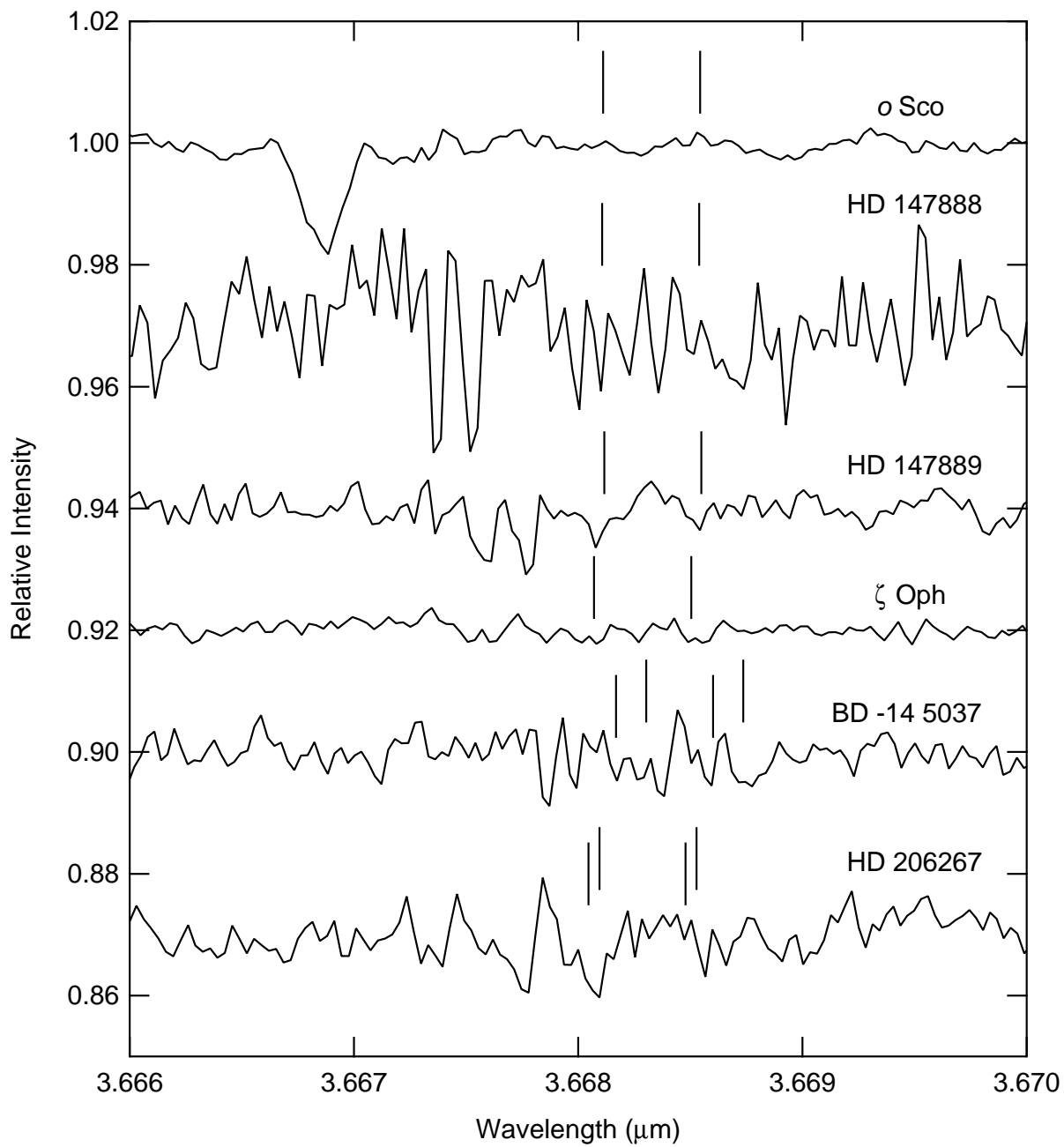
Figure 4.6: Non-detections of the $R(1,1)^u$ and $R(1,0)$ lines of H_3^+ taken with CGS4 at UKIRT. Sight lines include o Sco, HD 147888, HD 147889, ζ Oph, BD -14 5037, and HD 206267. Vertical lines mark the expected positions of absorption lines given gas velocities along each line of sight.
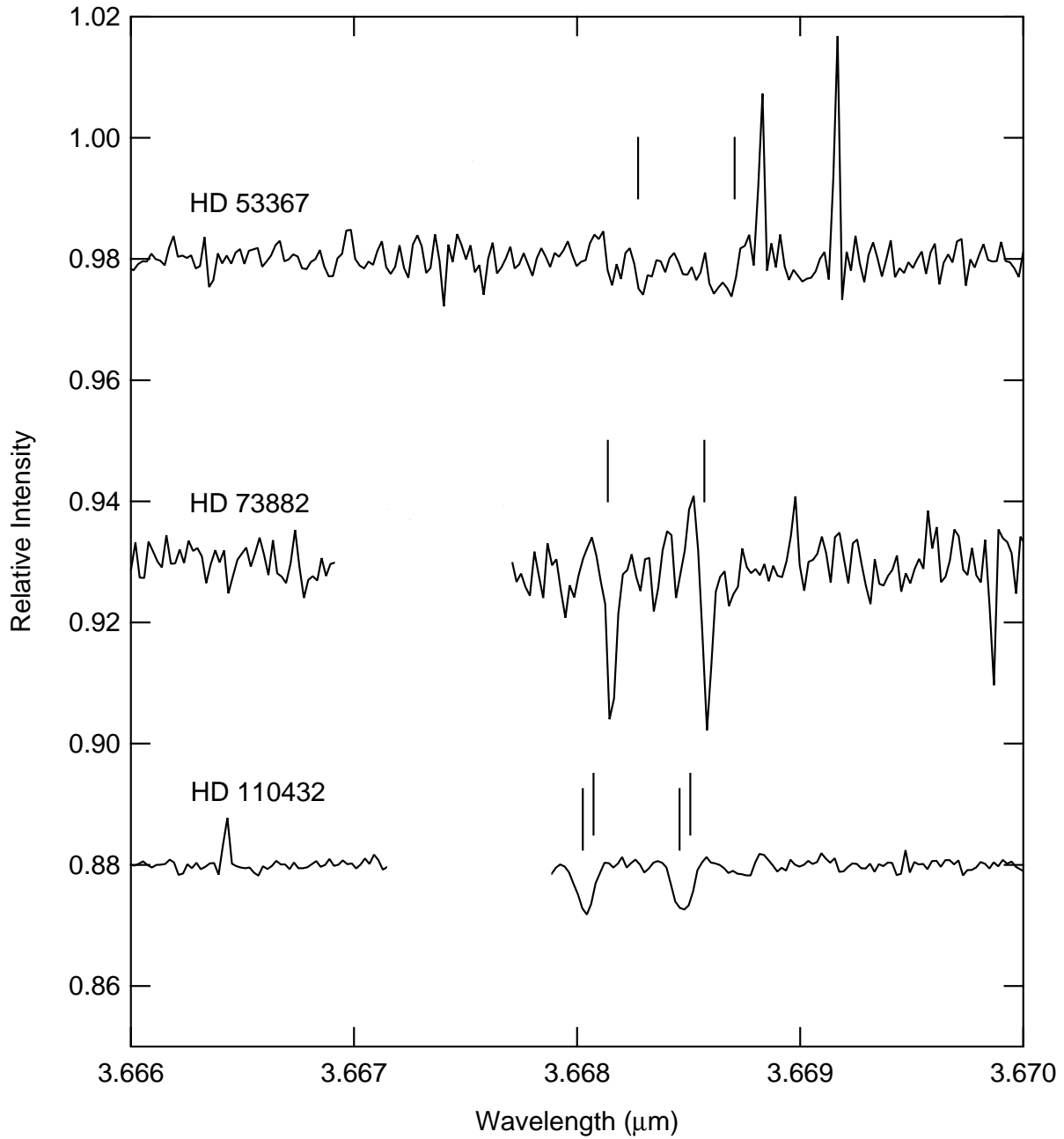
Figure 4.7: Spectra covering the $R(1,1)^u$ and $R(1,0)$ lines of H_3^+ taken with CRIRES at VLT. Sight lines include HD 53367, HD 73882, and HD 110432. Vertical lines mark the expected positions of absorption lines given gas velocities along each line of sight. Gaps in spectra are where the removal of atmospheric features was particularly poor. H_3^+ lines are detected toward HD 73882 and HD 110432.
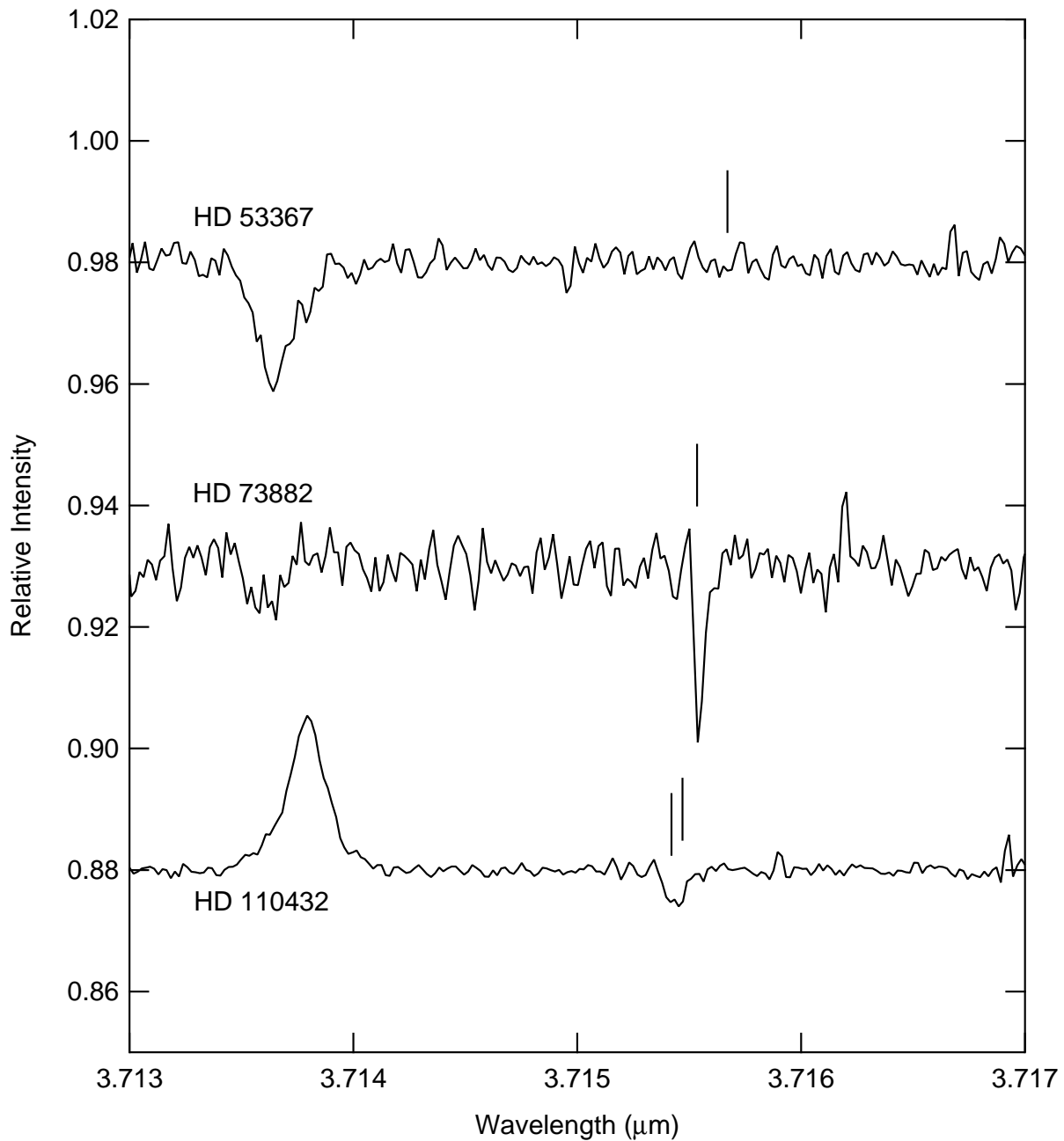
Figure 4.8: Spectra covering the $R(1,1)^l$ line of H_3^+ taken with CRIRES at VLT. Sight lines include HD 53367, HD 73882, and HD 110432. Vertical lines mark the expected positions of absorption lines given gas velocities along each line of sight. H_3^+ lines are detected toward HD 73882 and HD 110432. Features between 3.713 μm and 3.714 μm are artifacts resulting from imprecise removal of atmospheric absorption lines.
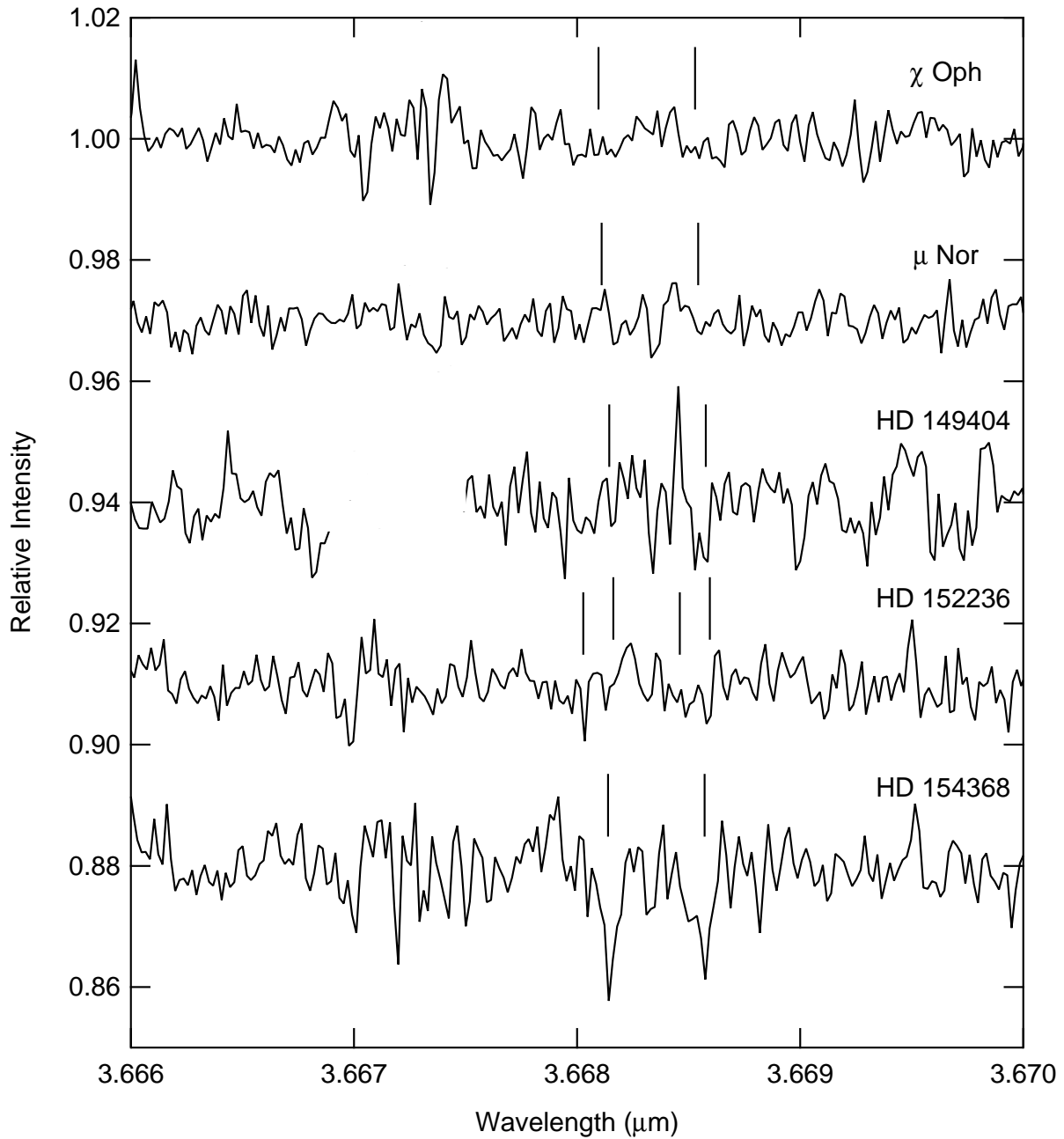
Figure 4.9: Spectra covering the $R(1,1)^u$ and $R(1,0)$ lines of H_3^+ taken with *Phoenix* at Gemini South. Sight lines include χ Oph, μ Nor, HD 149404, HD 152236, and HD 154368. Vertical lines mark the expected positions of absorption lines given gas velocities along each line of sight. Gaps in spectra are where the removal of atmospheric features was particularly poor. H_3^+ lines are detected only toward HD 154368.
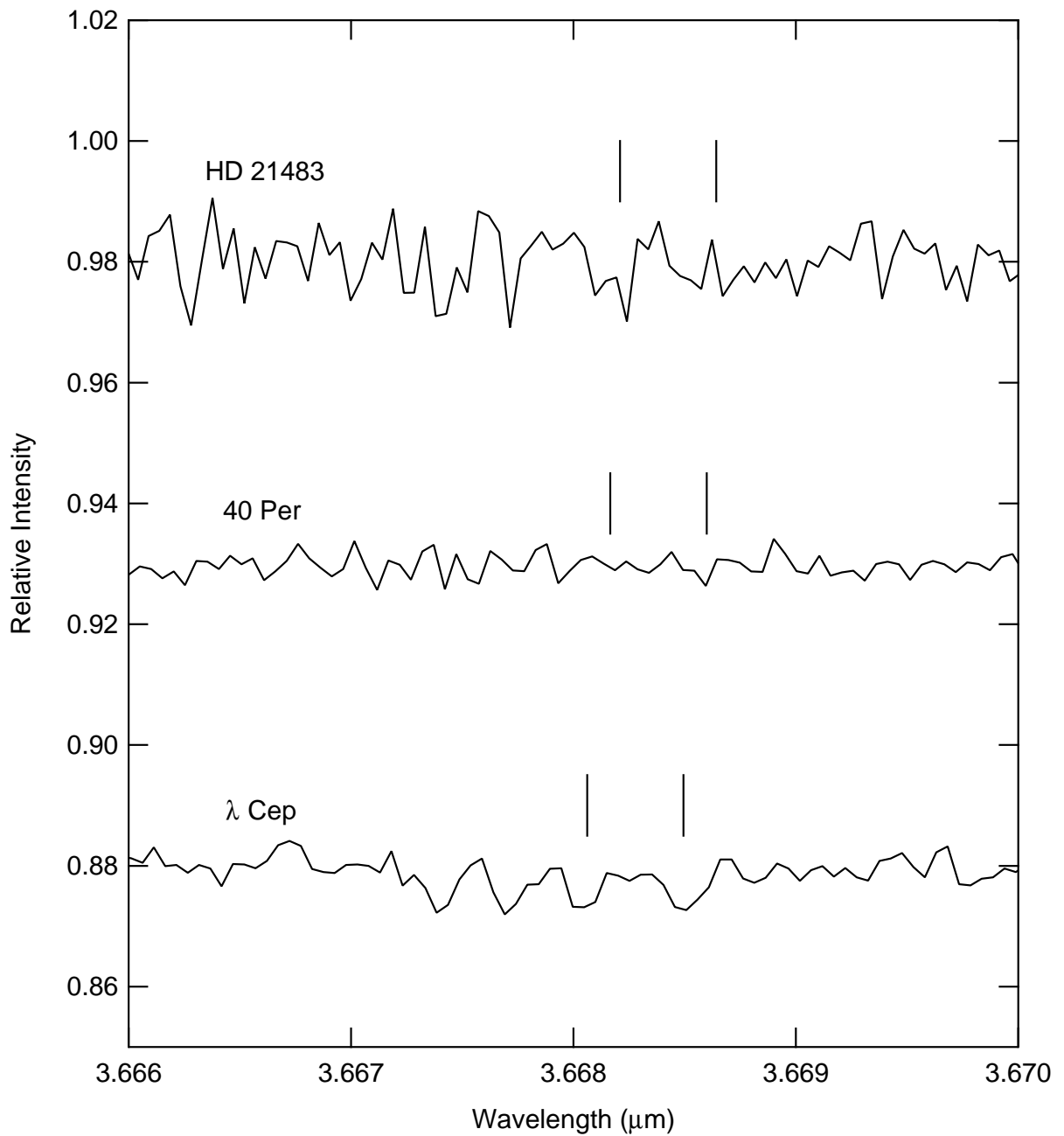
Figure 4.10: Spectra covering the $R(1,1)^u$ and $R(1,0)$ lines of H_3^+ taken with both CGS4 at UKIRT and NIRSPEC at Keck. Sight lines include HD 21483, 40 Per, and λ Cep. Vertical lines mark the expected positions of absorption lines given gas velocities along each line of sight. H_3^+ lines are detected toward λ Cep.
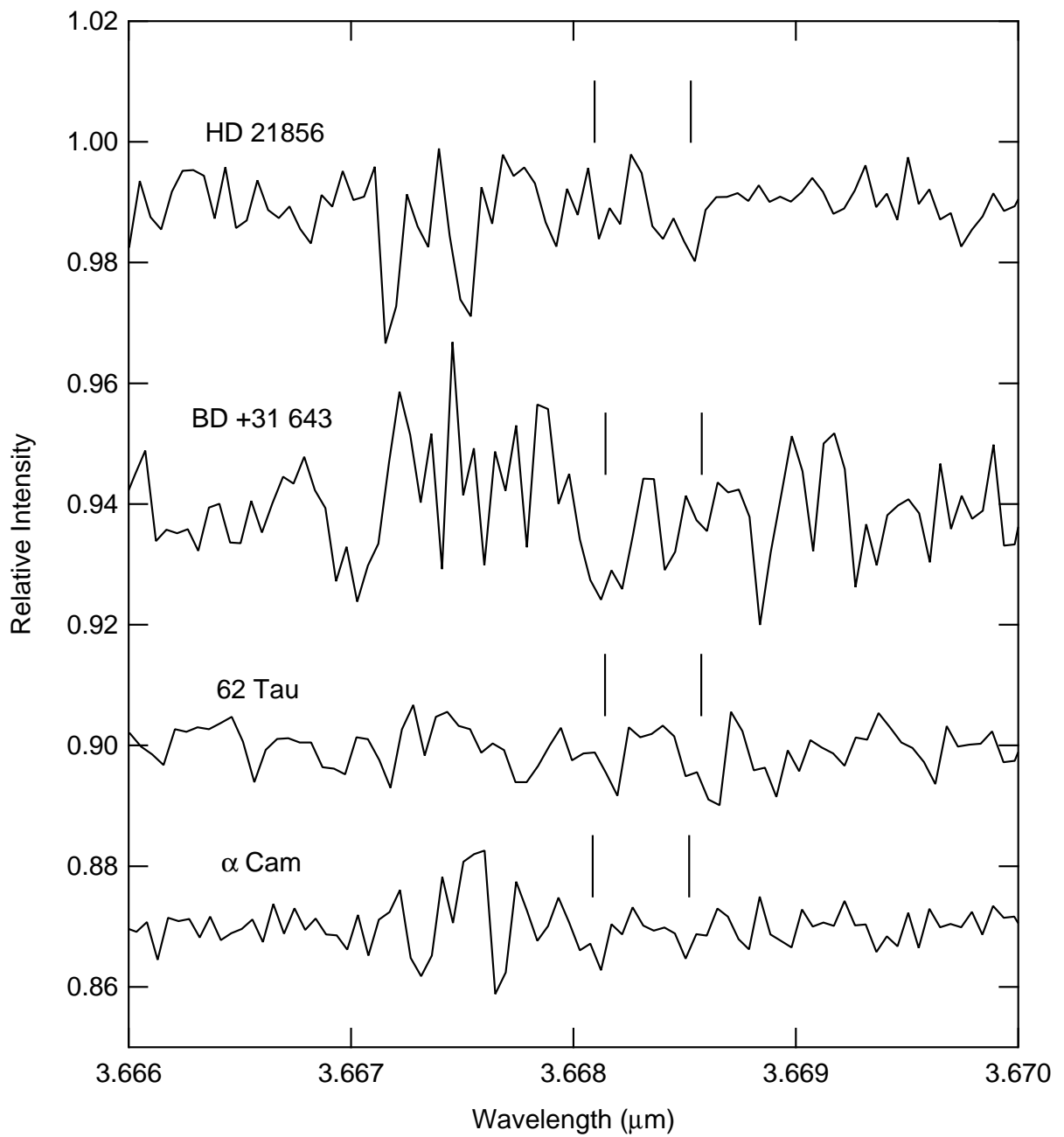
Figure 4.11: Spectra covering the $R(1,1)^u$ and $R(1,0)$ lines of H_3^+ taken with NIRSPEC at Keck. Sight lines include HD 21856, BD +31 643, 62 Tau, and α Cam. Vertical lines mark the expected positions of absorption lines given gas velocities along each line of sight.
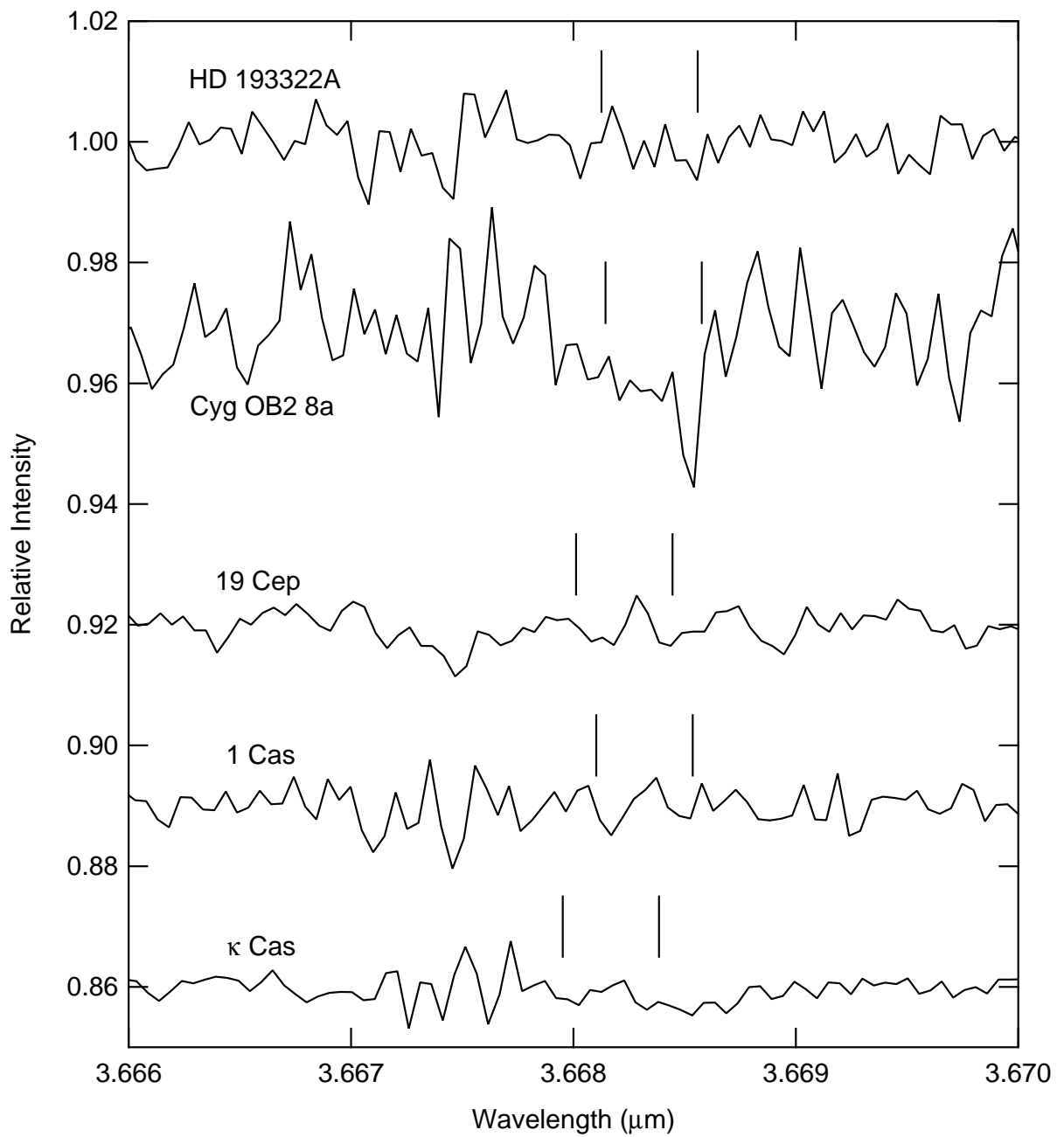
Figure 4.12: Spectra covering the $R(1,1)^u$ and $R(1,0)$ lines of H_3^+ taken with NIRSPEC at Keck. Sight lines include HD 193322A, Cyg OB2 8A, 19 Cep, 1 Cas, and κ Cas. Vertical lines mark the expected positions of absorption lines given gas velocities along each line of sight.
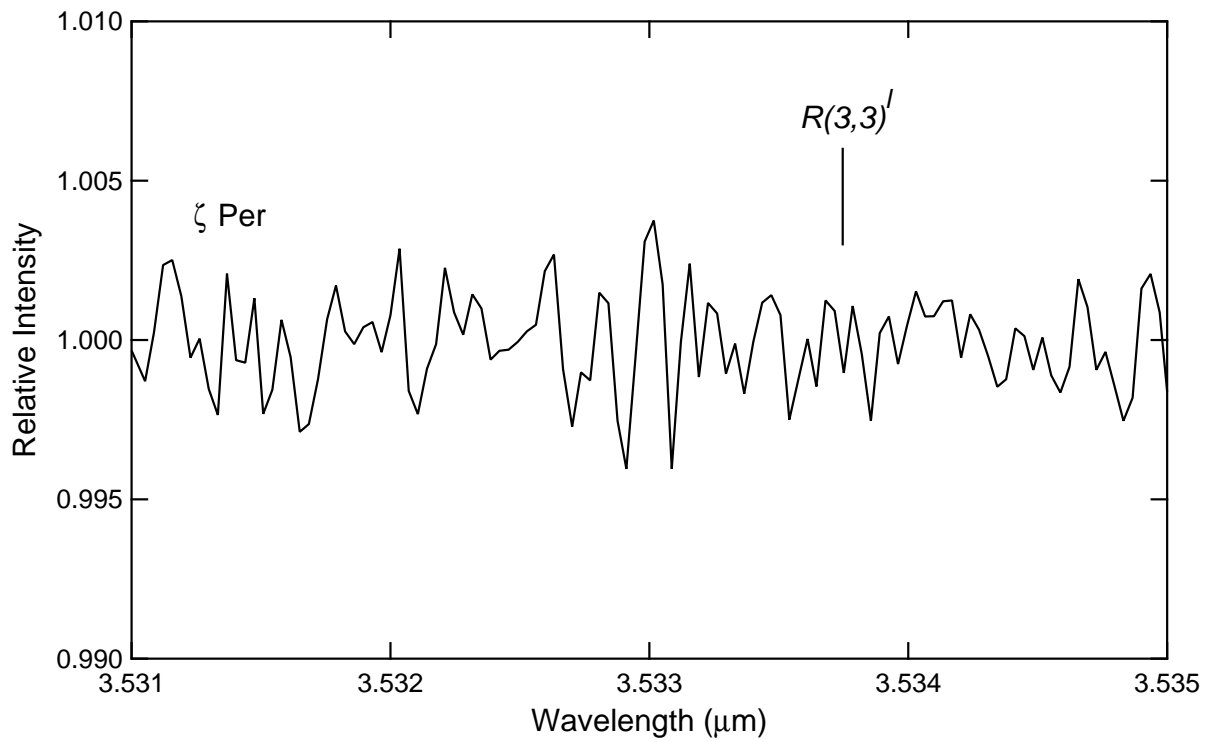
Figure 4.13: Spectrum covering the $R(3,3)^l$ line of H_3^+ toward ζ Per taken with CGS4 at UKIRT. The vertical line marks the expected position of the absorption line.

Chapter 5

Analysis of H_3^+ Spectra

5.1 Extraction of Column Densities and Upper Limits

Absorption features due to H_3^+ were fit with Gaussian functions in order to determine equivalent widths, velocity FWHM, and interstellar gas velocities. The fitting procedure uses the functional form of a Gaussian where the area (as opposed to amplitude) is a free parameter, and includes a fit to the continuum level; i.e.,

$$I = I_0 - \frac{A}{w\sqrt{\pi}} \exp\left[-\left(\frac{\lambda - \lambda_0}{w}\right)^2\right],$$ (5.1)

and was developed in Igor Pro. The free parameters here are the continuum level, I_0, the area of the Gaussian, A, the central wavelength of the Gaussian, λ_0, and the line width, w (n.b., the width used here is related to the "standard" Gaussian width, σ, by $w^2 = 2\sigma^2$). As the continuum level has already been normalized, an area determined using this fit is by definition an equivalent width, W_λ. In the case of the $R(1,1)^u$ and $R(1,0)$ lines, both absorption features are fit simultaneously and a single best-fit continuum level is found. Uncertainties on the equivalent widths (δW_λ) and continuum level (δI) — both at the 1σ level — are output by the fitting process. To estimate the systematic uncertainties due to continuum placement, the continuum level was forced to $I_0 + \delta I$ and $I_0 - \delta I$ and the absorption lines re-fit. Variations in the equivalent widths due to this shift are small compared to those reported by the fitting procedure and so have been ignored (i.e., $\sigma(W_\lambda) = \delta W_\lambda$). Assuming optically thin absorption lines and taking transition dipole moments and wavelengths from Table 2.1, column densities are derived from equivalent widths using the standard relation:

$$N(J,K) = \left(\frac{3hc}{8\pi^3}\right) \frac{W_\lambda}{\lambda} \frac{1}{|\mu|^2},$$ (5.2)

where $N(J,K)$ is the column density in the state from which the transition arises, h is Planck's constant, c is the speed of light, λ is the transition wavelength, and $|\mu|^2$ is the

square of the transition dipole moment.

In cases where H_3^+ absorption lines are not detected, upper limits to the equivalent width are computed as

$$W_\lambda < \sigma \lambda_{\mathrm{pix}} \sqrt{\mathcal{N}_{\mathrm{pix}}}, \tag{5.3}$$

where σ is the standard deviation on the continuum level near the expected H_3^+ lines, λ_{pix} is the wavelength coverage per pixel, and $\mathcal{N}_{\mathrm{pix}}$ is the number of pixels expected in an absorption feature. Upper limits to the column density are then determined via equation (5.2). Column densities, equivalent widths, velocity FWHM, and interstellar gas velocities for all of the sight lines shown in Chapter 4 are reported in Table 5.2.

5.2 Determination of the Cosmic-Ray Ionization Rate

As discussed in Section 1.1, the chemistry associated with H_3^+ in diffuse molecular clouds is rather simple. Assuming steady-state conditions, the formation and destruction rates of H_3^+ can be equated. In the simplified case of diffuse molecular clouds — where destruction occurs primarily via dissociative recombination with electrons — the result is (Geballe et al., 1999)

$$\zeta_2 n(H_2) = k_e n(H_3^+) n_e, \tag{5.4}$$

where ζ_2 is the ionization rate of H_2, n's are number densities, and k_e is the H_3^+-electron recombination rate coefficient (see Table 5.1). Substituting the electron fraction (defined as $x_e \equiv n_e/n_H$, where $n_H \equiv n(H) + 2n(H_2)$) into equation (5.4) and solving for the ionization rate gives

$$\zeta_2 = k_e x_e n_H \frac{n(H_3^+)}{n(H_2)}. \tag{5.5}$$

Although it would be desirable to trace the ionization rate as a function of position throughout the cloud, variations in density along the line of sight cannot be determined via observations. Instead, the average ionization rate in a cloud is inferred by using average number densities. By definition, $\langle n(H_3^+) \rangle$ and $\langle n(H_2) \rangle$ can be replaced with $N(H_3^+)/L$ and $N(H_2)/L$, respectively (where L is the cloud path length), thus putting equation (5.5) in terms of observables. As H_3^+ will form wherever there is an appreciable amount of H_2, it is reasonable to assume that the path length for both species is the same, such that

$$\zeta_2 = k_e x_e n_H \frac{N(H_3^+)}{N(H_2)}. \tag{5.6}$$

Because the ratio $n(\mathrm{H}_3^+)/n(\mathrm{H}_2)$ is not expected to vary widely in models of diffuse molecular clouds (e.g., Neufeld et al., 2005), this gives a representative value of the ionization rate throughout the entire cloud.

While equation (5.6) only considers one formation and destruction mechanism for H_3^+, comparison to a more complete chemical reaction network shows that it is a robust approximation given diffuse cloud conditions. Assuming steady-state for H_2^+ where destruction by electron recombination and charge transfer to protons (reactions 1.3 and 1.4) are considered, and steady-state for H_3^+ where destruction by proton transfer to CO and O (reactions 1.6a, 1.6b, and 1.7) is accounted for, gives the equations

$$\zeta_2 n(\mathrm{H}_2) = k_{1.3} n_e n(\mathrm{H}_2^+) + k_{1.4} n(\mathrm{H}) n(\mathrm{H}_2^+) + k_{1.2} n(\mathrm{H}_2) n(\mathrm{H}_2^+), \tag{5.7}$$

$$k_{1.2} n(\mathrm{H}_2) n(\mathrm{H}_2^+) = k_e n_e n(\mathrm{H}_3^+) + k_{\mathrm{CO}} n(\mathrm{CO}) n(\mathrm{H}_3^+) + k_{\mathrm{O}} n(\mathrm{O}) n(\mathrm{H}_3^+). \tag{5.8}$$

Solving for the ionization rate and making similar substitutions as before results in

$$\zeta_2 = \frac{N(\mathrm{H}_3^+)}{N(\mathrm{H}_2)} n_{\mathrm{H}} \left[k_e x_e + k_{\mathrm{CO}} x(\mathrm{CO}) + k_{\mathrm{O}} x(\mathrm{O}) \right] \left[1 + \frac{2 k_{1.3} x_e}{k_{1.2} f_{\mathrm{H}_2}} + \frac{2 k_{1.4}}{k_{1.2}} \left(\frac{1}{f_{\mathrm{H}_2}} - 1 \right) \right], \tag{5.9}$$

where relevant rate coefficients are given in Table 5.1, $k_{\mathrm{CO}} = k_{1.6a} + k_{1.6b}$, and $f_{\mathrm{H}_2} \equiv 2n(\mathrm{H}_2)/n_{\mathrm{H}}$ is the fraction of hydrogen nuclei in molecular form.

Table 5.1: Rate Coefficients for Reactions Involved in H_3^+ Chemistry

Reaction	Rate Coefficient (cm^3 s^{-1})	Reference
$\mathrm{H}_2^+ + \mathrm{H}_2 \rightarrow \mathrm{H}_3^+ + \mathrm{H}$	$k_{1.2} = 2.08 \times 10^{-9}$	1
$\mathrm{H}_2^+ + e^- \rightarrow \mathrm{H} + \mathrm{H}$	$k_{1.3} = 1.6 \times 10^{-8} (T/300)^{-0.43}$	2
$\mathrm{H}_2^+ + \mathrm{H} \rightarrow \mathrm{H}_2 + \mathrm{H}^+$	$k_{1.4} = 6.4 \times 10^{-10}$	3
$\mathrm{H}_3^+ + e^- \rightarrow \text{products}$	$k_{1.5} = k_e = -1.3 \times 10^{-8} + 1.27 \times 10^{-6} T_e^{-0.48}$	4
$\mathrm{H}_3^+ + \mathrm{CO} \rightarrow \mathrm{H}_2 + \mathrm{HCO}^+$	$k_{1.6a} = 1.36 \times 10^{-9} (T/300)^{-0.142} \exp(3.41/T)$	5
$\mathrm{H}_3^+ + \mathrm{CO} \rightarrow \mathrm{H}_2 + \mathrm{HOC}^+$	$k_{1.6b} = 8.49 \times 10^{-10} (T/300)^{0.0661} \exp(-5.21/T)$	5
$\mathrm{H}_3^+ + \mathrm{O} \rightarrow \mathrm{H}_2 + \mathrm{OH}^+$	$k_{1.7} = k_{\mathrm{O}} = 1.14 \times 10^{-9} (T/300)^{-0.156} \exp(-1.41/T)$	5
$\mathrm{H}_3^+ + \mathrm{N}_2 \rightarrow \mathrm{H}_2 + \mathrm{HN}_2^+$	$k_{1.8} = 1.8 \times 10^{-9}$	6

Notes: Numerical subscripts on the rate coefficients refer to the corresponding reaction numbers given in the text. The H_3^+-electron recombination rate coefficient, $k_{1.5}$, is referred to as k_e throughout the text. The rate coefficient for destruction via proton transfer to CO used in the text, k_{CO}, is equal to $k_{1.6a} + k_{1.6b}$. The rate coefficient for destruction via proton transfer to O, $k_{1.7}$, is referred to as k_{O} throughout the text.

References: (1) Theard & Huntress (1974); (2) Mitchell (1990); (3) Karpas et al. (1979); (4) McCall et al. (2004); (5) Klippenstein et al. (2010); (6) Rakshit (1982)

The cosmic-ray ionization rate as a function of electron fraction is plotted in Figure 5.1 for both equations (5.6) and (5.9). In all three panels the thick solid line shows the linear relationship given by equation (5.6), while the various other curves show the ionization rate determined using equation (5.9) and different values of $x(\mathrm{CO})$, $x(\mathrm{O})$, and $f_{\mathrm{H_2}}$. In the left panel $x(\mathrm{CO})$ is varied ($x(\mathrm{CO}) = 10^{-6}$ - dash-dot curve; 10^{-5} - dashed curve; 10^{-4} - dotted curve) with $x(\mathrm{O}) = 10^{-8}$ and $f_{\mathrm{H_2}} = 1$. In the center panel $x(\mathrm{O})$ is varied ($x(\mathrm{O}) = 10^{-6}$ - dash-dot curve; 10^{-5} - dashed curve; 10^{-4} - dotted curve; 3×10^{-4} - thin solid curve) with $x(\mathrm{CO}) = 10^{-8}$ and $f_{\mathrm{H_2}} = 1$. In the right panel $f_{\mathrm{H_2}}$ is varied ($f_{\mathrm{H_2}} = 0.67$ - dotted curve; 0.5 - dashed curve; 0.1 - dash-dot curve) with $x(\mathrm{CO}) = x(\mathrm{O}) = 10^{-8}$.

The left and center panels show that equation (5.9) only differs significantly from equation (5.6) when $x_e \lesssim 10^{-5}$, and for high fractional abundances of CO and O ($\gtrsim 10^{-4}$). These deviations occur when proton transfer to CO and O come to dominate over electron recombination as the primary destruction pathways for $\mathrm{H_3^+}$. The right panel shows that $f_{\mathrm{H_2}}$ affects the ionization rate for all values of x_e, but that rather low molecular hydrogen fractions are necessary to significantly alter the inferred value of ζ_2. With $f_{\mathrm{H_2}} = 0.5$ (i.e., twice as many H atoms as $\mathrm{H_2}$ molecules) the value output by equation (5.9) is about 1.6 times that from equation (5.6), while for $f_{\mathrm{H_2}} = 0.67$ (i.e., equal number of H and $\mathrm{H_2}$) the value output by equation (5.9) is about 1.3 times that from equation (5.6). This deviation is caused by the larger relative abundance of atomic hydrogen destroying $\mathrm{H_2^+}$ before it can form $\mathrm{H_3^+}$, and is represented by the final term in equation (5.9). The destruction of $\mathrm{H_2^+}$ by electron recombination does not play a major role in the chemical network used here, and its influence can only be seen in the slight deviation between equations (5.6) and (5.9) when $x_e \sim 10^{-2}$.

Although some of the sight lines studied herein have molecular hydrogen fractions of $f_{\mathrm{H_2}} = 0.2$ as determined from observations of H and $\mathrm{H_2}$ (Savage et al., 1977; Rachford et al., 2002, 2009), it must be remembered that these are line-of-sight fractions, while equation (5.9) requires local fractions. As it is expected that there will be atomic gas along a line of sight that is not associated with a cloud containing $\mathrm{H_2}$, the line-of-sight value of $f_{\mathrm{H_2}}$ *always* underestimates the value of $f_{\mathrm{H_2}}$ within a diffuse molecular cloud. It is generally assumed that the interior of a diffuse molecular cloud has conditions where $0.67 < f_{\mathrm{H_2}} < 1$ (i.e. somewhere between half and all of the hydrogen is in molecular form), such that reaction (1.4) will not be very important. Overall, Figure 5.1 demonstrates why equation (5.6) is a good approximation to equation (5.9) given average diffuse molecular cloud conditions ($x_e = x(\mathrm{C^+}) = 1.5 \times 10^{-4}$ Cardelli et al. (1996); Sofia et al. (2004); $x(\mathrm{O}) = 3 \times 10^{-4}$ Cartledge et al. (2004); Jensen et al. (2005); $x(\mathrm{CO}) \sim 10^{-6}$ Sonnentrucker et al. (2007); $f_{\mathrm{H_2}} \gtrsim 0.67$), and so I adopt equation (5.6) in computing ζ_2.
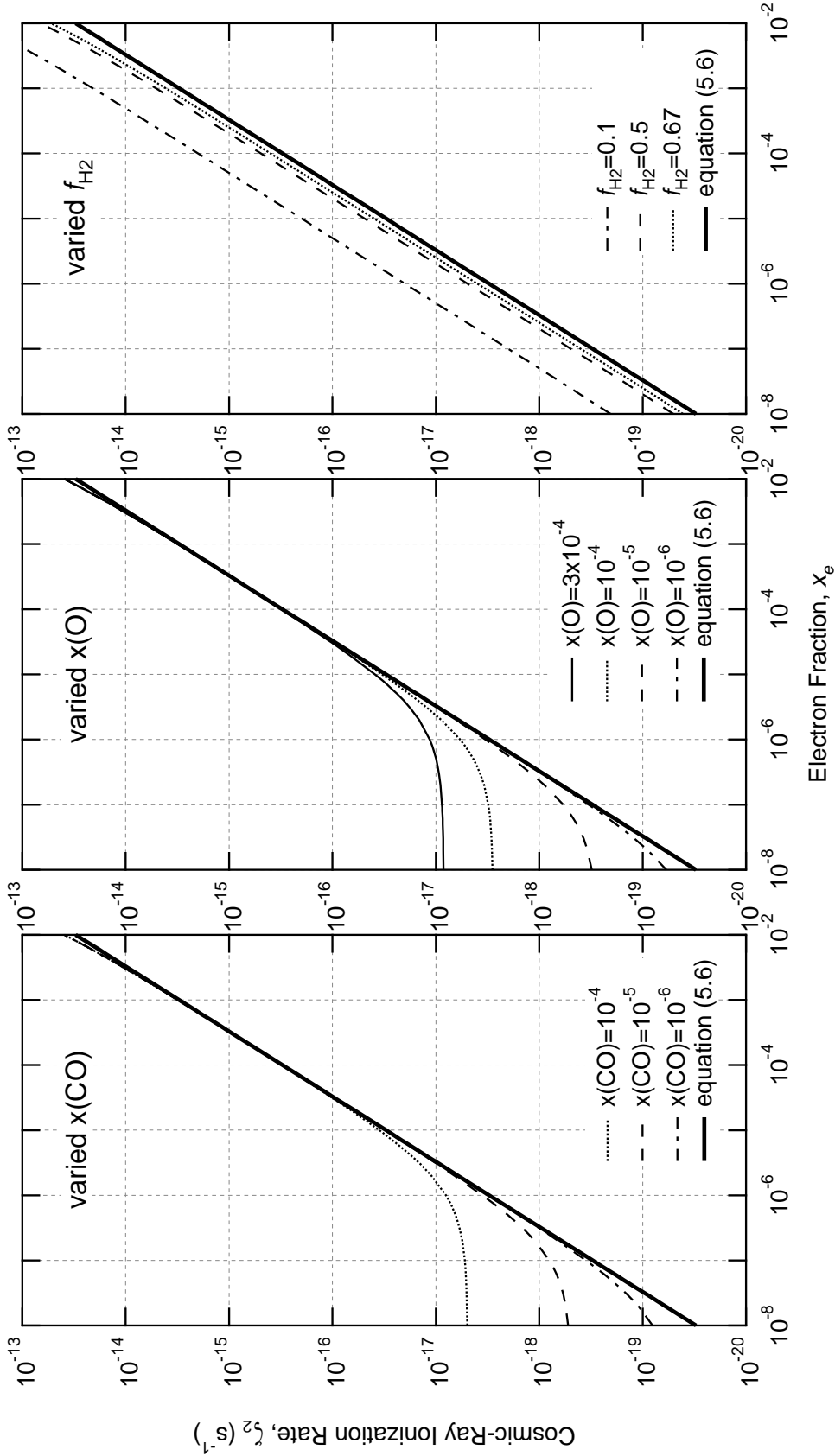
Figure 5.1: Cosmic-ray ionization rate (ζ_2) as a function of the electron fraction (x_e) for simplified chemistry (equation 5.6) and more complete chemistry (equation 5.9). In all cases $n_H = 200$ cm^{-3}, $N(H_3^+)/N(H_2) = 10^{-7}$, and $T = 70$ K. The thick solid line shows the linear approximation given by equation (5.6). The left panel shows the result of varying $x(CO)$, with $x(O) = 10^{-8}$ and $f_{H_2} = 1$; the middle panel shows the result of varying $x(O)$, with $x(CO) = 10^{-8}$ and $f_{H_2} = 1$; the right panel shows the result of varying f_{H_2}, with $x(CO) = 10^{-8}$ and $x(O) = 10^{-8}$.

52

With equation (5.6), the cosmic-ray ionization rate (ζ_2) can be determined from the H_3^+ column density ($N(H_3^+)$), H_2 column density ($N(H_2)$), total hydrogen density (n_H), electron fraction (x_e), and H_3^+-electron recombination rate coefficient (k_e). The electron fraction can be approximated by the fractional abundance of C^+ assuming that nearly all electrons are the result of singly photoionized carbon. In sight lines where C^+ has been observed, the measured value of $x(C^+)$ is used for x_e. For all other sight lines, the average fractional abundance measured in various diffuse clouds, $x(C^+) \approx 1.5 \times 10^{-4}$ (Cardelli et al., 1996; Sofia et al., 2004), is adopted for x_e. Uncertainties in x_e are assumed to be $\pm 20\%$, i.e., $\pm 3 \times 10^{-5}$. The H_3^+-electron recombination rate coefficient has been measured in the laboratory (McCall et al., 2004) and is presented in Table 5.1. When available the spin temperature of H_2, T_{01}, is used in calculating k_e; otherwise, an average value of 70 K is adopted. The total hydrogen number density is difficult to determine, but various studies have estimated n_H using a rotational excitation analysis of observed C_2 lines (Sonnentrucker et al., 2007), an analysis of H and the $J = 4$ level of H_2 (Jura, 1975), or a thermal pressure analysis of fine structure lines of C I (Jenkins et al., 1983). Number densities from these studies are presented in Table 5.3 when available. For sight lines without estimated densities, the rough average value of $n_H = 200$ cm^{-3} is adopted. Uncertainties in n_H are assumed to be ± 50 cm^{-3}. Absorption lines from electronic transitions of H_2 have been observed in the UV along many of the sight lines in this study (from which the aforementioned values of T_{01} are derived; Savage et al., 1977; Rachford et al., 2002, 2009). In sight lines where H_2 has not been observed, two other methods were used to estimate $N(H_2)$. The preferred method uses column densities of CH determined from observations in combination with the relation $N(CH)/N(H_2) = 3.5^{+2.1}_{-1.4} \times 10^{-8}$ from Sheffer et al. (2008). CH column densities utilized for such estimates are presented in Table B.2. In sight lines where neither H_2 nor CH has been observed, $N(H_2)$ is estimated from the color excess, $E(B - V)$, using the relation $N_H \approx E(B - V)5.8 \times 10^{21}$ cm^{-2} mag^{-1} from Bohlin et al. (1978), and assuming $f_{H_2} \approx 2N(H_2)/N_H = 0.67$. Molecular hydrogen column densities determined both from observations and estimates are presented in Table 5.3.

While Table 5.2 gives individual column densities for the lowest lying *ortho* and *para* levels of H_3^+, values of $N(H_3^+)$ in Table 5.3 are equal to the sum of the column densities in the $(1,1)$ and $(1,0)$ states (i.e., $N(H_3^+) = N(1,1) + N(1,0)$). In cases where observations of both the $R(1,1)^u$ and $R(1,1)^l$ lines produce independent values of $N(1,1)$, a variance weighted average,

$$N = \sum_{i=1}^{n}(N_i/\sigma_i^2)/\sum_{i=1}^{n}(1/\sigma_i^2), \tag{5.10}$$

is used to determine $N(1,1)$. Because there are only 2 independent measurements of $N(1,1)$, the uncertainty of the weighted average, $S[N(1,1)]$, is determined using an unbiased estimator of a weighted population variance for small samples. This is given by

$$S^2 = \frac{V_1}{V_1^2 - V_2} \sum_{i=1}^{n} w_i (N_i - \mu^*)^2, \tag{5.11}$$

where

$$w_i = \frac{1}{\sigma_i^2}, \tag{5.12}$$

$$V_1 = \sum_{i=1}^{n} w_i, \tag{5.13}$$

$$V_2 = \sum_{i=1}^{n} w_i^2, \tag{5.14}$$

and μ^* is the weighted average determined from equation (5.10). The uncertainty in the total H_3^+ column density is then computed as normal by adding $\sigma[N(1,1)]$ and $\sigma[N(1,0)]$ in quadrature. Upper limits to the H_3^+ column density should be taken as $3\sigma[N(H_3^+)]$.

Using equation (5.6), and taking the values described above and in Table 5.3, cosmic-ray ionization rates are inferred for all diffuse molecular clouds where H_3^+ observations have been made. These values of ζ_2 are presented in column 10 of Table 5.3, with uncertainties in column 11. As for the H_3^+ column densities, upper limits to the cosmic-ray ionization rate should be taken as $3\sigma(\zeta_2)$.

For one sight line however, that toward NGC 2024 IRS 1, a different analysis is used because recent observations suggest that the interstellar material is more likely dense than diffuse (T. Snow 2011, private communication). In this case, values appropriate for dense clouds ($x_e = 10^{-7}$, $f_{H_2} = 1$) are adopted, effectively simplifying equation (5.9) to

$$\zeta_2 = \frac{N(H_3^+)}{N(H_2)} n_H \left[k_{CO} x(CO) + k_O x(O) \right]. \tag{5.15}$$

The density and temperature are also set to average dense cloud values ($n_H = 10^4$ cm^{-3}, $T = 30$ K). The large CO column density ($N(CO) = 1.26 \times 10^{18}$ cm^{-2}; T. Snow 2011, private communication) results in $x(CO) = 1.28 \times 10^{-4}$, demonstrating that most of the carbon is in molecular form, and thus validating the low value of x_e assumed above. Oxygen abundances are typically about two times carbon abundances (Lodders, 2003), such that half of all O is expected to be in the form of CO. I assume the remainder to be in atomic form, and use

$x(\mathrm{O}) = x(\mathrm{CO})$ in equation (5.15). The resulting upper limit on the cosmic-ray ionization rate toward NGC 2024 IRS 1 is $\zeta_2 < 4.2 \times 10^{-17}$ s^{-1}. This lower value is expected in dense cloud conditions, as will be discussed in the following Chapter.

5.3 Tables

The Tables within this section are discussed throughout Chapter 5. They include Table 5.2, which presents the absorption line parameters extracted from H$_3^+$ spectra, and Table 5.3, which presents the inferred cosmic-ray ionization rate for each sight line and values necessary in its calculation.

Table 5.2: Absorption Line Parameters

Object	Transition	$v_{\rm LSR}$ (km s^{-1})	FWHM (km s^{-1})	W_λ (10^{-6} μm)	$\sigma(W_\lambda)$ (10^{-6} μm)	$N(J,K)$ (10^{13} cm^{-2})	$\sigma(N)$ (10^{13} cm^{-2})
HD 20041	$R(1,1)^u$	2.5	11.0	2.49	0.45	10.3	1.87
	$R(1,0)$	-0.9	10.1	3.03	0.41	7.67	1.04
HD 21389	$R(1,1)^u$	0.2	13.3	1.20	0.19	4.98	0.79
	$R(1,0)$	0.8	12.9	1.46	0.19	3.69	0.47
ζ Per	$R(1,1)^u$	8.0	10.3	0.99	0.11	4.09	0.46
	$R(1,0)$	8.4	8.7	0.86	0.10	2.17	0.25
	$R(3,3)^l$	...	10	...	0.10	...	0.37
X Per	$R(1,1)^u$	7.0	11.7	1.16	0.20	4.81	0.81
	$R(1,0)$	6.3	9.4	1.00	0.17	2.53	0.43
HD 29647	$R(1,1)^u$	8.0	8.6	1.62	0.21	6.72	0.88
	$R(1,0)$	8.2	11.0	2.06	0.26	5.21	0.67
HD 73882	$R(1,1)^u$	5.9	3.9	1.44	0.21	5.97	0.86
	$R(1,0)$	5.7	3.2	1.16	0.19	2.94	0.48
	$R(1,1)^l$	5.4	3.5	1.34	0.15	6.15	0.69
HD 110432	$R(1,1)^u$	-3.8	6.9	0.74	0.06	3.08	0.24
	$R(1,0)$	-3.3	7.5	0.83	0.07	2.11	0.17
	$R(1,1)^l$	-3.1	8.1	0.69	0.06	3.15	0.28
HD 154368	$R(1,1)^u$	5.4	5.8	1.57	0.28	6.51	1.16
	$R(1,0)$	4.6	5.1	1.13	0.25	2.86	0.63
HD 168607	$R(1,1)^u$	20.9	7.9	1.07	0.13	4.44	0.53
	$R(1,0)$	22.4	8.9	0.85	0.14	2.16	0.34
HD 168625	$R(1,1)^u$	19.5	9.5	1.58	0.19	6.55	0.78
	$R(1,0)$	22.0	9.1	1.59	0.19	4.02	0.48

Table 5.2: (continued)

Object	Transition	v_{LSR} (km s^{-1})	FWHM (km s^{-1})	W_λ (10^{-6} μm)	$\sigma(W_\lambda)$ (10^{-6} μm)	$N(J,K)$ (10^{13} cm^{-2})	$\sigma(N)$ (10^{13} cm^{-2})
HD 169454	$R(1,1)^u$	4.5	10.6	0.80	0.12	3.32	0.51
	$R(1,0)$	4.0	11.7	1.01	0.12	2.56	0.30
	$R(1,1)^l$	3.8	8.7	0.77	0.18	3.53	0.84
W40 IRS 1A	$R(1,1)^u$	5.9	8.9	4.19	0.64	17.4	2.66
	$R(1,0)$	7.4	7.8	4.48	0.60	11.3	1.51
	$R(1,1)^l$	6.1	4.5	2.80	0.71	12.8	3.26
HD 229059	$R(1,1)^u$	3.8	9.3	5.10	0.25	21.2	1.02
	$R(1,0)$	3.5	9.7	6.42	0.26	16.2	0.65
HD 204827	$R(1,1)^u$	-0.8	11.0	3.11	0.53	12.9	2.18
	$R(1,0)$	-0.9	8.7	2.41	0.51	6.10	1.29
λ Cep	$R(1,1)^u$	-2.9	10.7	1.04	0.23	4.31	0.95
	$R(1,0)$	-1.4	13.5	1.29	0.27	3.26	0.67
κ Cas	$R(1,1)^u$	...	15	...	0.19	...	0.77
	$R(1,0)$	...	15	...	0.19	...	0.47
HD 21483	$R(1,1)^u$	...	15	...	0.47	...	1.97
	$R(1,0)$	...	15	...	0.47	...	1.20
HD 21856	$R(1,1)^u$	...	15	...	0.46	...	1.92
	$R(1,0)$	...	15	...	0.46	...	1.17
40 Per	$R(1,1)^u$	...	15	...	0.18	...	0.74
	$R(1,0)$	...	15	...	0.18	...	0.45
o Per	$R(1,1)^u$	...	10	...	0.10	...	0.41
	$R(1,0)$	...	10	...	0.10	...	0.25
BD +31 643	$R(1,1)^u$	...	15	...	0.95	...	3.95
	$R(1,0)$	...	15	...	0.95	...	2.41

Table 5.2: (continued)

Object	Transition	$v_{\rm LSR}$ (km s^{-1})	FWHM (km s^{-1})	W_λ (10^{-6} μm)	$\sigma(W_\lambda)$ (10^{-6} μm)	$N(J,K)$ (10^{13} cm^{-2})	$\sigma(N)$ (10^{13} cm^{-2})
ϵ Per	$R(1,1)^u$	...	10	...	0.08	...	0.33
	$R(1,0)$	...	10	...	0.08	...	0.20
ξ Per	$R(1,1)^u$	...	10	...	0.11	...	0.44
	$R(1,0)$	...	10	...	0.11	...	0.27
62 Tau	$R(1,1)^u$	...	15	...	0.37	...	1.53
	$R(1,0)$	...	15	...	0.37	...	0.93
α Cam	$R(1,1)^u$	...	15	...	0.30	...	1.26
	$R(1,0)$	...	15	...	0.30	...	0.77
NGC 2024 IRS1	$R(1,1)^u$	...	10	...	0.26	...	1.09
	$R(1,0)$	...	10	...	0.26	...	0.66
HD 47129	$R(1,1)^u$	...	15	...	0.60	...	2.48
	$R(1,0)$	...	15	...	0.60	...	1.51
HD 53367	$R(1,1)^u$	...	5	...	0.12	...	0.50
	$R(1,0)$	...	5	...	0.12	...	0.30
	$R(1,1)^l$	...	5	...	0.07	...	0.32
o Sco	$R(1,1)^u$	...	10	...	0.08	...	0.35
	$R(1,0)$	...	10	...	0.08	...	0.21
HD 147888	$R(1,1)^u$	...	10	...	0.46	...	1.92
	$R(1,0)$	...	10	...	0.46	...	1.17
HD 147889	$R(1,1)^u$	...	10	...	0.18	...	0.74
	$R(1,0)$	...	10	...	0.18	...	0.45
χ Oph	$R(1,1)^u$	...	5	...	0.11	...	0.45
	$R(1,0)$	...	5	...	0.11	...	0.27

Table 5.2: (continued)

Object	Transition	v_{LSR} (km s^{-1})	FWHM (km s^{-1})	W_λ (10^{-6} μm)	$\sigma(W_\lambda)$ (10^{-6} μm)	$N(J,K)$ (10^{13} cm^{-2})	$\sigma(N)$ (10^{13} cm^{-2})
μ Nor	$R(1,1)^u$	...	5	...	0.12	...	0.49
	$R(1,0)$	...	5	...	0.12	...	0.30
HD 149404	$R(1,1)^u$	...	5	...	0.23	...	0.94
	$R(1,0)$	...	5	...	0.23	...	0.57
ζ Oph	$R(1,1)^u$	...	10	...	0.08	...	0.31
	$R(1,0)$	...	10	...	0.08	...	0.19
HD 152236	$R(1,1)^u$	...	5	...	0.14	...	0.59
	$R(1,0)$	...	5	...	0.14	...	0.36
BD -14 5037	$R(1,1)^u$	...	10	...	0.23	...	0.95
	$R(1,0)$	...	10	...	0.23	...	0.58
HD 193322A	$R(1,1)^u$	...	15	...	0.37	...	1.55
	$R(1,0)$	...	15	...	0.37	...	0.95
Cyg OB2 8A	$R(1,1)^u$	...	15	...	0.98	...	4.07
	$R(1,0)$	...	15	...	0.98	...	2.48
HD 206267	$R(1,1)^u$	...	10	...	0.30	...	1.25
	$R(1,0)$	...	10	...	0.30	...	0.76
19 Cep	$R(1,1)^u$	...	15	...	0.26	...	1.10
	$R(1,0)$	...	15	...	0.26	...	0.67
1 Cas	$R(1,1)^u$	...	15	...	0.29	...	1.21
	$R(1,0)$	...	15	...	0.29	...	0.74

Notes: Columns 6 ($\sigma(W_\lambda)$) and 8 ($\sigma(N)$) are 1σ uncertainties on the equivalent width and column density, respectively. The FWHM values in the case of non-detections are appropriate for the resolution of the instrument used in each observation, and are used in computing the value of $\mathcal{N}_{\mathrm{pix}}$ required in equation (5.3).

Table 5.3: Cosmic-Ray Ionization Rates

Object	$N(\mathrm{H_3^+})$ (10^13 cm^-2)	$\sigma[N(\mathrm{H_3^+})]$ (10^13 cm^-2)	$\mathrm{H_3^+}$ Reference	$N(\mathrm{H_2})$ (10^20 cm^-2)	$\sigma[N(\mathrm{H_2})]$ (10^20 cm^-2)	$\mathrm{H_2}$ Reference	n_H (cm^-3)	Density Reference	ζ_2 (10^-16 s^-1)	$\sigma(\zeta_2)$ (10^-16 s^-1)
HD 20041	23.7	5.13	1,2	11.4	6.24	5	200		9.48	6.38
HD 21389	8.67	0.92	1	5.57	3.06	5	200		7.11	4.61
ζ Per	6.26	0.52	1	4.75	0.95	6	215	10	5.55	2.03
X Per	7.34	0.92	1	8.38	0.89	7	325	10	5.85	2.18
HD 29647	11.9	1.11	1	22.9	12.5	5	200		2.38	1.54
HD 73882	9.02	0.50	3	12.9	2.39	7	520	10	9.71	2.88
HD 110432	5.22	0.17	3	4.37	0.29	7	140	10	3.86	1.61
HD 154368	9.37	1.32	1	14.4	3.99	7	240	10	4.19	1.79
WR 104	23.2	1.54	2	44.7	22.3	8	200		2.37	1.43
HD 168607	6.60	0.63	1	17.4	8.47	5	200		1.73	1.03
HD 168625	10.6	0.92	1	16.3	7.95	5	200		2.96	1.76
HD 169454	5.93	0.34	1	16.6	8.37	5	300	10	2.45	1.41
W40 IRS 1A	26.9	3.54	1	56.3	28.2	8	300	11	3.27	1.91
WR 118 (5)	29.4	7.07	2	43.3	21.7	8	200		3.10	2.00
WR 118 (47)	30.8	5.73	2	45.5	22.7	8	200		3.10	1.94
WR 121	22.0	2.60	2	34.0	17.0	8	200		2.96	1.80
HD 183143 (7)	11.3	2.98	2	4.86	2.38	5	200		10.6	6.84
HD 183143 (24)	13.5	2.81	2	7.91	3.85	5	200		7.82	4.87
HD 229059	37.4	1.20	1	65.7	51.2	5	200		2.60	2.20
Cyg OB2 5	24.0	3.29	2	15.2	7.39	5	225	10	8.13	4.81
Cyg OB2 12	34.3	5.89	2,4	80.0	69.1	5	300	10	2.93	2.70
HD 204827	19.0	2.54	1	20.9	10.2	5	450	10	9.32	5.22
λ Cep	7.58	1.17	1	6.88	0.48	7	115	10	2.84	1.44
κ Cas	...	0.91	1	1.88	0.20	6	200		...	1.78
HD 21483	...	2.30	1	11.9	5.91	5	200		...	0.88
HD 21856	...	2.25	1	1.10	0.12	6	200		...	8.42
40 Per	...	0.87	1	2.92	0.53	6	80	12	...	0.57
o Per	...	0.47	1	4.09	0.79	6	265	10	...	0.85
BD +31 643	...	4.63	1	12.4	4.39	7	200		...	1.67
ε Per	...	0.38	1	0.33	0.07	6	15	13	...	0.36
ξ Per	...	0.51	1	3.42	0.53	6	300	13	...	1.98
62 Tau	...	1.79	1	6.23	1.12	7	280	10	...	2.06
α Cam	...	1.48	1	2.17	0.26	6	150	13	...	2.17
χ^2 Ori	...	2.75	2	4.90	1.05	9	200		...	2.79
HD 47129	...	2.91	1	3.51	0.58	6	200		...	3.81
HD 53367	...	0.44	1	11.1	1.44	9	200		...	0.20

Table 5.3: (continued)

Object	$N(\mathrm{H_3^+})$ $(10^{13}\ \mathrm{cm^{-2}})$	$\sigma[N(\mathrm{H_3^+})]$ $(10^{13}\ \mathrm{cm^{-2}})$	$\mathrm{H_3^+}$ Reference	$N(\mathrm{H_2})$ $(10^{20}\ \mathrm{cm^{-2}})$	$\sigma[N(\mathrm{H_2})]$ $(10^{20}\ \mathrm{cm^{-2}})$	$\mathrm{H_2}$ Reference	n_{H} $(\mathrm{cm^{-3}})$	Density Reference	ζ_2 $(10^{-16}\ \mathrm{s^{-1}})$	$\sigma(\zeta_2)$ $(10^{-16}\ \mathrm{s^{-1}})$
o Sco	...	0.41	1	19.1	9.81	5	225	10	...	0.11
HD 147888	...	2.25	1	2.97	0.61	9	215	10	...	9.25
HD 147889	...	0.87	1	28.8	14.0	5	525	10	...	0.36
χ Oph	...	0.52	1	4.26	1.02	6	185	10	...	0.64
μ Nor	...	0.58	1	2.77	0.49	6	200		...	1.09
HD 149404	...	1.10	1	6.17	0.53	9	200		...	0.87
ζ Oph	...	0.37	1,2	4.49	0.42	6	215	10	...	0.39
HD 152236	...	0.69	1	5.34	1.32	9	200		...	0.63
BD -14 5037	...	1.11	1	38.6	23.6	5	200		...	0.13
P Cygni	...	1.84	2	3.14	1.61	5	200		...	2.67
HD 193322A	...	1.82	1	1.21	0.18	6	200		...	6.52
HD 194279	...	4.59	2	23.7	11.9	8	200		...	0.88
Cyg OB2 8A	...	4.77	1	9.26	4.58	5	200		...	2.35
HD 206267	...	1.47	1	7.18	0.59	7	200		...	0.97
19 Cep	...	1.28	1	1.21	0.18	6	200		...	4.60
1 Cas	...	1.41	1	1.40	0.19	6	200		...	4.18
NGC 2024 IRS 1	...	1.27	1	49.0	24.5	8	10000		...	0.14

Notes: The sight lines toward WR 118 and HD 183143 have 2 distinct velocity components observed in $\mathrm{H_3^+}$ by McCall et al. (2002), and each of these components is labeled with a number in parentheses that corresponds to its average LSR velocity. When no reference for n_{H} was available the value was set to 200 cm^{-3}, an average density for diffuse molecular clouds. Upper limits to the cosmic-ray ionization rate should be taken as 3 times $\sigma(\zeta_2)$.

$\mathrm{H_3^+}$ References: (1) this work; (2) McCall et al. (2002); (3) Crabtree et al. (2011); (4) McCall et al. (1998)

$\mathrm{H_2}$ References: (5) calculated from CH column densities (see Table B.2) using the relation $N(\mathrm{CH})/N(\mathrm{H_2}) = 3.5^{+2.1}_{-1.4} \times 10^{-8}$ from Sheffer et al. (2008); (6) Savage et al. (1977); (7) Rachford et al. (2002); (8) calculated from $E(B-V)$ (see Table 2.3) using the relation $N_{\mathrm{H}} \approx E(B-V)5.8 \times 10^{21}\ \mathrm{cm^{-2}\ mag^{-1}}$ from Bohlin et al. (1978), and assuming $2N(\mathrm{H_2})/N_{\mathrm{H}} = f_{\mathrm{H_2}} = 0.67$; (9) Rachford et al. (2009)

n_{H} References: (10) Sonnentrucker et al. (2007); (11) Shuping et al. (1999); (12) Jenkins et al. (1983); (13) Jura (1975)

Chapter 6

Examining Line of Sight Properties

6.1   Correlations Between H_3^+ and Other Molecules

One of the best ways to investigate chemistry in the ISM is to search for correlations in the abundances of different species. A strong correlation suggests that species are chemically related, while little or no correlation suggests that they are not. For example, the previously mentioned tight relationship between CH and H_2 (Federman, 1982; Mattila, 1986; Sheffer et al., 2008) alludes to H_2 being vital in forming CH. To check if various species are chemically related to H_3^+, I compiled abundances of CO, C, CH, CH^+, CN, OH, and HD from the literature (see Appendix B). In plotting the column density of H_3^+ versus the column densities of these other species, I find no significant correlations (see Figures 6.1 through 6.7). While this is somewhat expected — the OSU gas-phase reaction network[1] and UMIST database for astrochemistry (Woodall et al., 2007) do not have H_3^+ as an important immediate precursor to any of these species — it is always worthwhile to check for the unexpected.

   H_3^+ is, of course, closely linked to H_2 through reactions (1.1) and (1.2). A plot of $N(H_3^+)$ versus $N(H_2)$ is shown in Figure 6.8. Unfortunately, the overlap between sight lines with both H_2 and H_3^+ observations is rather small. When available, column densities from UV observations of H_2 are used; otherwise estimates from $N(CH)$ and $E(B - V)$, as discussed in section 5.2 and presented in Table 5.3, are utilized. In addition to the diffuse molecular cloud data presented herein, Figure 6.8 also includes observations of H_3^+ in dense clouds (McCall et al., 1999; Kulesa, 2002; Brittain et al., 2004; Gibb et al., 2010). In some of these sight lines $N(H_2)$ is determined directly from IR observations of H_2, but in most it is estimated from $E(B - V)$ or $N(CO)$. Detections of H_3^+ in diffuse clouds tend to cluster about $N(H_3^+)/N(H_2) \approx 10^{-7}$, while those in dense clouds are typically in the range $10^{-9} \lesssim N(H_3^+)/N(H_2) \lesssim 10^{-8}$. Rearranging equation (5.6) to the form

$$\frac{N(H_3^+)}{N(H_2)} = \frac{\zeta_2}{k_e x_e n_H} \tag{6.1}$$

---

[1]http://www.physics.ohio-state.edu/~eric/index.html

shows that $N(\mathrm{H}_3^+)/N(\mathrm{H}_2)$ is directly proportional to ζ_2, and inversely proportional to $k_e x_e n_\mathrm{H}$. As such, scatter about a central value of $N(\mathrm{H}_3^+)/N(\mathrm{H}_2)$ for diffuse clouds is likely due to variations in ζ_2 and electron density $(x_e n_\mathrm{H})$ between sight lines.

The much lower value of $N(\mathrm{H}_3^+)/N(\mathrm{H}_2)$ in dense clouds is the result of a higher density, different destruction partner, and lower ionization rate. Replacing electrons with CO as the dominant destruction partner in equation (6.1) leaves $N(\mathrm{H}_3^+)/N(\mathrm{H}_2)$ inversely proportional to $k_\mathrm{CO} x(\mathrm{CO}) n_\mathrm{H}$. The rate coefficient for destruction of H_3^+ by CO is about 2 orders of magnitude slower than by electrons (see Table 5.1), while the density of dense clouds is about 2–3 orders of magnitude larger than diffuse clouds (Snow & McCall, 2006). This means that ζ_2 must be about 1–2 orders of magnitude lower in dense clouds than in diffuse clouds to produce the observed results. Reasons for this difference are discussed in the following section.

6.2 Correlations Between ζ_2 and Line of Sight Parameters

With cosmic-ray ionization rates and upper limits inferred for over 50 diffuse cloud sight lines, it is interesting to study the sample as a whole. Inferred cosmic-ray ionization rates and upper limits are plotted in Figure 6.9. The mean ionization rate (calculated only from sight lines where H_3^+ is detected) is found to be $\zeta_2 = 3.3 \pm 0.4 \times 10^{-16}$ s^{-1}, about 1 order of magnitude larger than the canonical 3×10^{-17} s^{-1} widely adopted in the literature. Many of the lowest and highest ionization rates are not consistent with each other to within 1σ uncertainties, and several of the 3σ upper limits point to ionization rates lower than those inferred in sight lines with H_3^+ detections. This suggests that variations exist in the cosmic-ray ionization rate throughout the Galactic ISM.

In addition to studying the cosmic-ray ionization rate in and of itself, it is insightful to search for correlations between ζ_2 and various other sight line parameters. One of the most fundamental relationships to study is that between ζ_2 and location within the Galaxy. The cosmic-ray ionization rate is plotted against Galactic longitude in the bottom panel of Figure 6.10. The top panel is a map in Galactic coordinates and the middle panel gives the distance to background sources such that the reader can easily trace the ionization rates in the bottom panel to an actual on-sky position. Many of the lowest upper limits are from observations toward the Ophiuchus-Scorpio region, where H_3^+ was not detected in any sight line, despite appreciable H_2 column densities. Aside from this one region with no H_3^+ detections, there is no correlation between Galactic coordinates and the cosmic-ray ionization rate. To further

study the ionization rate as a function of position, it is compared to the Galactocentric radius (R) of the observed background sources in Figure 6.11. Dependence of ζ_2 on distance from the Galactic center would show up as a gradient in this plot. Although at first glance it may appear that ζ_2 increases with R, many of the upper limits at larger R argue against such a correlation. As no gradients are apparent in Figures 6.10 and 6.11, it would seem that the mechanism responsible for variations in the cosmic-ray ionization rate does not operate on large scales. Instead, it must operate on relatively small scales to cause variations between sight lines that are close to each other on the sky. Perhaps, then, properties of the observed clouds themselves are responsible for variations in ζ_2, and will show some correlation with the cosmic-ray ionization rate.

A parameter with which ζ_2 has been predicted to vary is the total hydrogen column density, N_H (Padovani et al., 2009). This is because the energy spectrum of cosmic-rays is expected to change with depth into a cloud. Lower-energy particles — those most efficient at ionization — will lose all of their energy to ionization interactions in the outer regions of a cloud, leaving only higher-energy particles to ionize the cloud interior. As such, the ionization rate in a cloud interior should be lower than in a cloud exterior. Because lower-energy particles can operate through a larger portion of clouds with lower column densities (Cravens & Dalgarno, 1978), it is expected that the inferred ζ_2 will decrease with increasing N_H. A plot of ζ_2 versus N_H (and equivalent $E(B-V)$) is shown in Figure 6.12. Included in Figure 6.12 are data from 4 dense cloud sight lines observed in H_3^+ by Kulesa (2002), and 5 dense cloud sight lines observed in $H^{13}CO^+$ by van der Tak & van Dishoeck (2000) for the purpose of extending the relationship to much higher N_H. There does not appear to be a correlation between ζ_2 and N_H when only the diffuse molecular cloud sight lines are considered. However, when the dense cloud ionization rates (most of which are of order a few times 10^{-17} s^{-1}) are included, it seems that ζ_2 does decrease in sight lines with higher column densities.

Given that ζ_2 does *not* decrease with increased N_H among diffuse cloud sight lines, but does when switching from the diffuse to dense cloud regime, the following conclusions can be drawn. First, the cosmic rays that are primarily responsible for ionization in diffuse clouds must be able to propagate entirely through such clouds. This could easily be done by 10 MeV protons, which have a range of $Rn \approx 2 \times 10^{22}$ cm^{-2} (Cravens & Dalgarno, 1978), about equal to the largest values of N_H in diffuse clouds studied here. However, a cloud with a large line-of-sight column density does not necessarily have a large column density in the plane of the sky. Even lower-energy particles then (e.g., 2 MeV protons with $Rn \approx 10^{21}$ cm^{-2}) could potentially cause ionization through the entire extent of an observed cloud.

Second, the cosmic rays that are responsible for most of the ionization in diffuse clouds

must not be able to penetrate to the interiors of dense clouds. Again, something like 2–10 MeV protons fit this picture well. Most of the sight lines where H_3^+ is observed in dense clouds use embedded objects as background sources. Regions surrounding these sources have been mapped in various molecular species (via emission at radio wavelengths), implying large column densities in the plane of the sky in addition to the large column densities observed along the line of sight. This increases the likelihood that much of the material being probed is deep within the observed cloud.

Taken together, the higher ionization rates inferred in diffuse clouds and lower ionization rates inferred in dense clouds suggest that differences in ζ_2 can be explained by the inability of low-energy cosmic rays to penetrate large columns of material. However, under the assumption that the cosmic-ray spectrum is uniform throughout the Galactic disk (Webber, 1998), this does not adequately explain differences in the cosmic-ray ionization rate amongst diffuse clouds. Instead, it would seem that the cosmic-ray spectrum — at least for particles in the energy range most efficient at ionization — must vary in space.

Despite the previously held assumption of a uniform cosmic-ray spectrum, it should not be surprising that the flux of low-energy particles varies across the Galaxy. Given a hydrogen density of 1 cm^{-3}, a 2 MeV proton will only travel about 320 pc (not necessary in a straight line) before losing all of its energy, meaning that any point that is a few hundred parsecs away from a site of particle acceleration will not experience the same flux of 2 MeV protons as a point that is much closer to an acceleration site. For low-energy particles to even enter a diffuse cloud then, the cloud must be relatively close to a site of particle acceleration.

Regardless of where most low-energy cosmic rays are accelerated, it is possible that differences in ζ_2 among diffuse cloud sight lines can be attributed to the distance between a cloud and acceleration site. Sight lines that probe material in close proximity to an acceleration site should show high ionization rates, while those that probe material farther away should show lower ionization rates. Unfortunately, defining acceleration sites and actually computing physical distances between those and the sample of observed clouds is difficult at best.

6.3   Motivation for Following Chapters

The next 3 chapters are based on published papers. I will therefore provide a brief introduction to each to describe how they are motivated by the work detailed so far.

6.3.1 The Implications of a High Cosmic-Ray Ionization Rate

As described above, cosmic-ray ionization rates inferred from H_3^+ observations in diffuse clouds are about 1 order of magnitude larger than previously thought. This implies a larger flux of low-energy particles, and I investigate the resulting effects on light element abundances, gamma-ray line fluxes, and heating of the ISM by testing different theoretical cosmic-ray spectra. I also attempt to reproduce the lower ionization rates inferred in dense clouds. By finding a best-fit spectrum, I can determine how many components are required to match observations (i.e., whether a single uniform interstellar spectrum is at work, or a locally accelerated particle spectrum must also be included). Such information can then be used to constrain the uniformity of the interstellar cosmic-ray spectrum, as well as whether strong (supernova remnants) or weak (stellar winds) shocks are responsible for accelerating the majority of low-energy cosmic rays. This work is described in Chapter 7, and published as Indriolo et al. (2009a).

6.3.2 Investigating the Cosmic-Ray Ionization Rate Near a Supernova Remnant

While cosmic rays do not point back to their places of origin, mounting evidence suggest that most Galactic cosmic rays are accelerated in supernova remnants by the process of diffusive shock acceleration. If this is the case, then clouds in close proximity to supernova remnants should experience a high flux of energetic particles, and exhibit a high ionization rate. To test this scenario, I developed a project to observe H_3^+ in diffuse molecular clouds known to be interacting with the supernova remnant IC 443. Chapter 8 describes this project, and is adapted from Indriolo et al. (2010a).

6.3.3 Metastable Helium as a Probe of the Cosmic-Ray Ionization Rate

Although H_3^+ is a powerful probe of the cosmic-ray ionization rate, it would be useful to have other such tracers. One candidate is metastable helium, He^*, which is expected to be ubiquitous in the diffuse molecular and diffuse atomic ISM. It can thus be used as a check on H_3^+ ionization rates where both species exist, and extend my work into atomic gas as well. An attempt to observe He^* and an updated reaction network is presented in Chapter 9 and published as Indriolo et al. (2009b).

6.4 Figures

This section contains the figures that are discussed throughout Chapter 6. They include plots of the H_3^+ column density versus those of CO, C, CH, CH^+, CN, OH, HD and H_2 (Figures 6.1 through 6.8, respectively), the distribution of cosmic-ray ionization rates in diffuse clouds (Figure 6.9), and plots of ζ_2 versus Galactic longitude (Figure 6.10), Galactocentric radius (Figure 6.11), and total hydrogen column density (Figure 6.12).
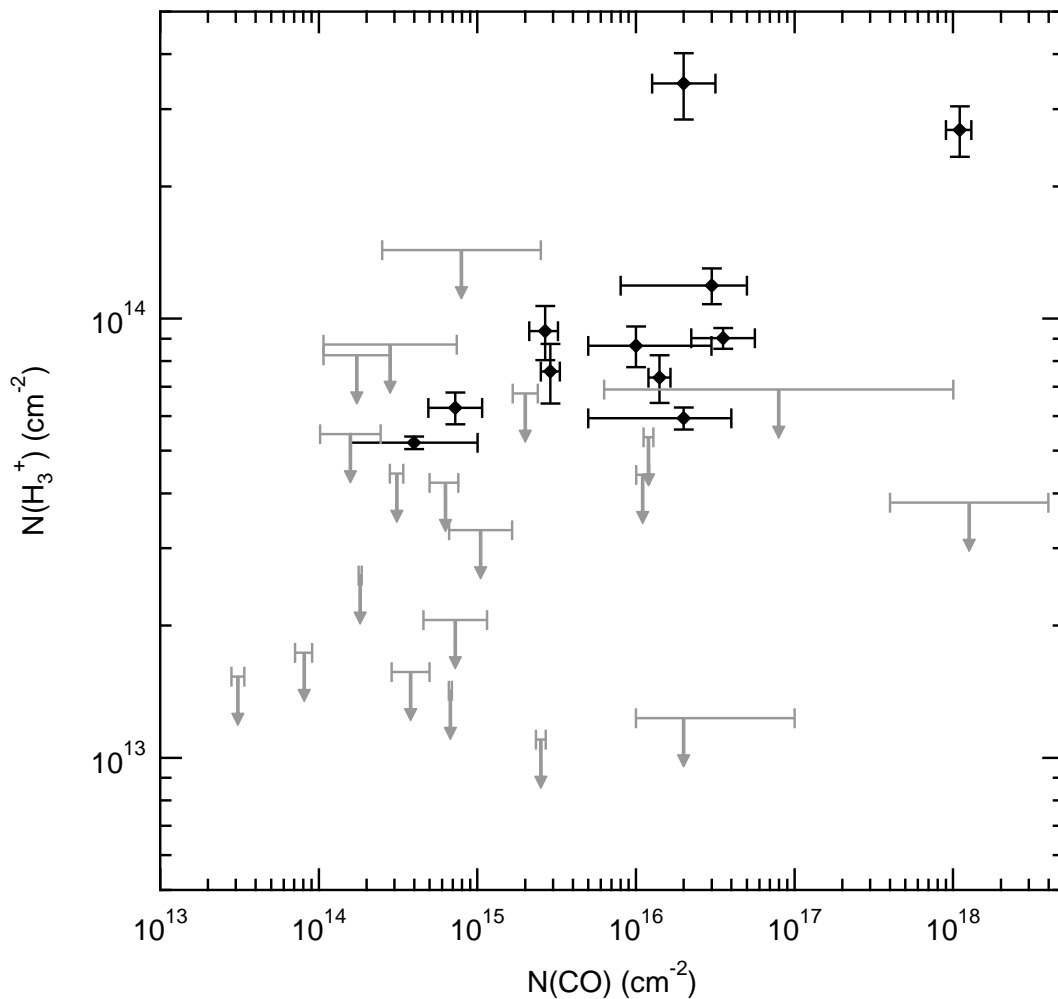
Figure 6.1: $N(H_3^+)$ versus $N(CO)$ for diffuse cloud sight lines. Filled diamonds are detections of H_3^+ with 1σ uncertainties, and 3σ upper limits on H_3^+ column densities are in grey. CO column densities are reported in Table B.1.
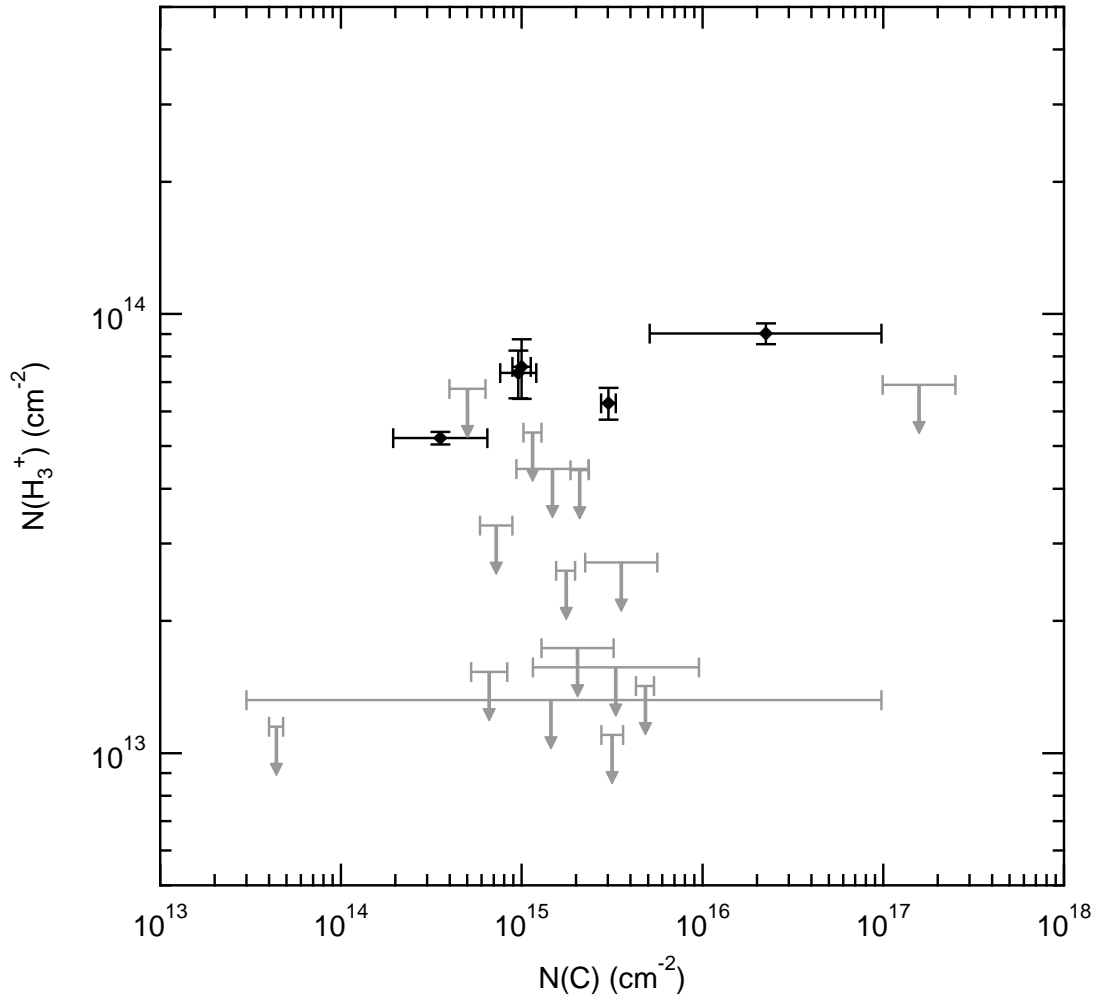
Figure 6.2: $N(H_3^+)$ versus $N(C)$ for diffuse cloud sight lines. Filled diamonds are detections of H_3^+ with 1σ uncertainties, and 3σ upper limits on H_3^+ column densities are in grey. C column densities are reported in Table B.1.
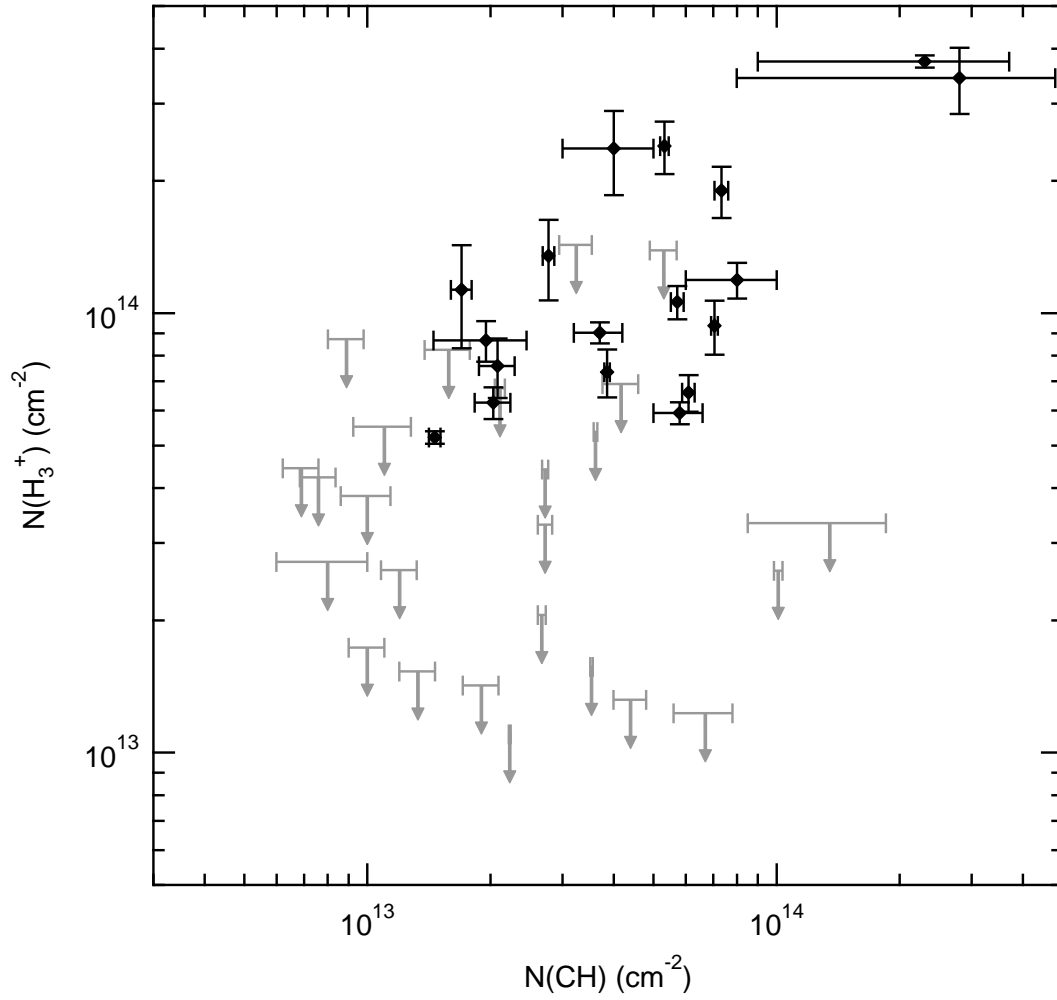
Figure 6.3: $N(\mathrm{H}_3^+)$ versus $N(\mathrm{CH})$ for diffuse cloud sight lines. Filled diamonds are detections of H_3^+ with 1σ uncertainties, and 3σ upper limits on H_3^+ column densities are in grey. CH column densities are presented in Table B.2.
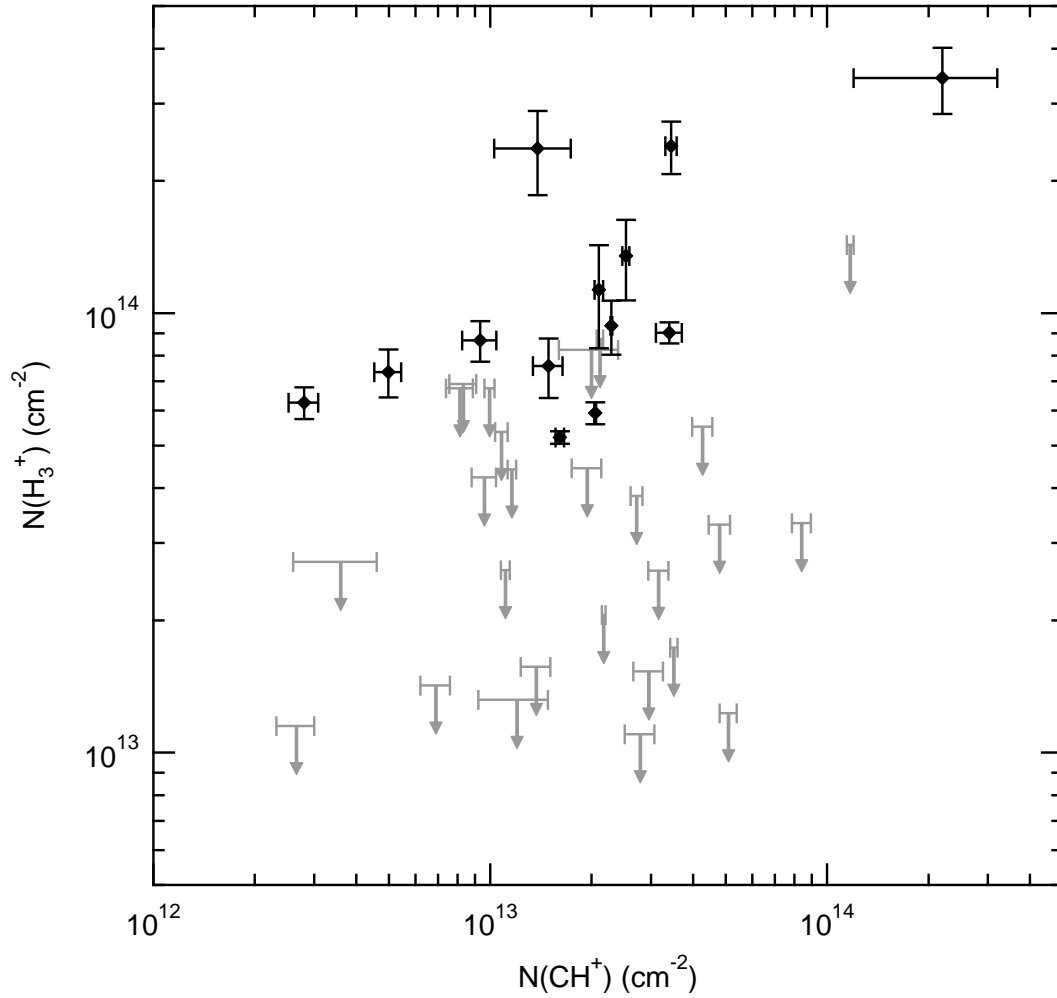
Figure 6.4: $N(\mathrm{H}_3^+)$ versus $N(\mathrm{CH}^+)$ for diffuse cloud sight lines. Filled diamonds are detections of H_3^+ with 1σ uncertainties, and 3σ upper limits on H_3^+ column densities are in grey. CH^+ column densities are presented in Table B.2.
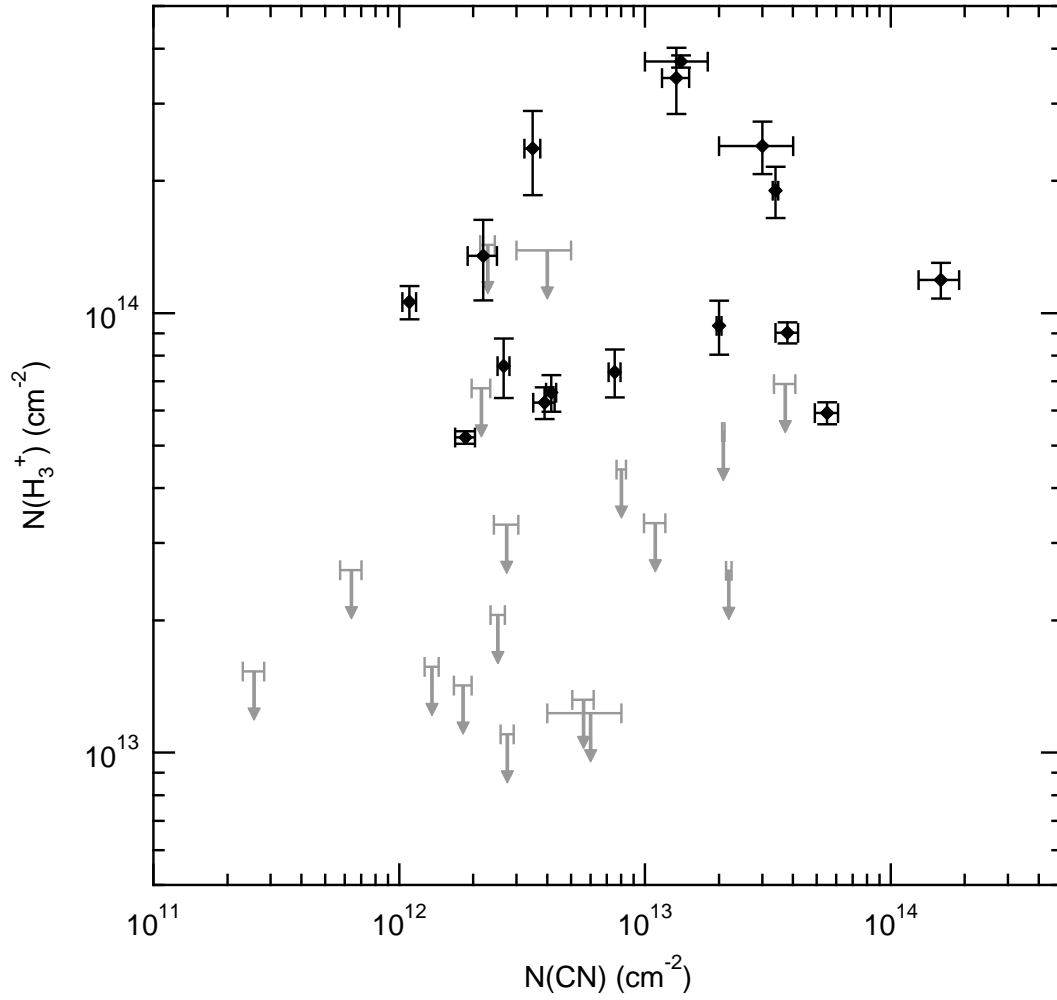
Figure 6.5: $N(\mathrm{H}_3^+)$ versus $N(\mathrm{CN})$ for diffuse cloud sight lines. Filled diamonds are detections of H_3^+ with 1σ uncertainties, and 3σ upper limits on H_3^+ column densities are in grey. CN column densities are presented in Table B.2.
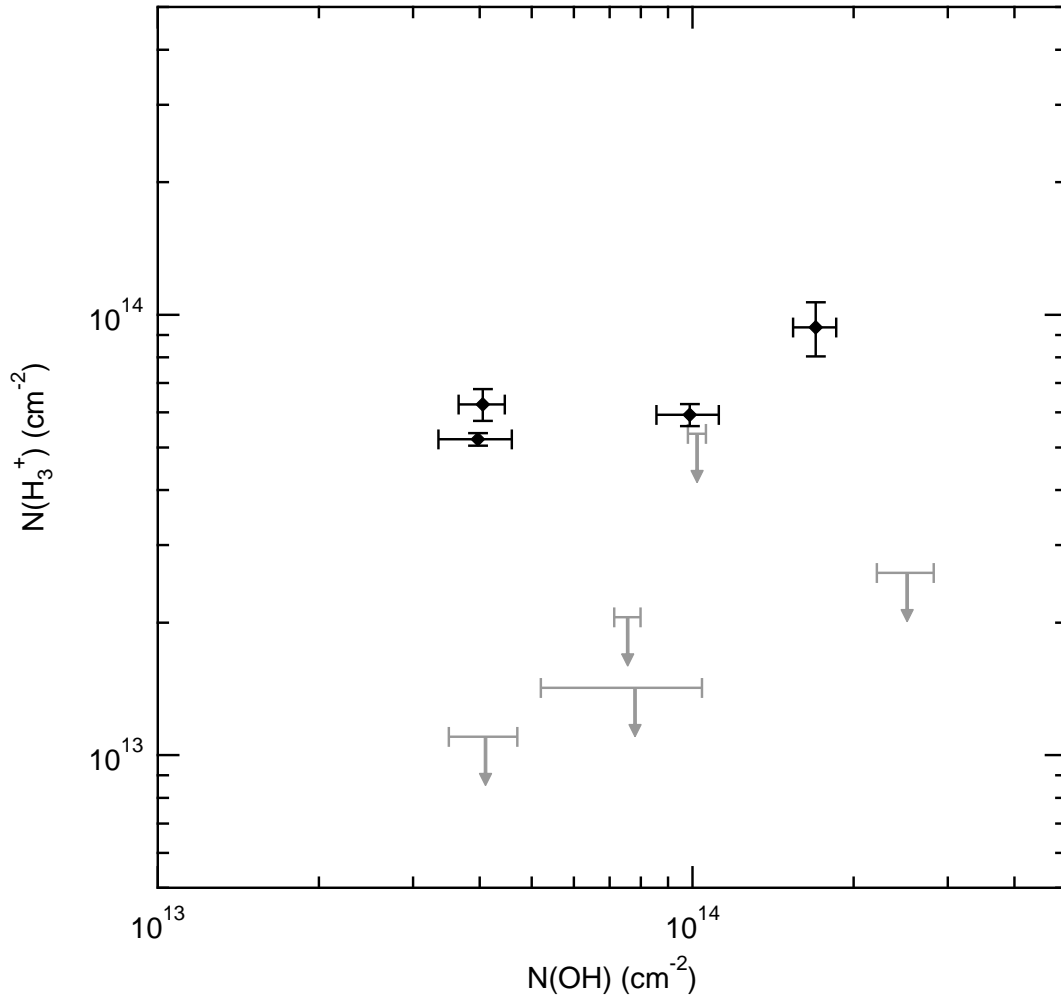
Figure 6.6: $N(\mathrm{H_3^+})$ versus $N(\mathrm{OH})$ for diffuse cloud sight lines. Filled diamonds are detections of $\mathrm{H_3^+}$ with 1σ uncertainties, and 3σ upper limits on $\mathrm{H_3^+}$ column densities are in grey. OH column densities are reported in Table B.4.
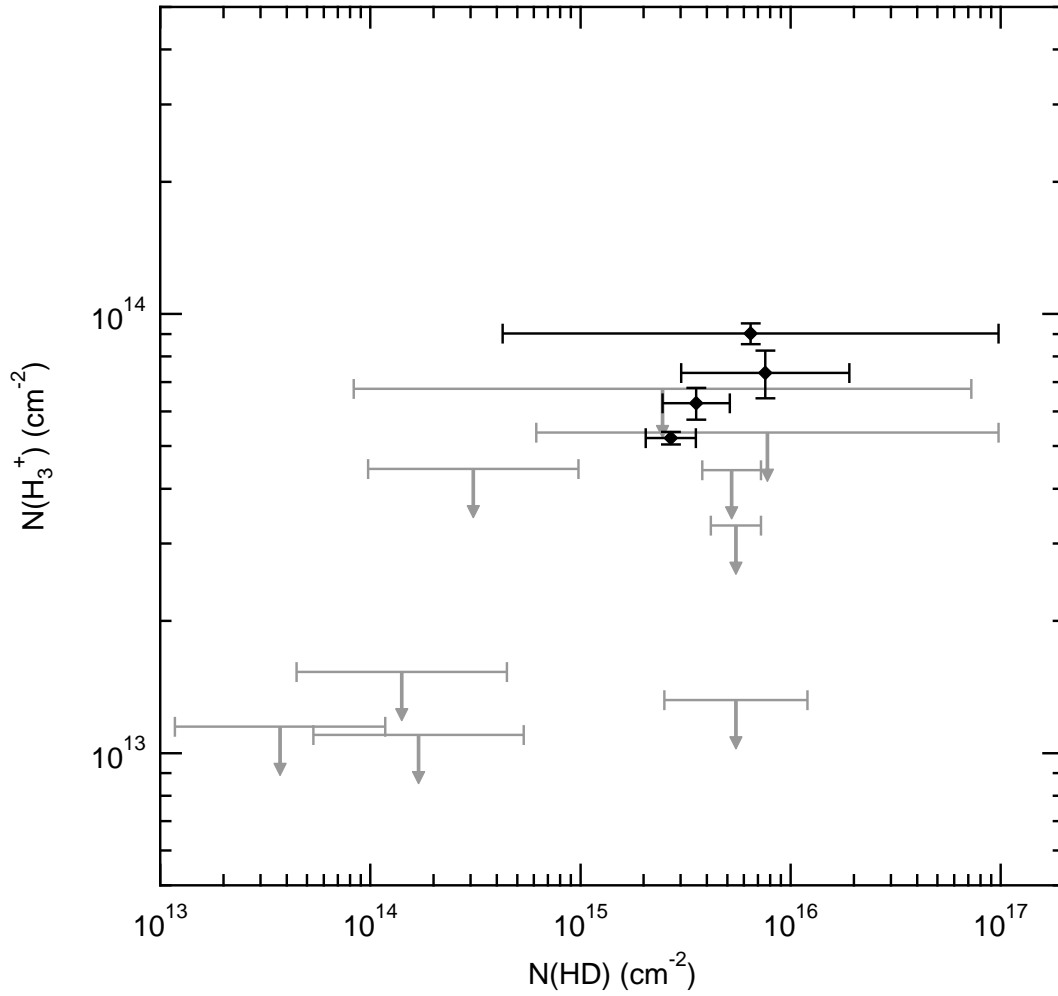
Figure 6.7: $N(\mathrm{H}_3^+)$ versus $N(\mathrm{HD})$ for diffuse cloud sight lines. Filled diamonds are detections of H_3^+ with 1σ uncertainties, and 3σ upper limits on H_3^+ column densities are in grey. HD column densities are presented in Table B.5.
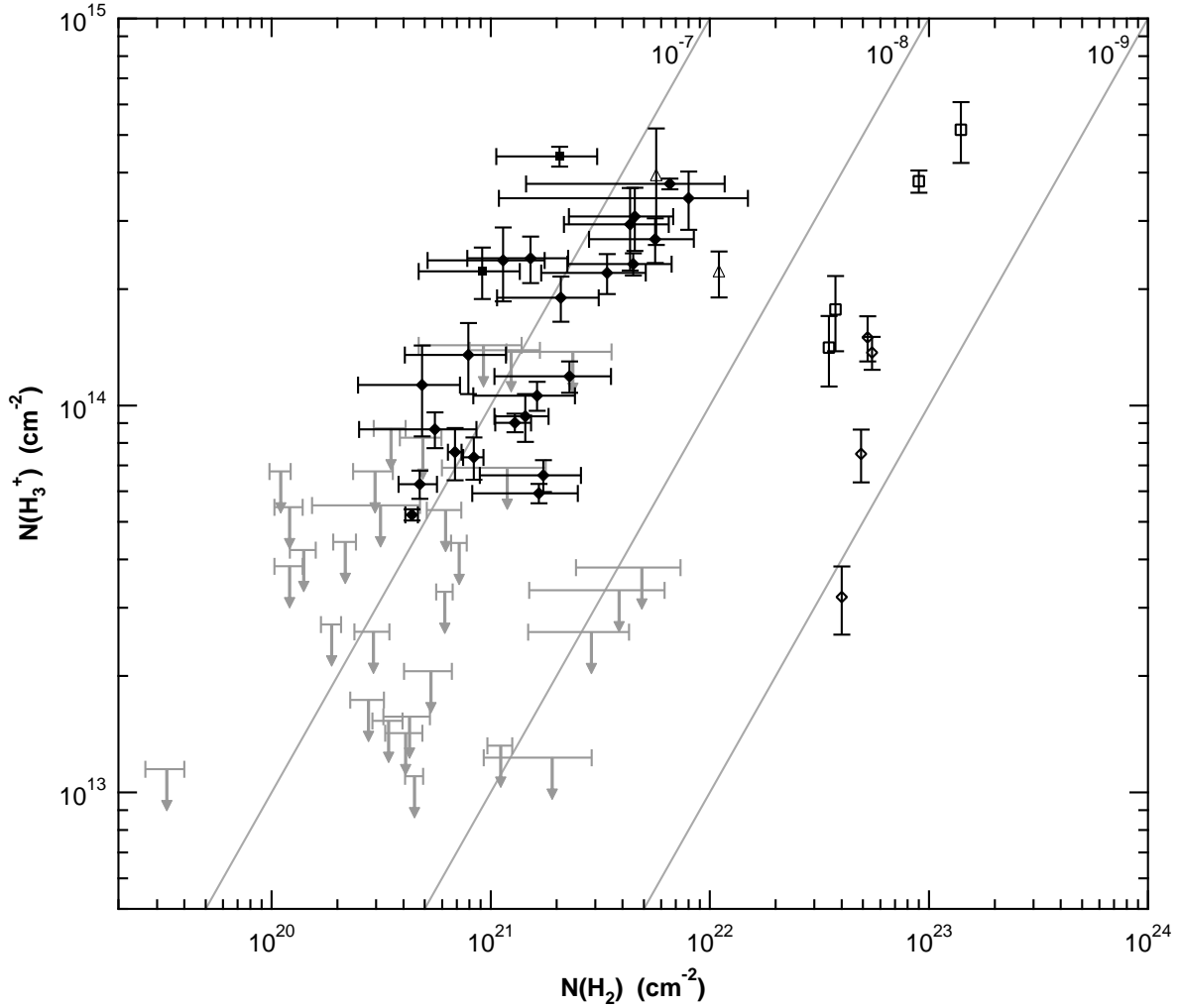
Figure 6.8: $N(\mathrm{H_3^+})$ versus $N(\mathrm{H_2})$ for diffuse clouds studied herein and various dense clouds reported in the literature. Symbols are as follows: filled diamonds - this study (detections); filled squares - Indriolo et al. (2010a); grey arrows - this study (3σ upper limits on $N(\mathrm{H_3^+})$); open squares - McCall et al. (1999); open diamonds - Kulesa (2002); open triangles - Brittain et al. (2004) and Gibb et al. (2010). The diagonal lines show constant values of $N(\mathrm{H_3^+})/N(\mathrm{H_2})$ and are labeled accordingly. Diffuse clouds cluster about $N(\mathrm{H_3^+})/N(\mathrm{H_2}) = 10^{-7}$, while dense clouds fall in the range between 10^{-8} and 10^{-9}. For diffuse cloud sight lines $N(\mathrm{H_2})$ is determined from UV $\mathrm{H_2}$ observations, estimated from $N(\mathrm{CH})$, or estimated from $E(B-V)$, and values used here are presented in Table 5.3. For dense cloud sight lines $N(\mathrm{H_2})$ is determined from IR $\mathrm{H_2}$ observations, estimated from A_V, or estimated from $N(\mathrm{CO})$.
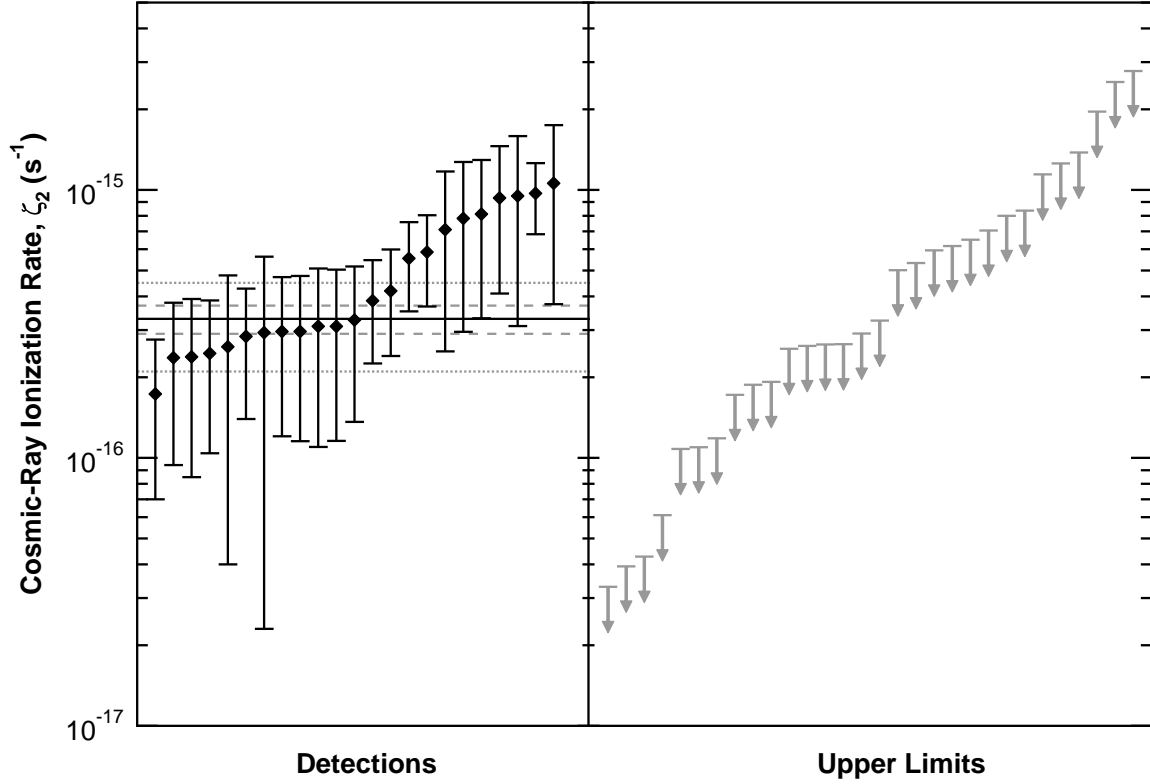
Figure 6.9: Cosmic-ray ionization rates and upper limits from the entire sample of target sight lines. The left panel shows ionization rates inferred from detections of H_3^+ with 1σ uncertainties. Points are spread out horizontally for clarity. The solid horizontal line is the weighted mean determined from detections alone (see equation 3.1), dashed grey lines are the 1σ uncertainties, and dotted grey lines are the 3σ uncertainties. The mean ionization rate plus or minus 1 standard deviation is: $\zeta_2 = 3.3 \pm 0.4 \times 10^{-16}$ s^{-1}. The right panel shows 3σ upper limits to the ionization rate inferred for sight lines where H_3^+ is not detected. Many of the lowest and highest ionization rates are not consistent with each other to within 1σ uncertainties, and several of the 3σ upper limits suggest ionization rates lower than those inferred in sight lines with H_3^+ detections. This likely points to variations in the cosmic-ray ionization rate between sight lines.
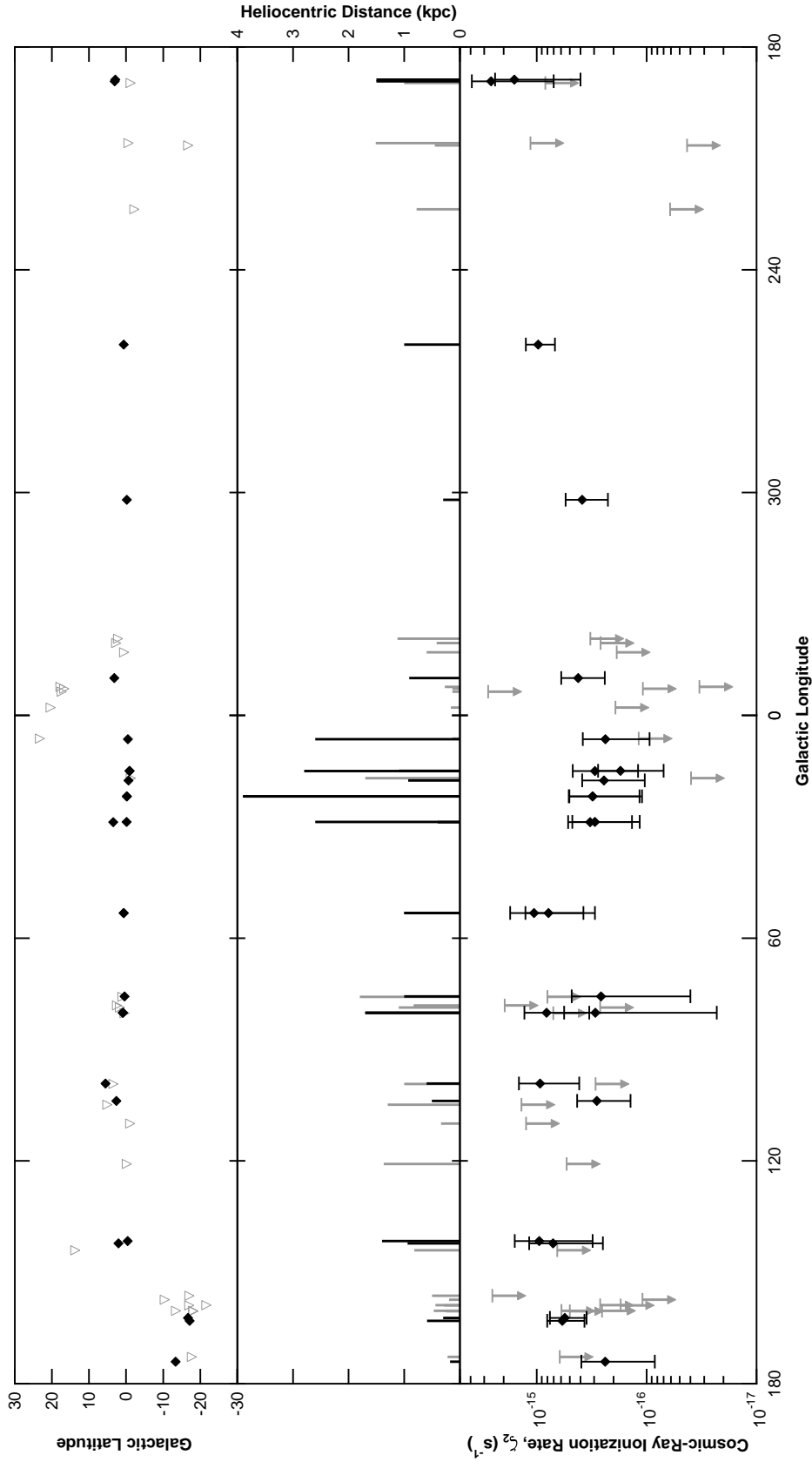
Figure 6.10: **Top panel:** Map showing the locations of targeted sight lines in Galactic coordinates. Black diamonds mark sight lines where H_3^+ absorption is observed, and open grey triangles mark sight lines where H_3^+ is not detected. **Middle panel:** Heliocentric distance of background sources with respect to Galactic longitude. Black lines mark sight lines where H_3^+ absorption is observed, and grey lines mark sight lines where H_3^+ is not detected. **Bottom panel:** The cosmic-ray ionization rate as a function of Galactic longitude. Black diamonds are inferred cosmic-ray ionization rates with 1σ uncertainties. Grey arrows are 3σ upper limits.
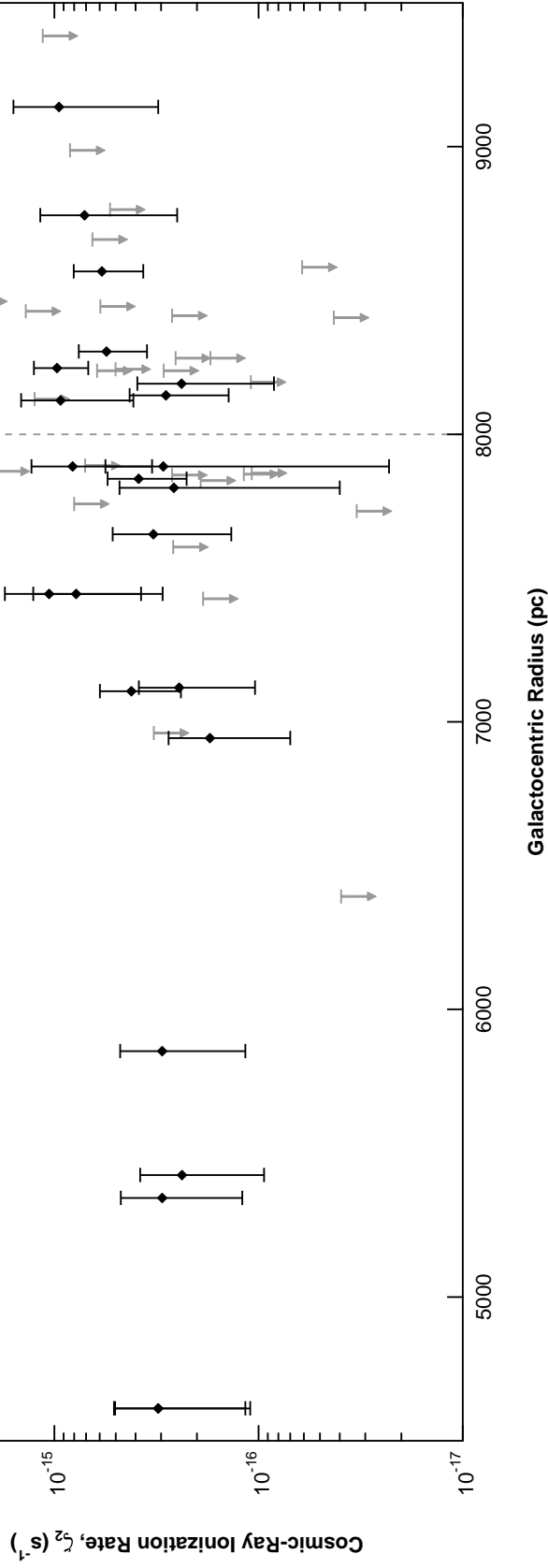
Figure 6.11: Cosmic-ray ionization rate versus Galactocentric radius of background sources. Black diamonds are inferred cosmic-ray ionization rates with 1σ uncertainties. Grey arrows are 3σ upper limits. Radii were calculated from distances and Galactic longitudes in Table 2.3 assuming the sun to be 8 kpc (marked by the vertical dashed line) from the Galactic center (Groenewegen et al., 2008). There is no correlation between Galactocentric radius and the cosmic-ray ionization rate.
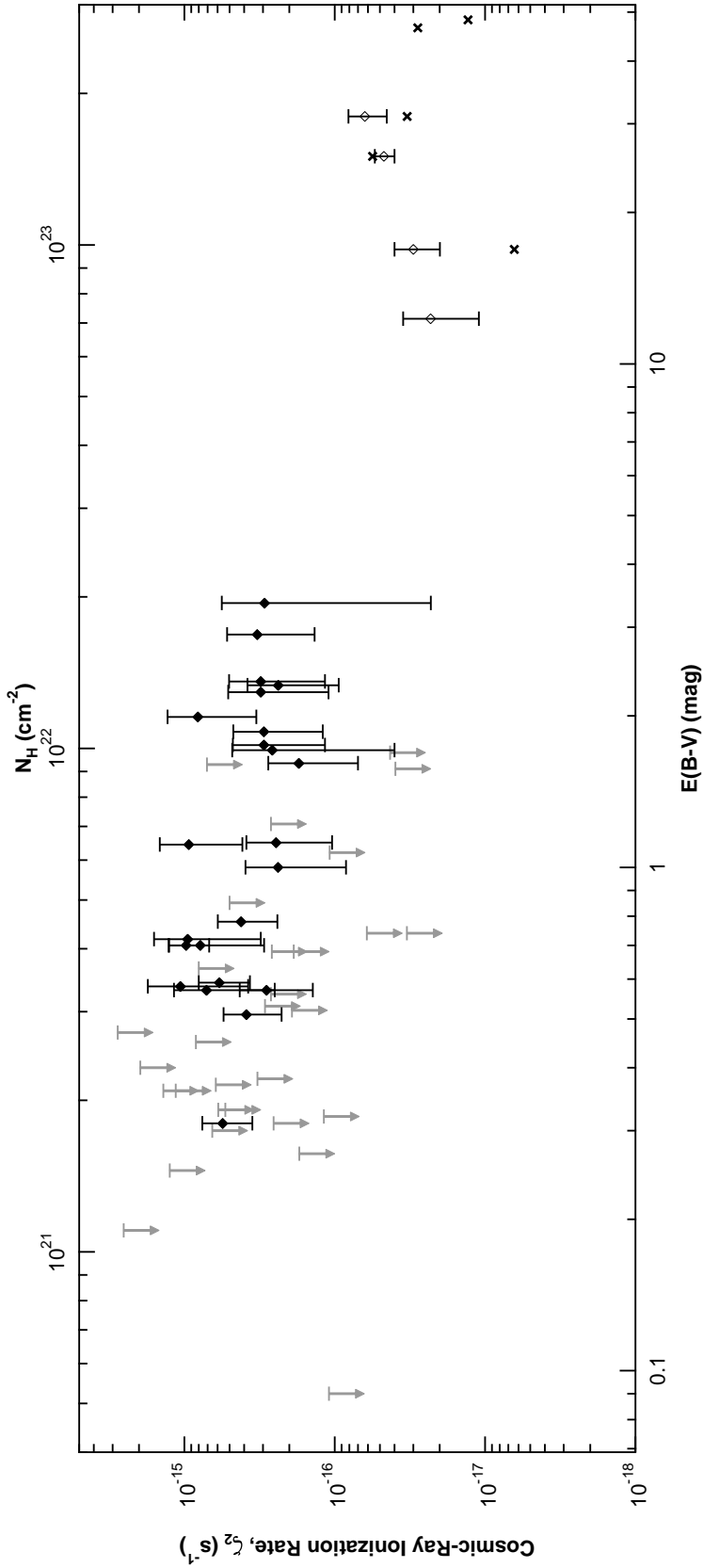
Figure 6.12: The cosmic-ray ionization rate as a function of total column density, N_H, and equivalent color excess, $E(B-V)$. Filled diamonds are cosmic-ray ionization rates with 1σ uncertainties inferred for diffuse molecular clouds in this study. Grey arrows are 3σ upper limits from this study. Open diamonds are ionization rates inferred for dense molecular clouds by Kulesa (2002). Sight lines and ionization rates inferred from H_3^+ observations for dense clouds by Kulesa (2002) include: NGC 2024 IRS 2 - $2.3 \pm 1.7 \times 10^{-17}$ s^{-1}; AFGL 490 - $3 \pm 1 \times 10^{-17}$ s^{-1}; AFGL 2591 - $4.7 \pm 0.7 \times 10^{-17}$ s^{-1}; AFGL 2136 - $6.3 \pm 1.8 \times 10^{-17}$ s^{-1}. The crosses are ionization rates inferred from H^{13}CO$^+$ observations in dense clouds by van der Tak & van Dishoeck (2000). Sight lines and ionization rates from van der Tak & van Dishoeck (2000) include: AFGL 2136 - 3.3×10^{-17} s^{-1}; AFGL 2591 - 5.6×10^{-17} s^{-1}; W33 A - 1.3×10^{-17} s^{-1}; W3 IRS 5 - 2.8×10^{-17} s^{-1}; Various models (e.g., Padovani et al., 2009) predict that ζ_2 should decrease with increased N_H as low-energy cosmic rays lose all of their energy in the outer regions of a cloud. While no strong correlation is apparent from the diffuse cloud data alone, the addition of the dense cloud ionization rates from sight lines with much higher N_H does suggest such a trend.

Chapter 7

The Implications of a High Cosmic-Ray Ionization Rate in Diffuse Interstellar Clouds

The content of this chapter was published in *ApJ* as Indriolo et al. (2009a). Work was done in collaboration with B. D. Fields (University of Illinois at Urbana-Champaign) and B. J. McCall (University of Illinois at Urbana-Champaign).

Diffuse interstellar clouds show large abundances of H_3^+ which can be maintained only by a high ionization rate of H_2. Cosmic rays are the dominant ionization mechanism in this environment, so the large ionization rate implies a high cosmic-ray flux, and a large amount of energy residing in cosmic rays. In this paper we find that the standard propagated cosmic-ray spectrum predicts an ionization rate much lower than that inferred from H_3^+. Low-energy (~ 10 MeV) cosmic rays are the most efficient at ionizing hydrogen, but cannot be directly detected; consequently, an otherwise unobservable enhancement of the low-energy cosmic-ray flux offers a plausible explanation for the H_3^+ results. Beyond ionization, cosmic rays also interact with the interstellar medium by spalling atomic nuclei and exciting atomic nuclear states. These processes produce the light elements Li, Be, and B, as well as gamma-ray lines. To test the consequences of an enhanced low-energy cosmic-ray flux, we adopt two physically-motivated cosmic-ray spectra which by construction reproduce the ionization rate inferred in diffuse clouds, and investigate the implications of these spectra on dense cloud ionization rates, light element abundances, gamma-ray fluxes, and energetics. One spectrum proposed here provides an explanation for the high ionization rate seen in diffuse clouds while still appearing to be broadly consistent with other observables, but the shape of this spectrum suggests that supernovae remnants may not be the predominant accelerators of low-energy cosmic rays.

7.1   Introduction

Several recent observations of H_3^+ in the diffuse interstellar medium indicate an average cosmic-ray ionization rate of molecular hydrogen of about 4×10^{-16} s^{-1} (McCall et al., 2003;

Indriolo et al., 2007). This value is about 1 order of magnitude larger than was previously inferred using other molecular tracers such as HD and OH (O'Donnell & Watson, 1974; Black & Dalgarno, 1977; Black et al., 1978; Hartquist et al., 1978a,b; Federman et al., 1996). However, several models have also required ionization rates on the order of 10^{-16} s^{-1} (van Dishoeck & Black, 1986; Liszt, 2003; Le Petit et al., 2004; Shaw et al., 2006, 2008) in order to reproduce the observed abundances of various atomic and molecular species. This agreement, coupled with the simplicity behind the chemistry of H_3^+, leads us to conclude that the newer measurements are most likely correct. In this paper, we explore the implications that a high ionization rate has for cosmic rays and related observables.

Aside from observational inferences, the cosmic-ray ionization rate can also be calculated theoretically using an ionization cross section and cosmic-ray energy spectrum. While the ionization cross section for hydrogen is well determined (Bethe, 1933; Inokuti, 1971), the cosmic-ray spectrum below about 1 GeV is unknown. This is because low energy cosmic rays are deflected from the inner solar system by the magnetic field coupled to the solar wind (an effect called modulation) and so the flux at these energies cannot be directly observed. This theoretical calculation of the ionization rate has been performed several times (e.g., Hayakawa et al., 1961; Spitzer & Tomasko, 1968; Nath & Biermann, 1994; Webber, 1998), with each study choosing a different low energy cosmic-ray spectrum for various reasons. Most recently, Webber (1998) predicted an ionization rate of $(3\text{--}4) \times 10^{-17}$ s^{-1} using interstellar proton, heavy nuclei, and electron cosmic-ray spectra. The proton and heavy nuclei spectra were found by attempting to remove the effects of solar modulation from *Pioneer* and *Voyager* observations, while the electron spectrum was derived from radio and low-energy gamma-ray measurements. Even having accounted for all of these components, this result falls about 1 order of magnitude short of the inference based on H_3^+, suggesting that the de-modulated solar system spectrum may not be the same as the interstellar spectrum in diffuse clouds, and/or that the Webber (1998) extrapolation to low energies underestimates the true interstellar value.

Together, all of the above studies have shown that the ionization of interstellar hydrogen is a powerful observable for probing cosmic-ray interactions with the environments through which they propagate. Beyond ionization though, cosmic rays will interact with the ISM in other ways which lead to additional and complementary observables. Namely, inelastic collisions between cosmic-rays and interstellar nuclei inevitably: (i) create light element isotopes ^{6}Li, ^{7}Li, ^{9}Be, ^{10}B, and ^{11}B when cosmic rays spall C, N, and O nuclei (Reeves, 1970; Meneguzzi et al., 1971), and (ii) excite nuclear states such as ^{12}C* and ^{16}O*, the decay of which produce gamma-ray lines, most prominently at 4.44 MeV and 6.13 MeV, respectively (Meneguzzi & Reeves, 1975b). Similar to the theoretical calculation of the ionization rate,
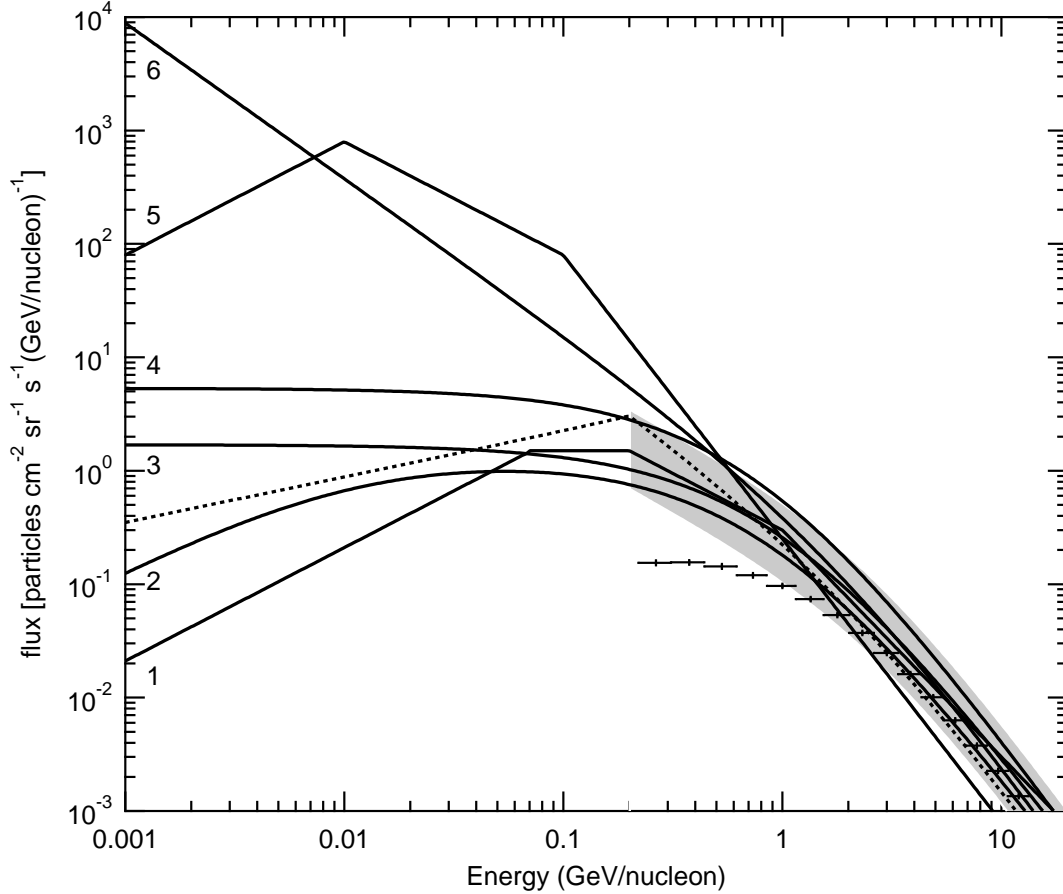
Figure 7.1: Example cosmic-ray spectra used in the literature over the past few decades. 1 - Herbst & Cuppen (2006); 2 - Spitzer & Tomasko (1968); 3 - Gloeckler & Jokipii (1969) (via fitting function of Kneller et al. (2003)); 4 - Ip & Axford (1985) (via fitting function of Valle et al. (2002)); 5 - Hayakawa et al. (1961); 6 - Nath & Biermann (1994). The dotted line is the propagated leaky box spectrum used in this paper, also shown in Figure 7.2. Note the agreement above and discrepancy below 1 GeV. These spectra were selected to be illustrative of choices in the literature used for different applications. Of these, it is worth noting that the Ip & Axford (1985) spectrum is the result of a calculation specifically designed to recover the (demodulated) propagated interstellar cosmic-ray spectrum. The shaded region shows the range of uncertainty in the demodulated proton spectrum as described by Mori (1997). Crosses are proton data from the top of the Earth's atmosphere (AMS Collaboration et al., 2002) and clearly show the effects of modulation below ~ 1 GeV.

a cosmic-ray spectrum and relevant cross sections can be used to determine the production rates of light elements and gamma-ray lines. Both the light element (e.g., Meneguzzi et al., 1971; Meneguzzi & Reeves, 1975a; Walker et al., 1985; Steigman & Walker, 1992; Prantzos et al., 1993; Vangioni-Flam et al., 1996; Valle et al., 2002; Kneller et al., 2003) and gamma-ray (e.g., Meneguzzi & Reeves, 1975b; Ramaty et al., 1979; Cassé et al., 1995; Fields et al., 1996; Tatischeff & Kiener, 2004) calculations have been performed multiple times, again with each study choosing a different low energy cosmic-ray spectrum.

Some of the spectra that have been used for these calculations are shown in Figure 7.1. While several more cosmic-ray spectra have been used, many share functional forms with those plotted and so have been omitted for the sake of clarity. Note that all of the spectra agree with demodulated data (shaded region) above a few hundred MeV and raw data (crosses) above a few GeV, but that they can differ by about 4 orders of magnitude at 1 MeV. Figure 7.1 is shown primarily to illustrate our poor understanding of the low-energy portion of the cosmic-ray spectrum.

In this study, we calculate the cosmic-ray ionization rate using several low energy cosmic-ray spectra in an attempt to reproduce the value inferred from H_3^+ observations. For the spectra that successfully predict ionization rates close to the inferred value of 4×10^{-16} s^{-1}, we further investigate the implications that they have on dense cloud ionization rates, light element abundances, gamma-ray fluxes, and energetics arguments.

7.2 The Ionization Rate Inferred From H_3^+

The chemistry behind H_3^+ in the diffuse ISM is rather simple. Its formation and destruction are given by the reactions:

$$CR + H_2 \rightarrow CR + H_2^+ + e^-, \tag{7.1}$$

$$H_2 + H_2^+ \rightarrow H_3^+ + H, \tag{7.2}$$

$$H_3^+ + e^- \rightarrow H_2 + H \text{ or } H + H + H. \tag{7.3}$$
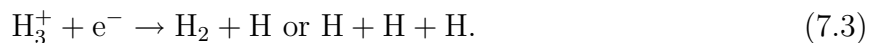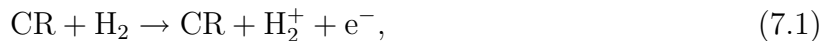
H_2 is first ionized, after which the H_2^+ ion quickly reacts with another H_2 molecule to form H_3^+. In diffuse (and dense) clouds it is assumed that this ionization is due almost entirely to cosmic rays, as the flux of photons with $E > 13.6$ eV will be quickly attenuated by atomic hydrogen in the outer regions of the cloud. The first step is many orders of magnitude slower, so it acts as the overall rate limiting step. The primary channel for destroying H_3^+ in diffuse clouds is recombination with an electron. H_3^+ is destroyed by reaction (7.3) on a time scale of about 100 years, much shorter than the $\sim 10^6$ yr lifetime of diffuse clouds

(Wagenblast & Hartquist, 1988), so the steady-state approximation is valid and the formation and destruction rates can be equated. This assumption yields (Geballe et al., 1999)

$$\zeta_2 n(\mathrm{H}_2) = k_e n(\mathrm{H}_3^+) n(e), \tag{7.4}$$

where ζ_2 is the ionization rate of H_2, k_e is the H_3^+-electron recombination rate constant, and $n(\mathrm{X})$'s are number densities. Spectroscopic observations of transitions from the two lowest rotational levels of H_3^+, the only levels populated at the low temperatures of diffuse interstellar clouds, provide the H_3^+ column density. The cloud path length is then found using the observed hydrogen column density and inferred hydrogen number density. Dividing the H_3^+ column by the path length gives $n(\mathrm{H}_3^+)$, and leaves three variables in the steady state equation: k_e, ζ_2, and $n(e)/n(\mathrm{H}_2)$. However, previous work has shown that the H_3^+-electron recombination rate (McCall et al., 2003, 2004) and the electron-to-hydrogen ratio (Cardelli et al., 1996) are relatively well constrained, leaving ζ_2 as the only free parameter. Starting from eq. (7.4) and using various other relationships and assumptions, Indriolo et al. (2007) derived an equation for the cosmic-ray ionization rate that depends on observables. This equation was then used to infer the ionization rate toward several diffuse cloud sight lines. From all of the sight lines with H_3^+ detections, the average cosmic-ray ionization rate of molecular hydrogen was found to be about 4×10^{-16} s^{-1} with a maximum uncertainty of about a factor of three either way (see Section 4.2 of Indriolo et al. (2007) for a discussion of the calculations and uncertainties).

7.3   Ionization Energetics: A Model-Independent Lower Bound

Assuming that the ionization rate above is uniform throughout the diffuse Galactic ISM, it is relatively simple to estimate the total, Galaxy-wide amount of power necessary to produce such a high value. While this assumption of uniformity is not strictly valid (there are diffuse clouds with $\zeta_2 \lesssim 10^{-16}$ s^{-1} and clouds in the Galactic center with $\zeta_2 \gtrsim 10^{-15}$ s^{-1} (Oka et al., 2005; Yusef-Zadeh et al., 2007; Goto et al., 2008)), the small sample size of sight lines does not allow for the determination of a meaningful relationship between position and ionization rate. Despite these fluctuations, if all atomic hydrogen experiences the same ionization rate *on average*, then the Galactic luminosity in ionizing cosmic rays, $L_{\mathrm{CR,ionize}}$, is given by

$$L_{\mathrm{CR,ionize}} = \zeta_{\mathrm{H}} \, \overline{\Delta E} \left(\frac{M_{\mathrm{H,diffuse}}}{m_{\mathrm{H}}} \right), \tag{7.5}$$

where $\overline{\Delta E}$ is the average energy lost by cosmic rays per ionization event. The number of hydrogen atoms in diffuse clouds is the ratio of the mass of all atomic hydrogen in diffuse clouds in the Galaxy, M_{H}, to the mass of a hydrogen atom, m_{H}. The ionization rate of *atomic* hydrogen, ζ_{H}, is related to the ionization rate of *molecular* hydrogen (the observable probed by H_3^+) by $2.3\zeta_{\mathrm{H}} = 1.5\zeta_2$ (Glassgold & Langer, 1974). The coefficients here are further explained in Section 7.5.

Given the ionization rates from the previous section, we may place a *model-independent lower limit* on the ionizing cosmic-ray luminosity as follows. Each ionization event requires a cosmic-ray energy input $\overline{\Delta E} > 13.6$ eV, the ionization potential of atomic hydrogen. On average cosmic rays will lose more than 13.6 eV in the ionization process though, so by setting $\overline{\Delta E} = 13.6$ eV in eq. (7.5) we calculate a hard lower limit on the power requirement. The gas mass relevant to eq. (7.5) is that of all neutral hydrogen in Galactic diffuse clouds, which we take to be $M_{\mathrm{H,diffuse}} = 5 \times 10^9 M_\odot$ (the average of Henderson et al. (1982), Sodroski et al. (1994), and Misiriotis et al. (2006)). This value results in a lower limit to the cosmic-ray luminosity of

$$L_{\mathrm{CR,ionize}} > 0.11 \times 10^{51} \text{ erg } (100 \text{ yr})^{-1} \left(\frac{M_{\mathrm{H,diffuse}}}{5 \times 10^9 M_\odot} \right). \tag{7.6}$$

Note that this cosmic-ray "energy demand" is in addition to the requirements found based on cosmic-ray energy lost as the particles escape the Galaxy. Fields et al. (2001) estimated the sum of both contributions, and found $L_{\mathrm{CR,tot}} \simeq 0.5 \times 10^{51}$ erg $(100 \text{ yr})^{-1}$ which is consistent with eq. (7.6) but also implies that ionization represents a significant part of the cosmic-ray energy budget.

However, eq. (7.6) is only the lower limit to the amount of cosmic-ray energy that goes into ionization. We can get an actual estimate on the luminosity of ionizing cosmic rays by accounting for molecular hydrogen and by using a more precise value of $\overline{\Delta E}$. According to Cravens & Dalgarno (1978) the average energy lost during an ionization event is about 30 eV, which by itself increases $L_{\mathrm{CR,ionize}}$ to 0.24×10^{51} erg $(100 \text{ yr})^{-1}$. The inclusion of H_2 is more complicated. The mass of H_2 is about the same as that of H in the Galaxy, but most H_2 resides in dense molecular clouds (Brinks, 1990) which do not experience the same cosmic-ray ionization rate as the diffuse ISM (Dalgarno, 2006). Assuming half of all Galactic H_2 experiences the ionization rate used above, $L_{\mathrm{CR,ionize}} \approx 0.33 \times 10^{51}$ erg $(100 \text{ yr})^{-1}$, a large fraction of the result found by Fields et al. (2001).

As it is currently believed that Galactic cosmic rays are accelerated in supernova remnants (SNR), these results have implications for the efficiency with which supernova mechanical energy is transferred to particle acceleration. If a typical supernova releases 10^{51} erg of mechanical energy (e.g., Arnett, 1987; Woosley, 1988) and 3 ± 2 supernovae (SNe) occur

each century in the Galaxy (van den Bergh & Tammann, 1991; Dragicevich et al., 1999), then at least 4% of the energy released in SNe must accelerate the cosmic rays which ionize hydrogen in the ISM. This efficiency climbs to 12% if we take the more realistic estimate instead of the lower limit. However, uncertainties in the supernova rate, supernova energy, and mass of hydrogen in the Galaxy lead to a total uncertainty of about a factor of 5 either way for this value. It is important to note though that this calculation depends only on the cosmic-ray ionization rate, and not on an adopted form of the cosmic-ray spectrum. In contrast, calculating the ionization rate is highly dependent on the cosmic-ray spectrum, to which we now turn.

7.4   Possible Spectra of Low-Energy Cosmic-Rays

Given the well-understood physics of the passage of energetic particles through matter, the ionization rate completely reflects the spectrum of cosmic rays. In particular, the ionization cross section (below, eq. 7.12) grows towards low energies as $\sigma_{\text{ion}} \sim v^{-2} \sim E^{-1}$ which means that the lowest-energy particles have the strongest effect on ionization. Given our lack of direct observational constraints on cosmic rays at low energies, we will examine the ionization arising from various possible low-energy behaviors which are physically motivated and/or have been suggested in the literature. Here we summarize in a somewhat pedagogical way some of the main features of the current understanding of cosmic-ray acceleration and propagation.

The cosmic-ray spectrum with the strongest physical motivation (in our view) takes supernova explosions to be the engines of Galactic cosmic-ray acceleration. That is, supernovae remnants provide the sites for diffusive shock acceleration and thus act as cosmic-ray sources. At these sources, diffusive shock acceleration creates particles with spectra which are close to simple power-laws in (relativistic) momentum p. Specifically, consider the "test-particle" limit when particle acceleration has a negligible effect on the shock energy and structure. In this limit, the cosmic-ray production rate, q, per unit volume and time and per unit interval in relativistic momentum has famously been analytically shown to be (e.g., Krymskii, 1977; Bell, 1978; Blandford & Ostriker, 1978)

$$q_{\text{shock accel}} = \frac{d\mathcal{N}_{\text{accel}}}{dV \, dt \, dp} \ \propto \ p^{-\chi}, \tag{7.7}$$

i.e., a power-law in momentum. Here the momentum index in the case of strong shocks is $\chi = 2 + 4/\mathcal{M}^2$, where the shock Mach number is $\mathcal{M} = v_{\text{shock}}/c_{\text{sound,ism}} \gg 1$. The upshot is that for strong shocks (large $\mathcal{M}$) as one would find in supernova remnants, the acceleration

power law is just slightly steeper than the flattest (i.e., largest at high-energy) limiting power-law spectrum allowed by energy conservation: $q_{\mathrm{lim}} \propto p^{-2}$. Going beyond the test-particle limit requires nonlinear treatment of the feedback of cosmic ray energy and pressure on the shock structure and evolution; the study of this nonlinear shock acceleration remains a vital field, but several groups (e.g., Kang & Jones, 1995; Berezhko & Ellison, 1999; Blasi, 2002) find that the accelerated particles have a spectrum which is roughly similar to the test-particle result, but which shows some concavity in momentum space, i.e., the effective spectral index $\chi = d \ln q / d \ln p$ does show a modulation around the constant test-particle value. Intriguingly, there seems to be agreement on the qualitative result that the low-energy flux will be higher than for the test-particle predictions. Unfortunately, the quantitative results remain at present rather model-dependent. For the purposes of our analysis, we will simply adopt test-particle power-law acceleration spectra as in eq. (7.7). Our results can then be viewed as testing the validity of the test-particle approximation at low energies.

Once produced at acceleration sites, cosmic rays propagate away, and eventually are removed either by escape from the Galaxy or by stopping in the ISM due to energy losses (predominantly by energy transfer to the ISM, either ionization or excitation of atoms or molecules). Propagation alters the spectra of cosmic rays from those at the sources. Theoretical treatments of these effects typically make the simplifying assumption of a steady state balance between production and losses. The resulting "propagated" spectrum should represent the flux as seen by an average region of the interstellar medium, far from cosmic-ray sources (elegantly reviewed in Strong et al., 2007).

A full calculation of cosmic-ray propagation at minimum involves the particle "flows" in energy space; the simplest such treatment is the classic "leaky-box" model which treats the Galaxy as a medium with sources distributed homogeneously. More sophisticated models account for the inhomogeneous Galaxy and effects such as diffusion and re-acceleration. In general, when models include the low-energy regime (e.g., Lerche & Schlickeiser, 1982; Shibata et al., 2006), they find that when initially accelerated or "injected" spectra are power-laws in momentum, the resulting propagated spectra are very nearly also power laws, with fairly abrupt changes of spectral indices at characteristic energy scales ("breaks") at which one loss mechanism comes to dominate over another. To fix notation, for our purposes cosmic rays are most usefully characterized by the propagated cosmic-ray flux (strictly speaking, specific intensity) $\phi(E) = d\mathcal{N}_{\mathrm{cr}} / dA \, dt \, d\Omega \, dE$ per unit energy interval. For all but the most ultra-high energies, cosmic rays are observed to be isotropic, in which case the flux is related to the cosmic-ray number density n via $4\pi\phi(E) = v \, dn/dE$. Here E is the cosmic-ray kinetic energy; the total relativistic energy is thus $E_{\mathrm{tot}} = E + mc^2$. Relativistic energy and momentum are related by $E_{\mathrm{tot}}^2 = (cp)^2 + (m_p c^2)^2$, and $v/c = cp/E_{\mathrm{tot}}$. Using these, it follows

86

that the flux per unit energy is equal to the particle number density per unit momentum: $4\pi\phi(E) = dn/dp$. Hence, a number spectrum dn/dp that is a power law in p gives a flux with the same power-law of $p(E)$.

As a result, we characterize possible propagated proton spectra with a piecewise power law in relativistic momentum $p(E)$:

$$\phi_p(E) = \begin{cases} \phi_p(E_1) \left(\frac{p(E)}{p(E_1)}\right)^{\gamma_{\text{high}}}, & \text{if } E > E_2 \\[2em] \phi_p(E_1) \left(\frac{p(E_2)}{p(E_1)}\right)^{\gamma_{\text{high}}} \left(\frac{p(E)}{p(E_2)}\right)^{\gamma_{\text{low}}}, & \text{if } E_{\text{cut}} \leq E \leq E_2 \\[2em] 0, & \text{if } E < E_{\text{cut}} \end{cases} \quad . \tag{7.8}$$

Here $E_1 = 1$ GeV is the arbitrary energy at which the flux is normalized to fit observations; following Mori (1997) we take $\phi_p(E_1) = 0.22$ cm^{-2} s^{-1} sr^{-1} GeV^{-1}. This and the observed (high-energy) spectral index $\gamma_{\text{high}} \approx -2.7$ fixes the high-energy region of the spectrum.

The low-energy portion of the spectrum is crucial for this paper, and we take the high/low energy break to be $E_2 = 0.2$ GeV, which is roughly where ionization losses begin to dominate diffusion and/or escape losses. The power law index for energies below E_2 is γ_{low}, and eq. (7.8) is arranged to guarantee that the flux is continuous across this break. Finally, an effective low energy cutoff, E_{cut}, is chosen, below which the flux is zero. Despite the fact that the flux will change as cosmic rays travel into a cloud, we assume a steady state such that the spectrum is the same everywhere. We also neglect the possible effects of self-confinement proposed by Padoan & Scalo (2005), in which magnetohydrodynamics can spatially confine cosmic rays to given regions due to changes in the ambient density.

In the case of the propagated spectrum, the momentum index $\gamma_{\text{low}} = 3 + \gamma_{\text{source}} = 0.8$, which corresponds to a source spectrum with $q(p) \propto p^{-2.2}$ and propagation dominated by energy losses (the "thick-target" approximation). This spectrum is shown as the dotted curve in both Figures 7.1 & 7.2. The two vertical dashed lines in Figure 7.2 represent low energy cutoffs at 2 MeV and 10 MeV. These were chosen because cosmic rays with these energies have ranges roughly corresponding to the column densities of diffuse and dense clouds, respectively (Cravens & Dalgarno, 1978). Following this reasoning, cosmic rays with $E < 2$ MeV should not penetrate diffuse clouds, and so will not contribute to the ionization rate there. Likewise, cosmic rays with energies below 10 MeV will not affect the ionization rate in dense clouds.

Another spectrum we consider is modeled after Meneguzzi et al. (1971) and Meneguzzi & Reeves (1975a,b) who added a second sharply-peaked component – dubbed a "carrot"
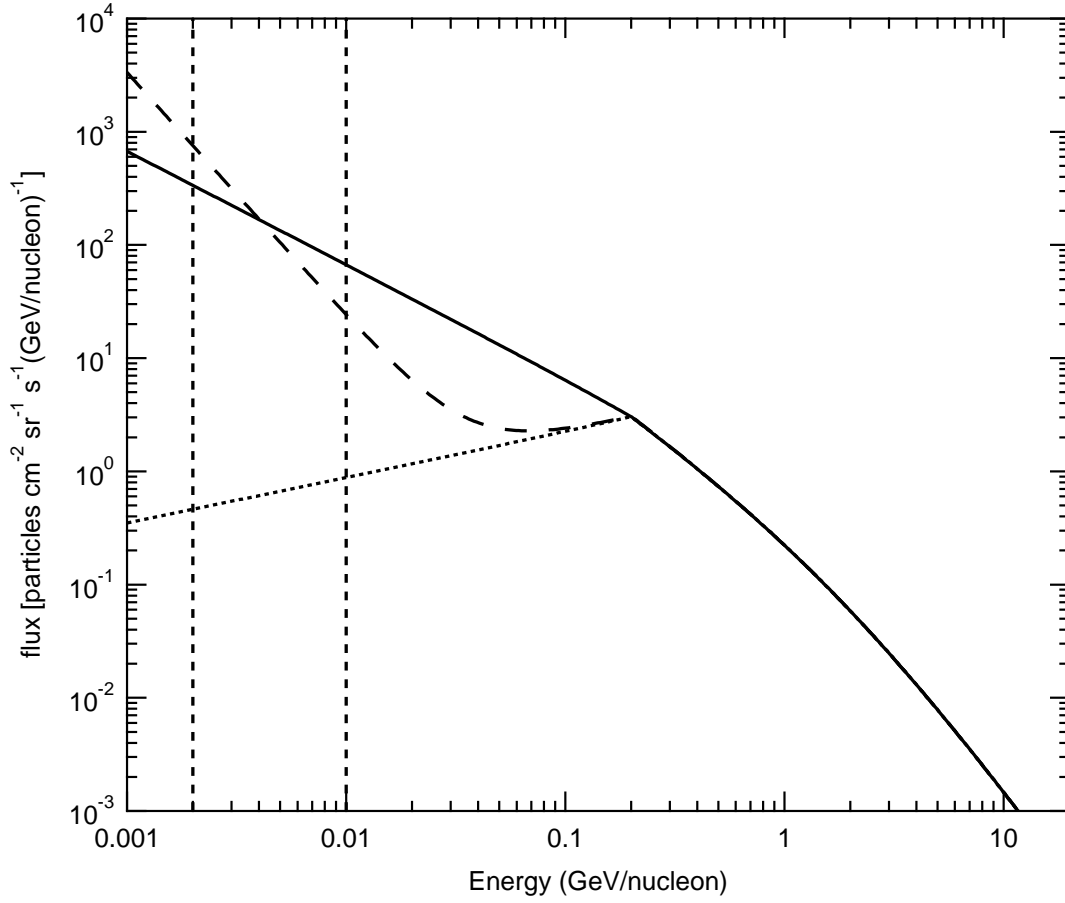
Figure 7.2: Cosmic-ray spectra used in Indriolo et al. (2009a): dotted curve is the leaky box propagated spectrum ($\gamma_{\mathrm{low}} = 0.8$); solid curve is the broken power law spectrum with $\gamma_{\mathrm{low}} = -2.0$; dashed curve is the carrot spectrum with $\alpha = -4.3$, $f = 0.01$; above 0.2 GeV all three spectra are identical; vertical dashed lines represent 2 MeV and 10 MeV low energy cutoffs.

– to the propagated spectrum to give a high flux at energies of a few MeV. The physical reasoning behind such a component is that in addition to the propagated spectrum, there is some local source of cosmic rays formed in weak shocks, represented by a steeper power law. This component is given by

$$\phi_p(E) = f\phi_p(E_1) \left(\frac{p(E_2)}{p(E_1)}\right)^{\gamma_{\text{high}}} \left(\frac{p(E)}{p(E_2)}\right)^{\alpha},\tag{7.9}$$

where f sets the flux of the carrot component to be some fraction of the propagated spectrum at E_2, and the total cosmic-ray spectrum is taken to be the sum of the propagated and carrot components. To ensure that the carrot does not conflict with observations at high energies, f should be relatively small ($\lesssim 0.1$) and α must be less than γ_{high}.

In addition to the cosmic-ray spectra proposed above, we also consider several which have been used in the past for similar calculations (see Section 7.1 and Figure 7.1). Determining the ionization rate produced by these spectra allowed us to check that our numerical integration code was working properly, and to see exactly what energy range of cosmic rays is responsible for the high ionization rate inferred from H_3^+.

7.5 Ionization Energetics: Theoretical Estimates

Given a cosmic-ray spectrum and relevant ionization cross section, the cosmic-ray ionization rate is readily calculable. Namely, the ionization rate of species X due to cosmic rays is given by:

$$\zeta_{\text{x}} = 4\pi\xi_{\text{x}}(1 + G_{7.10}) \int_{E_{\text{low}}}^{E_{\text{high}}} \phi_p(E)\sigma_{\text{ion}}(E)\ dE,\tag{7.10}$$

where $\phi_p(E)$ is the flux of cosmic-ray protons as a function of kinetic energy, $\sigma_{\text{ion}}(E)$ is the ionization cross section of atomic hydrogen as a function of kinetic energy, $G_{7.10}$ is a coefficient accounting for ionization by heavier cosmic ray nuclei, and ξ_{x} converts between the primary ionization rate of atomic hydrogen (ζ_p), computed by the integral, and the total ionization rate for a given species X. This conversion factor includes ionization due to secondary electrons produced in the initial event, and accounts for the difference in the ionization cross section between H and X ($\zeta_{\text{x}} = \xi_{\text{x}}\zeta_p$). The coefficients for atomic (ξ_{H}) and molecular (ξ_2) hydrogen are 1.5 and 2.3, respectively (Glassgold & Langer, 1974). For the ionization rate calculation $G_{7.10} = 0.5$ (The coefficient G_n changes based on context, and is labeled with a subscript indicating which equation it applies to, e.g. $n = 7.10$ in this case. See Section 7.9 for a more detailed discussion). The Bethe (1933) cross section for primary

ionization of atomic hydrogen

$$\sigma_{\rm ion} = 2\pi(0.285)\frac{e^4}{m_ec^2{\rm Ry}}\frac{Z^2}{\beta^2}\left[\ln\frac{2m_ec^2\beta^2}{0.048(1-\beta^2){\rm Ry}}-\beta^2\right] \tag{7.11}$$

$$= 1.23\times10^{-20}\frac{Z^2}{\beta^2}\left(6.2+\log_{10}\frac{\beta^2}{1-\beta^2}-0.43\beta^2\right)\ {\rm cm}^2, \tag{7.12}$$

is used, where $\beta = v/c$ is the velocity of the cosmic ray in units of the speed of light, ${\rm Ry} = 13.6$ eV is the hydrogen binding energy, and Z is the cosmic-ray charge. Because the ionization cross section is well determined, variation of the cosmic-ray spectrum must be used to match the ionization rate inferred from observations.

Performing a numerical integration[1] of eq. (7.10) using the cross section from eq. (7.12) and the propagated spectrum ($\gamma_{\rm low} = 0.8$) form of eq. (7.8) with $E_{\rm cut} = 2$ MeV produces a cosmic-ray ionization rate of $\zeta_2 = 1.4\times10^{-17}$ s^{-1}, about 30 times smaller than the value inferred from H$_3^+$. This large discrepancy shows that a simple cosmic-ray spectrum based on the propagation of the source spectrum resulting from strong shocks is inconsistent with the ionization rate inferred from H$_3^+$. To reproduce the observational results then, we maintained the well-constrained high energy behavior of the cosmic-ray spectrum, but varied $\gamma_{\rm low}$ despite the fact that this removes the initial physical motivation for the low-energy portion of the spectrum. After several trials, we found that with $E_{\rm cut} = 2$ MeV and $\gamma_{\rm low} = -2.0$ (shown as the solid curve in Figure 7.2), the above calculation gives an ionization rate of $\zeta_2 = 3.6\times10^{-16}$ s^{-1}. However, when $E_{\rm cut} = 10$ MeV is used to account for dense clouds, the calculated ionization rate is $\zeta_2 = 8.6\times10^{-17}$ s^{-1}, a bit larger than inferred values (Williams et al., 1998; McCall et al., 1999; van der Tak & van Dishoeck, 2000).

We next attempted to reproduce the inferred ionization rate by using several cosmic-ray spectra in the literature. These include spectra previously used to calculate light element abundances (Valle et al., 2002; Kneller et al., 2003), desorption from interstellar ices (Herbst & Cuppen, 2006), and the ionization rate[2] (Hayakawa et al., 1961; Spitzer & Tomasko, 1968; Nath & Biermann, 1994). The results of our calculations using these spectra are shown in Table 7.1, along with the results from the 3 spectra proposed in this paper. It is interesting that none of the previous spectra are capable of reproducing the ionization rate in diffuse clouds to within even the correct order of magnitude, thus highlighting the need for the present study.

---

[1]Integration was performed using the `qromb`, `trapzd`, and `polint` routines of Numerical Recipes in FORTRAN (Press et al., 1992).

[2]In these cases we use the same coefficients and low-energy cutoffs as for our proposed spectra, so our results differ slightly from those of the original respective papers.

Table 7.1: Cosmic-Ray Ionization Rates (10^{-17} s^{-1})

Spectrum	ζ_2 $E_{\mathrm{cut}} = 2$ MeV (diffuse)	ζ_2 $E_{\mathrm{cut}} = 10$ MeV (dense)
Propagated[a]	1.4	1.3
Broken Power Law[a]	36	8.6
Carrot[a]	37	2.6
Hayakawa et al. (1961)	165	96
Spitzer & Tomasko (1968)	0.7	0.7
Nath & Biermann (1994)	260	34
Kneller et al. (2003)	1.3	1.0
Ip & Axford (1985)[b]	3.6	2.7
Herbst & Cuppen (2006)	0.9	0.9
Observational Inferences	~ 40[c]	~ 3[c]

Notes: Ionization rates calculated are for molecular hydrogen due to a spectrum of cosmic-ray protons and heavier nuclei with abundances greater than 10^{-5} with respect to hydrogen. Factors such as the 5/3 and 1.89 used by Spitzer & Tomasko (1968) have been removed to calculate the primary ionization rate due to protons, which is then multiplied by 1.5 to account for the heavy nuclei $(1 + G_{7.10})$, and 2.3 (Glassgold & Langer, 1974) to find the H$_2$ ionization rate.

References: (a) this study; (b) via fitting function of Valle et al. (2002); (c) Indriolo et al. (2007): H$_3^+$; (d) van der Tak & van Dishoeck (2000): H^{13}CO$^+$.

To match the ionization rate in both diffuse and dense clouds, we then turned to the carrot spectrum, which, as mentioned above, must rise faster than $\phi_p \propto p^{-2.7}$ to low energies. Choosing $f = 0.01$ and $\alpha = -4.3$ (these values optimize the ionization and light element results as discussed in Section 7.6.1), and using $E_{\mathrm{cut}} = 2$ MeV generates an ionization rate of 3.7×10^{-16} s^{-1}. The carrot spectrum with these parameters is shown in Figure 7.2 as the dashed curve. Changing the low energy cutoff to 10 MeV to simulate a dense cloud environment predicts $\zeta_2 = 2.6 \times 10^{-17}$ s^{-1}, also in accord with observations. This demonstrates that the steeper slope of the carrot component is better able to reproduce the roughly 1 order of magnitude difference in the ionization rate between diffuse and dense

clouds. It is also interesting to note that the large majority of ionizing cosmic rays have kinetic energies between 2 and 10 MeV: $\sim 95\%$ in the case of the carrot spectrum and $\sim 80\%$ for the broken power law.

7.6 Other Observable Signatures of Low-Energy Cosmic-Ray Interactions

As stated in Section 7.1, cosmic rays produce light elements and gamma rays via spallation and the excitation of nuclear states, respectively. Like the ionization rate, the production rates of these processes can be computed using eq. (7.10). In these cases, σ_{ion} is replaced with the relevant cross section for each process, $\xi_{\mathrm{x}} = 1$, and $G_{7.10} = 0$.

7.6.1 Light Elements

To calculate the total production rates of the light element species ^{6}Li, ^{7}Li, ^{9}Be, ^{10}B, and ^{11}B (often collectively referred to as LiBeB), 32 reactions were considered. These include the spallation (fragmentation) reactions $[p, \alpha] + [\mathrm{C}, \mathrm{N}, \mathrm{O}] \rightarrow [\mathrm{LiBeB}] + \cdots$, which make all of the LiBeB nuclides, as well as the fusion reaction $\alpha + \alpha \rightarrow {}^{6,7}\mathrm{Li} + \ldots$, which can only make the lithium isotopes. Tabulated cross sections were taken from Read & Viola (1984), and for energies above ~ 50 MeV nucleon^{-1} the $\alpha + \alpha$ processes were supplemented with data from Mercer et al. (2001). In the case of all α particle processes, the fluxes of the cosmic-ray spectra were reduced to 9.7% of the fluxes used in the ionization calculations because of the relative solar abundance between helium and hydrogen (Anders & Grevesse, 1989). Using these cross sections and the spectra from Section 7.5, we calculated the present-day instantaneous production rate of each species from each process.

Of course, the observed light element abundances are the result of cosmic-ray interactions with the ISM throughout the history of the Galaxy, meaning that they are dependent on the cosmic-ray history and chemical evolution of the Galaxy. A full calculation of these effects and a comparison with LiBeB abundance evolution as traced by Galactic stars is a worthy subject of future work, but is beyond the scope of this paper. To estimate the accumulated LiBeB abundances, we follow the original approach of Reeves (1970) to roughly quantify the *solar* LiBeB abundances expected from spallation processes with our trial spectra. Our estimate assumes that both the cosmic-ray spectrum and CNO abundances have remained constant throughout the history of the Galaxy. Also, we assume that once created, the light element isotopes are not destroyed. As we know that light elements are destroyed

("astrated") in stellar interiors, this assumption leads to further uncertainty in our model. In addition to cosmic-ray spallation, ^{7}Li and ^{11}B are produced by other mechanisms: neutrino spallation processes in Type II SNe for both isotopes (Dearborn et al., 1989; Woosley et al., 1990), and also primordial nucleosynthesis in the case of ^{7}Li. Both of these mechanisms will contribute to the observed abundances, but we have chosen to omit their effects with the understanding that our ^{7}Li and ^{11}B abundances should be lower than the net Galactic levels. These effects both add to and subtract from our estimate based on a constant production rate. Based on more detailed models which include these effects (Fields & Olive, 1999; Fields et al., 2000; Prodanović & Fields, 2006) we expect our calculations of the *absolute* abundances to be accurate only to within factors of 2–3. Our results appear in Table 7.2, along with solar-system light element abundances as measured from meteorites and the solar photosphere.

As seen in Table 7.2, the conventional propagated spectrum reproduces each of the ^{6}Li, ^{9}Be, and ^{10}B abundances and their ratios well, to within 10-30%, while severely underproducing ^{7}Li and ^{11}B. This well-known pattern is characteristic of cosmic-ray nucleosynthesis predictions (e.g., Fields et al., 2001; Vangioni-Flam et al., 2000, and references therein) and follows our expectations given the omission of non-cosmic-ray ^{7}Li and ^{11}B processes mentioned above. However, as we have shown, this spectrum leads to an ionization rate which falls far short of that required by H_3^+ data.

Table 7.2: Light Element Abundances

Ratio	Solar System	Carrot	Broken Power Law	Propagated
$10^{10} \times {}^6$Li/H	1.5	2.5	8.2	1.3
$10^{10} \times {}^7$Li/H	19	5.8	18	1.9
$10^{10} \times {}^9$Be/H	0.26	0.35	0.59	0.33
$10^{10} \times {}^{10}$B/H	1.5	1.4	2.5	1.3
$10^{10} \times {}^{11}$B/H	6.1	3.2	6.4	2.8
^{6}Li/^{9}Be	5.8	7.1	13.9	4.0
^{10}B/^{9}Be	5.8	4.0	4.3	3.9

Notes: For all three spectra calculations were done using $E_{\text{cut}} = 2$ MeV. Calculated values were found by integrating the instantaneous rates over 10 Gyr. Solar System abundances are from Anders & Grevesse (1989).

Turning to the spectra with low-energy enhancements and associated high ionization rates, the LiBeB production presents a mixed picture. Here, we focus on the species with only cosmic-ray sources: ^{6}Li, ^{9}Be, and ^{10}B. In Table 7.2 we see that the carrot spectrum reproduces ^{10}B quite well, and overproduces ^{6}Li and ^{9}Be by factors of 1.7 and 1.3, respectively, still well within the uncertainties of our rough calculation. For the broken power law spectrum, however, all of these absolute abundances exceed observations by factors of about 2-5.

It is quite striking that there is only a factor of a few difference between the LiBeB abundances predicted by the propagated and carrot/broken power law spectra compared to the factor of about 30 difference for the ionization rate. This is due to two properties of the LiBeB production cross sections. First, most of the cross sections have low-energy thresholds in the tens of MeV, meaning that the high flux in the few MeV range has no effect on LiBeB production. Second, the cross sections do not fall off steeply as energy increases, so the cosmic-ray flux in the hundreds of MeV range (where all three spectra are identical) is important. This contrasts with the case of ionization where cosmic rays with the lowest energies above the cutoff dominate.

However, much more significant than the absolute abundances are the *ratios* of these isotopes, which effectively remove the systematic uncertainties in the absolute abundances introduced by the simplicity of our model and directly reflect the shape of the cosmic-ray spectrum. While both of the low-energy-enhanced spectra underestimate the ^{10}B/^{9}Be ratio by about a factor of 1.5, the carrot spectrum does a much better job of reproducing the ^{6}Li/^{9}Be ratio; it overestimates the ratio by a factor of only ~ 1.2 compared to the broken power law's 2.4.

This success of the carrot spectrum is not surprising though, as we chose the input parameters to best reproduce the observed ionization rates and light element ratios. These "optimal" parameters were found by using various combinations of f and α to compute the ionization rate with a 2 and 10 MeV cutoff, and the ^{6}Li/^{9}Be and ^{10}B/^{9}Be ratios. Figure 7.3 is a plot in (f, α) space where the contours represent deviations of 10% and 25% from inferred values of ζ_2 in diffuse and dense clouds, and from measured meteoritic LiBeB ratios. It is clear from Figure 7.3 that there is an overlapping region around $f \sim 0.01$ and $\alpha \sim -4.5$ where ζ_2 for diffuse and dense clouds and ^{6}Li/^{9}Be are all within 25% of observed values. In making the diffuse cloud ionization rate as close to 4×10^{-16} s^{-1} as possible, we chose $f = 0.01$ and $\alpha = -4.3$ (indicated by the triangle in Figure 7.3) as the parameters for the carrot spectrum.

While ζ_2 and ^{6}Li/^{9}Be can be matched well, no combination of f and α is able to successfully reproduce the ^{10}B/^{9}Be ratio to within 25% simultaneously with any of the other observables. Almost the entire range of Figure 7.3 is within the 50% contour of ^{10}B/^{9}Be
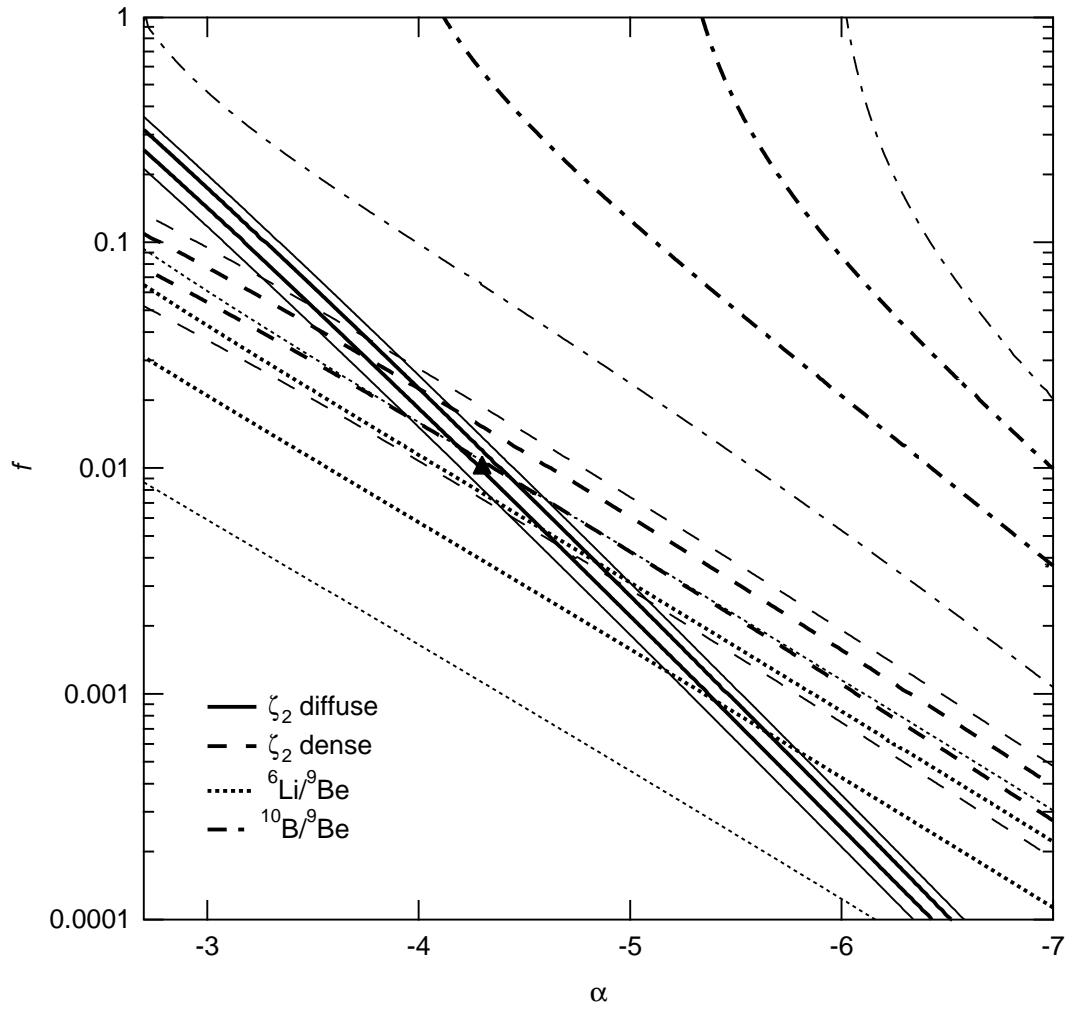
Figure 7.3: Plot in (f, α) space showing how well various combinations reproduce the observed ionization rates and light element ratios. Thicker lines represent 10% deviation from observed values, and thinner lines show 25% deviation. Different styles have the following meanings: solid - ζ_2 in diffuse clouds; dashed - ζ_2 in dense clouds; dotted - ^{6}Li/^{9}Be; dash-dot - ^{10}B/^{9}Be. The triangle shows the parameters chosen for the carrot spectrum: $f = 0.01$, $\alpha = -4.3$

though, so our carrot spectrum is not completely out of the question. Indeed, the carrot spectrum predicts almost the same ^{10}B/^{9}Be ratio as does the propagated spectrum, so the introduction of the carrot leaves the agreement with solar system data no worse than in the standard case.

7.6.2 Gamma Rays

In computing the production rates of gamma-rays, 6 total reactions were used. These include $[p, \alpha] + {}^{12}\text{C} \rightarrow {}^{12}\text{C}^* \rightarrow {}^{12}\text{C} + \gamma_{4.44}$; $[p, \alpha] + {}^{16}\text{O} \rightarrow {}^{16}\text{O}^* \rightarrow {}^{16}\text{O} + \gamma_{6.13}$; and $[p, \alpha] + {}^{16}\text{O} \rightarrow {}^{12}\text{C}^* + \alpha \rightarrow {}^{12}\text{C} + \alpha + \gamma_{4.44}$, where the de-excitations of $^{12}\text{C}^*$ and $^{16}\text{O}^*$ produce 4.44 MeV and 6.13 MeV gamma rays, respectively. Cross sections for all of the above processes come from Ramaty et al. (1979) (and references therein). Along a line of sight with hydrogen column density N_H, the gamma-ray line intensity is

$$I_\gamma = N_\text{H} \int \phi(E) \sigma_\gamma(E) \; dE, \tag{7.13}$$

with units [photons cm^{-2} s^{-1} sr^{-1}], and where for each line the product $\phi\sigma$ represents a sum over appropriately weighted projectiles and targets. If all diffuse clouds experience the same cosmic-ray flux and the column of such clouds through the Galactic plane is about $N_\text{H} = 10^{23}$ cm^{-2}, our calculations predict that the Galactic plane should have the diffuse γ-ray fluxes shown in Table 7.3. Assuming the intensity in eq. (7.13) is uniform in the Galactic plane, we integrated over the solid angle within $|l| < 30°$, $|b| < 10°$ to find the total flux in the central radian of the Galaxy (a typical region over which diffuse γ-ray fluxes are quoted, with units [cm^{-2} s^{-1} rad^{-1}]). Also shown in Table 7.3 is the large-scale sensitivity of the *INTEGRAL* spectrometer at ~ 5 MeV (Teegarden & Watanabe, 2006). Our predicted fluxes are below currently available detector limits of *INTEGRAL*. Thus the presence of low-energy cosmic-rays sufficient to give the ionization levels required by H$_3^+$ does not violate gamma-ray constraints.

Indeed, the gamma-ray line predictions in Table 7.3 lie tantalizingly close to present limits. While this does not provide a test of the predicted cosmic-ray spectra at present, it may be possible that *INTEGRAL* itself, and certainly the next generation gamma-ray observatory, will have the ability to detect these lines. In any case, the results show that our proposed spectra are not inconsistent with observations.

Table 7.3: Diffuse Gamma-Ray Flux from the Central Radian (10^{-5} s^{-1} cm^{-2} rad^{-1})

Energy	*INTEGRAL* sensitivity	Carrot	Broken Power Law	Propagated
4.44 MeV	10	3.0	8.3	0.9
6.13 MeV	10	2.4	5.9	0.4

Notes: Predicted fluxes for the 4.44 and 6.13 MeV γ-ray lines using our carrot, broken power law, and propagated spectra. All calculations were done using $E_{\text{cut}} = 2$ MeV. Also shown are the most directly comparable sensitivities of the *INTEGRAL* spectrometer given by Teegarden & Watanabe (2006). For the central radian we considered uniform emission within $|l| < 30°$ and $|b| < 10°$.

7.6.3 Energetics

Similar to the calculations in Section 7.3, we can determine the energy budget for a given cosmic-ray spectrum. Unlike the previous calculation though, in this case the shape of the spectrum is important as we compute the energy loss rate of all of the cosmic rays in the spectrum. This is done via the usual Bethe-Bloch expression for energy loss dE per unit mass column $dR = \rho dx = \rho v dt$:

$$\frac{dE}{dR} = \frac{4\pi z Z^2 e^4}{A\langle m \rangle m_e v^2} \left[\ln \left(\frac{2\gamma^2 m_e v^2}{I} \right) - \beta^2 \right], \tag{7.14}$$

which is closely related to the ionization cross section above (eq. 7.12). Here we use $z = Z = A = 1$, $\langle m \rangle = 1.4 m_{\text{p}}$, and $I = 13.6$ eV (see Prodanović & Fields (2003) for a complete description of the variables involved). The rate of cosmic-ray energy loss per unit mass of neutral hydrogen is

$$\frac{L_{\text{CR}}}{M_{\text{H}}} = 4\pi (1 + G_{7.15}) \int_{E_{\text{low}}}^{E_{\text{high}}} \phi_p(E) \, \frac{dE}{dR} \, dE, \tag{7.15}$$

where $G_{7.15} = 0.1$ (see Section 7.9). Again using a Galactic hydrogen mass of $M_{\text{H}} = 5 \times 10^9 M_\odot$, the carrot and broken power law spectra require energy inputs of $L_{\text{CR}} = 0.18 \times 10^{51}$ erg (100 yr)$^{-1}$ and 0.17×10^{51} erg (100 yr)$^{-1}$, respectively. These represent large fractions of the total mechanical energy released in SNe. Like in Section 7.3, they are also consistent with the 0.5×10^{51} erg (100 yr)$^{-1}$ found by Fields et al. (2001) which accounted for both energy needed for ionization of the ISM and escape from the Galaxy. Finally, we note that
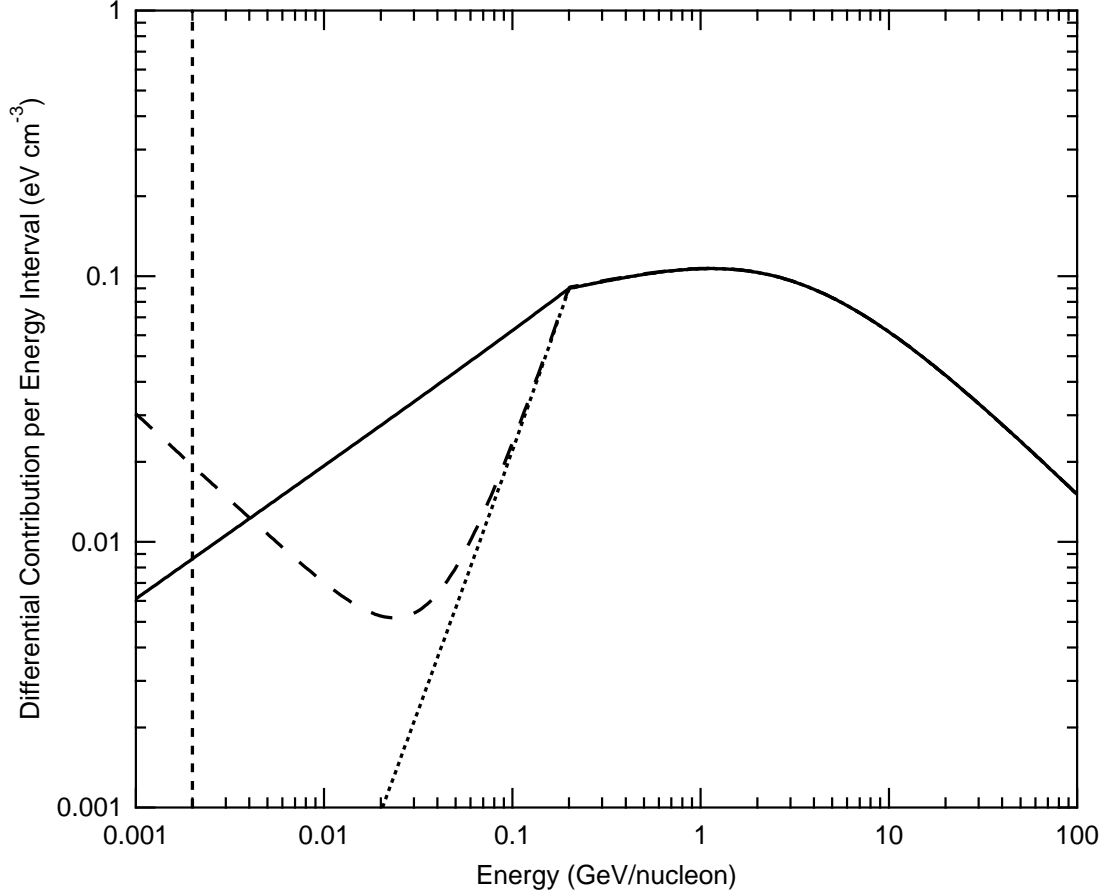
Figure 7.4: Contribution to the energy density of cosmic rays as a function of kinetic energy per nucleon. As in Figure 7.2, the dotted curve is the leaky box propagated spectrum, the solid curve is the broken power law spectrum, the dashed curve is the carrot spectrum, and the vertical dashed line shows the 2 MeV low energy cutoff. The vertical axis is given by $Ed\epsilon/dE$, where $d\epsilon/dE = 4\pi E\phi_p(E)/v(E)$.

the large amounts of energy and high acceleration efficiencies required may help to resolve the superbubble "energy crisis" described by Butt & Bykov (2008).

Beyond the total input energy requirement, each cosmic-ray spectrum will also have a particular energy density and pressure. Energy density can be calculated from

$$\epsilon_{\rm CR} = 4\pi(1 + G_{7.16})\int_{E_{\rm low}}^{E_{\rm high}} E\frac{\phi_p(E)}{v(E)}dE, \tag{7.16}$$

where $v(E)$ is the velocity and $G_{7.16} = 0.42$ (see Section 7.9), and pressure from

$$P_{\rm CR} = \frac{4\pi}{3}(1 + G_{7.17})\int_{E_{\rm low}}^{E_{\rm high}} \phi_p(E)p(E)dE, \tag{7.17}$$

98

where $p(E)$ is again relativistic momentum, and $G_{7.17} = 0.42$. Performing these calculations with $E_{\text{cut}} = 2$ MeV results in energy densities of 0.77 eV cm^{-3} and 0.89 eV cm^{-3}, and pressures (P_{CR}/k_B) of 4300 K cm^{-3} and 5200 K cm^{-3} for the carrot and broken power law spectra, respectively. Both pressures are in rough accord with the average thermal pressure in the diffuse ISM of $(P/k_B) = 2700$ K cm^{-3} reported by Jenkins & Tripp (2007). The energy densities in both spectra, however, are about one half of the value reported by Webber (1998). While this result may at first seem counterintuitive, it is best clarified graphically by Figure 7.4. Here, it is shown that cosmic rays with energies between about 0.1 GeV and 10 GeV completely dominate in contributing to the energy density. This was previously demonstrated by the analogous plot (Fig. 7) in Webber (1998), from which the author concluded that low energy components, such as those proposed in this paper, would have little effect on the cosmic-ray energy density. As for why our spectra have lower energy densities, this is almost entirely dependent on the flux normalization at higher energies. At about 1 GeV the fluxes in our spectra are about one half that of the local interstellar spectrum used by Webber (1998), thus resulting in the corresponding factor of 2 difference in energy densities.

7.6.4 Cloud Heating

One further effect that cosmic rays have is to heat the ISM via energy lost during the ionization process. On average, 30 eV are lost by a cosmic ray during each ionization event (Cravens & Dalgarno, 1978). Using $\zeta_2 = 4 \times 10^{-16}$ s^{-1} and the corresponding $\zeta_H = 1.5\zeta_2/2.3$ and assuming that the number density of atomic hydrogen is roughly equal to that of molecular hydrogen, and that all of the lost energy eventually goes into heating, we find a heating rate due to cosmic rays of $\Gamma_{\text{CR}} = 3 \times 10^{-26}$ erg s^{-1} (H atom)$^{-1}$. This can be compared to the heating rate due to the photoelectric effect calculated by Bakes & Tielens (1994) of $\Gamma_{\text{PE}} = 1.5 \times 10^{-25}$ erg s^{-1} (H atom)$^{-1}$ for the diffuse cloud sight line toward ζ Oph. The heating rate caused by cosmic-ray ionization is about 5 times smaller than the heating rate due to the photoelectric effect, demonstrating that even with such a high ionization rate, cosmic rays do not significantly alter the heating rate in diffuse clouds. This large difference in heating rates is further illustrated by Figure 10 of Wolfire et al. (2003). Because the high flux of low energy cosmic rays we use will not dominate cloud heating, our spectra do not imply cloud temperatures that are inconsistent with observations.

7.7 Discussion

7.7.1 Cosmic-Ray Spectra

As described in Section 7.4, the spectrum with seemingly the best physical motivation is one that arises from the propagation of particles accelerated by strong shocks in supernova remnants. This spectrum follows a $p^{-2.7}$ relationship above a few hundred MeV, matching observations, and a $p^{0.8}$ relationship below a few hundred MeV in the ionization-dominated regime. A similar behavior is apparent in the spectra used by Hayakawa et al. (1961), Spitzer & Tomasko (1968), and Herbst & Cuppen (2006) (see Figure 7.1), except they follow power laws closer to p^2 at low energies. Even the more sophisticated models such as those considering re-acceleration (Shibata et al., 2006) or distributed cosmic-ray sources and a Galactic wind (Lerche & Schlickeiser, 1982) follow these general power laws. Because they decrease at low energy though, all of these spectra (except Hayakawa et al. (1961) which does not begin decreasing until $E \leq 10$ MeV) are unable to provide enough flux at the energies where ionization is most efficient, and thus cannot generate the high ionization rate inferred from H_3^+. It seems then that the propagation of cosmic rays accelerated by SNRs (with test-particle power-law spectra) cannot explain the high flux of low energy cosmic rays necessary in our spectra. However, plentiful evidence supports the idea that high-energy ($\gtrsim 1$ GeV) Galactic cosmic rays *do* originate in supernovae: synchrotron emission in supernova remnants indicates electron acceleration and strongly suggests ion acceleration, and Galaxy-wide cosmic-ray energetics are in line with supernova expectations and difficult to satisfy otherwise. For this reason we retained the propagated cosmic-ray spectrum to represent the supernova-accelerated Galactic cosmic-ray component at high energies ($\gtrsim 1$ GeV), but also considered *additional* cosmic-ray components which dominate at low energies where the ionization efficiency is high.

While our carrot and broken power law spectra do not follow the conventional strong-shock thick-target $\phi \propto p^{0.8}$ relationship in the low-energy regime, recent studies are beginning to find possible sources for the proposed high flux of low energy cosmic rays. Weak shocks will accelerate cosmic rays with preferentially steeper power laws (see Section 7.4), and may be ubiquitous in the ISM, caused by star forming regions, OB associations, and even low mass stars like the sun. Stone et al. (2005) investigated the flux of termination shock protons at the heliosheath using the *Voyager* spacecraft. Their study showed that at low energies, 0.5 MeV $\lesssim E \lesssim 3.5$ MeV, $\phi_p \propto E^{-1.4}$ ($\propto p^{-2.8}$), and that from about 3.5-10 MeV, this relationship steepened to $\phi_p \propto E^{-2}$ ($\propto p^{-4}$). These so-called "anomalous" cosmic rays (ACRs) clearly demonstrate that real sources exist in nature which can produce a

high particle flux at low energies, though these measurements and the anomalous cosmic rays themselves are located in the heliosphere, not interstellar space. Scherer et al. (2008) modeled the effects from the astropauses of all F, G, and K type stars in the Galaxy to find a power of 2.2×10^{49} erg $(100 \text{ yr})^{-1}$ in ACRs. This accounts for only about 10% of the power needed to produce the ionization rate inferred from H_3^+. However, their analysis did not include the effects of winds from the much more luminous O and B stars. To our knowledge, no study has computed the interstellar cosmic-ray spectrum arising from the ACRs of all stellar winds in the Galaxy, but it may indeed be an important contribution to the flux of low energy cosmic rays.

Another intriguing possibility is that supernova shocks are considerably more efficient at low-energy particle acceleration than simple test-particle results would indicate. Indeed, theoretical non-linear shock acceleration calculations (e.g., Kang & Jones, 1995; Berezhko & Ellison, 1999; Blasi, 2002) do predict that low-energy particles have higher fluxes than in the test-particle limit. This result goes in the right direction qualitatively. However, published source spectra we are aware of do not appear steep enough at low energies – particularly after ionization losses are taken into account in propagation – to reproduce the observed ionization rate. It remains an interesting question whether more detailed nonlinear calculations, focussing on the low-energy regime, might provide a solution to the ionization problem; in this case, ionization rates and gamma-ray lines would become new probes of feedback processes in supernova remnants.

In addition to protons and heavy nuclei, it has been proposed that cosmic-ray electrons may make a significant contribution to the ionization rate. Webber (1998) showed that the local interstellar spectrum of cosmic-ray electrons produces a primary ionization rate of $\sim 2 \times 10^{-17}$ s^{-1} when considering energies above ~ 2 MeV. While this is roughly equal to the ionization rate inferred for diffuse clouds at that time, electrons only account for about 10% of the primary ionization rate inferred from H_3^+ (Indriolo et al., 2007). As a result, we have neglected the effect of cosmic-ray electrons in the present study. It is worth noting, however, that low-energy cosmic-ray electrons are probed by very low-frequency radio emission, and indeed cosmic-ray electron emission provides a major foreground for present and future facilities aimed at the measurement of cosmological 21-cm emission from high-redshift sources, including LOFAR (Röttgering, 2003) and the Square Kilometer Array (Beck, 2005). Such observations should provide a detailed picture of low-energy cosmic-ray electrons, whose behavior can in turn be compared to the proton and nuclear components probed by the other observables considered in this paper.

Finally, we have found that the carrot spectrum produces ^{6}Li/^{9}Be in good agreement with solar system data, and a ^{10}B/^{9}Be ratio which is almost identical to the standard propagated

result but which is somewhat low with respect to the solar system value. To the extent that the isotope ratios are not in perfect agreement with solar system data, one possible explanation could be time variations of the cosmic-ray spectral shape over Galactic history. If supernovae are the agents of cosmic-ray acceleration, then presumably strong shocks will always lead to high-energy source spectra with $\gamma_{\text{source}} \sim -2.2$ as we have today. However, the low-energy component responsible for the carrot derives from weaker shocks which in turn may reflect time-dependent properties of, e.g., star-forming regions. Moreover, cosmic-ray *propagation* is much more sensitive to the details of the interstellar environment, particularly the nature of Galactic magnetic fields. Prantzos et al. (1993) suggested that such variations in the early Galaxy might explain the B/Be ratios in primitive (Population II) halo stars. Similarly, if such variations were present in the later phases of Galactic evolution (e.g., during major merger events) then it is possible that the propagated cosmic-ray spectra could have differed substantially. The resulting LiBeB contributions could alter the ratios from the simple time-independent estimates we have made.

Another possible explanation to bring the theoretical LiBeB ratios into better agreement with observations would arise if the LiBeB isotopes suffer significantly different amounts of destruction (astration) in stellar interiors. Because the binding energies are in the hierarchy $B(^6\text{Li}) < B(^9\text{Be}) < B(^{10}\text{B})$, there should be a similar ranking of the fraction of the initial stellar abundance of these isotopes which survives to be re-ejected at a star's death. If the amount of ^6Li destroyed is greater than ^9Be, which is in turn greater than ^{10}B, then the results from our carrot spectrum may be correct before accounting for astration. Assuming this preferential destruction decreases our calculated $^6\text{Li}/^9\text{Be}$ and increases $^{10}\text{B}/^9\text{Be}$, moving both closer to the measured ratios. That said, conventional stellar models (e.g., Sackmann & Boothroyd, 1999) and their implementation in Galactic chemical evolution (Alibés et al., 2002) find different, but still small, survival fractions for all isotopes, $\lesssim 10\%$ for ^{10}B. As a result, this scenario would seem to require large upward revisions to the survival of ^9Be and ^{10}B in stars.

7.7.2 Astrochemistry

Gas phase chemistry in the ISM is driven by ion-molecule reactions. Photons with $E > 13.6$ eV are severely attenuated in diffuse and dense clouds, meaning that cosmic rays are the primary ionization mechanism in such environments. As a result, the cosmic-ray ionization rate has a large effect on the chemical complexity of the cold neutral medium. In fact, it has a direct impact on the abundances of H_3^+, OH, HD, HCO^+, and H_3O^+, to name a few molecules. This makes the cosmic-ray ionization rate an important input parameter for

astrochemical models which predict the abundances of various atomic and molecular species.

However, based on the current theoretical study it seems that instead of having a uniform Galactic value, the cosmic-ray ionization rate should vary between sight lines. This has to do with the source behind cosmic-ray acceleration. While it has typically been assumed that low energy cosmic rays are accelerated in supernovae remnants, the spectra making this assumption were unable to reproduce the ionization rate inferred from H_3^+. Instead, a low energy carrot was required, most likely produced by particles accelerated in weaker, more localized shocks. Unlike the SNe cosmic rays which are assumed to diffuse throughout the Galaxy, cosmic rays accelerated in weak local shocks could lead to significant enhancements in the local ionization rate. Observations of H_3^+ have shown that the cosmic-ray ionization rate is in fact variable between different diffuse cloud sight lines. The H_2 ionization rates toward ζ Per and X Per are about 7×10^{-16} s^{-1} (Indriolo et al., 2007), while 3σ upper limits toward ζ Oph and o Sco are as low as 1.6×10^{-16} s^{-1} and 1.2×10^{-16} s^{-1}, respectively[3]. Like the results of van der Tak et al. (2006) for dense clouds, this demonstrates that the cosmic-ray ionization rate can vary significantly between diffuse clouds as well. Also, it suggests that instead of searching for or adopting a "canonical" ionization rate, sight lines must be evaluated on a case-by-case basis.

In order to test the theory that low energy cosmic rays are primarily accelerated by localized shocks, we propose two complementary observational surveys. First, the ionization rate should be inferred along several diffuse cloud sight lines which are surrounded by different environments. Observations of H_3^+ in sight lines near OB associations and sight lines near low mass stars should provide data in regions near and far from energetic sources. We expect the sight lines near more energetic regions to show higher ionization rates than those near less energetic regions. If observations confirm these predictions, then we will be able to more confidently conclude that most of the low energy ionizing cosmic rays are accelerated in localized shocks.

The second set of observations we propose examines the ionization rate in regions of varying density. Following the reasoning of Section 7.4 where we assume that the lower energy cosmic rays do not penetrate denser clouds, the ionization rate should be inversely related to the cloud density. Observing H_3^+ in diffuse clouds, dense clouds, and in sight lines with intermediate densities should provide us with a range of ionization rates. We can then use the carrot spectrum with appropriate low energy cutoffs to reproduce the inferred ionization rates from each environment, thus constraining the slope of the carrot component. This slope will then allow us to roughly determine the strength (or rather weakness) of the

---

[3]These limits are based on observations performed after the publication of Indriolo et al. (2007), and will be described in more detail in a future publication

103

shock necessary to produce such a steep power law, and thus infer the source of the shock.

7.8   Conclusions

Three theoretical low energy cosmic-ray spectra have been examined, all of which are consistent with direct cosmic-ray observations at high energies. We first adopted the standard $q \propto p^{-2.2}$ source spectrum resulting from cosmic-ray acceleration by strong shocks in supernovae. The propagated version of this spectrum produced an ionization rate about 30 times smaller than that inferred from H_3^+, thus demanding that additional low-energy cosmic-rays be responsible for the observed ionization.

We thus studied the effects of *ad hoc* but physically motivated low-energy cosmic-ray components. We found that the carrot and broken power law spectra could be fashioned so as to reproduce observed results for diffuse clouds. Out of these two, the carrot spectrum did a much better job of matching the ionization rate in dense clouds. Unlike the broken power law, the carrot spectrum was also capable of matching observed light element abundances to within a factor of 2 for the three isotopes produced solely by cosmic-ray spallation. These results are well within the expected uncertainties of LiBeB Galactic chemical evolution.

Predictions for the gamma-ray line fluxes for both the carrot and broken power law were below the limits of current instruments, so these spectra are not inconsistent with data. Indeed, our estimates are close to the detection limits of *INTEGRAL*, and thus motivate a search for the 4.44 MeV and 6.13 MeV lines (or limits to their intensity) in the gamma-ray sky.

Finally, the energy necessary to accelerate all of the cosmic rays in these spectra is about 0.2×10^{51} erg $(100 \text{ yr})^{-1}$. This is a substantial fraction of the mechanical energy released in supernovae explosions, although based on our results it may be necessary that much of this energy come from weak shocks in order to produce a high flux of low energy cosmic rays.

Together, all of these calculations demonstrate that the proposed carrot spectrum is consistent with astrochemical and astrophysical constraints. Whether or not low-energy cosmic rays take precisely this spectral form, at the very least this example serves as a proof by construction that one can make cosmic-ray models which contain low-energy enhancements required by the high ionization rate inferred from H_3^+, while not grossly violating other observational constraints. This motivates future work which looks in more detail at the impact of low-energy cosmic rays.

7.9 Effects of Heavy Cosmic-Ray Nuclei

For the sake of clarity, discussions of the cosmic-ray spectra in the body of the paper focused only on the proton spectrum. Our calculations, however, included the effects of heavier nuclei cosmic rays as a coefficient in eqs. (7.10, 7.15, 7.16, & 7.17). This appendix discusses in more detail the calculations that went into determining the coefficients G_n.

We assume that all heavy cosmic-ray nuclei have the same spectral shape as protons, but that their fluxes are shifted down by their respective relative abundances to hydrogen (e.g. $\phi_{\mathrm{He}}(E) = 0.097\phi_p(E)$). With this assumption, the contribution to the ionization rate due to heavy nuclei can be calculated from

$$G_{7.10} = \sum_i Z_i^2 g_i, \tag{7.18}$$

where Z_i^2 is the charge which comes from eq. (7.12), g_i is the fractional abundance with respect to hydrogen, and the index i sums over all species with solar abundances $g_i > 10^{-5}$ (^{4}He, ^{12}C, ^{14}N, ^{16}O, ^{20}Ne, ^{24}Mg, ^{28}Si, ^{32}S, ^{56}Fe (Meyer et al., 1998)). Performing this summation results in the value of $G_{7.10} = 0.5$ used in the ionization calculations of Section 7.5. In Section 7.6.3, however, the energy loss per unit hydrogen mass (eq. 7.15) is controlled by the particle energy loss per unit mass column $dE/dR \propto Z^2/A$ (eq. 7.14). This changes the heavy nuclei coefficient to

$$G_{7.15} = \sum_i \frac{Z_i^2 g_i}{A_i}, \tag{7.19}$$

where the atomic mass, A_i, is now included because of eq. (7.14). As a result, for the energy loss rate calculation $G_{7.15} = 0.1$. Also in Section 7.6.3, the energy density (eq. 7.16) and pressure (eq. 7.17) calculations both require the coefficient

$$G_{7.16} = G_{7.17} = \sum_i A_i g_i. \tag{7.20}$$

Here, A_i is required because E and thus $p(E)$ are both in units of per nucleon throughout the paper. In this case, $G_{7.16} = G_{7.17} = 0.42$ for both the cosmic-ray energy density and pressure calculations.

However, if the relative abundances of Galactic cosmic rays (GCRs) measured at higher

energies (Meyer et al., 1998) are used instead of solar abundances, the above coefficients change. This is because the abundances of most heavy nuclei are enhanced in GCRs when compared to solar. For the case of ionization, $G_{7.10}$ becomes 1.4, making heavy nuclei more important than protons. Because the integral is multiplied by $(1 + G_{7.10})$ though, the overall difference in the ionization rate between using solar and GCR abundances is only a factor of 2.4/1.5=1.6. Using GCR abundances to calculate the energy loss rate changes $G_{7.15}$ by a negligible amount, from 0.1 to 0.11. Finally, GCR abundances only change $G_{7.16}$ and $G_{7.17}$ from 0.42 to 0.46 for the energy density and pressure calculations. Despite the fact that heavy nuclei are measured to be more abundant in Galactic cosmic rays than in the solar system, we have chosen to use solar abundances in our calculations. This is because the high energy cosmic rays observed are accelerated in metal-rich SNRs, while the high flux of low energy cosmic rays is most likely due to weak shocks associated with low mass stars and the ISM. Due to this source difference, we find it justifiable to use solar abundances instead of the measured high energy GCR abundances.

Chapter 8

Investigating the Cosmic-Ray Ionization Rate Near the Supernova Remnant IC 443 through H_3^+ Observations

The content of this chapter is adapted from material published in the Astrophysical Journal as Indriolo et al. (2010a). Work was done in collaboration with G. A. Blake (California Institute of Technology), M. Goto (Max-Planch Institut für Astronomie), T. Usuda (Subaru Telescope), T. Oka (University of Chicago), T. R. Geballe (Gemini Observatory), B. D. Fields (University of Illinois at Urbana-Champaign) and B. J. McCall (University of Illinois at Urbana-Champaign). Portions of the paper (i.e., observation specifics and data reduction procedure) which are discussed elsewhere in my dissertation have been omitted to avoid redundancy.

Observational and theoretical evidence suggests that high-energy Galactic cosmic rays are primarily accelerated by supernova remnants. If also true for low-energy cosmic rays, the ionization rate near a supernova remnant should be higher than in the general Galactic interstellar medium. We have searched for H_3^+ absorption features in 6 sight lines which pass through molecular material near IC 443—a well-studied case of a supernova remnant interacting with its surrounding molecular material—for the purpose of inferring the cosmic-ray ionization rate in the region. In 2 of the sight lines (toward ALS 8828 and HD 254577) we find large H_3^+ column densities, $N(H_3^+) \approx 3 \times 10^{14}$ cm^{-2}, and deduce ionization rates of $\zeta_2 \approx 2 \times 10^{-15}$ s^{-1}, about 5 times larger than inferred toward average diffuse molecular cloud sight lines. However, the 3σ upper limits found for the other 4 sight lines are consistent with typical Galactic values. This wide range of ionization rates is likely the result of particle acceleration and propagation effects, which predict that the cosmic-ray spectrum and thus ionization rate should vary in and around the remnant. While we cannot determine if the H_3^+ absorption arises in post-shock (interior) or pre-shock (exterior) gas, the large inferred ionization rates suggest that IC 443 is in fact accelerating a large population of low-energy cosmic rays. Still, it is unclear whether this population can propagate far enough into the

ISM to account for the ionization rate inferred in diffuse Galactic sight lines.

8.1   Introduction

As cosmic rays propagate through the interstellar medium they interact with the ambient material. These interactions include excitation and ionization of atoms and molecules, spallation of nuclei, excitation of nuclear states, and the production of neutral pions (π^0) which decay into gamma-rays. Evidence suggests that Galactic cosmic rays are primarily accelerated by supernova remnants through the process of diffusive shock acceleration (e.g. Drury, 1983; Blandford & Eichler, 1987), so interstellar clouds in close proximity to an SNR should provide a prime "laboratory" for studying these interactions. IC 443 represents such a case, as portions of the SNR shock are known to be interacting with the neighboring molecular clouds.

IC 443 is an intermediate age remnant (about 30,000 yr; Chevalier, 1999) located in the Galactic anti-center region $(l, b) \approx (189°, +3°)$ at a distance of about 1.5 kpc in the Gem OB1 association (Welsh & Sallmen, 2003), and is a particularly well-studied SNR. Figure 8.1 shows the red image of IC 443 taken during the Second Palomar Observatory Sky Survey. The remnant is composed of subshells A and B; shell A is to the NE—its center at $\alpha = 06^h17^m08.4^s$, $\delta = +22°36'39.4''$ J2000.0 is marked by the cross—while shell B is to the SW. Adopting a distance of 1.5 kpc, the radii of subshells A and B are about 7 pc and 11 pc, respectively. Between the subshells is a darker lane that runs across the remnant from the NW to SE. This is a molecular cloud which has been mapped in ^{12}CO emission (Cornett et al., 1977; Dickman et al., 1992; Zhang et al., 2010), and is known to be in the foreground because it absorbs X-rays emitted by the hot remnant interior (Troja et al., 2006). Aside from this quiescent foreground cloud, observations of the $J = 1 \rightarrow 0$ line of ^{12}CO also show shocked molecular material coincident with IC 443 (Denoyer, 1979; Huang et al., 1986; Dickman et al., 1992; Wang & Scoville, 1992). These shocked molecular clumps first identified by Denoyer (1979) and Huang et al. (1986) in CO have also been observed in several atomic and small molecular species (e.g. White et al., 1987; Burton et al., 1988; van Dishoeck et al., 1993; White, 1994; Snell et al., 2005), and are thought to be the result of the expanding SNR interacting with the surrounding ISM. While many of the shocked clumps are coincident with the quiescent gas, it is unclear whether or not they are part of the foreground cloud (i.e. the back portions of the foreground cloud are beginning to interact with the SNR blast wave), or if the foreground cloud is separated from IC 443.

Chemical analyses performed in various studies of the shocked clumps around IC 443
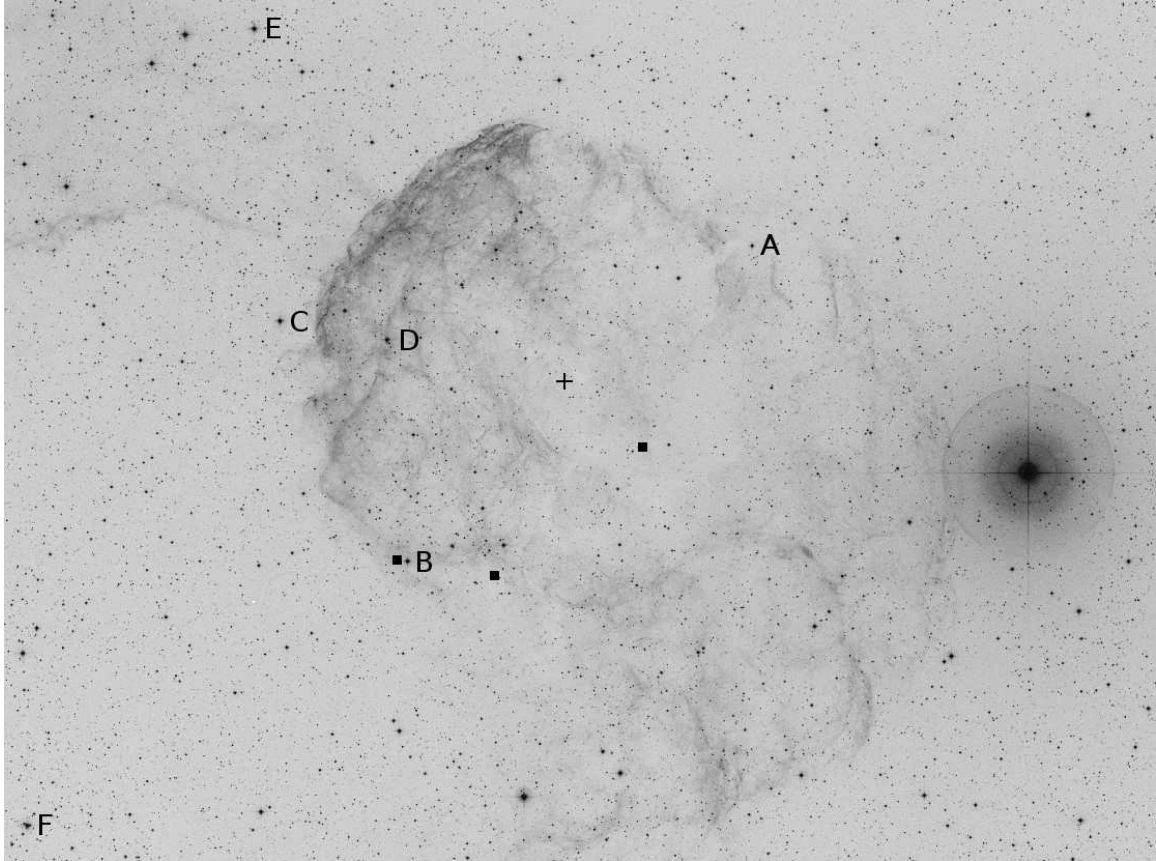
Figure 8.1: This image of IC 443 is from the Second Palomar Observatory Sky Survey (POSS-II) using the red filter, and was obtained from the STScI Digitized Sky Survey. Target background stars are to the immediate left of the uppercase letters, and are labeled as follows: A-ALS 8828; B-HD 254577; C-HD 254755; D-HD 43582; E-HD 43703; F-HD 43907. The cross marks the center of subshell A (the shell on the northeast side of IC 443) at $\alpha = 06^{\mathrm{h}}17^{\mathrm{m}}08.4^{\mathrm{s}}$, $\delta = +22°36'39.4''$ J2000.0. The three black squares mark the positions of OH (1720 MHz) maser emission reported by Hewitt et al. (2006).

suggest an enhanced ionization rate due to cosmic rays. White (1994) found a C/CO ratio much higher than in typical dense clouds and concluded that shocks and/or a large flux of cosmic rays must be responsible. Both Claussen et al. (1997) and Hewitt et al. (2006) observed OH (1720 MHz) masers toward some of these clumps. It is thought that this OH is formed when the free electrons produced during ionization events collide with and excite H_2, which in turn emits UV photons that dissociate H_2O (Wardle & Yusef-Zadeh, 2002). In order to convert nearly all of the H_2O into OH, thus generating the large column of OH necessary to produce the observed masers, a high ionization rate due to X-rays and/or cosmic rays is required. Estimates of the ionization rate due to X-rays (Yusef-Zadeh et al., 2003) and cosmic rays (Hewitt et al., 2009) near IC 443 are similar (a few times 10^{-16} s^{-1}), so it may be that both play a role in generating OH. However, none of these analyses alone can determine exactly how important cosmic-ray ionization and excitation are to the processes considered.

Recently, many studies of IC 443 have focused on the production of pionic gamma-rays via interactions between hadronic cosmic rays and ambient nucleons. Gamma-ray observations of IC 443 have been performed by *EGRET* (Esposito et al., 1996), *MAGIC* (Albert et al., 2007), *VERITAS* (Acciari et al., 2009), *Fermi* LAT (Abdo et al., 2010c), and *AGILE* (Tavani et al., 2010). All show gamma-ray emission that appears to be coincident with gas in the vicinity of IC 443, thus supporting an enhanced cosmic ray flux in the region. Because π^0 production requires cosmic-ray protons with $E_{kin} > 280$ MeV, gamma-ray observations cannot constrain the cosmic-ray flux at lower energies.

To investigate the flux of lower-energy cosmic rays, we study the cosmic-ray ionization of H_2, a process dominated by protons with 1 MeV $\leq E_{kin} \leq$ 1 GeV (Indriolo et al., 2009a; Padovani et al., 2009). The ionization rate of H_2, ζ_2, can be inferred from observations of H_3^+ assuming a rather simple chemical network. H_2 is first ionized, after which the ion collides with another H_2, thus forming H_3^+. Either dissociative recombination with electrons (diffuse clouds) or proton transfer to CO, O, and C (dense clouds) are the primary destruction routes for H_3^+ depending on the environment. In this paper, we present observations searching for absorption lines of H_3^+ along sight lines which pass through molecular material near IC 443. We then use the results of these observations in combination with the simple chemical scheme outlined above to infer the cosmic-ray ionization rate of H_2.
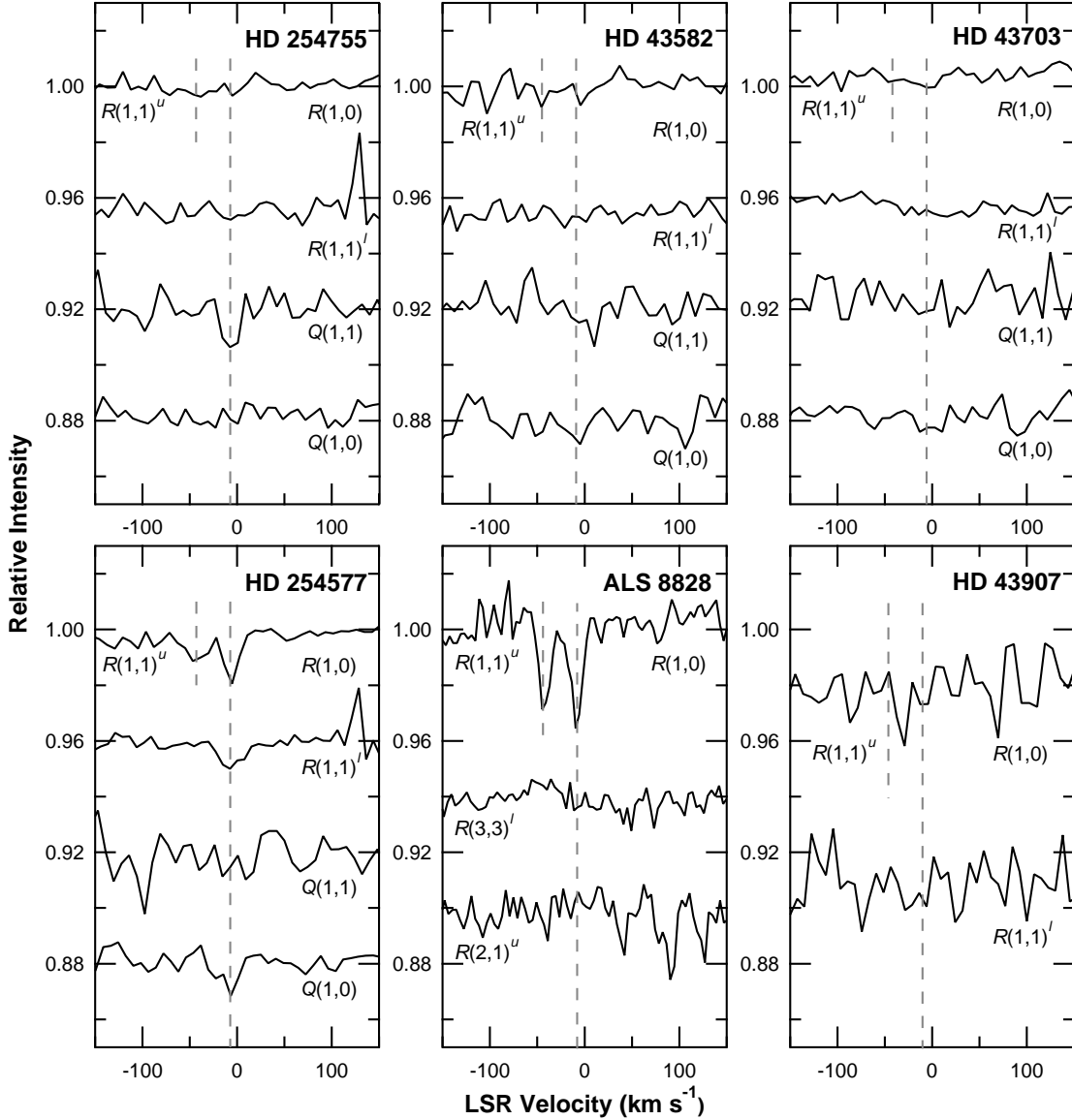
Figure 8.2: Spectra of six stars in the IC 443 region covering various H_3^+ transitions. Vertical dashed lines show the expected position of absorption lines due to H_3^+ given the velocities reported by Hirschauer et al. (2009) for cloud components with the most CH absorption. The shorter dashed line in the $R(1,1)^u$–$R(1,0)$ spectra shows the position of the $R(1,1)^u$ line, which is 36 km s^{-1} away from the $R(1,0)$ line. For HD 254755, HD 43582, HD 43703, and HD 254577, the $R(1,1)^u$–$R(1,0)$ spectra are the combination of NIRSPEC and IRCS data, while the $R(1,1)^l$, $Q(1,1)$, and $Q(1,0)$ spectra are only from IRCS. All of the ALS 8828 spectra are from NIRSPEC, and HD 43907 spectra are from IRCS. Of these six sight lines, only HD 254577 and ALS 8828 show H_3^+ absorption features. The $R(1,1)^u$, $R(1,0)$, $R(1,1)^l$, and $Q(1,0)$ lines are visible toward HD 254577 (the lower S/N in the $Q(1,1)$ spectrum and smaller dipole moment of that transition precludes its detection). For ALS 8828, relatively strong $R(1,1)^u$ and $R(1,0)$ lines are visible. Even with a large amount of H_3^+ along the sight line though, the $R(2,1)^u$ and $R(3,3)^l$ transitions arising from higher energy states are not detected.

111

8.2 Observations & Data Reduction

This project examined 6 target sight lines toward the stars ALS 8828, HD 254577, HD 254755, HD 43582, HD 43703, and HD 43907, all of which are shown in Figure 8.1 to the immediate left of the labels A–F, respectively. Target selection was based on various criteria, including L-band magnitude, previously detected molecules, and evidence that the background stars were in fact behind the SNR (Welsh & Sallmen, 2003; Hirschauer et al., 2009). Basic properties of these sight lines are available in Hirschauer et al. (2009), as well as Table 2.3. Observations focused primarily on transitions arising from the $(J, K) = (1, 1)$ and $(1, 0)$ levels of the ground vibrational state of H_3^+, the only levels significantly populated at average diffuse cloud temperatures ($T \sim 60$ K). Transitions from higher energy levels (e.g. $(2, 1)$ and $(3, 3)$) were covered as allowed by the instrument, but absorption at these wavelengths was not expected.

Details regarding instrument and telescope settings are discussed in Chapter 2, and a log containing the list of science targets and exposure times for each night is included in Table 2.4. The procedures used in reducing these data are described in Chapter 3, and the resulting spectra are presented in Figure 8.2.

8.3 Results & Analysis

It is clear from Figure 8.2 that H_3^+ absorption is only detected in the sight lines toward ALS 8828 and HD 254577. The $R(1, 1)^u$ and $R(1, 0)$ lines are quite strong toward ALS 8828. Absorption from the higher energy (3,3) and (2,1) states was not detected, as expected given diffuse molecular cloud conditions. The sight line toward HD 254577 shows absorption from the $R(1, 1)^u$, $R(1, 0)$, $R(1, 1)^l$ and $Q(1, 0)$ transitions of H_3^+. Absorption due to the $Q(1, 1)$ transition must also be present, but it is not detected. This is probably the result of 3 factors: (1) the intrinsic strength of the $Q(1, 1)$ transition is the weakest of the 5 transitions examined (see Table 2.1); (2) the spectrum near the $Q(1, 1)$ transition has a low S/N due to lower illumination of the echelle order in which it appears; (3) the $Q(1, 1)$ transition is overlapped by a strong atmospheric N_2O line (see panel 4 of Figure 2.1), making removal of telluric features uncertain. Imperfect removal of this atmospheric line is also the most likely cause of the feature in the $Q(1, 1)$ spectrum of HD 254755 that appears at the expected velocity. This feature cannot be due to H_3^+, as there is no absorption by any of the other stronger H_3^+ transitions which arise from the same state. The positive spike near 130 km s^{-1} in the $R(1, 1)^l$ spectra of HD 254577 and HD 254755 is an instrumental artifact. Spectra of HD 43582, HD 43703, and HD 43907 also show no absorption features from H_3^+.

Table 8.1: Absorption Line Parameters Toward IC 443

Object	Transition	v_{LSR} (km s^{-1})	FWHM (km s^{-1})	W_λ (10^{-6} μm)	$\sigma(W_\lambda)$ (10^{-6} μm)	$N(J,K)$ (10^{14} cm^{-2})	$\sigma(N)$ (10^{14} cm^{-2})
ALS 8828	$R(1,1)^u$	-6.0	14.0	6.4	0.5	2.64	0.22
	$R(1,0)$	-8.3	14.1	7.0	0.5	1.76	0.14
HD 254577	$R(1,1)^u$	-6.7	24.9	3.0	0.4	1.22	0.15
	$R(1,0)$	-6.2	16.2	3.8	0.3	0.95	0.07
	$R(1,1)^l$	-6.2	27.0	3.4	0.4	1.55	0.17
	$Q(1,1)$	...	16	< 3.2	...	< 1.54	...
	$Q(1,0)$	-6.1	14.3	2.5	0.5	0.59	0.12
HD 254755	$R(1,1)^u$	...	16	< 1.2	...	< 0.49	...
	$R(1,0)$	...	16	< 1.2	...	< 0.30	...
	$R(1,1)^l$	...	16	< 1.4	...	< 0.64	...
	$Q(1,1)$	...	16	< 3.3	...	< 1.58	...
	$Q(1,0)$	...	16	< 1.5	...	< 0.36	...
HD 43582	$R(1,1)^u$	...	16	< 1.9	...	< 0.78	...
	$R(1,0)$	...	16	< 1.9	...	< 0.48	...
	$R(1,1)^l$	...	16	< 1.5	...	< 0.68	...
	$Q(1,1)$	...	16	< 3.2	...	< 1.55	...
	$Q(1,0)$	...	16	< 3.0	...	< 0.71	...
HD 43703	$R(1,1)^u$	...	16	< 1.2	...	< 0.50	...
	$R(1,0)$	...	16	< 1.2	...	< 0.31	...
	$R(1,1)^l$	...	16	< 1.3	...	< 0.62	...
	$Q(1,1)$	...	16	< 3.5	...	< 1.68	...
	$Q(1,0)$	...	16	< 2.3	...	< 0.56	...
HD 43907	$R(1,1)^u$	...	16	< 4.4	...	< 1.83	...
	$R(1,0)$	...	16	< 4.4	...	< 1.12	...
	$R(1,1)^l$	...	16	< 5.3	...	< 2.41	...

Notes: Column 3 (v_{LSR}) gives the interstellar gas velocity in the local standard of rest frame. Column 4 (FWHM) gives the full width at half-maximum of the absorption features. In the case of non-detections, the FWHM was set to 16 km s^{-1}, the resolving power of IRCS on Subaru in our particular setup, for the purpose of computing column density upper limits. Columns 5 and 6 show the equivalent width, W_λ, and its 1σ uncertainty, $\sigma(W_\lambda)$, respectively. Upper limits to W_λ are equal to $3\sigma(W_\lambda)$. Columns 7 and 8 give the column density of H_3^+ in the state each transition probes, $N(J,K)$, and its uncertainty, $\sigma(N)$, respectively. Upper limits to the H_3^+ column density are equal to $3\sigma(N)$.

Equivalent widths and column densities were determined using the methods discussed in Section 5.1, and are presented in Table 8.1. Equation (5.6) was utilized in inferring the cosmic-ray ionization rate, as described in Section 5.2. As before, x_e is approximated by $N(\mathrm{C}^+)/N_{\mathrm{H}} \sim 1.5 \times 10^{-4}$. The hydrogen number density can be estimated by both

a rotation-excitation analysis of C_2 observations and a restricted chemical analysis based on CN observations (Hirschauer et al., 2009). The C_2 analysis also gives a best-fit kinetic temperature which we use in calculating k_e. While molecular hydrogen has not been observed in absorption along any of our target sight lines, abundances of H_2 and CH tend to be linearly related in diffuse clouds (Federman, 1982; Mattila, 1986; Sheffer et al., 2008). We use the relationship derived from the largest, most recent data set—$N(\text{CH})/N(\text{H}_2) = 3.5^{+2.1}_{-1.4} \times 10^{-8}$ (Sheffer et al., 2008)—in combination with CH column densities reported by Hirschauer et al. (2009) to estimate $N(\text{H}_2)$. Finally, the total H_3^+ column density is determined by adding $N(1,0)$ and $N(1,1)$. These input values and/or the parameters on which they depend, as well as the inferred ionization rates are shown in Table 8.2.

Table 8.2: Properties of Sight Lines Observed Near IC 443

Target	r	T	n_H	N_H	L	$N(\text{H}_2)$	$N(\text{H}_3^+)$	ζ_2
	(pc)	(K)	(cm^{-3})	(10^{21} cm^{-2})	(pc)	(10^{21} cm^{-2})	(10^{14} cm^{-2})	(10^{-16} s^{-1})
ALS 8828	6.8	60	300	3.0	3.2	$2.1^{+1.4}_{-0.8}$	4.4 ± 0.26	16^{+8}_{-12}
HD 254577	7.0	35	325	3.6	3.6	$0.9^{+0.6}_{-0.3}$	2.2 ± 0.34	26^{+13}_{-19}
HD 254755	8.6	35	200	2.5	4.0	$1.1^{+0.7}_{-0.4}$	< 0.6	< 3.5
HD 43582	5.4	60	200	1.9	3.0	$0.5^{+0.3}_{-0.2}$	< 0.8	< 9.0
HD 43703	13.9	60	300	1.7	1.8	$0.8^{+0.5}_{-0.3}$	< 0.6	< 5.7
HD 43907	20.6	60	300	1.5	1.6	$0.4^{+0.3}_{-0.2}$	< 2.1	< 40

Notes: Various parameters used in our analysis for the target sight lines in this study. Column 2 gives the on-sky distance (r) from the center of shell A of IC 443 ($\alpha = 06^\text{h}17^\text{m}08.4^\text{s}$, $\delta = +22°36'39.4''$ J2000.0) to each sight line assuming the remnant is at a distance of 1.5 kpc. The radius of shell A is about 7 pc. Temperatures (T) were taken from the C_2 rotation-excitation analysis when available or set to 60 K, and number densities (n_H) were taken from either the C_2 rotation-excitation analysis or restricted chemical analysis, both reported in Hirschauer et al. (2009). Uncertainties in n_H are taken to be ±100 cm^{-3}. Color excesses were decreased by 0.3 mag to remove the contribution from foreground gas (color excesses and the foreground correction are given in Hirschauer et al., 2009), and the relationship $N_\text{H} \approx E(B-V) \times 5.8 \times 10^{21}$ cm^{-2} mag^{-1} (Bohlin et al., 1978; Rachford et al., 2002) was used to compute the total hydrogen column densities, N_H. Path lengths (L) were calculated from n_H and N_H. Molecular hydrogen column densities were calculated from the relationship $N(\text{CH})/N(\text{H}_2) = 3.5^{+2.1}_{-1.4} \times 10^{-8}$ (Sheffer et al., 2008) using the dominant CH components from Hirschauer et al. (2009). Uncertainties in $N(\text{H}_2)$ are dominated by the scatter in the above relationship, not uncertainties in $N(\text{CH})$. Upper limits for $N(\text{H}_3^+)$ are the 3σ uncertainties from the observations, and the upper limits for ζ_2 are based solely on those values. To account for the uncertainty in $N(\text{H}_2)$, the upper limits for ζ_2 should be multiplied by 1.5.

While H_2 is ionized by both cosmic rays and X-rays, most of the X-ray flux should be attenuated in a relatively thin layer at the cloud exterior (Glassgold & Langer, 1974). The ionization rate due to X-rays at the edge of IC 443 was estimated to be $\zeta_\text{X} = 3.6 \times 10^{-16}$ s^{-1}

(Yusef-Zadeh et al., 2003), and must be much lower in cloud interiors. As a result, the ionization rates we infer should be primarily due to cosmic rays.

8.4 Discussion

Having computed the cosmic-ray ionization rate for clouds in the vicinity of IC 443, we compare our results to those from previous studies. The average ionization rate in diffuse molecular clouds found by Indriolo et al. (2007) using H_3^+ was $\zeta_2 = 4 \times 10^{-16}$ s^{-1}, several times lower than found toward ALS 8828 and HD 254577 ($\zeta_2 = 16^{+8}_{-12} \times 10^{-16}$ s^{-1} and $26^{+13}_{-19} \times 10^{-16}$ s^{-1}, respectively). In fact, the ionization rates inferred for these 2 sight lines are more than twice the highest rates previously found in diffuse molecular clouds toward ζ Per and X Per ($\zeta_2 \approx 7 \times 10^{-16}$ s^{-1}). While ALS 8828 and HD 254577 present exceptionally high ionization rates, the other 3 sight lines observed near IC 443 do not (due to the low S/N obtained toward HD 43907, the derived upper limit for that particular sight line is not exceptionally meaningful, and so we exclude it from further consideration). Instead, the 3σ upper limits for ζ_2 presented in Table 8.2 are consistent with ionization rates of a few times 10^{-16} s^{-1}, typical of diffuse molecular clouds. These differences are quite striking, and warrant discussion.

There are two plausible explanations for why H_3^+ would be detected toward ALS 8828 and HD 254577 but not HD 254755, HD 43582, HD 43703, and HD 43907, and they can most easily be seen when equation (5.6) is rearranged to show that $N(H_3^+) \propto \zeta_2/(x_e n_H)$. Given this scaling we can posit that either the product $x_e n_H$ (i.e. the electron density) is lower along these 2 sight lines, or ζ_2 is higher, and we examine these possibilities in turn.

8.4.1 Lower Electron Density

As stated in Section 8.3, we have assumed an electron fraction that is consistent with observations of C^+ in several diffuse molecular clouds. In denser environments though, the predominant form of carbon shifts from C^+ to C, and eventually to CO, thus decreasing the electron density. Adopting a reduced value for $x_e n_H$ requires a corresponding decrease in ζ_2 to match the observed H_3^+ column density. It could then be argued that the enhanced ionization rate we calculate for the 2 sight lines where we detect H_3^+ is actually just an artifact of not recognizing a decreased destruction rate.

However, there are observations which seem to argue against this possibility. The C_2 rotation-excitation and CN restricted chemical analyses performed by Hirschauer et al. (2009) suggest densities of $200 - 400$ cm^{-3}, typical of diffuse molecular clouds, not dense clouds.

Also, we can estimate the fractional abundance of CO ($x(\mathrm{CO}) = N(\mathrm{CO})/N_\mathrm{H}$) in the observed sight lines and compare it to the solar system abundance of carbon ($x(\mathrm{C_{tot}}) = 2.9 \times 10^{-4}$; Lodders, 2003) to determine if CO is the dominant carbon bearing species. We estimate N_H from the color excess (see Table 8.2), and use observed relationships between $N(\mathrm{CH})$, $N(\mathrm{CN})$, and $N(\mathrm{CO})$ (Sonnentrucker et al., 2007; Sheffer et al., 2008), in concert with CH and CN column densities (Hirschauer et al., 2009) to estimate $N(\mathrm{CO})$. In the ALS 8828 and HD 254577 sight lines $x(\mathrm{CO}) \sim 5 \times 10^{-6}$ and 2×10^{-6}, respectively, much smaller than the assumed total carbon budget. In the other 3 sight lines $x(\mathrm{CO})$ ranges from about 1×10^{-7} to about 1×10^{-6}. These estimates show that most carbon is not in the form of CO, but does not rule out C as the dominant carbon bearing species. To do so, we use the observed relationship between $\mathrm{CO/H_2}$ and $(\mathrm{C+CO})/\mathrm{C_{tot}}$ shown in Figure 6 of Burgh et al. (2010). For $\mathrm{CO/H_2} \sim 8 \times 10^{-6}$—the largest value estimated along any of our sight lines—observations show that both CO and C account for only a small fraction of the total carbon budget, thus indicating that carbon is predominantly in ionized form.

To improve upon these rough arguments though, observations yielding the relative abundances of $\mathrm{C^+}$, C, and CO are necessary. The v=1–0 fundamental and v=2–0 overtone rovibrational bands of CO near 4.6 μm and 2.3 μm, respectively, can be observed with NIRSPEC and IRCS. Various electronic transitions of CO and C I are available in the far ultraviolet (1100 Å–1700 Å), and can be observed with either COS or STIS aboard *Hubble*. Finally, a weak intersystem line of C II is at 2325 Å, and may also be observable with COS and/or STIS. Combined, these observations would allow us to determine the predominant carbon-bearing species along each sight line, and give us a better understanding of cloud conditions being probed.

8.4.2 Higher Ionization Rate

If the gas conditions in all of our observed sight lines are similar, then the cosmic-ray ionization rate must be higher toward ALS 8828 and HD 254577. Such varied ionization rates can be the result of differing cosmic-ray fluxes in each sight line. If we assume that the SNR accelerates particles isotropically (i.e. the spectrum of cosmic rays leaving the remnant is identical everywhere along the blast wave) then the different cosmic-ray spectra operating in each sight line must be due to propagation effects.

To determine whether or not cosmic rays accelerated by IC 443 can even produce the high inferred ionization rates, we use the methods described in Indriolo et al. (2009a) to compute the expected ionization rate for various cosmic-ray spectra. Abdo et al. (2010c), Torres et al. (2008), and Torres et al. (2010) constrain the proton spectrum above $\sim 100\,\mathrm{MeV}$

near IC 443 from the observed gamma-ray spectrum. Although the broken power-law proton spectrum in Abdo et al. (2010c) is given as a power law in kinetic energy (flux $\propto E_{kin}^{-2.09}$ when $E_{kin} < 69$ GeV), we change this to a power law in momentum (flux $\propto p^{-2.09}$, where $pc = [(E_{kin} + m_p c^2)^2 - (m_p c^2)^2]^{0.5}$) to account for the fact that diffusive shock acceleration is expected to produce a spectrum of this form. This substitution only differs from the relation considered by Abdo et al. (2010c) in the non-relativistic regime where $p \propto E_{kin}^{0.5}$. As we extrapolate the spectrum to lower energies then, the particle distribution is flattened relative to a pure power law in kinetic energy.

Integrating this extrapolated spectrum to a low-energy cutoff of 5 MeV, we find $\zeta_2 \sim 10^{-14}$ s^{-1}. A 5 MeV cutoff was used because particles of this energy have a range of a few times 10^{21} cm^{-2} (Padovani et al., 2009), similar to the sight lines we consider here. Using the $d = 10$ pc continuous injection spectrum (also extrapolated to low energies as above) from Torres et al. (2008) produces similar results, while their $d = 30$ pc spectrum fails to reproduce even the ionization rate predicted by the local interstellar cosmic-ray spectrum ($\zeta_2 \sim 4 \times 10^{-17}$ s^{-1}; Webber, 1998). Note that the difference between the 10 pc and 30 pc theoretical spectra is *not* the result of energy losses, but due to the fact that lower energy particles have not yet had sufficient time to travel far from IC 443 given its age of 30,000 yr. Although these spectra are not particularly well suited for estimating the cosmic-ray ionization rate—they are based on observations which depend on processes requiring $E_{kin} > 280$ MeV and so are not well constrained at energies of a few MeV where ionization is much more efficient—they do suggest that cosmic-rays accelerated by IC 443 are capable of generating the ionization rate inferred from H$_3^+$, and also provide independent constraints on the flux of high-energy cosmic rays near IC 443 which complement the low-energy component studied in this paper.

The propagation effects included in the model cosmic-ray spectra presented in Torres et al. (2008, 2010) may also be able to explain the differences inferred in ζ_2. Those authors suggest that the difference in centroid position between the GeV (*EGRET* and *Fermi* LAT) and TeV (*MAGIC* and *VERITAS*) gamma-ray sources can be explained by having the gamma rays of different energies originate in separate clouds. They propose that the lower energy gamma rays arise from π^0 decay in a cloud 3–6 pc away from the expanding shell of IC 443, and the higher energy gamma rays in a cloud about 10 pc in front of the SNR. This explanation requires that cosmic-ray propagation is energy dependent, such that high energy particles have diffused farther away from the SNR than low energy particles. In such a model, the cosmic-ray spectrum varies as a function of position, and so the ionization rate must as well.

Because lower energy cosmic rays have yet to propagate very far from IC 443, the ionization rate should decrease with increased distance away from the SNR. If the clouds probed

by ALS 8828 and HD 254577 are closer to IC 443 than the clouds probed by the other 3 sight lines, then the difference in inferred ionization rates is easily explained. The positions of our target sight lines with respect to IC 443 are shown in Figure 8.1, and the on-sky distances from the center of subshell A to each of the background stars is listed in Table 8.2. Of the 5 sight lines, only HD 43703 is a considerable distance away from the remnant, so differences in the remaining 4 sight lines must be due to line-of-sight distances. Gas velocities for the dominant CH components reported by Hirschauer et al. (2009) vary by only about 3 km s^{-1} between all of our sight lines, suggesting that the absorption may arise from the same cloud complex, but because IC 443 is located near the Galactic anti-center such an analysis is highly uncertain. The HD 254577 sight line passes through regions of HCO$^+$ emission (Dickman et al., 1992) and H$_2$ emission (Burton et al., 1988; Inoue et al., 1993; Rho et al., 2001), both of which trace shocked gas, and is in close proximity to an OH (1720 MHz) maser which requires shocked gas and a high ionization rate (Hewitt et al., 2006), so it is plausible that the observed H$_3^+$ absorption arises in material very close to the SNR shock. The ALS 8828 sight line, however, is not coincident with shock tracers, so it is unclear at this location how close the foreground cloud is to the SNR. Still, given the drastic difference in the 10 pc and 30 pc cosmic-ray spectra from Torres et al. (2008) (see their Figure 1), the gas probed by the 3 sight lines without observed H$_3^+$ would not have to be that much farther away than the gas probed by ALS 8828 to explain the inferred ionization rates; something on the order of 10 pc farther away would suffice.

Aside from the distance between the site of particle acceleration and the clouds in question, various other propagation and acceleration effects could account for the difference in inferred ionization rates. Cosmic rays diffuse through space as they scatter off of Alfvén waves which are presumed to be generated by the particles themselves. For clouds with higher densities of neutral gas, the damping of these waves (via ion-neutral collisions) becomes more efficient and the streaming velocity of cosmic rays thus increases (Padoan & Scalo, 2005). Instead of diffusing then, particles will free-stream and spend much less time in the cloud (i.e. have fewer chances to ionize ambient material). As a result, regions of low gas density should be expected to have higher ionization rates than regions of high gas density. Another possibility is that the net flux of cosmic rays into a cloud (due to ionization losses, nuclear interactions, etc. within the cloud) sets up an anisotropy that causes the growth of Alfvén waves in the plasma surrounding the cloud. Lower energy particles (E_{kin} less than a few hundred MeV) scatter off of these waves and are impeded from entering the cloud (Skilling & Strong, 1976). Because the particles most efficient at ionizing hydrogen are excluded from denser clouds, this effect also predicts a higher ionization rate in regions of lower density. However, due to the similar densities reported in Hirschauer et al. (2009)

for our target sight lines, these effects seem unlikely candidates for causing the difference in inferred ionization rates.

The final effect we consider in attempting to explain these variations in the ionization rate is the escape of cosmic rays upstream from the shock where diffusive shock acceleration occurs (i.e. away from the SNR). This subject has been the focus of several recent studies (e.g. Caprioli et al., 2009, 2010; Reville et al., 2009; Ohira et al., 2010) which find that particles *can* escape in the upstream direction, although these tend to be only the particles with the highest energies. For the discussion above, we have assumed that low-energy cosmic rays have escaped from the shock and are diffusing away from the SNR. However, if low-energy cosmic rays do not escape, but are instead preferentially advected downstream (i.e. into the SNR), then the ionization rate in the post-shock gas inside the SNR should be higher than in the gas exterior to the remnant. The differing ionization rates could then be explained if the sight lines toward ALS 8828 and HD 254577 probed gas interior to IC 443. As mentioned above, the HD 254577 sight line is coincident with various shock tracers, as well as an OH (1720 MHz) maser (which arises from the post-shock gas inside the SNR). Additionally, the velocity of this maser, -6.85 km s^{-1}, is consistent with the H$_3^+$ velocities reported in Table 8.1, making it highly plausible that the H$_3^+$ absorption toward HD 254577 arises from shocked gas inside of IC 443. Consequently, the inability of low-energy cosmic rays to escape from IC 443 provides an alternative to the diffusion of particles and differing distances between the remnant and gas probed by our sight lines in explaining the inferred ionization rates.

8.4.3 Implications

Given either of the cases discussed above (low electron density or high ionization rate), we can comment on the flux of low-energy cosmic rays accelerated by SNRs. In the case that the exceptional H$_3^+$ column densities observed are due to a lower destruction rate (i.e. lower electron density), then the ionization rate near IC 443 is no higher than already found toward various diffuse molecular cloud sight lines. This would indicate that the flux of low energy cosmic rays near SNRs is not substantially different than in the Galactic ISM, and suggest that either SNRs are not the primary accelerators of such particles, or that low energy particles have yet to escape from IC 443.

In the case that the inferred ionization rates of a few times 10^{-15} s^{-1} are correct, IC 443 must be accelerating a large population of low-energy cosmic rays. Either this population must be escaping upstream from the site of diffusive shock acceleration (i.e. traveling outward from the SNR shock) such that the clouds closest to the remnant are experiencing a large

flux of cosmic rays, or the 2 sight lines with H_3^+ detections probe gas inside of IC 443 where low-energy cosmic rays have been advected downstream. In either situation, it is unclear if such a population of cosmic rays accelerated by all SNRs within the Galaxy will propagate far enough from their sources to affect the flux of cosmic rays at some arbitrary position. As a result, it is difficult to definitively say whether or not SNRs are responsible for accelerating the large flux of low-energy cosmic rays necessary to produce the $\zeta_2 \sim 4 \times 10^{-16}$ s^{-1} ionization rate inferred in many diffuse Galactic sight lines.

8.5   Conclusions

We have searched for H_3^+ absorption along 6 sight lines that pass through molecular material in the vicinity of the SNR IC 443. Two of the observed sight lines, ALS 8828 and HD 254577, have large column densities of H_3^+, while the other 4 show no absorption features. The cosmic-ray ionization rates inferred from the 2 detections are a few times 10^{-15} s^{-1}, higher than ever previously found in diffuse molecular clouds. Upper limits to the ionization rate in the other sight lines, however, are consistent with values found along average Galactic sight lines of about 4×10^{-16} s^{-1}. These differences may be due to overestimates of the electron fraction or cosmic-ray propagation and acceleration effects, but the complexity of the region makes it difficult to attribute the results to any one cause. Future observations of C II, C I, and CO toward our target sight lines should allow us to better discriminate between the two possibilities, and thus determine whether or not IC 443 produces a large flux of low-energy cosmic rays.

In addition, surveys of H_3^+ near IC 443 and other SNRs thought to be interacting with molecular clouds (e.g. Vela, W 28, W 44, W 51C) should allow us to further investigate cosmic-ray acceleration in such environments. By more extensively mapping H_3^+ absorption near supernova remnants, we can determine where the H_3^+ resides (interior post-shock gas or exterior pre-shock gas), and thus where the flux of low-energy cosmic rays is highest. Such observations may also provide insight into the efficiency with which accelerated particles are advected downstream into remnants, and so add important constraints to models of cosmic-ray acceleration.

Chapter 9

Interstellar Metastable Helium Absorption as a Probe of the Cosmic-Ray Ionization Rate

The content of this chapter was published in *ApJ* as Indriolo et al. (2009b). Work was done in collaboration with L. M. Hobbs (University of Chicago, Yerkes Observatory), K. H. Hinkle (National Optical Astronomy Observatories), and B. J. McCall (University of Illinois at Urbana-Champaign).

The ionization rate of interstellar material by cosmic rays has been a major source of controversy, with different estimates varying by three orders of magnitude. Observational constraints of this rate have all depended on analyzing the chemistry of various molecules that are produced following cosmic-ray ionization, and in many cases these analyses contain significant uncertainties. Even in the simplest case (H_3^+) the derived ionization rate depends on an (uncertain) estimate of the absorption path length. In this paper we examine the feasibility of inferring the cosmic-ray ionization rate using the 10830 Å absorption line of metastable helium. Observations through the diffuse clouds toward HD 183143 are presented, but yield only an upper limit on the metastable helium column density. A thorough investigation of He^+ chemistry reveals that only a small fraction of He^+ will recombine into the triplet state and populate the metastable level. In addition, excitation to the triplet manifold of helium by secondary electrons must be accounted for as it is the dominant mechanism which produces He* in some environments. Incorporating these various formation and destruction pathways, we derive new equations for the steady state abundance of metastable helium. Using these equations in concert with our observations, we find $\zeta_{He} < 1.2 \times 10^{-15}$ s^{-1}, an upper limit about 5 times larger than the ionization rate previously inferred for this sight line using H_3^+. While observations of interstellar He* are extremely difficult at present, and the background chemistry is not nearly as simple as previously thought, potential future observations of metastable helium would provide an independent check on the cosmic-ray ionization rate derived from H_3^+ in diffuse molecular clouds, and, perhaps more importantly, allow the first direct measurements of the ionization rate in diffuse atomic clouds.

9.1 Introduction

9.1.1 Motivation

Over the past several decades, the assumed value of the cosmic-ray ionization rate of interstellar hydrogen has fluctuated up and down. Various theories and models have predicted ionization rates from 10^{-18} s^{-1} to 10^{-15} s^{-1} in the diffuse interstellar medium (e.g. Spitzer & Tomasko, 1968; van Dishoeck & Black, 1986; Webber, 1998; Le Petit et al., 2004). On the other hand, observations of molecules such as HD and OH typically resulted in estimates of the ionization rate that were on the order of 10^{-17} s^{-1} (O'Donnell & Watson, 1974; Black & Dalgarno, 1977; Black et al., 1978; Hartquist et al., 1978a,b; Federman et al., 1996). However, these estimates depend on gas phase abundances of O, OH, D, and HD, values which are often difficult to measure precisely. More recently, observations of H$_3^+$ have again revised the cosmic-ray ionization rate upward to a few times 10^{-16} s^{-1} (McCall et al., 2003; Indriolo et al., 2007). Deriving the ionization rate from H$_3^+$ requires only one uncertain parameter, the absorption path length. While the higher ionization rates derived from H$_3^+$ are becoming generally accepted (Dalgarno, 2006), it is desirable to search for new observables which can offer independent and less uncertain estimates of the ionization rate.

In this report, we investigate the possibility of observationally determining the total ionization rate of helium atoms by cosmic rays in diffuse clouds. The basic premise is that in a sufficiently reddened cloud, the column density of neutral helium atoms excited to the metastable 1s2s ^{3}S$_1$ level may be high enough to be measured by means of interstellar absorption lines arising from that level. The high cosmic abundance of helium and the long radiative lifetime of the metastable level, $A^{-1} = 2.5$ hr, may compensate for the difficulty of populating this highly excited level, which lies 19.8 eV above the ground level. Previously, it has been assumed that this level should be populated almost entirely by cosmic-ray ionization of helium atoms, followed by radiative recombination of the ions with electrons. Figure 9.1 schematically shows the processes conventionally used in describing the (de)population of the metastable state.

9.1.2 Background

A simple reaction network – consisting of (i) cosmic-ray ionization of He^0 atoms in the 1s^2 ^{1}S$_0$ ground level, (ii) radiative recombination of He$^+$ ions with electrons to the metastable 1s2s ^{3}S$_1$ level, and (iii) forbidden spontaneous emission to the ground level – was first used by Scherb (1968) and Rees et al. (1968) in proposing the observability of interstellar metastable helium. However, both of these studies considered 2-photon emission from the metastable

123
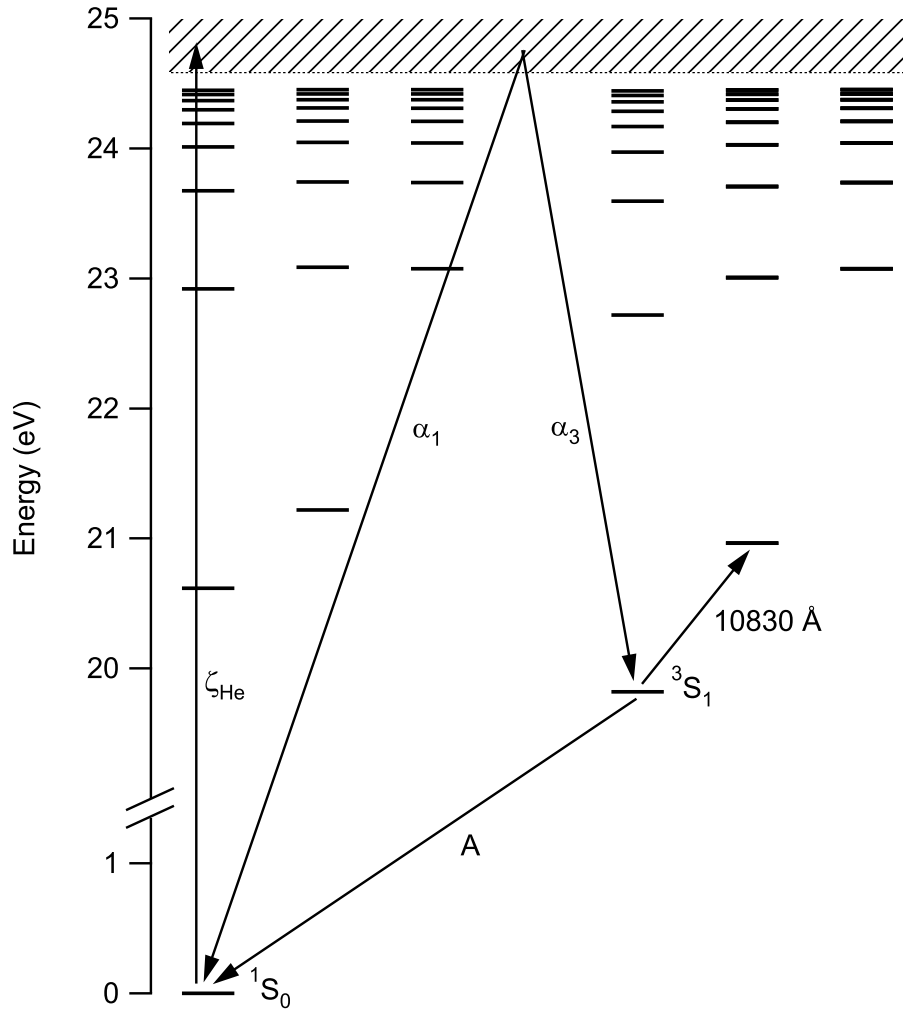
Figure 9.1: Simplified energy level diagram of atomic helium, showing only S, P, and D terms up through a principal quantum number of 10. The key processes thought to control the abundance of the metastable $2\,^3S_1$ state, along with the absorption line from this state at 10830 Å, are indicated. It is assumed that all electron recombinations into either the singlet or triplet manifold quickly lead to the ground state of that manifold by allowed spontaneous emission.

state, then thought to be the dominant method of depopulation. This 2-photon decay proceeds on a timescale of $A^{-1} \gtrsim 116$ days (Drake & Dalgarno, 1968). In the following year, the radiative lifetime associated with 1-photon decay was computed to be $A^{-1} \approx 7$ hours (Griem, 1969), nearly 400 times faster than the 2-photon decay. This value was later refined to $A^{-1} = 2.5$ hours (Woodworth & Moos, 1975; Hata & Grant, 1981), still much faster, and as a result the analyses performed by Scherb (1968) and Rees et al. (1968) had greatly overestimated the population in the metastable state (this possibility was noted by Rees et al., 1968). Consequently, the thought of observing interstellar metastable helium was abandoned.

Because of the high ionization rate inferred from H_3^+, we decided to revisit these calculations considering up-to-date rate coefficients and improved telescope/detector capabilities. Assuming the same chemical scheme as in the past, we can derive the steady state equations for the ground, ionized, and metastable states:

$$\alpha_1 n_e n_i + n_m A = n_g \zeta_{\mathrm{He}}, \tag{9.1}$$

$$n_g \zeta_{\mathrm{He}} = (\alpha_1 + \alpha_3) n_e n_i, \tag{9.2}$$

$$\alpha_3 n_e n_i = n_m A. \tag{9.3}$$

Here, n_g, n_i, and n_m denote the populations of the ground, ionized, and metastable levels, respectively; ζ_{He}, the total ionization rate of He^0 atoms due to cosmic rays, including the effects of secondary electrons; α_1 and α_3, the total, direct recombination rates to all singlet levels and to all triplet levels, respectively; n_e, the electron density in the gas; and A, the Einstein coefficient for spontaneous emission from the metastable level. The units of each term in equations (9.1) through (9.3) are $\mathrm{cm}^{-3}\ \mathrm{s}^{-1}$. All recombinations to triplet levels above the metastable level are assumed to produce subsequent radiative cascades to the metastable level that are effectively instantaneous, owing to the long lifetime of the latter level. Similarly, all recombinations to singlet levels are assumed to cascade promptly to the ground level. Equations (9.2) and (9.3) can be solved for the ratios n_i/n_g and n_m/n_i, and thus for n_m/n_g as well. These ratios can be substituted into the definition of the fractional population of the metastable level,

$$f_m = \frac{n_m}{(n_m + n_i + n_g)}, \tag{9.4}$$

in order to obtain the desired relation between the fractional metastable population f_m and

the ionization rate ζ_{He},

$$\frac{1}{f_m} = 1 + \frac{A}{(\alpha_3 n_e)} + \frac{A}{(b\zeta_{\text{He}})}. \tag{9.5}$$

The triplet branching fraction for recombinations at 70 K is $b = \alpha_3/(\alpha_1 + \alpha_3) = 0.62$, since $\alpha_1 = 4.0 \times 10^{-12}$ cm^3 s^{-1} and $\alpha_3 = 6.6 \times 10^{-12}$ cm^3 s^{-1} (R. Porter 2009, private communication). Radiative decay to the ground level is by far the fastest of the three processes mentioned above, with $A = 1.1 \times 10^{-4}$ s^{-1}. In contrast, $n_e = 0.02$ cm^{-3}, $\alpha_3 n_e = 1.3 \times 10^{-13}$ s^{-1}, and $\zeta_{\text{He}} = 3 \times 10^{-16}$ s^{-1} are representative values in diffuse clouds. Given these values, $1 \ll A/(\alpha_3 n_e) \ll A/(b\zeta_{\text{He}})$, and equation (9.5) can be approximated by

$$\frac{1}{f_m} \approx \frac{A}{b\zeta_{\text{He}}}. \tag{9.6}$$

Owing to the very large differences among the rates, this approximation to equation (9.5) is nearly exact. This holds true as long as $\zeta_{\text{He}} \ll n_e(\alpha_1 + \alpha_3) \sim 10^{-13}$ s^{-1}, such that ionization of helium by cosmic-rays is the rate-limiting step in the path to the metastable state. In this limit f_m effectively depends on ζ_{He} alone – apart from the well-determined atomic constants b and A – thus suggesting metastable helium as a fairly robust indicator of the cosmic-ray ionization rate.

9.2 Observations

9.2.1 Predictions

The fundamental question remaining then is whether the interstellar lines of He* arising from a suitable diffuse cloud are likely to be detectable. The strengths of these lines are fixed by the cloud's column density of metastable atoms, N_m, which can be calculated from

$$N_m = f_m N(\text{He}) = f_m A(\text{He}) N_{\text{H}}, \tag{9.7}$$

where $N(\text{He})$ is the total column density of helium atoms in all states, N_{H} is the total column density of hydrogen nuclei $[N_{\text{H}} = N(\text{H}) + 2N(\text{H}_2)]$, and $A(\text{He}) = N(\text{He})/N_{\text{H}} = 0.097$ is the relative abundance of helium with respect to hydrogen (Anders & Grevesse, 1989). The fraction of interstellar helium sequestered in the grains has also been assumed negligible. If a direct measurement of N_{H} is not available, an alternative is to use $N_{\text{H}} = \beta E(B-V)$, where $E(B-V)$ is the observed color excess, and $\beta = N_{\text{H}}/E(B-V) = 5.8 \times 10^{21}$ cm^{-2} mag^{-1} is the interstellar gas-to-dust ratio (Bohlin et al., 1978).

To estimate the expected line strengths, we assume $E(B - V) = 1.0$ mag and $\zeta_{\text{He}} = 3 \times 10^{-16}$ s^{-1} in a suitable, individual interstellar cloud. The former value leads to $N_{\text{H}} = 5.8 \times 10^{21}$ cm^{-2} and $N(\text{He}) = 5.6 \times 10^{20}$ cm^{-2}. A substitution of the assumed value of ζ_{He} into equation (9.6) gives $f_m = 1.7 \times 10^{-12}$. Then, $N_m = f_m N(\text{He}) = 9.5 \times 10^8$ cm^{-2}. The best choice among the available He I* lines is the 1s2s ^{3}S - 1s2p ^{3}P multiplet located near 10830 Å. Data for the transitions associated with this multiplet are shown in Table 9.1, where column 4 gives the oscillator strengths. These lines are stronger than other transitions arising from the metastable level (such as the multiplet near 3889 Å), and the near-infrared wavelength is advantageous in observations of heavily reddened stars with large total column densities of helium.

Table 9.1: The 1s2s ^{3}S - 1s2p ^{3}P Multiplet of He I

λ_{air} (Å)	J(lower)	J(upper)	f
10829.0911	1	0	0.060
10830.2501	1	1	0.180
10830.3398	1	2	0.300

Notes: Wavelengths and oscillator strengths are from the NIST Atomic Spectra Database (Ralchenko et al., 2008)

Assuming $N_m = 9.5 \times 10^8$ cm^{-2}, the equivalent width of an unresolved blend of the two strongest lines of the multiplet, which are separated by only 2.5 km s^{-1}, would be $W_\lambda = 0.47$ mÅ. If a spectrometer with a resolving power of 70,000 were used, the line would have a central depth of $\sim$0.30%, thus demanding a signal-to-noise ratio (S/N) of $\sim$1000 on the continuum for a 3σ detection. Modern optical echelle spectrographs can easily reach S/N exceeding 2000 (e.g., Ádámkovics et al., 2003), but reaching such a high S/N in the near-infrared is a significant challenge.

9.2.2 Target Selection

In choosing a target, we searched for sight lines that had a combination of several desirable characteristics: high color excess; high cosmic-ray ionization rate as inferred from H$_3^+$; relatively bright J-band magnitude; few interstellar velocity components; well-behaved stellar absorption features. Using these criteria, we arrived at HD 183143 as our most favorable

target, with $J = 4.18$, $V = 6.86$, $E(B-V) = 1.27$, and a spectral type of B7Iae. The star's photospheric He I absorption lines at 5875, 6678, and 7065 Å are relatively broad, with FWHM ≥ 66 km s^{-1}, and they are also free from any interfering emission components (Thorburn et al., 2003). This suggests that the photospheric 10830 Å line may desirably provide a smooth background with a shallow slope, against which one could search for the much narrower, weak interstellar lines. In addition, many interstellar absorption lines along this line of sight have been previously studied, including CH and CH$^+$ (Gredel et al., 1993), and CN, H$_3^+$, and ^{12}CO (McCall et al., 2002). These observations reveal that there are two distinct interstellar cloud groups at different velocities. Although this means that not all of the interstellar helium is at one velocity, it does provide a very useful method for potentially confirming a detection. Additionally, H$_3^+$ observations have been used to determine the ionization rate of molecular hydrogen, ζ_2, in this sight line (Indriolo et al., 2007).

Using values specific to the HD 183143 sight line ($E(B-V) = 1.27$; $\zeta_{\mathrm{He}} = 3.5 \times 10^{-16}$ s^{-1}) we can again perform the calculations in Section 9.2.1 to determine the expected line strength. The resulting equivalent width is $W_\lambda = 0.70$ mÅ. Because the sight line has 2 velocity components though, we assume equal amounts of material in each cloud, and thus expect 2 absorption lines with $W_\lambda = 0.35$ mÅ. These would require S/N$\sim$1300 for a 3σ detection given the same instrument capabilities assumed above. While obtaining a S/N this high is difficult in the near-infrared, some of the most advanced telescope/detector combinations are capable of approaching such results, so we proceeded with observations.

9.2.3 Execution

Data were taken near the He I* line at 10830 Å using the Phoenix spectrometer (Hinkle et al., 2003) on the Gemini South Telescope. The spectrometer was used with its echelle grating and 0''.17 slit to produce a resolving power of $\sim$70,000, and the J9232 filter to select the correct order. Observations of both the target (HD 183143) and standard (α Aql) stars were taken on May 25, 2008 and June 28, 2008. Total integration times were 33 and 30 minutes for the target and 1.9 and 1.4 minutes for the standard on each night, respectively. During each set of observations, the star was nodded along the slit in an ABBA pattern to allow for the later subtraction of neighboring images, and thus the removal of the atmospheric background and detector bias levels.

9.3 Data Reduction

A significant portion of the data reduction – dark current subtraction, subtraction of neighboring images, removal of bad pixels, flat fielding, combination of exposures with the spectral image in the same nod position, fitting of the spectral response, and spectral extraction – was performed using NOAO's IRAF package. During this process, we combined the methods outlined by Kulesa (2002) with those given by NOAO's online Phoenix documentation[1] in order to obtain the best possible S/N. Once the one-dimensional spectra were extracted, they were imported to IGOR Pro, where we have macros set up to complete the reduction (McCall, 2001).

Because of the annual shift in the relative positions of (inter)stellar and atmospheric features with time, the data from different nights were first analyzed separately. In all cases, however, the expected locations of the interstellar He I* lines lie within the broad stellar absorption line. Because the S/N of the standard star was actually *lower* than that of the target in the June data, we decided to forego the process of ratioing by the standard star and we instead directly fit the stellar absorption feature. Both the A and B beams for each night were wavelength calibrated using atmospheric lines and then added together. The broad stellar absorption feature was then fit using the summation of three Gaussian functions, all of which were constrained to have FWHM at least 3 times that of the 10 km s^{-1} measured for interstellar absorption features along the line of sight. The spectra from each night were then divided by their respective fits and shifted to be in the local standard of rest (LSR) frame. Finally, the fully reduced spectra from both nights were added together and converted to velocity space to produce the top spectrum shown in Figure 9.2.

9.4 Results

There is no indication of interstellar He* absorption at either of the expected velocities. While we did obtain a relatively high S/N (~ 700) for high-resolution infrared spectroscopy, we were unable to achieve the desired S/N ~ 1300. The non-detection of the He I* lines enabled us to calculate an upper limit to the column density of metastable helium along this line of sight. First, the upper limit to the equivalent width, W_λ, was computed via

$$W_\lambda < \sigma \lambda_{\mathrm{pix}} \sqrt{\mathcal{N}_{\mathrm{pix}}}, \tag{9.8}$$

---

[1]See http://www.noao.edu/usgp/phoenix/phoenix.html

129
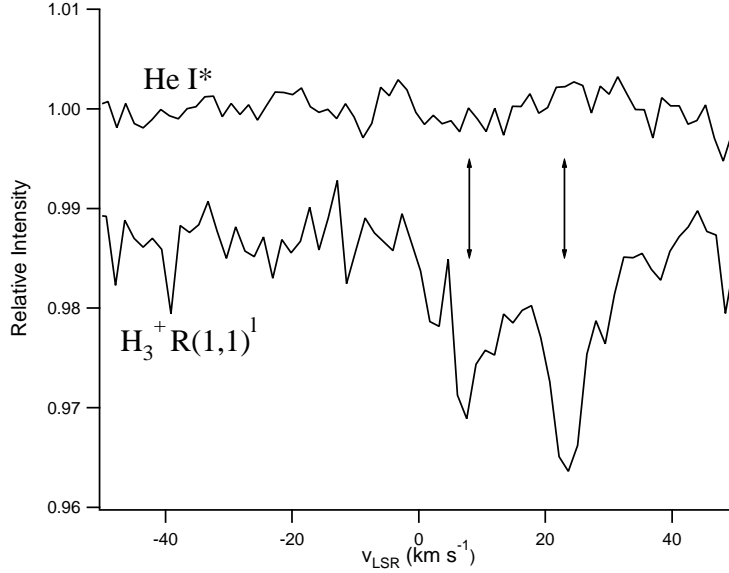
Figure 9.2: Spectra of HD 183143 in velocity space. The top spectrum, observed with Phoenix at Gemini South, has been adjusted for the centroid of the unresolved blend of the 1-1 and 1-2 members of the He I* multiplet, and the broad photospheric line has been divided out. The bottom spectrum (from McCall et al., 2002) shows the $R(1,1)^l$ transition of H_3^+ for reference. Arrows indicate the two interstellar velocity components which have been observed in various molecules (CH, CH^+, CN, ^{12}CO, H_3^+).

where $\sigma = 0.00145$ is the standard deviation in the spectrum, $\lambda_{pix} = 0.05$ Å is the wavelength per pixel, and $\mathcal{N}_{pix} = 13$ is the number of pixels expected in a single absorption component given a 10 km s^{-1} FWHM (this is the average FWHM of H_3^+ lines reported by McCall et al. (2002)). These quantities result in an upper limit to the equivalent width of $W_\lambda < 0.26$ mÅ ($W_\lambda < 0.78$ mÅ at the 3σ level).

Next, the standard relation between equivalent width and column density was used:

$$N = \frac{W_\lambda m_e c^2}{\lambda^2 \pi e^2 f}, \tag{9.9}$$

where m_e is the electron mass, c is the speed of light, λ is the wavelength of the transition, e is the electron charge, and $f = 0.48$ is the sum of the oscillator strengths of the 2 strongest, blended lines. Inserting the known parameters results in a 3σ upper limit to the column density $N_m < 1.6 \times 10^9$ cm^{-2} in a single velocity component. However, there are 2 cloud components along this sight line, so the total line of sight limit is $N_m < 3.2 \times 10^9$ cm^{-2}.

9.5 Analysis

9.5.1 Reaction Network Revisited

In planning observations and calculating predicted line strengths, we relied on the simple chemical scheme that only considers the destruction of He^+ via electron recombination. However, during the course of this study we identified (from advanced chemical models, e.g. Woodall et al. (2007)) several competing reactions that could be important in destroying He^+ in diffuse clouds:

$$He^+ + H \rightarrow He + H^+, \tag{9.10}$$

$$He^+ + H_2 \rightarrow He + H_2^+, \tag{9.11}$$

$$He^+ + H_2 \rightarrow He + H + H^+, \tag{9.12}$$

$$He^+ + CO \rightarrow He + O + C^+. \tag{9.13}$$

Rate coefficients for these reactions, as well as the electron recombination reactions, can be determined for a specific temperature, T (in Kelvin), using the fitting parameters (α, β, and γ) in Table 9.2 in conjunction with the expression

$$k = \alpha \left(\frac{T}{300} \right)^{\beta} e^{-\gamma/T} \text{ cm}^3 \text{ s}^{-1}. \tag{9.14}$$

Unlike the case of electron recombination, these reactions should not lead to metastable helium. Simple energetics arguments demonstrate why this is the case. The energy difference between the ionization potential of helium (24.6 eV) and the excitation energy of the metastable state (19.8 eV) is only 4.8 eV. In order to dissociate and/or ionize the reaction partners of He^+, reactions (9.10 – 9.13) require energies of 13.6, 15.4, 18.1, and 22.5 eV, respectively (assuming all reactants are in the ground electronic state). At diffuse cloud temperatures ($\sim$70 K) thermal energy is much less than 1 eV, and so the kinetic energy of the reactants will have no effect. Following these arguments, the neutral helium product can only be in the ground state as more than 4.8 eV of the helium ionization potential must be used in each reaction. As a result, accounting for these reactions greatly decreases the fraction of helium ions which pass through the triplet manifold, and thus the population of the metastable state.

However, we also made the assumption that the metastable state is only populated via cosmic-ray ionization of He, followed by electron recombination. Given that a smaller branching fraction limits this pathway, electron impact excitation into the triplet manifold will be

a competing formation mechanism. Cross sections for ionization and excitation of helium by electrons in the 10–1000 eV range are shown in Dalgarno et al. (1999) figures 2a & 2b. To compute the rate of ionization and excitation, one must perform an integral in energy space over the product of each cross section with the differential energy spectrum of electrons in the ISM. This full calculation is hindered by the fact that the spectrum of secondary electrons (those produced during ionization events) is unknown, and cannot be derived from the differential energy spectrum of cosmic-ray protons which is also unknown below ~ 1 GeV. The complexity associated with deriving the spectrum of secondary electrons is beyond the scope of this paper, thus we make some simplifications in estimating the importance of electron impact excitation into the triplet manifold of helium.

Table 9.2: Rate Coefficients for Reactions Involving Ionized Helium

Reaction	α	β	γ	Coefficient at 70 K $(\mathrm{cm}^3\ \mathrm{s}^{-1})$	References
$\mathrm{He}^+ + \mathrm{H} \rightarrow \mathrm{He} + \mathrm{H}^+$	1.2×10^{-15}	0.25	0	$k_{9.10} = 8.3 \times 10^{-16}$	1
$\mathrm{He}^+ + \mathrm{H}_2 \rightarrow \mathrm{He} + \mathrm{H}_2^+$	7.2×10^{-15}	0	0	$k_{9.11} = 7.2 \times 10^{-15}$	2
$\mathrm{He}^+ + \mathrm{H}_2 \rightarrow \mathrm{He} + \mathrm{H} + \mathrm{H}^+$	3.7×10^{-15}	0	35	$k_{9.12} = 2.2 \times 10^{-14}$	2
$\mathrm{He}^+ + \mathrm{CO} \rightarrow \mathrm{He} + \mathrm{O} + \mathrm{C}^+$	1.6×10^{-9}	0	0	$k_{9.13} = 1.6 \times 10^{-9}$	3,4
$\mathrm{He}^+ + e \rightarrow \mathrm{He}(1\ ^1\mathrm{S}) + h\nu$	1.76×10^{-12}	-0.56	0	$\alpha_1 = 4.0 \times 10^{-12}$	5
$\mathrm{He}^+ + e \rightarrow \mathrm{He}(2\ ^3\mathrm{S}) + h\nu$	2.84×10^{-12}	-0.59	0	$\alpha_3 = 6.6 \times 10^{-12}$	5

Notes: Coefficients at temperatures between about 10 and 300 K can be derived using α, β, γ, and equation (9.14). Rate coefficients and their references for reactions (9.10), (9.11), (9.12), and (9.13) were found at http://www.udfa.net/.
References: (1) Stancil et al. (1998); (2) Barlow (1984); (3) Laudenslager et al. (1974); (4) Anicich et al. (1977); (5) R. Porter 2009, private communication

Assuming that all secondary electrons have the same energy, the ratio between the rate of excitation into all triplet states and the rate of ionization can be determined by taking the ratio of the respective cross sections at a given energy. We take this ratio at 30 eV (the mean value given by Cravens & Dalgarno (1978)), and find the rate of excitation into all triplet states to be 2 times faster than the rate of ionization by secondary electrons. To determine the overall importance of electron impact excitation then, we need to find a relationship between

132

the total ionization rate of helium and the ionization rate due to secondaries. Using relations between the primary ionization rates of hydrogen and helium (Habing & Goldsmith, 1971; Liszt, 2003) and between the primary ionization rate of hydrogen and the total ionization rate of helium (Glassgold & Langer, 1974; Tielens, 2005), we estimate that ionization by secondary electrons accounts for about 1/6 of the total ionization rate of helium. This, in turn, leads to the approximation that the rate for electron impact excitation into the triplet manifold — and thus the metastable state (which we denote δ_{He^*}) — should be roughly 1/3 that of the total ionization rate of helium (i.e. $\delta_{\mathrm{He}^*} \approx \zeta_{\mathrm{He}}/3$; we use this relation for the remainder of this paper).

Mathematically, these additional formation and destruction reactions can easily be included by altering the steady state equations in Section 9.1.2, resulting in 2 changes to our analysis. First, due to the additional destruction pathways of He$^+$, the branching fraction, b, must be redefined as

$$b \equiv \frac{\alpha_3 n_e}{n(\mathrm{H})k_{9.10}+n(\mathrm{H_2})(k_{9.11}+k_{9.12})+n(\mathrm{CO})k_{9.13}+n_e(\alpha_1+\alpha_3)}. \tag{9.15}$$

In many cases, however, absolute abundances are not known and it is thus convenient to recast equation (9.15) in terms of fractional abundances as

$$b = \frac{\alpha_3 x_e}{(1-f_{\mathrm{H_2}})k_{9.10}+f_{\mathrm{H_2}}(k_{9.11}+k_{9.12})/2+x_{\mathrm{CO}}k_{9.13}+x_e(\alpha_1+\alpha_3)}, \tag{9.16}$$

where $x_j \equiv n_j/n_{\mathrm{H}}$, $n_{\mathrm{H}} \equiv n(\mathrm{H}) + 2n(\mathrm{H_2})$, and the molecular hydrogen fraction $f_{\mathrm{H_2}} \equiv 2n(\mathrm{H_2})/n_{\mathrm{H}}$. Second, equation (9.6) must be recast to include electron impact excitation into the metastable state, and becomes

$$\frac{1}{f_m} \approx \frac{A}{b\zeta_{\mathrm{He}} + \delta_{\mathrm{He}^*}}. \tag{9.17}$$

While the analysis now includes many more parameters, we can still calculate the fractional abundance of metastable helium, and thus the expected line strength, toward HD 183143. We assume that fractional abundances are constant throughout the cloud, allowing us to substitute column densities for number densities when available (i.e. $x_j = N_j/N_{\mathrm{H}}$). Using the color excess as in Section 9.2.1 gives $N_{\mathrm{H}} = 7.4 \times 10^{21}$ cm^{-2}. This is used in conjunction with spectroscopic observations of CO which indicate $N(\mathrm{CO}) \approx 10^{15}$ cm^{-2} (McCall et al., 2002) to compute x_{CO}. The assumption that there are equal amounts of atomic and molecular hydrogen is quantified by $f_{\mathrm{H_2}} = 2/3$. Finally, observations of C$^+$ in diffuse clouds have shown that $x_e \sim 1.4 \times 10^{-4}$, assuming that nearly all electrons come from

this singly ionized carbon (Cardelli et al., 1996). Combining these data and assumptions with the rate coefficients in Table 9.2, the new branching fraction is $b = 0.08$, about one-eighth of the value considering electrons alone. Substituting this branching fraction and the relevant parameters from Sections 9.2.1-9.2.2 into equation (9.17) results in values of $f_m = 1.3 \times 10^{-12}$, $N_m = 9.3 \times 10^8$ cm^{-2}, and $W_\lambda = 0.46$ mÅ. Again splitting the material into 2 equal cloud components decreases the equivalent widths to $W_\lambda = 0.23$ mÅ, which would require a S/N$\sim$ 2000 for a 3σ detection.

9.5.2 Cosmic-Ray Ionization Rate of Helium

Re-arranging equation (9.17), we can turn this problem around and compute an upper limit to the cosmic-ray ionization rate of helium using our observations. Given the upper limit to the metastable column density, $N_m < 3.2 \times 10^9$ cm^{-2}, and the estimated total helium column, $N(\text{He}) = \beta A(\text{He})E(B-V) = 7.1 \times 10^{20}$ cm^{-2}, the 3σ upper limit to the fractional metastable population is $f_m < 4.5 \times 10^{-12}$. Using this in concert with the branching fraction above, $b = 0.08$, results in $\zeta_{\text{He}} < 1.2 \times 10^{-15}$ s^{-1}. This upper limit is about 5 times larger than the ionization rate inferred from H$_3^+$ observations (assuming the relation between the ionization rate of helium and molecular hydrogen is given by $2.3\zeta_{\text{He}} = 1.5\zeta_2$ (Glassgold & Langer, 1974)). Because of electron impact excitation into the metastable state though, this determination of the ionization rate relies on a much more indirect analysis than was initially proposed. Comparing $b\zeta_{\text{He}}$ to δ_{He^*}, we can compute the relative importance of each formation mechanism via

$$P(\delta_{\text{He}^*}) = \frac{\delta_{\text{He}^*}}{b\zeta_{\text{He}} + \delta_{\text{He}^*}} = (3b+1)^{-1}. \tag{9.18}$$

In doing so, we find that electron impact excitation accounts for 80% of the metastable population while ionization and electron recombination accounts for 20%.

9.6 Discussion

While the reactions associated with metastable helium are more complex than previously presented, we still see it as a viable tracer of the cosmic-ray ionization rate. As such, we decided to investigate the prospects for He* detections in various interstellar environments, including diffuse molecular clouds ($100 \lesssim n_\text{H} \lesssim 500$ cm^{-3}, $f_{\text{H}_2} \gtrsim 0.1$), dense clouds ($n_\text{H} \gtrsim 10^4$ cm^{-3}, $f_{\text{H}_2} \approx 1$), and diffuse atomic clouds ($n_\text{H} \lesssim 100$ cm^{-3}, $f_{\text{H}_2} \lesssim 0.1$) (Snow & McCall, 2006). The following analyses will highlight the branching fraction in each environment, as

well as the relative importance of electron impact excitation vs. ionization + recombination using equation (9.18).

9.6.1 Diffuse Molecular Clouds

Given that the analysis in Section 9.2.1 did not account for the processes examined in Section 9.5.1, we felt it prudent to revisit the calculations for diffuse molecular clouds. We use the same values as before ($E(B - V) = 1$; $\zeta_{\text{He}} = 3 \times 10^{-16}$ s^{-1}), but now also assume $f_{\text{H}_2} = 2/3$, $x_e = 1.4 \times 10^{-4}$, and $x_{\text{CO}} = 10^{-7}$. The general results for this environment ($b = 0.08$; $f_m = 1.1 \times 10^{-12}$; $N_m = 6.3 \times 10^8$ cm^{-2}; $W_\lambda = 0.31$ mÅ) are similar to those for the specific diffuse molecular sight line HD 183143, with the differences due to the lower color excess. Assuming that all of the material has the same velocity, metastable helium absorption should be observable in diffuse molecular clouds at a 3σ level with S/N$\sim$ 1500. Given the small branching fraction above, $P(\delta_{\text{He}^*}) = 0.8$ and we conclude that metastable helium is predominantly formed via electron impact excitation in diffuse molecular clouds.

9.6.2 Dense Clouds

Dense clouds, while providing a larger total helium column, have several characteristics detrimental to the formation of metastable helium. The cosmic-ray ionization rate tends to be about 1 order of magnitude lower in dense clouds than in diffuse clouds (Dalgarno, 2006). Also, the fractional abundance of electrons is much lower, $x_e \approx 4 \times 10^{-8}$, while the fractional abundance of CO is much higher, $x_{\text{CO}} \approx 1.4 \times 10^{-4}$ (Woodall et al., 2007). Because $k_{9.13}$ is so much larger than any of the other rate coefficients, collisions with CO will dominate the destruction of He$^+$ and equation (9.16) can be simplified to

$$b \approx \frac{x_e \alpha_3}{x_{\text{CO}} k_{\text{CO}}}. \tag{9.19}$$

Given the fractional abundances above and the relevant rate coefficients (α_3 and k_{CO} were computed for $T = 40$ K), the branching fraction is $b \sim 10^{-6}$. As a result, $P(\delta_{\text{He}^*}) \approx 1$, meaning that metastable helium is formed exclusively by electron impact excitation in dense clouds. Even with this formation mechanism though, the expected equivalent width ($W_\lambda = 0.13$ mÅ) and necessary S/N for a 3σ detection (S/N$\sim$ 3700), coupled with the large attenuation of the background star's flux at 1 μm, make the detection of He* in dense clouds highly unlikely.

9.6.3 Diffuse Atomic Clouds

Diffuse atomic clouds, on the other hand, have negligible concentrations of H_2 and CO (Snow & McCall, 2006) and presumably share the high ionization rate of diffuse molecular clouds. In purely atomic conditions, electron recombination only has to compete with reaction (9.10) and equation (9.16) can be approximated as

$$b \approx \frac{x_e \alpha_3}{k_{9.10} + x_e(\alpha_1 + \alpha_3)}. \tag{9.20}$$

The simplified result for atomic clouds is then $b \approx 0.40$, with a corresponding $P(\delta_{\mathrm{He}^*}) = 0.45$, meaning that ionization and electron impact excitation play roughly equal roles in forming metastable helium in such environments. Despite this branching fraction being closer to the ideal case of $b = 0.62$, the low amount of material along such a sight line ($E(B - V) \sim 0.1$) results in a predicted equivalent width of $W_\lambda \approx 0.06$ mÅ. However, there are some diffuse atomic sight lines with more favorable conditions. One such candidate, σ Sco, has $E(B - V) = 0.40$ (Clayton & Hanson, 1993) and thus a predicted equivalent width of $W_\lambda \approx 0.22$ mÅ using equations (9.17) & (9.20). However, σ Sco also has measured values of $N(\mathrm{H}) = 2.4 \times 10^{21}$ cm^{-2}, $N(\mathrm{H}_2) = 6.2 \times 10^{19}$ cm^{-2} (Savage et al., 1977), and $N(\mathrm{CO}) = 6.5 \times 10^{12}$ cm^{-2} (Allen et al., 1990), which correspond to $f_{\mathrm{H}_2} = 0.049$ and $x_{\mathrm{CO}} = 2.6 \times 10^{-9}$. Using these values and equation (9.16), we can test the accuracy of equation (9.20) at small molecular fractions. The result is $b = 0.31$, or about a 30% error in the approximation. At $f_{\mathrm{H}_2} = 0.15$, equation (9.20) overestimates b by a factor of 2, so this approximation should only be applied for $f_{\mathrm{H}_2} \lesssim 0.1$. Taking the branching fraction from the full calculation, we predict an equivalent width of $W_\lambda \approx 0.20$ mÅ, and a corresponding S/N ~ 2400 necessary for a 3σ detection. If such a detection can be made, however, it will provide the exciting opportunity to probe the cosmic-ray ionization rate in an environment where H_3^+ observations cannot be made due to the low molecular fraction.

9.7 Conclusions

We have analyzed the possibility of detecting absorption lines due to interstellar metastable helium at 10830 Å. Observations toward the diffuse cloud sight line HD 183143 were taken, and a spectrum with S/N$\sim$700 was obtained, but no interstellar He I* lines were detected. In examining the chemistry associated with metastable helium, we have identified important formation and destruction pathways, and have derived new equations for the steady state analysis of He*. While these reactions have been known for some time, this is the first in-

stance where they have been applied to metastable helium chemistry. Using our observations and the newly derived equations, we inferred an upper limit for the cosmic-ray ionization rate of helium which, although consistent with other studies, is about 5 times larger than previously inferred values.

To determine if future observations of interstellar He* are warranted, we predicted the S/N ratios necessary for 3σ detections in various environments. Diffuse molecular clouds are the most promising targets with S/N$\sim$1500 required, while favorable diffuse atomic clouds need S/N$\sim$2400. While such observations are extremely challenging at present, advancements in telescope and near-infrared detector technology may one day make metastable helium a widely applicable probe of the cosmic-ray ionization rate. In diffuse molecular clouds, He* will act as a cosmic-ray probe independent of H_3^+, and together with H_3^+ it will also enable determination of the absorption path length and average cloud density. He* observations will also be especially important for diffuse atomic clouds, where there are no other reliable tracers of the ionization rate.

Note added in proof: We would like to thank Nick Abel for bringing to our attention the reaction $He^+ + H \rightarrow HeH^+ + h\nu$, which acts in a similar manner as reactions (9.10)-(9.13). The rate coefficient for this reaction at about 70 K is $k \sim 2 \times 10^{-15}$ s^{-1} (Roberge & Dalgarno, 1982; Kraemer et al., 1995). Adding this reaction to our analysis has a negligible effect on the dense cloud and diffuse molecular cloud results, but changes the results for the diffuse atomic cloud σ Sco as follows: $b = 0.19$, $P(\delta_{He^*}) = 0.64$, $W_\lambda \approx 0.16$ mÅ, and S/N$\sim$3000.

Chapter 10

Conclusions

10.1 Summary of Findings

The survey of H_3^+ in diffuse molecular clouds now covers 50 sight lines, with detections in 21 of those. Cosmic-ray ionization rates (and upper limits) are inferred in all of these sight lines. Where H_3^+ is detected, ionization rates are in the range $(1.7 \pm 1.0) \times 10^{-16}$ s$^{-1} < \zeta_2 < (10.6 \pm 6.8) \times 10^{-16}$ s^{-1}, with a mean value of $\zeta_2 = (3.3 \pm 0.4) \times 10^{-16}$ s^{-1}. This is about 1 order of magnitude larger than ionization rates inferred from previous observations of other molecular species (e.g., OH and HD), although recent observations of OH$^+$ and H$_2$O$^+$ with *Herschel* are suggestive of high ionization rates as well (0.6×10^{-16} s$^{-1} < \zeta_H < 2.4 \times 10^{-16}$ s^{-1}; Neufeld et al., 2010). The lowest 3σ upper limits found for sight lines where H_3^+ is not detected are about $\zeta_2 < 0.4 \times 10^{-16}$ s^{-1}. Together, the wide range of inferred ionization rates and the low upper limits allude to variations in ζ_2 between different diffuse cloud sight lines.

Comparisons of ζ_2 with various line-of-sight properties (including Galactic latitude, Galactic longitude and Galactocentric radius) show no strong correlations. This suggests that variations in the cosmic-ray ionization rate between different sight lines are caused not by large scale, but local effects. A comparison of ζ_2 with the total hydrogen column density (N_H) shows no strong correlation when only diffuse clouds are considered. When ionization rates inferred for dense cloud sight lines with much higher N_H are included though, ζ_2 is seen to decrease with increased N_H. This correlation is expected as low-energy cosmic rays — those most efficient at ionization — will lose all of their energy before reaching the interiors of dense clouds. The lack of a correlation amongst diffuse cloud sight lines suggests that the particles primarily responsible for ionization must be able to completely penetrate diffuse clouds, while the difference in ζ_2 between diffuse and dense clouds indicates that these same particles must be stopped in the outer layers of dense clouds.

Given that total column density — at least in the case of diffuse clouds — is unable to explain variations in the ionization rate, the concept of a cosmic-ray spectrum that is uniform throughout the Galaxy must be reconsidered. Instead, the flux of low-energy (MeV) cosmic rays is most likely controlled by proximity to local sites of particle acceleration. In this

scenario, clouds that are closer to acceleration sites will show a higher ionization rate than those that are more distant. To test this hypothesis, observations were made searching for H_3^+ in 6 sight lines that probe molecular material in the vicinity of the supernova remnant IC 443. H_3^+ is detected in 2 of these, and inferred ionization rates are about $\zeta_2 = (20\pm10)\times10^{-16}$ s^{-1}, higher than for any other diffuse cloud sight lines. This is further evidence supporting supernova remnants as sites of cosmic-ray acceleration. However, H_3^+ is not detected in the other 4 sight lines, and upper limits to the ionization rate in those are consistent with elsewhere in the Galaxy. The large differences between the ionization rates inferred for sight lines with and without detections of H_3^+ near IC 443 point to variations in the cosmic-ray spectrum on parsec size scales.

Theoretical calculations of the cosmic-ray ionization rate were performed for the purpose of determining the shape of the cosmic-ray spectrum best capable of simultaneously reproducing values of ζ_2 inferred in both diffuse and dense clouds, as well as observed light element (^{6}Li,^{7}Li,^{9}Be,^{10}B,^{11}B) abundances. The preferred spectrum consists of 2 components: (1) the propagated spectrum from a standard leaky-box model; and (2) a component with the relation $\phi \propto p^{-4.3}$ that provides a high flux of particles at low energies. The necessity of a component beyond the standard interstellar cosmic-ray spectrum suggests a local flux of particles in addition to the uniform Galactic spectrum, and the steep slope of the 2nd component is indicative of particle acceleration in weak shocks. This presents the possibility that some fraction of low-energy cosmic rays are accelerated in stellar winds or similar weak, localized shocks.

Ionization rates inferred from observations of H_3^+, in concert with theoretical models of the cosmic-ray spectrum, have greatly increased our understanding of cosmic rays in the interstellar medium. This, in turn, improves our ability to model interstellar chemistry. As more molecules are observed in the ISM, constraints on ζ_2 will only improve, and variations in the cosmic-ray ionization rate can be studied in more detail.

10.2 Future Prospects

Several projects, both on the observational and theoretical fronts, can serve to better our understanding of the cosmic-ray ionization rate in the Galactic ISM. Brief discussions of some of these are presented below in no particular order.

10.2.1 Comparing ζ_2 Inferred from H_3^+ to ζ_H Inferred from OH^+, H_2O^+, and H_3O^+

Aside from H_3^+, other molecular ions such as OH^+, H_2O^+, and H_3O^+ are now being used to infer the cosmic-ray ionization rate in diffuse clouds (Gerin et al., 2010; Neufeld et al., 2010; Gupta et al., 2010). These three species are observable with *Herschel*, and have already been observed toward regions where H_3^+ is detected (e.g., W51, W33 A, the Galactic center). This means that independent estimates of the ionization rate can be directly compared in the same sight line, thus allowing for a check on the assumed reaction network surrounding each species, as well as a search for systematic differences. Additionally, all 4 species can be used together in a more complete chemical model to infer a single ionization rate consistent with all observations for a given line of sight. Further observations of H_3^+ where OH^+, H_2O^+, and H_3O^+ have been detected — and vice versa — will expand upon the sample of sight lines where such comparisons can be made, and improve our understanding of diffuse cloud chemistry. Unfortunately, the limited lifetime of *Herschel* and the requirement that background sources be bright at both L-band and in the THz regime will restrict the overlap between H_3^+ and oxygen bearing ions to only a handful of sight lines (likely $\lesssim 10$).

10.2.2 Further Study of H_3^+ Near Supernova Remnants

As the results from H_3^+ observations near IC 443 are interesting (if puzzling), it would be worthwhile to try this experiment near more supernova remnants. Although IC 443 is the most well-studied case of a supernova remnant interacting with its surrounding molecular material, many more such objects exist, including W28, W44, W51 C, and 3C 391. All of these objects are coincident with gamma-ray emission, thought to be the result of decaying neutral pions produced by inelastic collisions between the ambient gas and accelerated hadrons (Aharonian et al., 2008; Abdo et al., 2009, 2010a,b; Castro & Slane, 2010), and present prime targets for future H_3^+ observations. However, the necessity for background stars with $L < 7.5$ severely limits potential target sight lines at present. Of the 4 supernova remnants listed above, only W28 has multiple background sources bright enough for H_3^+ spectroscopy. These include the already observed sight line toward WR 104, and 3 others currently in queue to be observed by CRIRES at VLT. Observations will be completed by October 2011, and analysis of the H_3^+ and CO spectra shortly thereafter.

Another potential target for this project is the Vela supernova remnant. While it does not exhibit gamma-ray emission, various other studies suggest that the remnant is interacting with the surrounding material (Moriguchi et al., 2001; Nichols & Slavin, 2004). Because

Vela is relatively nearby ($d = 250$–600 pc), and is in front of the Vel OB1 and Vel OB2 associations (Cha & Sembach, 2000, and references therein), there are many background sources suitable for H_3^+ spectroscopy. In fact, H_3^+ has already been observed toward one star in the Vela SNR region, HD 73882, and the inferred ionization rate along this sight line is $\zeta_2 = 9.7 \pm 2.8 \times 10^{-16}$ s^{-1} — not quite as high as toward IC 443, but higher than the mean value in diffuse clouds. A proposal to observe H_3^+ and CO with CRIRES in 8 more sight lines toward the Vela SNR has been submitted for ESO period 88 (October 2011–March 2012).

10.2.3 Addition of a Depth-Dependent Cosmic-Ray Ionization Rate to 1D Cloud Models

The most commonly used archetype in modeling the chemistry of diffuse clouds involves a plane-parallel slab of uniform density gas illuminated by one side with UV radiation (e.g., Neufeld et al., 2005). At present, however, all such models use a constant cosmic-ray ionization rate throughout the cloud. The effects of different ionization rates on chemical abundances are determined by simply changing ζ between model runs. Given that depth-dependent cosmic-ray ionization rates are now available (Padovani et al., 2009, also modeled for a 1D plane-parallel slab), the obvious next step is to combine the two. Using the output column densities from such a model, ζ_2 as inferred from equation (5.6) could be compared to the known input ionization rate at different cloud depths. This would serve to improve our understanding of line-of-sight effects in inferring the cosmic-ray ionization rate from observations.

10.2.4 Improved Constraints on Parameters Used to Infer ζ_2

A large amount of the uncertainty in inferred cosmic-ray ionization rates (see Table 5.3) is due to the uncertainties in $N(H_2)$, n_H, and x_e. Molecular hydrogen column densities are most accurately determined directly from observations of H_2 in the UV and IR. Unfortunately, *FUSE* (the Far Ultraviolet Spectroscopic Explorer) is no longer operative, and COS (the Cosmic Origins Spectrograph) aboard *HST*, while capable of performing such observations, suffers from lower resolution. As such, observations of H_2 in the UV along sight lines where H_3^+ has been detected are unlikely in the near future. Observations of H_2 in absorption in the IR rely on electric quadrupole transitions which are incredibly weak, and have only been detected in dense cloud sight lines with large column densities ($N(H_2) \gtrsim 10^{22}$ cm^{-2}; Lacy et al., 1994; Kulesa, 2002; Usuda & Goto, 2005). For the time being then, observing CH for the purpose of estimating $N(H_2)$ is the best option for constraining this parameter.

The majority of densities (n_H) used in calculating ζ_2 are from one source: Sonnentrucker et al. (2007). These are based on the rotational excitation analysis of C_2, a molecule that has been observed in 18 out of the 50 diffuse cloud sight lines presented herein. Observations of C_2 in more sight lines where H_3^+ is detected would be helpful in lowering the uncertainty of inferred ionization rates, and provide a useful check on whether or not the material being probed is truly diffuse.

Finally, x_e has simply been set to 1.5×10^{-4} in all sight lines except the 5 among our sample where C^+ is detected (see Table B.3). Observations of C^+ are extremely difficult — the weak intersystem line at 2325 Å requires long integration times even with STIS aboard *HST* (Sofia et al., 2004), and the much stronger lines at 1334 Å are difficult to analyze (Sofia et al., 2011) — so more direct observations of C^+ are unlikely. However, observations of CO and C can be used to constrain what portion of the carbon budget is in the form of C^+. Absorption lines of both CO and C are available in the UV, and can be observed with COS on *HST*, and vibrational transitions of CO near 4.65 μm can be targeted from the ground using the same facilities capable of observing H_3^+. In constraining the fraction of carbon that exists as CO and C, such observations also help to determine whether the interstellar material is diffuse or dense.

10.2.5 Continued Survey of H_3^+ in the ISM

Of course, more observations of H_3^+ will always increase the sample of sight lines where the cosmic-ray ionization rate has been inferred. Although some of the best instruments capable of H_3^+ observations have recently become unavailable (CGS4 and *Phoenix*), CRIRES will be in operation for the foreseeable future. As H_3^+ has predominantly been observed from the northern hemisphere and CRIRES affords coverage of the southern sky, the opportunity exists to significantly expand the sample of diffuse clouds with H_3^+ observations. Increasing the sample in the northern sky, though, will likely depend on a high resolution (< 5 km s^{-1}) mid-infrared spectrograph being installed on an 8 m class telescope.

Abundant data that are already in hand but unutilized as of yet are observations toward the Galactic center performed by our collaborators Tom Geballe, Takeshi Oka, Miwa Goto, and Tomonori Usuda. Both H_3^+ and CO have been observed in several sight lines toward the Galactic center (Geballe et al., 1999; Goto et al., 2002, 2008, 2011; Oka et al., 2005; Geballe & Oka, 2010), and these observations contain a wealth of data about the Galactic center and intervening spiral arms. So far, however, absorption arising from gas in the spiral arms has simply been treated as foreground interference and subtracted to facilitate study of the Galactic center. Investigating H_3^+ in the spiral arms will add to the regions

of our Galaxy in which the cosmic-ray ionization rate has been inferred. Also, because the spiral arms are separated by several kpc and are at known distances, such a study will reveal any gradients in the ionization rate with Galactocentric radius. This may provide vital information concerning the propagation of cosmic-rays on Galactic scales, as well as the uniformity (or lack thereof) of the particle spectrum and cosmic-ray ionization rate throughout our Milky Way.

Appendix A

Computer Code

A.1 IRAF Script for Interweaving CGS4 Data and Subtracting Neighboring Images

The following sample code was used in the processing of CGS4 Data from UKIRT. The *imslice* command cuts each of the 3 input images into 256 individual images (i.e. columns of the array). The *imstack* command then pieces together all 768 columns in the order listed in the file weaverlist.txt. Finally, the *imdel* command deletes the 768 images so that the generic names a001.fits through a256.fits can be reused in processing the next set of input images. This is done for 2 consecutive observations that were taken in the A and B nod positions. The *imarith* commands then subtract the neighboring 123 images from each other, and likewise for the 456 images. Neighbor-subtracted images are identified as beginning with an 's' as opposed to a 'c'.

```
imslice c20080123_00011.I1.fits,c20080123_00011.I2.fits,c20080123_00011.I3.fits a,b,c 1
imstack @weaverlist.txt c20080123_00011_123
imdel @weaverlist.txt
imslice c20080123_00011.I4.fits,c20080123_00011.I5.fits,c20080123_00011.I6.fits a,b,c 1
imstack @weaverlist.txt c20080123_00011_456
imdel @weaverlist.txt
imslice c20080123_00012.I1.fits,c20080123_00012.I2.fits,c20080123_00012.I3.fits a,b,c 1
imstack @weaverlist.txt c20080123_00012_123
imdel @weaverlist.txt
imslice c20080123_00012.I4.fits,c20080123_00012.I5.fits,c20080123_00012.I6.fits a,b,c 1
imstack @weaverlist.txt c20080123_00012_456
imdel @weaverlist.txt
imarith c20080123_00012_123.fits - c20080123_00011_123.fits s20080123_00012_123.fits
imarith s20080123_00012_123.fits * -1. s20080123_00011_123.fits
imarith c20080123_00012_456.fits - c20080123_00011_456.fits s20080123_00012_456.fits
imarith s20080123_00012_456.fits * -1. s20080123_00011_456.fits
```

A.2 IRAF Script for Extracting 1-D Spectra from CGS4 Images

The following sample code was used to extract one-dimensional spectra in TXT format from the interwoven, neighbor-subtracted FITS files. The argument in brackets is given as

$$[xstart : xend, ystart : yend],$$

and will, using the first line of code as an example, extract the pixel values in row 95 of the array. My naming convention for output files is *objectname_nnn_i_r*.txt, where *nnn* is a shortened version of the original observation number (observation numbers at UKIRT never exceeded 999, so shortening to 3 digits from 5 simply removes the 2 leading zeroes), *i* is either 1 or 4 and denotes whether the image was woven together from images 1, 2, & 3 or 4, 5, & 6, respectively, and *r* is either *a*, *b*, or *c*, and refers to the array row extracted from the image. For a given nod position, the row on which the most flux of the spectral image is concentrated is given the label *b*, while the adjacent rows are labeled *a* and *c* (e.g., row 95 → *a*; row 96 → *b*; row 97 → *c*).

```
wspectext s20080123_00011_123.fits[95:95,1:768] bs936a_011_1_a.txt
wspectext s20080123_00011_123.fits[96:96,1:768] bs936a_011_1_b.txt
wspectext s20080123_00011_123.fits[97:97,1:768] bs936a_011_1_c.txt
wspectext s20080123_00011_456.fits[95:95,1:768] bs936a_011_4_a.txt
wspectext s20080123_00011_456.fits[96:96,1:768] bs936a_011_4_b.txt
wspectext s20080123_00011_456.fits[97:97,1:768] bs936a_011_4_c.txt
wspectext s20080123_00012_123.fits[103:103,1:768] bs936a_012_1_a.txt
wspectext s20080123_00012_123.fits[104:104,1:768] bs936a_012_1_b.txt
wspectext s20080123_00012_123.fits[105:105,1:768] bs936a_012_1_c.txt
wspectext s20080123_00012_456.fits[103:103,1:768] bs936a_012_4_b.txt
wspectext s20080123_00012_456.fits[104:104,1:768] bs936a_012_4_b.txt
wspectext s20080123_00012_456.fits[105:105,1:768] bs936a_012_4_c.txt
```

Appendix B

Supplementary Tables

The Tables within this appendix contain column densities of H_2, CO, C, CH, CH^+, CN, C^+, OH, and HD compiled from the literature for sight lines studied herein. These data were used in creating Figures 6.1 through 6.7.

Table B.1: Column Densities of H_2, CO, and C Reported in the Literature

Object	$\log N(H_2)$ (cm^{-2})	$\log \sigma[N(H_2)]$ (cm^{-2})	H_2 Reference	$\log N(CO)$ (cm^{-2})	$\log \sigma[N(CO)]$ (cm^{-2})	CO Reference	$\log N(C)$ (cm^{-2})	$\log \sigma[N(C)]$ (cm^{-2})	C Reference
HD 20041	⋯	⋯		< 14.97	⋯	4	⋯	⋯	
HD 21389	⋯	⋯		16.00	0.30	5	⋯	⋯	
ζ Per	20.68	0.09	1	14.86	0.17	6	15.48	0.04	6
X Per	20.92	0.05	2	16.15	0.07	7	14.98	0.10	21
HD 29647	⋯	⋯		16.48	0.50	5	⋯	⋯	
HD 73882	21.11	0.08	2	16.55	0.20	7	16.35	0.64	22
HD 110432	20.64	0.03	2	14.60	0.40	8	14.55	0.26	22
HD 154368	21.16	0.12	2	15.43	0.10	9	⋯	⋯	
WR 104	⋯	⋯		15.98	0.02	10	⋯	⋯	
HD 168607	⋯	⋯		⋯	⋯		⋯	⋯	
HD 168625	⋯	⋯		⋯	⋯		⋯	⋯	
HD 169454	⋯	⋯		16.30	0.50	5	⋯	⋯	
W40 IRS 1A	⋯	⋯		18.04	0.08	11	⋯	⋯	
WR 118 (5)	⋯	⋯		16.16	0.02	10	⋯	⋯	
WR 118 (47)	⋯	⋯		16.27	0.02	10	⋯	⋯	
WR 121	⋯	⋯		⋯	⋯		⋯	⋯	
HD 183143 (7)	⋯	⋯		⋯	⋯		⋯	⋯	
HD 183143 (24)	⋯	⋯		15.19	0.03	10	⋯	⋯	
HD 229059	⋯	⋯		⋯	⋯		⋯	⋯	
Cyg OB2 5	⋯	⋯		15.54	0.07	10	⋯	⋯	
Cyg OB2 12	⋯	⋯		16.30	0.20	12	⋯	⋯	
HD 204827	⋯	⋯		⋯	⋯		⋯	⋯	
λ Cep	20.84	0.03	2	15.46	0.06	7	15.00	0.05	21

Table B.1: (continued)

Object	$\log N(\mathrm{H_2})$ (cm^{-2})	$\log \sigma[N(\mathrm{H_2})]$ (cm^{-2})	H$_2$ Reference	$\log N(\mathrm{CO})$ (cm^{-2})	$\log \sigma[N(\mathrm{CO})]$ (cm^{-2})	CO Reference	$\log N(\mathrm{C})$ (cm^{-2})	$\log \sigma[N(\mathrm{C})]$ (cm^{-2})	C Reference
κ Cas	20.27	0.05	1	...	...		15.55	0.20	23
HD 21483	...	...		16.90	1.10	13	17.20	0.20	13
HD 21856	20.04	0.05	1	...	...		...	...	
40 Per	20.46	0.08	1	14.26	0.01	9	15.25	0.05	24
o Per	20.61	0.08	1	14.83	0.01	9	15.68	0.05	24
BD +31 643	21.09	0.15	2	...	...		...	...	
ϵ Per	19.52	0.09	1	11.93	0.08	14	13.64	0.04	25
ξ Per	20.53	0.07	1	13.49	0.04	15	14.82	0.10	15
62 Tau	20.79	0.08	2	16.08	0.03	7	15.06	0.05	21
α Cam	20.34	0.05	1	14.49	0.05	14	15.17	0.20	23
χ^2 Ori	20.69	0.09	3	14.24	0.21	16	...	...	
HD 47129	20.55	0.07	1	14.45	0.42	16	...	...	
HD 53367	21.04	0.06	3	...	...		15.16	1.83	22
o Sco	...	...		16.30	0.50	5	...	...	
HD 147888	20.47	0.09	3	15.30	0.08	7	14.70	0.10	21
HD 147889	...	...		...	...		...	...	
χ Oph	20.63	0.10	1	14.58	0.12	17	15.52	0.46	23
μ Nor	20.44	0.08	1	13.91	0.06	14	15.31	0.20	23
HD 149404	20.79	0.04	3	15.02	0.20	16	14.86	0.09	22
ζ Oph	20.65	0.04	1	15.40	0.03	18	15.50	0.06	26
HD 152236	20.73	0.11	3	14.86	0.20	16	...	...	
BD -14 5037	...	...		...	...		...	...	
P Cygni	...	...		...	...		...	...	

Table B.1: (continued)

Object	$\log N(\mathrm{H_2})$ (cm^{-2})	$\log \sigma[N(\mathrm{H_2})]$ (cm^{-2})	H$_2$ Reference	$\log N(\mathrm{CO})$ (cm^{-2})	$\log \sigma[N(\mathrm{CO})]$ (cm^{-2})	CO Reference	$\log N(\mathrm{C})$ (cm^{-2})	$\log \sigma[N(\mathrm{C})]$ (cm^{-2})	C Reference
HD 193322A	20.08	0.06	1	14.20	0.19	16	…	…	
HD 194279	…	…		…	…		…	…	
Cyg OB2 8A	…	…		14.90	0.50	19	…	…	
HD 206267	20.86	0.04	2	16.04	0.04	7	15.32	0.05	21
19 Cep	20.08	0.06	1	…	…		…	…	
1 Cas	20.15	0.06	1	14.80	0.09	14	…	…	
NGC 2024 IRS 1	…	…		18.10	0.50	20	…	…	

Notes: Column densities of CO reported in McCall et al. (2002) are calculated assuming lines are optically thin. As such, they represent lower limits.

References: (1) Savage et al. (1977); (2) Rachford et al. (2002); (3) Rachford et al. (2009); (4) Dickman et al. (1983); (5) van Dishoeck et al. (1991); (6) Snow (1977); (7) Sonnentrucker et al. (2007); (8) Rachford et al. (2001); (9) Sheffer et al. (2007); (10) McCall et al. (2002); (11) Shuping et al. (1999); (12) McCall et al. (1998); (13) Joseph et al. (1986); (14) Crenny & Federman (2004); (15) Smith et al. (1991); (16) Tarafdar & Krishna Swamy (1982); (17) Federman et al. (2003); (18) Lambert et al. (1994); (19) Snow et al. (2010); (20) T. Snow (private communication); (21) Burgh et al. (2010); (22) Snow et al. (2008); (23) Jenkins et al. (1983); (24) Wannier et al. (1999); (25) Zsargó & Federman (2003); (26) Jenkins & Shaya (1979)

Table B.2: Column Densities of CH, CH$^+$, and CN Reported in the Literature

Object	N(CH) (10^{13} cm^{-2})	$\sigma[N$(CH)] (10^{13} cm^{-2})	CH Reference	N(CH$^+$) (10^{13} cm^{-2})	$\sigma[N$(CH$^+$)] (10^{13} cm^{-2})	CH$^+$ Reference	N(CN) (10^{13} cm^{-2})	$\sigma[N$(CN)] (10^{13} cm^{-2})	CN Reference
HD 20041	4.00	1.00	1	1.38	0.35	2	0.35	0.03	4
HD 21389	1.95	0.50	2	0.93	0.11	2	u.l.	0.02	1
ζ Per	2.03	0.20	3	0.28	0.03	3	0.39	0.04	17
X Per	3.85	0.06	4	0.50	0.05	15	0.75	0.04	4
HD 29647	8.00	2.00	1	u.l.	1.00	2	16.0	3.00	18
HD 73882	3.70	0.50	5	3.40	0.30	5	3.80	0.40	5
HD 110432	1.46	0.05	4	1.61	0.05	15	0.19	0.02	4
HD 154368	7.05	0.13	4	2.29	0.01	16	2.00	0.05	4
WR 104	...	...		...	...		...	...	
HD 168607	6.09	0.22	4	...	...		0.42	0.02	4
HD 168625	5.72	0.21	4	...	...		0.11	0.01	4
HD 169454	5.80	0.80	6	2.05	0.01	16	5.50	0.60	6
W40 IRS 1A	...	...		...	...		...	...	
WR 118 (5)	...	...		...	...		...	...	
WR 118 (47)	...	...		...	...		...	...	
WR 121	...	...		...	...		...	...	
HD 183143 (7)	1.70	0.10	7	2.10	0.06	7	...	...	
HD 183143 (24)	2.77	0.09	7	2.53	0.06	7	0.22	0.03	1
HD 229059	23.0	14.0	6	1.l.	9.55	2	1.40	0.40	1
Cyg OB2 5	5.32	0.13	7	3.44	0.13	7	3.00	1.00	1
Cyg OB2 12	28.0	20.0	8	22.0	10.0	8	1.34	0.17	7
HD 204827	7.33	0.28	4	1.l.	3.55	2	3.40	0.09	4
λ Cep	2.08	0.21	3	1.49	0.15	3	0.27	0.02	4

Table B.2: (continued)

Object	N(CH) (10^{13} cm^{-2})	$\sigma[N$(CH)$]$ (10^{13} cm^{-2})	CH Reference	N(CH$^+$) (10^{13} cm^{-2})	$\sigma[N$(CH$^+$)$]$ (10^{13} cm^{-2})	CH$^+$ Reference	N(CN) (10^{13} cm^{-2})	$\sigma[N$(CN)$]$ (10^{13} cm^{-2})	CN Reference
κ Cas	0.80	0.20	9	0.36	0.10	9	u.l.	0.02	2
HD 21483	4.17	0.42	10	0.83	0.08	2	3.72	0.37	10
HD 21856	...	...		1.00	0.03	15	...	...	
40 Per	1.20	0.12	11	1.11	0.03	15	0.06	0.01	11
o Per	1.90	0.19	3	0.69	0.07	3	0.18	0.02	4
BD +31 643	5.30	0.40	1	1l.	4.27	2	0.40	0.10	1
ϵ Per	u.l.	0.20	2	0.27	0.03	15	...	...	
ξ Per	1.33	0.13	3	2.96	0.30	3	0.03	0.00	17
62 Tau	3.61	0.04	4	1.08	0.05	15	2.08	0.03	4
α Cam	0.69	0.07	3	1.94	0.19	3	u.l.	0.07	1
χ^2 Ori	1.58	0.20	3	2.00	0.40	3	u.l.	0.08	1
HD 47129	0.89	0.09	12	2.12	0.05	15	...	...	
HD 53367	4.40	0.40	1	1.20	0.28	13	0.56	0.06	10
o Sco	6.70	1.10	13	5.10	0.30	13	0.60	0.20	6
HD 147888	2.11	0.06	4	0.81	0.08	2	0.22	0.02	4
HD 147889	10.1	0.25	4	3.16	0.22	2	2.19	0.06	4
χ Oph	3.53	0.02	4	1.37	0.14	3	0.14	0.01	4
μ Nor	1.00	0.10	12	3.51	0.09	15	...	...	
HD 149404	2.72	0.11	4	4.80	0.35	13	0.27	0.03	4
ζ Oph	2.23	0.01	4	2.79	0.28	3	0.28	0.02	4
HD 152236	2.67	0.06	4	2.17	0.03	16	0.25	0.02	4
BD -14 5037	13.5	5.00	6	8.40	0.54	13	1.10	0.11	19
P Cygni	1.10	0.18	2	4.27	0.30	2	...	...	

Table B.2: (continued)

Object	N(CH) $(10^{13}$ cm$^{-2})$	$\sigma[N($CH$)]$ $(10^{13}$ cm$^{-2})$	CH Reference	N(CH$^+$) $(10^{13}$ cm$^{-2})$	$\sigma[N($CH$^+)]$ $(10^{13}$ cm$^{-2})$	CH$^+$ Reference	N(CN) $(10^{13}$ cm$^{-2})$	$\sigma[N($CN$)]$ $(10^{13}$ cm$^{-2})$	CN Reference
HD 193322A	...	...		...	...		...	...	
HD 194279	...	...		...	...		...	...	
Cyg OB2 8A	3.24	0.30	14	11.7	0.27	14	0.23	0.02	14
HD 206267	2.72	0.05	4	1.16	0.03	15	0.80	0.04	4
19 Cep	1.00	0.14	2	2.72	0.11	15	...	...	
1 Cas	0.76	0.08	9	0.96	0.08	15	u.l.	0.07	1
NGC 2024 IRS 1	...	...		...	...		...	...	

Notes: In cases where the column density is reported as u.l. or l.l., the value in the corresponding uncertainty column is an upper limit or lower limit, respectively.

References: (1) Thorburn et al. (2003); (2) D. E. Welty 2002, private communication; (3) Crane et al. (1995); (4) Weselak et al. (2008b); (5) Gredel et al. (2002); (6) van Dishoeck & Black (1989); (7) McCall et al. (2002); (8) Indriolo et al. (2010b); (9) Federman (1982); (10) Federman et al. (1994); (11) Sheffer et al. (2008); (12) Danks et al. (1984); (13) Gredel et al. (1993); (14) Snow et al. (2010); (15) Weselak et al. (2008a); (16) Ritchey et al. (2011); (17) Federman et al. (1984); (18) Crutcher (1985); (19) Gredel et al. (1991)

Table B.3: Column Densities of C$^+$ Reported in the Literature

Object	N(C$^+$) $(10^{17}$ cm$^{-2})$	$\sigma[N$(C$^+$)$]$ $(10^{17}$ cm$^{-2})$	Reference
ζ Per	1.84	0.32	1
X Per	2.70	0.80	2
ξ Per	4.92	1.35	3
62 Tau	u.l.	2.19	4
HD 147888	9.97	1.75	4
ζ Oph	1.80	0.42	3

Notes: For 62 Tau the value in the uncertainty column is an upper limit.

References: (1) Cardelli et al. (1996); (2) Sofia et al. (1998); (3) Cardelli et al. (1993); (4) Sofia et al. (2004)

Table B.4: Column Densities of OH Reported in the Literature

Object	N(OH) $(10^{13}$ cm$^{-2})$	$\sigma[N$(OH)$]$ $(10^{13}$ cm$^{-2})$	Reference
ζ Per	4.05	0.40	1
HD 110432	3.97	0.62	2
HD 154368	17.0	1.57	3
HD 169454	9.88	1.32	3
o Per	7.80	2.60	4
62 Tau	10.2	0.40	1
HD 147889	25.2	3.07	3
ζ Oph	4.10	0.60	3
HD 152236	7.56	0.43	2

References: (1) Felenbok & Roueff (1996); (2) Weselak et al. (2010); (3) Weselak et al. (2009); (4) Roueff (1996)

Table B.5: Column Densities of HD Reported in the Literature

Object	$\log N(\mathrm{HD})$ (cm^{-2})	$\log \sigma[N(\mathrm{HD})]$ (cm^{-2})	Reference
ζ Per	15.55	0.16	1
X Per	15.88	0.40	2
HD 73882	15.81	1.18	2
HD 110432	15.43	0.12	2
ϵ Per	13.57	0.50	3
ξ Per	14.15	0.50	3
62 Tau	15.89	1.10	2
α Cam	14.49	0.50	3
HD 53367	15.74	0.34	2
HD 147888	15.39	1.47	2
HD 149404	15.74	0.12	2
ζ Oph	14.23	0.50	3
HD 206267	15.72	0.14	2

Notes: Column densities from Spitzer et al. (1973) were calculated assuming that lines were unsaturated.

References: (1) Snow (1977); (2) Snow et al. (2008); (3) Spitzer et al. (1973)

References

Abdo, A. A., et al. 2009, ApJ, 706, L1

—. 2010a, ApJ, 718, 348

—. 2010b, Science, 327, 1103

—. 2010c, ApJ, 712, 459

Acciari, V. A., et al. 2009, ApJ, 698, L133

Ádámkovics, M., Blake, G. A., & McCall, B. J. 2003, ApJ, 595, 235

Aharonian, F., et al. 2008, A&A, 481, 401

Albert, J., et al. 2007, ApJ, 664, L87

Alibés, A., Labay, J., & Canal, R. 2002, ApJ, 571, 326

Allen, M. M. 1994, ApJ, 424, 754

Allen, M. M., Snow, T. P., & Jenkins, E. B. 1990, ApJ, 355, 130

AMS Collaboration et al. 2002, Phys. Rep., 366, 331

Anders, E., & Grevesse, N. 1989, Geochim. Cosmochim. Acta, 53, 197

Anicich, V. G., Laudenslager, J. B., Huntress, Jr., W. T., & Futrell, J. H. 1977, J. Chem. Phys., 67, 4340

Arnett, W. D. 1987, ApJ, 319, 136

Bakes, E. L. O., & Tielens, A. G. G. M. 1994, ApJ, 427, 822

Barlow, S. E. 1984, PhD thesis, University of Colorado at Boulder

Beck, R. 2005, Astronomische Nachrichten, 326, 608

Bell, A. R. 1978, MNRAS, 182, 147

Berezhko, E. G., & Ellison, D. C. 1999, ApJ, 526, 385

Bethe, H. 1933, Handbuch der Physik, Vol. 24 (Berlin: Springer) (Pt. 1)

Black, J. H., & Dalgarno, A. 1977, ApJS, 34, 405

Black, J. H., Hartquist, T. W., & Dalgarno, A. 1978, ApJ, 224, 448

Black, J. H., van Dishoeck, E. F., Willner, S. P., & Woods, R. C. 1990, ApJ, 358, 459

Blandford, R., & Eichler, D. 1987, Phys. Rep., 154, 1

Blandford, R. D., & Ostriker, J. P. 1978, ApJ, 221, L29

Blasi, P. 2002, Astroparticle Physics, 16, 429

Bohlin, R. C., Savage, B. D., & Drake, J. F. 1978, ApJ, 224, 132

Brinks, E. 1990, in Astrophysics and Space Science Library, Vol. 161, The Interstellar Medium in Galaxies, ed. H. A. Thronson Jr. & J. M. Shull, 39–65

Brittain, S. D., Simon, T., Kulesa, C., & Rettig, T. W. 2004, ApJ, 606, 911

Burgh, E. B., France, K., & Jenkins, E. B. 2010, ApJ, 708, 334

Burton, M. G., Geballe, T. R., Brand, P. W. J. L., & Webster, A. S. 1988, MNRAS, 231, 617

Butt, Y. M., & Bykov, A. M. 2008, ApJ, 677, L21

Caprioli, D., Amato, E., & Blasi, P. 2010, Astroparticle Physics, 33, 307

Caprioli, D., Blasi, P., & Amato, E. 2009, MNRAS, 396, 2065

Cardelli, J. A., Mathis, J. S., Ebbets, D. C., & Savage, B. D. 1993, ApJ, 402, L17

Cardelli, J. A., Meyer, D. M., Jura, M., & Savage, B. D. 1996, ApJ, 467, 334

Cartledge, S. I. B., Lauroesch, J. T., Meyer, D. M., & Sofia, U. J. 2004, ApJ, 613, 1037

Cassé, M., Lehoucq, R., & Vangioni-Flam, E. 1995, Nature, 373, 318

Castro, D., & Slane, P. 2010, ApJ, 717, 372

Cha, A. N., & Sembach, K. R. 2000, ApJS, 126, 399

Chaffee, Jr., F. H., & White, R. E. 1982, ApJS, 50, 169

Chevalier, C., & Ilovaisky, S. A. 1998, A&A, 330, 201

Chevalier, R. A. 1999, ApJ, 511, 798

Claussen, M. J., Frail, D. A., Goss, W. M., & Gaume, R. A. 1997, ApJ, 489, 143

Clayton, G. C., & Hanson, M. M. 1993, AJ, 105, 1880

Cohen, J. G. 1973, ApJ, 186, 149

Conti, P. S., & Vacca, W. D. 1990, AJ, 100, 431

Cornett, R. H., Chin, G., & Knapp, G. R. 1977, A&A, 54, 889

Crabtree, K. N., Indriolo, N., Kreckel, H., Tom, B. A., & McCall, B. J. 2011, ApJ, 729, 15

Crane, P., Lambert, D. L., & Sheffer, Y. 1995, ApJS, 99, 107

Cravens, T. E., & Dalgarno, A. 1978, ApJ, 219, 750

Crawford, I. A. 1995, MNRAS, 277, 458

Crenny, T., & Federman, S. R. 2004, ApJ, 605, 278

Crutcher, R. M. 1985, ApJ, 288, 604

Crutcher, R. M., & Chu, Y. H. 1982, in Astrophysics and Space Science Library, Vol. 93, Regions of Recent Star Formation, ed. R. S. Roger & P. E. Dewdney, 53–60

Dalgarno, A. 2006, Proc. Nat. Acad. Sci., 103, 12269

Dalgarno, A., Yan, M., & Liu, W. 1999, ApJS, 125, 237

Danks, A. C., Federman, S. R., & Lambert, D. L. 1984, A&A, 130, 62

Dearborn, D. S. P., Schramm, D. N., Steigman, G., & Truran, J. 1989, ApJ, 347, 455

Denoyer, L. K. 1979, ApJ, 232, L165

Dickman, R. L., Snell, R. L., Ziurys, L. M., & Huang, Y. 1992, ApJ, 400, 203

Dickman, R. L., Somerville, W. B., Whittet, D. C. B., McNally, D., & Blades, J. C. 1983, ApJS, 53, 55

Douglas, A. E., & Herzberg, G. 1941, ApJ, 94, 381

Dragicevich, P. M., Blair, D. G., & Burman, R. R. 1999, MNRAS, 302, 693

Drake, G. W. F., & Dalgarno, A. 1968, ApJ, 152, L121

Drury, L. O. 1983, Reports on Progress in Physics, 46, 973

Dunham, Jr., T. 1937, PASP, 49, 26

Emprechtinger, M., et al. 2009, A&A, 496, 731

Esposito, J. A., Hunter, S. D., Kanbach, G., & Sreekumar, P. 1996, ApJ, 461, 820

Federman, S. R. 1982, ApJ, 257, 125

Federman, S. R., Danks, A. C., & Lambert, D. L. 1984, ApJ, 287, 219

Federman, S. R., & Lambert, D. L. 1992, AJ, 104, 691

Federman, S. R., Lambert, D. L., Sheffer, Y., Cardelli, J. A., Andersson, B.-G., van Dishoeck, E. F., & Zsargó, J. 2003, ApJ, 591, 986

Federman, S. R., Strom, C. J., Lambert, D. L., Cardelli, J. A., Smith, V. V., & Joseph, C. L. 1994, ApJ, 424, 772

Federman, S. R., Weber, J., & Lambert, D. L. 1996, ApJ, 463, 181

Felenbok, P., & Roueff, E. 1996, ApJ, 465, L57

Fields, B. D., Casse, M., Vangioni-Flam, E., & Nomoto, K. 1996, ApJ, 462, 276

Fields, B. D., & Olive, K. A. 1999, ApJ, 516, 797

Fields, B. D., Olive, K. A., Cassé, M., & Vangioni-Flam, E. 2001, A&A, 370, 623

Fields, B. D., Olive, K. A., Vangioni-Flam, E., & Cassé, M. 2000, ApJ, 540, 930

Fruscione, A., Hawkins, I., Jelinsky, P., & Wiercigroch, A. 1994, ApJS, 94, 127

Geballe, T. R., Goto, M., Usuda, T., Oka, T., & McCall, B. J. 2006, ApJ, 644, 907

Geballe, T. R., McCall, B. J., Hinkle, K. H., & Oka, T. 1999, ApJ, 510, 251

Geballe, T. R., & Oka, T. 1989, ApJ, 342, 855

—. 1996, Nature, 384, 334

—. 2010, ApJ, 709, L70

Gerin, M., et al. 2010, A&A, 518, L110

Gibb, E. L., Brittain, S. D., Rettig, T. W., Troutman, M., Simon, T., & Kulesa, C. 2010, ApJ, 715, 757

Glassgold, A. E., & Langer, W. D. 1974, ApJ, 193, 73

Gloeckler, G., & Jokipii, J. R. 1969, Physical Review Letters, 22, 1448

Goto, M., McCall, B. J., Geballe, T. R., Usuda, T., Kobayashi, N., Terada, H., & Oka, T. 2002, PASJ, 54, 951

Goto, M., Usuda, T., Geballe, T. R., Indriolo, N., McCall, B. J., Henning, T., & Oka, T. 2011, PASJ, 63, L13

Goto, M., et al. 2008, ApJ, 688, 306

Gredel, R., Pineau des Forêts, G., & Federman, S. R. 2002, A&A, 389, 993

Gredel, R., van Dishoeck, E. F., & Black, J. H. 1991, A&A, 251, 625

—. 1993, A&A, 269, 477

Griem, H. R. 1969, ApJ, 156, L103

Groenewegen, M. A. T., Udalski, A., & Bono, G. 2008, A&A, 481, 441

Gupta, H., et al. 2010, A&A, 521, L47

Habing, H. J., & Goldsmith, D. W. 1971, ApJ, 166, 525

Hartquist, T. W., Black, J. H., & Dalgarno, A. 1978a, MNRAS, 185, 643

Hartquist, T. W., Doyle, H. T., & Dalgarno, A. 1978b, A&A, 68, 65

Hata, J., & Grant, I. P. 1981, Journal of Physics B Atomic Molecular Physics, 14, 2111

Hayakawa, S., Nishimura, S., & Takayanagi, T. 1961, PASJ, 13, 184

Henderson, A. P., Jackson, P. D., & Kerr, F. J. 1982, ApJ, 263, 116

Herbst, E., & Cuppen, H. M. 2006, Proceedings of the National Academy of Science, 103, 12257

Herbst, E., & Klemperer, W. 1973, ApJ, 185, 505

Hess, V. F. 1912, Physik Zeit., 13, 1084

Hewitt, J. W., Yusef-Zadeh, F., & Wardle, M. 2009, ApJ, 706, L270

Hewitt, J. W., Yusef-Zadeh, F., Wardle, M., Roberts, D. A., & Kassim, N. E. 2006, ApJ, 652, 1288

Hinkle, K. H., et al. 2003, Proc. SPIE, 4834, 353

Hirschauer, A., Federman, S. R., Wallerstein, G., & Means, T. 2009, ApJ, 696, 1533

Hobbs, L. M., Black, J. H., & van Dishoeck, E. F. 1983, ApJ, 271, L95

Huang, Y., Dickman, R. L., & Snell, R. L. 1986, ApJ, 302, L63

Indriolo, E. 2009, PhD thesis, Purdue University

Indriolo, N., Blake, G. A., Goto, M., Usuda, T., Oka, T., Geballe, T. R., Fields, B. D., & McCall, B. J. 2010a, ApJ, 724, 1357

Indriolo, N., Fields, B. D., & McCall, B. J. 2009a, ApJ, 694, 257

Indriolo, N., Geballe, T. R., Oka, T., & McCall, B. J. 2007, ApJ, 671, 1736

Indriolo, N., Hobbs, L. M., Hinkle, K. H., & McCall, B. J. 2009b, ApJ, 703, 2131

Indriolo, N., Oka, T., Geballe, T. R., & McCall, B. J. 2010b, ApJ, 711, 1338

Inokuti, M. 1971, Reviews of Modern Physics, 43, 297

Inoue, M. Y., et al. 1993, PASJ, 45, 539

Ip, W., & Axford, W. I. 1985, A&A, 149, 7

Jenkins, E. B., Jura, M., & Loewenstein, M. 1983, ApJ, 270, 88

Jenkins, E. B., & Shaya, E. J. 1979, ApJ, 231, 55

Jenkins, E. B., & Tripp, T. M. 2007, in Astronomical Society of the Pacific Conference Series, Vol. 365, SINS - Small Ionized and Neutral Structures in the Diffuse Interstellar Medium, ed. M. Haverkorn & W. M. Goss, 51

Jensen, A. G., Rachford, B. L., & Snow, T. P. 2005, ApJ, 619, 891

Joseph, C. L., Snow, Jr., T. P., Seab, C. G., & Crutcher, R. M. 1986, ApJ, 309, 771

Jura, M. 1975, ApJ, 197, 581

Kang, H., & Jones, T. W. 1995, ApJ, 447, 944

Karpas, Z., Anicich, V., & Huntress, W. T. 1979, J. Chem. Phys., 70, 2877

Käufl, H., et al. 2004, Proc. SPIE, 5492, 1218

Klippenstein, S. J., Georgievskii, Y., & McCall, B. J. 2010, J. Phys. Chem. A, 114, 278

Kneller, J. P., Phillips, J. R., & Walker, T. P. 2003, ApJ, 589, 217

Kobayashi, N., et al. 2000, Proc. SPIE, 4008, 1056

Kraemer, W. P., ŠPirko, V., & Juřek, M. 1995, Chemical Physics Letters, 236, 177

Krymskii, G. F. 1977, Akademiia Nauk SSSR Doklady, 234, 1306

Kulesa, C. A. 2002, PhD thesis, The University of Arizona

Lacy, J. H., Knacke, R., Geballe, T. R., & Tokunaga, A. T. 1994, ApJ, 428, L69

Lambert, D. L., Sheffer, Y., Gilliland, R. L., & Federman, S. R. 1994, ApJ, 420, 756

Laudenslager, J. B., Huntress, Jr., W. T., & Bowers, M. T. 1974, J. Chem. Phys., 61, 4600

Le Petit, F., Roueff, E., & Herbst, E. 2004, A&A, 417, 993

Lerche, I., & Schlickeiser, R. 1982, MNRAS, 201, 1041

Liszt, H. 2003, A&A, 398, 621

Lodders, K. 2003, ApJ, 591, 1220

Lord, S. D. 1992, NASA Technical Memorandum 103957

Lovas, F. J., & Snyder, L. E. 2010, "Interstellar Molecules" in CRC Handbook of Chemistry and Physics, 91st Edition, ed. W. M. Haynes (CRC Press: Boca Raton, FL), 14–7

Maíz-Apellániz, J., Walborn, N. R., Galué, H. Á., & Wei, L. H. 2004, ApJS, 151, 103

Martin, D. W., McDaniel, E. W., & Meeks, M. L. 1961, ApJ, 134, 1012

Mattila, K. 1986, A&A, 160, 157

McCall, B. J. 2001, PhD thesis, The University of Chicago

McCall, B. J., Geballe, T. R., Hinkle, K. H., & Oka, T. 1998, Science, 279, 1910

—. 1999, ApJ, 522, 338

McCall, B. J., et al. 2002, ApJ, 567, 391

—. 2003, Nature, 422, 500

—. 2004, Phys. Rev. A, 70, 052716

—. 2010, ApJ, 708, 1628

McLean, I. S., et al. 1998, Proc. SPIE, 3354, 566

Meneguzzi, M., Audouze, J., & Reeves, H. 1971, A&A, 15, 337

Meneguzzi, M., & Reeves, H. 1975a, A&A, 40, 99

—. 1975b, A&A, 40, 91

Mercer, D. J., et al. 2001, Phys. Rev. C, 63, 065805

Meyer, J., Drury, L. O., & Ellison, D. C. 1998, Space Sci. Rev., 86, 179

Millikan, R. A. 1926, Proc. Nat. Acad. Sci., 12, 48

Misiriotis, A., Xilouris, E. M., Papamastorakis, J., Boumis, P., & Goudis, C. D. 2006, A&A, 459, 113

Mitchell, J. B. A. 1990, Phys. Rep., 186, 215

Mori, M. 1997, ApJ, 478, 225

Moriguchi, Y., Yamaguchi, N., Onishi, T., Mizuno, A., & Fukui, Y. 2001, PASJ, 53, 1025

Mountain, C. M., Robertson, D. J., Lee, T. J., & Wade, R. 1990, Proc. SPIE, 1235, 25

Nath, B. B., & Biermann, P. L. 1994, MNRAS, 267, 447

Neufeld, D. A., Wolfire, M. G., & Schilke, P. 2005, ApJ, 628, 260

Neufeld, D. A., et al. 2010, A&A, 521, L10

Nichols, J. S., & Slavin, J. D. 2004, ApJ, 610, 285

Nota, A., Pasquali, A., Clampin, M., Pollacco, D., Scuderi, S., & Livio, M. 1996, ApJ, 473, 946

O'Donnell, E. J., & Watson, W. D. 1974, ApJ, 191, 89

Ohira, Y., Murase, K., & Yamazaki, R. 2010, A&A, 513, A17

Oka, T. 1980, Phys. Rev. Lett., 45, 531

—. 1981, Philos. Trans. R. Soc. London A, 303, 543

Oka, T., Geballe, T. R., Goto, M., Usuda, T., & McCall, B. J. 2005, ApJ, 632, 882

Padoan, P., & Scalo, J. 2005, ApJ, 624, L97

Padovani, M., Galli, D., & Glassgold, A. E. 2009, A&A, 501, 619

Pan, K., Federman, S. R., Cunha, K., Smith, V. V., & Welty, D. E. 2004, ApJS, 151, 313

Pasquali, A., Nota, A., Smith, L. J., Akiyama, S., Messineo, M., & Clampin, M. 2002, AJ, 124, 1625

Prantzos, N., Casse, M., & Vangioni-Flam, E. 1993, ApJ, 403, 630

Press, W. H., Teukolsky, S. A., Vetterling, W. T., & Flannery, B. P. 1992, Numerical recipes in FORTRAN. The art of scientific computing, ed. Press, W. H., Teukolsky, S. A., Vetterling, W. T., & Flannery, B. P. (Cambridge: University Press, —c1992, 2nd ed.)

Prodanović, T., & Fields, B. D. 2003, ApJ, 597, 48

—. 2006, ApJ, 645, L125

Rachford, B. L., et al. 2001, ApJ, 555, 839

—. 2002, ApJ, 577, 221

—. 2009, ApJS, 180, 125

Rakshit, A. B. 1982, International Journal or Mass Spectrometry and Ion Physics, 41, 185

Ralchenko, Y., Kramida, A. E., Reader, J., & NIST ASD Team. 2008, NIST Atomic Spectra Database (version 3.1.5; Gaithersburg, MD: National Institute of Standards and Technology), http://physics.nist.gov/asd3

Ramaty, R., Kozlovsky, B., & Lingenfelter, R. E. 1979, ApJS, 40, 487

Read, S. M., & Viola, Jr., V. E. 1984, Atomic Data and Nuclear Data Tables, 31, 359

Rees, M. J., Sciama, D. W., & Stobbs, S. H. 1968, Astrophys. Lett., 2, 243

Reeves, H. 1970, Nature, 226, 727

Reville, B., Kirk, J. G., & Duffy, P. 2009, ApJ, 694, 951

Rho, J., Jarrett, T. H., Cutri, R. M., & Reach, W. T. 2001, ApJ, 547, 885

Ritchey, A. M., Federman, S. R., & Lambert, D. L. 2011, ApJ, 728, 36

Roberge, W., & Dalgarno, A. 1982, ApJ, 255, 489

Roberts, Jr., L. C., et al. 2010, AJ, 140, 744

Röttgering, H. 2003, New Astron. Rev., 47, 405

Roueff, E. 1996, MNRAS, 279, L37

Sackmann, I., & Boothroyd, A. I. 1999, ApJ, 510, 217

Savage, B. D., Bohlin, R. C., Drake, J. F., & Budich, W. 1977, ApJ, 216, 291

Scherb, F. 1968, ApJ, 153, L55

Scherer, K., Fichtner, H., Ferreira, S. E. S., Büsching, I., & Potgieter, M. S. 2008, ApJ, 680, L105

Shaw, G., Ferland, G. J., Srianand, R., & Abel, N. P. 2006, ApJ, 639, 941

Shaw, G., Ferland, G. J., Srianand, R., Abel, N. P., van Hoof, P. A. M., & Stancil, P. C. 2008, ApJ, 675, 405

Sheffer, Y., Rogers, M., Federman, S. R., Abel, N. P., Gredel, R., Lambert, D. L., & Shaw, G. 2008, ApJ, 687, 1075

Sheffer, Y., Rogers, M., Federman, S. R., Lambert, D. L., & Gredel, R. 2007, ApJ, 667, 1002

Shibata, T., Hareyama, M., Nakazawa, M., & Saito, C. 2006, ApJ, 642, 882

Shuping, R. Y., Snow, T. P., Crutcher, R., & Lutz, B. L. 1999, ApJ, 520, 149

Skilling, J., & Strong, A. W. 1976, A&A, 53, 253

Słyk, K., Bondar, A. V., Galazutdinov, G. A., & Krełowski, J. 2008, MNRAS, 390, 1733

Smith, A. M., Bruhweiler, F. C., Lambert, D. L., Savage, B. D., Cardelli, J. A., Ebbets, D. C., Lyu, C.-H., & Sheffer, Y. 1991, ApJ, 377, L61

Smith, I. W. M., Herbst, E., & Chang, Q. 2004, MNRAS, 350, 323

Snell, R. L., Hollenbach, D., Howe, J. E., Neufeld, D. A., Kaufman, M. J., Melnick, G. J., Bergin, E. A., & Wang, Z. 2005, ApJ, 620, 758

Snow, T. P., Destree, J. D., Burgh, E. B., Ferguson, R. M., Danforth, C. W., & Cordiner, M. 2010, ApJ, 720, L190

Snow, T. P., & McCall, B. J. 2006, ARA&A, 44, 367

Snow, T. P., Ross, T. L., Destree, J. D., Drosback, M. M., Jensen, A. G., Rachford, B. L., Sonnentrucker, P., & Ferlet, R. 2008, ApJ, 688, 1124

Snow, Jr., T. P. 1977, ApJ, 216, 724

Sodroski, T. J., et al. 1994, ApJ, 428, 638

Sofia, U. J., Fitzpatrick, E., & Meyer, D. M. 1998, ApJ, 504, L47

Sofia, U. J., Lauroesch, J. T., Meyer, D. M., & Cartledge, S. I. B. 2004, ApJ, 605, 272

Sofia, U. J., Parvathi, V. S., Babu, B. R. S., & Murthy, J. 2011, AJ, 141, 22

Sonnentrucker, P., Welty, D. E., Thorburn, J. A., & York, D. G. 2007, ApJS, 168, 58

Spitzer, L., Drake, J. F., Jenkins, E. B., Morton, D. C., Rogerson, J. B., & York, D. G. 1973, ApJ, 181, L116

Spitzer, Jr., L., & Tomasko, M. G. 1968, ApJ, 152, 971

Stancil, P. C., Lepp, S., & Dalgarno, A. 1998, ApJ, 509, 1

Stancil, P. C., Schultz, D. R., Kimura, M., Gu, J., Hirsch, G., & Buenker, R. J. 1999, A&AS, 140, 225

Steigman, G., & Walker, T. P. 1992, ApJ, 385, L13

Stone, E. C., Cummings, A. C., McDonald, F. B., Heikkila, B. C., Lal, N., & Webber, W. R. 2005, Science, 309, 2017

Strong, A. W., Moskalenko, I. V., & Ptuskin, V. S. 2007, Annual Review of Nuclear and Particle Science, 57, 285

Swordy, S. P. 2001, Space Sci. Rev., 99, 85

Tarafdar, S. P., & Krishna Swamy, K. S. 1982, MNRAS, 200, 431

Tatischeff, V., & Kiener, J. 2004, New Astron. Rev., 48, 99

Tavani, M., et al. 2010, ApJ, 710, L151

Teegarden, B. J., & Watanabe, K. 2006, ApJ, 646, 965

Theard, L. P., & Huntress, W. T. 1974, J. Chem. Phys., 60, 2840

Thomson, J. J. 1911, Phil. Mag., 21, 225

Thorburn, J. A., et al. 2003, ApJ, 584, 339

Tielens, A. G. G. M. 2005, The Physics and Chemistry of the Interstellar Medium (Cambridge: Cambridge University Press)

Torres, D. F., Marrero, A. Y. R., & de Cea Del Pozo, E. 2010, MNRAS, 408, 1257

Torres, D. F., Rodriguez Marrero, A. Y., & de Cea Del Pozo, E. 2008, MNRAS, 387, L59

Troja, E., Bocchino, F., & Reale, F. 2006, ApJ, 649, 258

Tuthill, P. G., Monnier, J. D., Lawrance, N., Danchi, W. C., Owocki, S. P., & Gayley, K. G. 2008, ApJ, 675, 698

Usuda, T., & Goto, M. 2005, in High Resolution Infrared Spectroscopy in Astronomy, ed. H. U. Käufl, R. Siebenmorgen, & A. Moorwood, 248–251

Valle, G., Ferrini, F., Galli, D., & Shore, S. N. 2002, ApJ, 566, 252

van den Bergh, S., & Tammann, G. A. 1991, ARA&A, 29, 363

van der Tak, F. F. S., Belloche, A., Schilke, P., Güsten, R., Philipp, S., Comito, C., Bergman, P., & Nyman, L. 2006, A&A, 454, L99

van der Tak, F. F. S., & van Dishoeck, E. F. 2000, A&A, 358, L79

van Dishoeck, E. F., & Black, J. H. 1986, ApJS, 62, 109

—. 1989, ApJ, 340, 273

van Dishoeck, E. F., Black, J. H., Phillips, T. G., & Gredel, R. 1991, ApJ, 366, 141

van Dishoeck, E. F., Jansen, D. J., & Phillips, T. G. 1993, A&A, 279, 541

van Leeuwen, F. 2007, A&A, 474, 653

Vangioni-Flam, E., Cassé, M., & Audouze, J. 2000, Phys. Rep., 333, 365

Vangioni-Flam, E., Casse, M., Fields, B. D., & Olive, K. A. 1996, ApJ, 468, 199

Wagenblast, R., & Hartquist, T. W. 1988, MNRAS, 230, 363

Walker, T. P., Viola, V. E., & Mathews, G. J. 1985, ApJ, 299, 745

Wang, Z., & Scoville, N. Z. 1992, ApJ, 386, 158

Wannier, P., Andersson, B.-G., Penprase, B. E., & Federman, S. R. 1999, ApJ, 510, 291

Wardle, M., & Yusef-Zadeh, F. 2002, Science, 296, 2350

Watson, W. D. 1973, ApJ, 183, L17

Webber, W. R. 1998, ApJ, 506, 329

Webber, W. R., & Higbie, P. R. 2009, Journal of Geophysical Research (Space Physics), 114, A02103

Welsh, B. Y., & Sallmen, S. 2003, A&A, 408, 545

Welty, D. E., & Hobbs, L. M. 2001, ApJS, 133, 345

Weselak, T., Galazutdinov, G., Beletsky, Y., & Krełowski, J. 2009, A&A, 499, 783

Weselak, T., Galazutdinov, G., Musaev, F., & Krełowski, J. 2008a, A&A, 479, 149

Weselak, T., Galazutdinov, G. A., Beletsky, Y., & Krełowski, J. 2010, MNRAS, 402, 1991

Weselak, T., Galazutdinov, G. A., Musaev, F. A., & Krełowski, J. 2008b, A&A, 484, 381

White, G. J. 1994, A&A, 283, L25

White, G. J., Rainey, R., Hayashi, S. S., & Kaifu, N. 1987, A&A, 173, 337

Williams, J. P., Bergin, E. A., Caselli, P., Myers, P. C., & Plume, R. 1998, ApJ, 503, 689

Wolfire, M. G., McKee, C. F., Hollenbach, D., & Tielens, A. G. G. M. 2003, ApJ, 587, 278

Woodall, J., Agúndez, M., Markwick-Kemper, A. J., & Millar, T. J. 2007, A&A, 466, 1197

Woodworth, J. R., & Moos, H. W. 1975, Phys. Rev. A, 12, 2455

Woosley, S. E. 1988, ApJ, 330, 218

Woosley, S. E., Hartmann, D. H., Hoffman, R. D., & Haxton, W. C. 1990, ApJ, 356, 272

Yusef-Zadeh, F., Muno, M., Wardle, M., & Lis, D. C. 2007, ApJ, 656, 847

Yusef-Zadeh, F., Wardle, M., Rho, J., & Sakano, M. 2003, ApJ, 585, 319

Zhang, Z., Gao, Y., & Wang, J. 2010, Science in China G: Physics and Astronomy, 53, 1357

Zsargó, J., & Federman, S. R. 2003, ApJ, 589, 319

Vita

Nicholas Indriolo was born on December 6, 1982 in Akron, Ohio to parents Tom and Betty Indriolo, one year, one month, and minus one day after his sister Emily. He spent the first 7 years of his life in Cuyahoga Falls, Ohio before moving to Canton, Ohio, where, in 1996, upon placing 10th in *Reach for the Stars* at the National Science Olympiad Tournament, he decided that a career in astronomy was the path of least resistance. In 2001 he graduated from GlenOak High School, and in 2005 he graduated *magna cum laude* from Case Western Reserve University with a B.S. in Astronomy. After receiving a Ph.D. in Astronomy from the University of Illinois in 2011, he will begin work with David Neufeld at Johns Hopkins University as an Assistant Research Scientist.